Cooling Flow Effects on Rotor Heat Transfer Distribution in Highly Loaded Axial Turbines

A thesis submitted to attain the degree of

DOCTOR OF SCIENCES of ETH ZURICH

(Dr. sc. ETH Zurich)

presented by

DOMINIC D. HÄNNI

MSc ETH ME, ETH Zurich
born on 31.05.1990
citizen of Toffen BE, Switzerland

accepted on the recommendation of
Prof. Dr. Reza S. Abhari, examiner
Prof. Dr. Thomas Rösgen, co-examiner
Prof. Dr. Anestis I. Kalfas, co-examiner

2020

Acknowledgements

Abstract

In addition to their efficiency, the versatility of gas turbines is a major driver in their development for aero engines and power production. Advanced materials, cooling and thermal management are the main factors driving the reliable operation of gas turbines with main gas temperatures above their metal melting temperature. While adequate cooling is highly necessary, it comes at a cost. An improved understanding of heat transfer can reduce cooling requirements for components and shift the trade-off between increasing turbine inlet temperatures and associated cooling requirements for higher efficiencies. Improvements to design methods and new manufacturing techniques—such as neural network-based computational fluid dynamic optimisations and 3D printing—broaden the design space for engineers and facilitate increasingly integrated component designs. This results in a strong need for cost- and time-effective experimental testing and verification of numerical predictions.

Due to the complexity of measuring high-resolution heat transfer on rotating components in gas turbine research facilities, relatively little experimental data are available in the open literature. Instead, most investigations are based on experiments in linear cascades with low geometrical complexity and simple inflow conditions. In particular, the unsteady flow field and interactions between main flow and cavity flows is not representative in such experiments. Established techniques used on rotating components such as thin-film gauges provide only single-point measurement data.

This thesis contributes to the experimental setup and instrumentation for high-resolution heat transfer measurements on rotating turbomachinery components by improving a novel setup using a high-speed infrared-based technique. The rotor hub endwall heat transfer coefficient and purge flow cooling effectiveness of an endwall with contouring extended into the disc cavity is investigated for various purge flow injection rates. Using numerical simulations, the capabilities and challenges on heat transfer are assessed.

The work in this thesis was performed within a joint industrial and academic research project to investigate the effect of advanced airfoil designs on the aerothermodynamics of gas turbines with cooling flows, with a special focus on heat transfer. Experimental measurements were performed in a state of the art and highly accurate axial turbine research facility. Aerodynamic measurements using pneumatic five-hole probes and fast response aerodynamic probes were performed to characterise the flow field, define boundary conditions and validate the numerical simulations. Moreover, a previously developed heat transfer measurement setup was improved for highly curved surfaces and rotor blade tip measurements. Insert-based custom-made thin-film resistive heaters based on chemical deposited nickel on a low thermal conductive substrate were manufactured and integrated on an aluminium bladed disk rotor to create controlled heat flux boundary conditions. The pressure and temperature on the rotor and the power for the heating platforms were acquired and controlled using a rotating data acquisition system mounted on the rotor. The test facility was modified to integrate the injection of dry cold air from a secondary loop to create a temperature difference between the injection cooling air and the main flow. A modular tip instrumentation setup was introduced to allow tip cooling integration for bladed disk rotors and simultaneous tip heat transfer measurements in a rainbow rotor approach with multiple geometries in a single test run. Complementary numerical investigations were performed using a Navier-Stokes solver for turbomachinery applications on a high-performance computing cluster.

The developed technique for nickel thin-film resistance heaters was demonstrated to be reliable and versatile for complex geometries with high uniformity in the heat flux produced. The variable blade tip instrumentation was successfully implemented, used for measurement and proven to be robust with over 120 turbine start-ups and nearly 1000 turbine operating hours. For the investigated endwall geometry, local variations in heat transfer coefficient above $\pm 20\,\%$ were observed between the blade suction side and the endwall hill for purge flow rate variations between $0.0\,\%$ and $1.2\,\%$. The steep contouring hill deflects the main flow into the cavity and promotes a jet-like purge flow ejection from the cavity, thereby limiting the cooled platform area from the purge flow. The effect of purge flow on the endwall is limited to the front part of the platform upstream from the cross-passage migration of the secondary flow structures. Notably, both steady-state and unsteady simulations predicted the distribution of local heat transfer coeffi-

cients reasonably well in comparison to the experimental results. Regarding cooling effectiveness, an overestimation by the steady-state solution was observed due to suppression of the unsteady interaction between the main flow and cavity as well as the mixing of the two. To the best of the author's knowledge, this study provides the first high-resolution heat transfer measurements at rotor blade tips performed in a rotating facility using a high-speed infrared camera and heat flux controlled boundary conditions. A unique data set of heat transfer coefficient data for various rotor blade tip geometries—with and without film cooling—has been acquired.

Pronounced geometrical features on the rotor platform, such as upstream and cavity extended endwall contouring, can introduce regions of increased heat transfer that are not caused by secondary flows structures created in the passage and should be considered in the design phase. Due to the unsteady nature of the cavity and main flow interaction, unsteady simulations are required to correctly predict the cooling effect of purge flow injection on the hub endwall.

Kurzfassung

Neben ihrem Wirkungsgrad ist die Vielseitigkeit von Gasturbinen ein wichtiger Faktor bei ihrer Entwicklung für Flugzeugtriebwerke und für die Stromerzeugung. Fortschrittliche Werkstoffe, die Kühlung sowie das Wärmemanagement sind die Hauptfaktoren, welche den zuverlässigen Betrieb von Gasturbinen mit Hauptgastemperaturen höher als der Schmelztemperatur ihrer Komponenten erlauben. Eine angemessene Kühlung ist zwar dringend erforderlich, hat aber ihren Preis. Ein besseres Verständnis der Wärmeübertragung kann den Bedarf an Kühlluft für die verschiedenen Komponenten verringern und den Kompromiss zwischen steigenden Turbineneintrittstemperaturen und dem damit verbundenen Kühlungsbedarf zugunsten höhere Wirkungsgrade verschieben. Verbesserungen der Konstruktionsmethoden und neue Fertigungstechniken—wie auf neuronalen Netzen basierende rechnergestützte Optimierungen der Strömungsdynamik und 3D-Drucken—erweitern den Konstruktionsraum für Ingenieure und erleichtern die zunehmend integrierte Komponentenkonstruktionen. Daraus ergibt sich ein starker Bedarf an kosten- und zeiteffektiven experimentellen Tests zur Verifizierung numerischer Vorhersagen.

Da hochauflösende Messungen des Wärmeübergangs an rotierenden Gasturbinenkomponenten in Prüfständen sehr komplex sind, gibt es in der Literatur nur sehr wenig experimentell gemessene Daten. Stattdessen basieren die meisten Untersuchungen auf Experimenten durchgeführt in linearen Kaskaden mit geringer geometrischer Komplexität und einfachen Anströmungsbedingungen. Insbesondere das instationäre Strömungsfeld und die Wechselwirkungen zwischen Hauptströmung und Sekundärströmungen sind bei solchen Experimenten nicht repräsentativ. Etablierte Techniken die an rotierenden Komponenten eingesetzt werden, wie beispielsweise Wärmestromdichte-Streifen, können nur Daten an einzelnen Messpunkten erfassen.

Diese Arbeit leistet einen Beitrag zum experimentellen Aufbau und zur Instrumentierung für hochauflösende Wärmeübertragungsmessungen an

rotierenden Turbomaschinenkomponenten durch die Verbesserung eines neuartigen Aufbaus unter Verwendung einer Hochgeschwindigkeits-Infrarot-basierten Technik. Die Verteilung des Wärmeübertragungskoeffizienten auf der Laufradplattform sowie die Kühleffektivität der Laufradscheibenkühlluft werden für eine verlängerte konturierte Plattform für verschiedene Spülströmungen untersucht. Mithilfe numerischer Simulationen werden die Fähigkeiten und Herausforderungen dieser bei der Vorhersage der Wärmeübertragung bewertet.

Diese Dissertation wurde im Rahmen eines gemeinsamen Forschungsprojekt mit der Industrie durchgeführt, welches die Auswirkungen fortschrittlicher Schaufelkonstruktionen auf die aero-thermische Leistung von Gasturbinen mit Kühlströmungen zu untersuchen. Experimentelle Messungen wurden in einem rotierenden Gasturbinenprüfstand durchgeführt. Zur Charakterisierung des Strömungsfeldes wurden aerodynamische Messungen mit pneumatischen und schnell ansprechenden Sonden durchgeführt, welche zum Definieren der Randbedingungen der numerischen Simulationen dienten. Darüber hinaus wurde ein zuvor entwickelter Wärmeübertragungsmessaufbau für Messungen an stark gekrümmte Oberflächen und Laufradblattspitzen verbessert. Speziell angefertigte Einsätze mit einer Dünnschicht-Widerstandsheizung, welche auf einem Substrat mit geringer Wärmeleitfähigkeit und einem chemisch abgeschiedenem Nickel Film basieren, wurden hergestellt und in einem Turbinenlaufrad integriert um kontrollierte Wärmestrom-Randbedingungen zu schaffen. Druck- und Temperaturmessungen auf dem Laufrad sowie die Leistung für die Heizplattformen wurden mit einem auf dem Laufrad montiertem rotierenden Datenerfassungssystem erfasst und gesteuert. Die Versuchsanlage wurde modifiziert, sodass trockene Kaltluft aus einem Sekundärkreislauf als Kühlluft verwendet werden konnte um eine Temperaturdifferenz zwischen Hauptstrom und Kühlluft zu erzeugen. Eine modulare Instrumentierung für aero-thermische Messungen an Laufradschaufelspitzen wurde eingeführt, welche auch eine Versorgung einzelner Schaufeln mit Kühlluft erlaubte. Durch diese Instrumentierung war es möglich, mehrere verschiedene Schaufelspitzengeometrien auf einem einzelnen Laufrad zu integrieren und Messungen in einem Testlauf durchzuführen.

Die entwickelte Technik für Nickel-Dünnschicht-Widerstandsheizungen erwies sich als zuverlässig und vielseitig einsetzbar für komplexe Geometrien mit hoher Gleichförmigkeit des erzeugten Wärmestroms. Die Instrumentie-

rung mit variabler Schaufelspitze wurde erfolgreich für Messung eingesetzt und erwies sich nach über 120 Turbinenstarts und fast 1000 Turbinenbetriebsstunden als robust. Für die untersuchte Laufradplatform wurden lokale Variationen des Wärmeübergangskoeffizienten von mehr als $\pm 20\,\%$ zwischen der Schaufelsaugseite und dem Hügel der Plattformkonturierung für Laufradscheibenkühlluftraten zwischen $0.0\,\%$ und $1.2\,\%$ beobachtet. Die steile Konturierung des Plattformhügels lenkt Teile des Hauptstroms in den Laufradscheibenraum ab und fördert eine Strahlförmige Kühlluftausblasung aus dem Zwischenraum, wodurch die davon gekühlte Fläche der Plattform begrenzt wird. Die Kühlwirkung auf die Laufradplattform beschränkt sich auf den vorderen Teil der Plattform stromaufwärts der druckgetriebenen Migration der Laufradsekundärströmungen zur Saugseite. Bemerkenswert ist, dass sowohl stationäre als auch instationäre Simulationen die Verteilung der lokalen Wärmeübertragungskoeffizienten im Vergleich zu den experimentellen Ergebnissen gut vorhersagen. Hinsichtlich der Kühleffektivität wurde eine Überschätzung durch die stationäre Lösung aufgrund der Unterdrückung der zeitaufgelösten Wechselwirkung zwischen der Hauptströmung und dem Hohlraum sowie der Vermischung der beiden beobachtet.

Nach bestem Wissen des Autors liefert diese Untersuchung die ersten hochauflösenden Wärmeübergangsmessungen an Laufradblattspitzen, die in einem rotierenden Prüfstand mit einer Hochgeschwindigkeits-Infrarotkamera und kontrollierten thermischen Randbedingungen durchgeführt wurden. Es wurde ein einzigartiger Datensatz von Wärmeübergangskoeffizientenverteilungen für verschiedene Laufradblattspitzengeometrien—mit und ohne Filmkühlung—erfasst.

Ausgeprägte geometrische Merkmale auf der Laufradplattform, wie z.B. die stromaufwärts gerichtete und Laufradnebenraum erweiterte Konturierung, können Bereiche mit erhöhtem Wärmeübergang einführen die nicht durch sekundäre Strömungsstrukturen der Turbinenschaufeln verursacht werden und in der Konstruktionsphase berücksichtigt werden sollten. Aufgrund der instationären Natur der Strömung im Laufradnebenraum und der Interaktion mit der Hauptströmung sind zeitaufgelöste Simulationen erforderlich um den Kühleffekt der Laufradscheibenkühlluft auf die Laufradplattform korrekt vorherzusagen.

Contents

1. Introduction

1.1. Motivation

The rapid technological developments of the past century have brought considerable social wealth and amenities to people. The driving forces behind economic growth and globalisation include energy systems and transportation. To date, most power generation and transportation systems have been based on the use of fossil fuels. This rapid growth using fossil fuels has resulted in a massive amount of greenhouse gas emissions being released into the atmosphere, where unprecedented levels of carbon dioxide, methane and nitrous oxides concentrations are present. According to the Intergovernmental Panel on Climate Change (IPPC), the human influence on earth's climate system is clear and greenhouse gases are likely the dominant cause of the global warming observed since the mid-20th century [79]. Climate change has become a dominant topic in national and global politics, which has resulted in energy transformation strategies being discussed and implemented. Nearly 190 parties have become part of the Paris Agreement, which has the long-term goal of keeping the increase in global average temperature well below 2 °C above pre-industrial levels [122]. The continuous economic growth and increased demand for mobility—especially in emerging countries—will further increase the pressure to reduce global emissions. Additionally, the anticipated increase in the world population from 7.7 billion in 2019 to an estimated 10.1 billion in 2050 [123] will impact future total energy demand. Therefore, future technological developments are influenced by a combination of economic, social and environmental aspects.

Energy Market

In recent years, most countries implemented policies to promote the use of renewable energies. Undoubtedly the CO_2 neutral energy supply of the future will be based on renewable energy sources such as hydro, solar, wind and geothermal power. From the perspective of energy transition, natural

gas can provide near-term benefits when replacing more polluting fuels [6]. According to projections from the U.S. Energy Information Administration, energy consumption will rise by nearly 50 % between 2018 and 2050 [5]. The greatest amount of growth (70 %) is expected among non-OECD countries. While renewable energy will become the leading source of primary energy, the consumption of all other energy sources is also projected to increase (Figure 1.1).
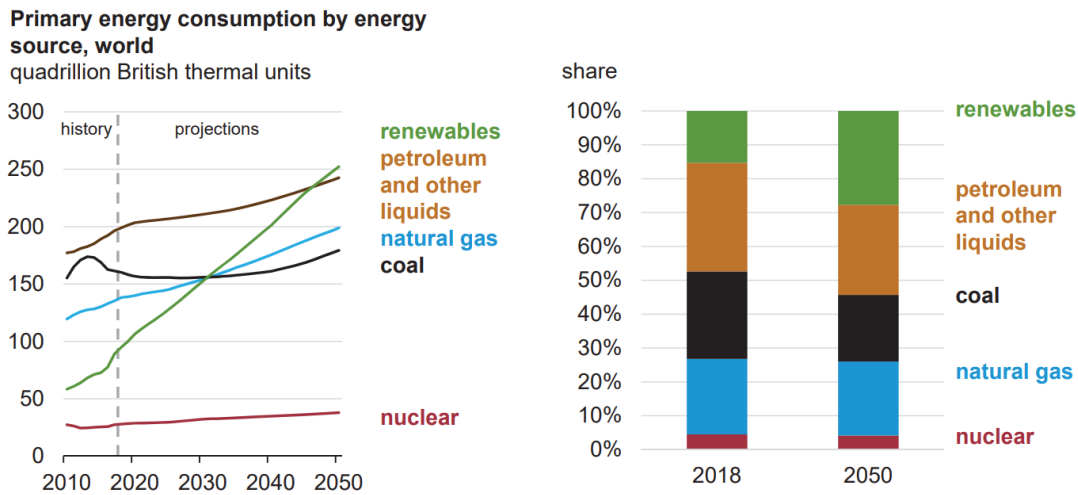
Figure 1.1.: Projected world primary energy consumption by energy source [5].

For the electricity sector, renewable energy sources will cover nearly 50 % of energy production until 2050 [5] (Figure 1.2). This will be particularly evident in the residential sector due to increased income and urban migration as well as the shift to battery-powered vehicles increasing electricity consumption.

The increased penetration of renewable energy sources in electricity generation imposes new challenges for grid stability and security of supply. The intermittency of renewable energy sources must be dealt with using "smart grid" solutions, short- and long-term energy storage or rapidly available energy sources. This is where gas turbine power plants are projected to serve a major role in the near future. Their short ramp-up time enable operators to flexible begin producing electricity according to demand. Furthermore, rotating machines running synchronously also bring stability and resilience to power systems. For conventional power plant operators, the operational flexibility and future impact of CO_2 regulations are of primary concern. The first simple cycle gas turbine for commercial power generation (installed

Net electricity generation by fuel, world
trillion kilowatthours

Share of net electricity generation, world
percent
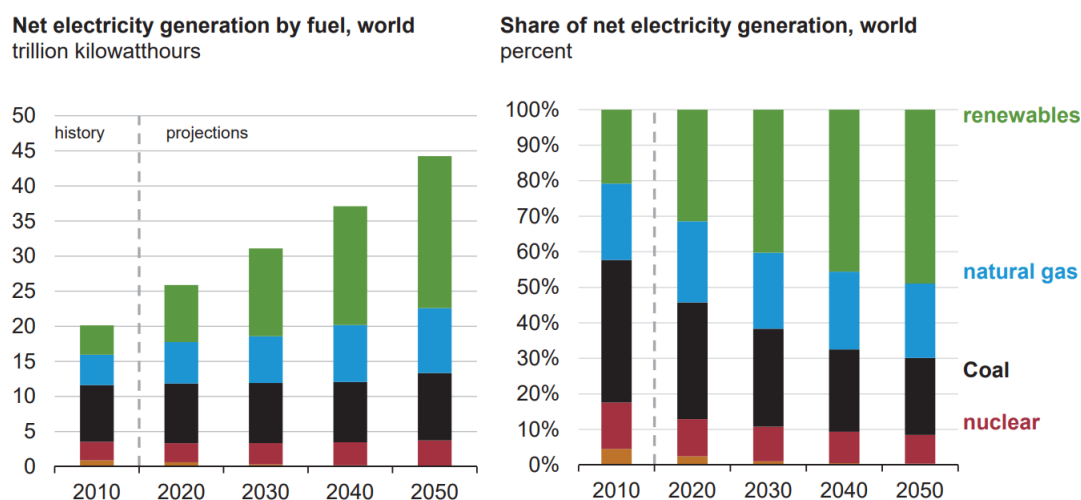
Figure 1.2.: Projected net electricity generation (left) and share (right) by fuel until 2050 [5].

1939 in Neuchâtel, Switzerland) was a technical milestone, however, it only reached an efficiency of 17.4%. With technical progress, combined cycle gas turbine plants—where hot exhaust gases are used for an additional steam cycle—currently reach thermal efficiencies above 60%. The current global thermal efficiency record (63.08%) was achieved by the Nishi-Nagoya Thermal Power Station in Japan in 2018. Since fuel costs account for up to four-fifths of the total running cost for gas turbine power plants, even small improvements in efficiency can have significant impacts for operators and emissions. Therefore, the continuous push for high efficiency with improved thermal designs for increased ramp-up times is driving the development of stationary gas turbines.

Air Transportation

Much like the energy sector, air transportation is also facing similar challenges related to climate change. Despite producing only $\sim 2\%$ of human-induced global carbon dioxide emissions in 2019 [60], the aviation industry is often a specific target for climate activist movements. In the context of reducing the human impact on global warming, the International Air Transport Association (IATA) set targets to reduce CO_2 emissions by the aviation industry. The targets include the carbon-neutral growth of air transport from 2020 onward and a 50% reduction in net aviation CO_2 emissions by 2050 (compared to 2005 levels). Notably, technological improvement represents one of the four pillars of the strategy used to reach these goals.
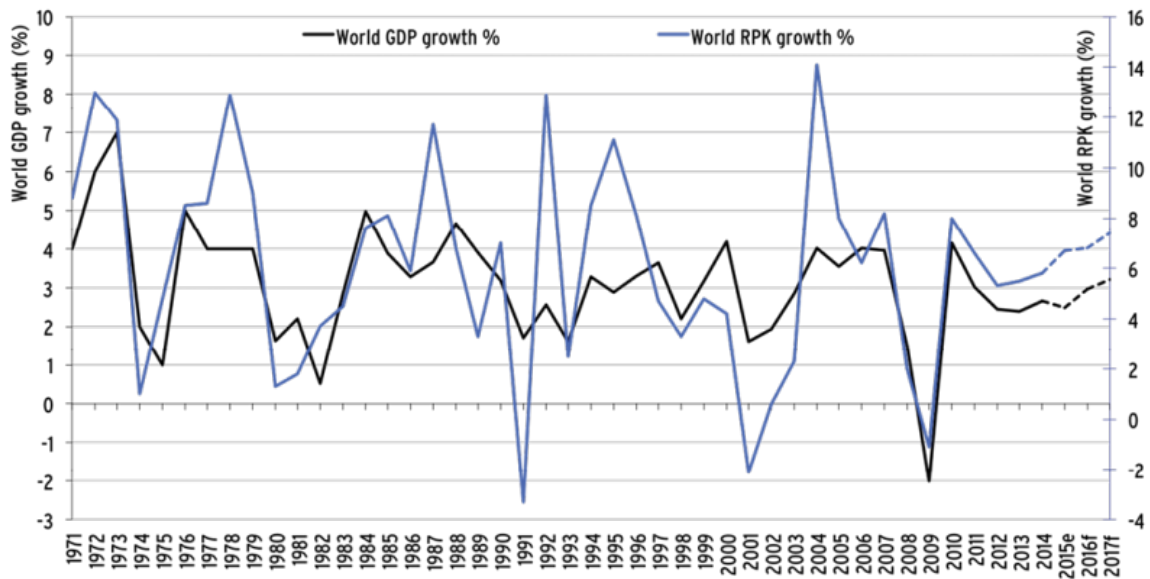
Figure 1.3.: Development of global GDP growth versus revenue passenger kilometres (RPK) growth between 1971 and 2014 [51].

These ambitious goals aim to reach a growing market. Recently, the total number of air passengers carried increased to a total of 4.3 billion [78]. Moreover, a projection by the IATA predicts a near doubling of passengers (8.2 billion) by 2037 [77]. This good prospect for the aviation industry could only be clouded by a global recession or crisis since. Passenger and air freight demand are tightly coupled with the gross domestic product (GDP) growth. Figure 1.3 illustrates the growth in global GDP revenue versus passenger kilometre (RPK) growth until 2014. A pandemic, such as the coronavirus (COVID-19) outbreak of 2019 was not predicted and has had a tremendous impact on the industry. Travel bans in most countries have drastically decreased the demand for air travel and led to a temporary grounding of major portions of global airlines fleets. The short-term impact on the industry is massive and the questions of if and when the aviation industry will fully recover from the effects of the pandemic remain unanswered.

Since their first use in a commercial aircraft in 1952 (de Havilland Comet), jet engines began their triumphant march in aircraft propulsion. All large commercial aircraft designed in the last 40 years are powered by gas turbine engines. Despite discussions on electrification and other alternative means of aircraft propulsion, gas turbine engines represent the only viable means of propulsion for commercial aviation for the foreseeable future[50].

Fuel is a major expense in the airline industry, accounting for approximately 20 % of total operating expenses. Therefore, fuel efficiency is the major

driver for developing new engines and airframes. A major leap forward in jet aircraft efficiency has been achieved over the past 50 (Figure 1.4a).
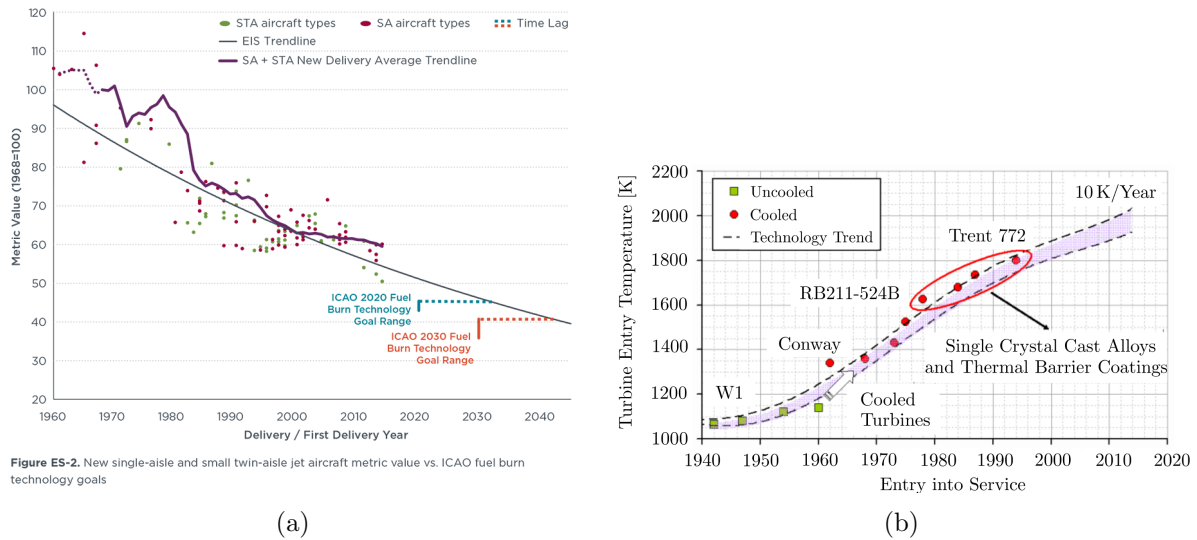
Figure 1.4.: The development of new jet aircraft efficiency normalised to 1968 values [85] (a) and increase of turbine inlet temperature with active cooling [90] (b).

New engine developments have been major contributors to improving aircraft fuel efficiency and emission reductions. For example, major improvements in thrust-specific fuel consumption were achieved by the transition from pure turbojets to high-bypass turbofan engines. Moreover, thermal efficiency improvements were driven by increasing turbine inlet temperatures. A continuous increase has been achieved since the first uncooled jet engines were developed between 1940 and 1960, which was only possible due to progress in materials and manufacturing as well as active cooling technologies (Figure 1.4b b). In modern engines, up to 20 % of the main flow is bled off for cooling and sealing of the hot section components. However, the amount of cooling air should be minimised since it represents high-value air that is not producing any work. Clever cooling strategies and an improved understanding of cooling flows and their effects are thus critical to further efficiency gains in gas turbine engines.

1.2. Literature Review

The design and manufacturing of highly efficient and reliable gas turbines are multidisciplinary and complex processes. A profound understanding of the flow physics, as well as excellence in materials and manufacturing,

are required to build state-of-the-art machines. Thus, it is unsurprising that the earliest use of the term "state-of-the-art" was in the context of gas turbines, dating back to an engineering manual written by Henry Harrison Suplee [169] in 1910. According to Bradshaw [30], axial flow turbines likely represent the most complicated fluid dynamic devices ever invented. This section briefly reviews the literature relevant to this work.

Losses and Secondary Flows in Axial Turbines

Efficiency is one of the most important performance factors for gas turbine engines. However, increasing the efficiency of such machines requires a profound understanding of loss mechanisms. Denton [39] outlined the origin and effects of losses in his Scholar Lecture for the International Gas Turbine Institute (IGTI), in which he also formulated losses as any flow feature that reduces efficiency and contributes to entropy production. Historically, losses were divided into "profile loss", "endwall loss" and "leakage loss". However, these loss mechanisms are seldom fully independent of each other. Additionally, Denton [39] identified three fluid dynamic processes that contribute to entropy generation: viscus effects, heat transfer and non-equilibrium processes.

The presence of walls and pressure gradients, as well as the three-dimensional flow in axial turbines, lead to the formation of complex flow structures. These secondary flow structures can account for $30\,\%$ to $50\,\%$ of total aerodynamic losses [165] and are of particular interest in turbomachinery research. The research addressing this topic goes back to the early 1950s, with publications by Hawthorne and von Karman [69], Squire and Winter [168], Herzig et al. [71] and Hawthorne [68], among others. Moreover, concise reviews of research on secondary flow structures were presented by Sieverding [166] and later by Langston [93]. Illustrative flow models on secondary flow structures (Figure 1.5) presented by Langston [92], Goldstein and Spores [55] and others are widely used in the turbomachinery community.

Apart from some smaller vortices (e.g. corner vortices), the two predominant endwall secondary flow structures include the horseshoe vortex and the passage vortex. The static pressure field of the blade leading edge leads to a stagnation point upstream where the low momentum boundary layer of the incoming fluid rolls up as horseshoe vortices. Due to the cross-passage pressure gradient, the pressure side vortex leg is pushed towards the blade suction side. The suction side vortex leg remains close to the blade suction side and lifts off of the endwall once the suction side leg hits the blade.
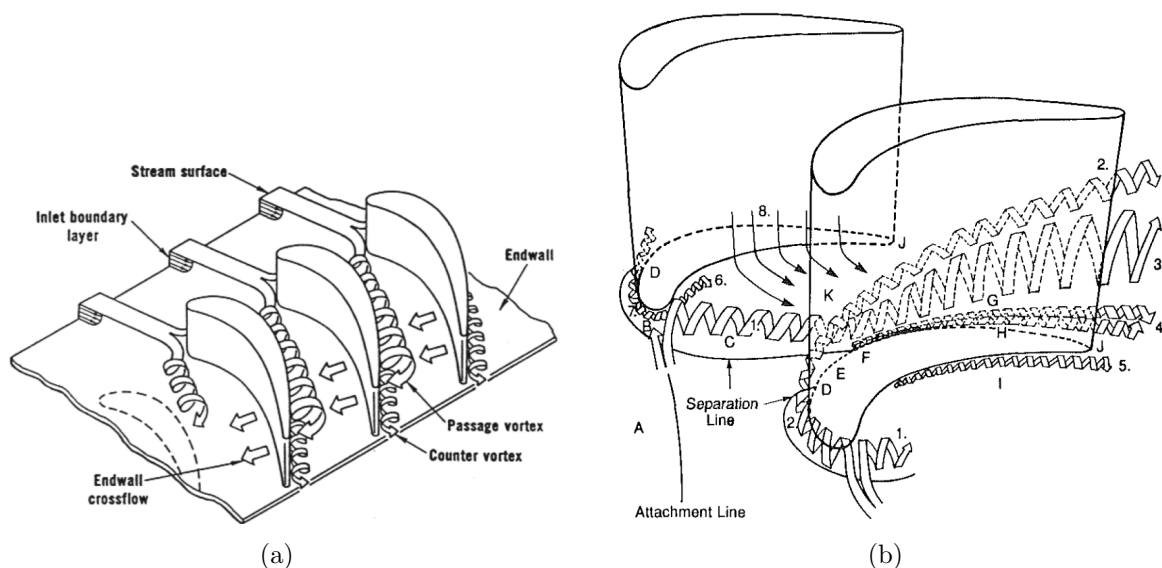
Figure 1.5.: Secondary flow models in a turbine passage from Langston [92] (a) and Gold-
stein and Spores [55] (b).

The new low-momentum endwall boundary layer formed behind the separa-
tion line of the pressure side horseshoe vortex is swept towards the blade
suction side due to the crosswise pressure gradient in the passage. The fluid
then rolls up and builds the passage vortex. The passage vortex is typi-
cally one of the largest secondary flow structures found in a turbomachine.
The size and strength of the vortex depends on the cross-passage pressure
gradient, hence the loading of the blades and the near endwall pressure
distribution.

Non-Axisymmetric Endwall Contouring

In addition to three dimensional blade designs with lean and skew, non-
axisymmetric endwall contouring is a powerful tool used to reduce secondary
flows [67]. This design intends to reduce the cross-passage pressure gradient
at the endwall to control the formation of secondary flows and improve
efficiency.

Notably, cascade measurements by Hartland et al. [64] confirmed a 30 %
reduction of secondary losses. Experiments on a model rig of the Rolls-Royce
Trent 500 engine quantified the performance benefit of non-axisymmetric
endwall contouring with efficiency improvements of 0.59 percentage points
(p.p.) ([149]) for the high-pressure turbine and 0.9 p.p. for the intermedi-
ate pressure turbine ([65]) under design point conditions. The principal
benefit of endwall profiling was the constraint of secondary losses closer

to the endwall. Further experimental evidence on the positive effect of endwall contouring on aerodynamic efficiency was reported by Snedden et al. [167] and Schuepbach et al. [161] for a high work turbine. A recent computational fluid dynamics (CFD) study by Papagiannis [132] on a steam turbine representative geometry emphasised the need to include unsteady flow phenomena and cavities in optimisations for endwall contouring. He demonstrated that steady-state simulations only predicted an efficiency gain of $0.06\,\%$ when compared to the unsteady prediction ($0.27\,\%$).

While studies have assessed the aerodynamic benefit of well-designed endwall contouring, relatively few heat transfer studies have investigated the effect of non-axisymmetric endwall contouring. In the early work of LaFleur et al. [91] in which contouring was derived using the ice formation design method, a Stanton number reduction of $24\,\%$ on a stator 2 vane was achieved compared to a rotationally symmetric geometry. Reduced Nusselt numbers along the endwall—especially upstream of the mid-passage locations—were also reported by Mahmood and Acharya [106] for a contoured endwall due to a weaker and smaller passage vortex in a cascade with a first stage GE-E3-based design. The same effect of weaker secondary flows on a contoured endwall was showing a $8\,\%$ reduction in average heat transfer compared to a flat endwall using CFD simulations by Saha and Acharya [154]. Even higher reductions (up to a factor of 3) were found locally. Furthermore, a $20\,\%$ reduction in heat transfer was also reported by Lynch et al. [105] for measurements in a cascade. Conversely, a $4.8\,\%$ increase in area-averaged thermal loads for a contoured compared to a flat endwall in a cascade was reported by Laveau et al. [96], with local variations of up to $70\,\%$. They strongly suggested considering endwall contouring effects on local heat transfer during the cooling design process. Moreover, Panchal et al. [129] noted local hot spots with significantly higher heat transfer near the leading and trailing edge pressure surface for aerodynamically optimised endwall contouring. They also achieved area-averaged Stanton number reductions of $13.1\,\%$ and $10.7\,\%$ for heat transfer optimised and aerodynamically optimised endwalls, respectively, compared to a non-contoured baseline.

Rim Seal Purge Flow

Modern gas turbines without cooling are unimaginable since main gas temperatures exceed blade melting temperature in the first turbine stages. Rim seal leakage (or purge) flow is bypassed air bled from the compressor
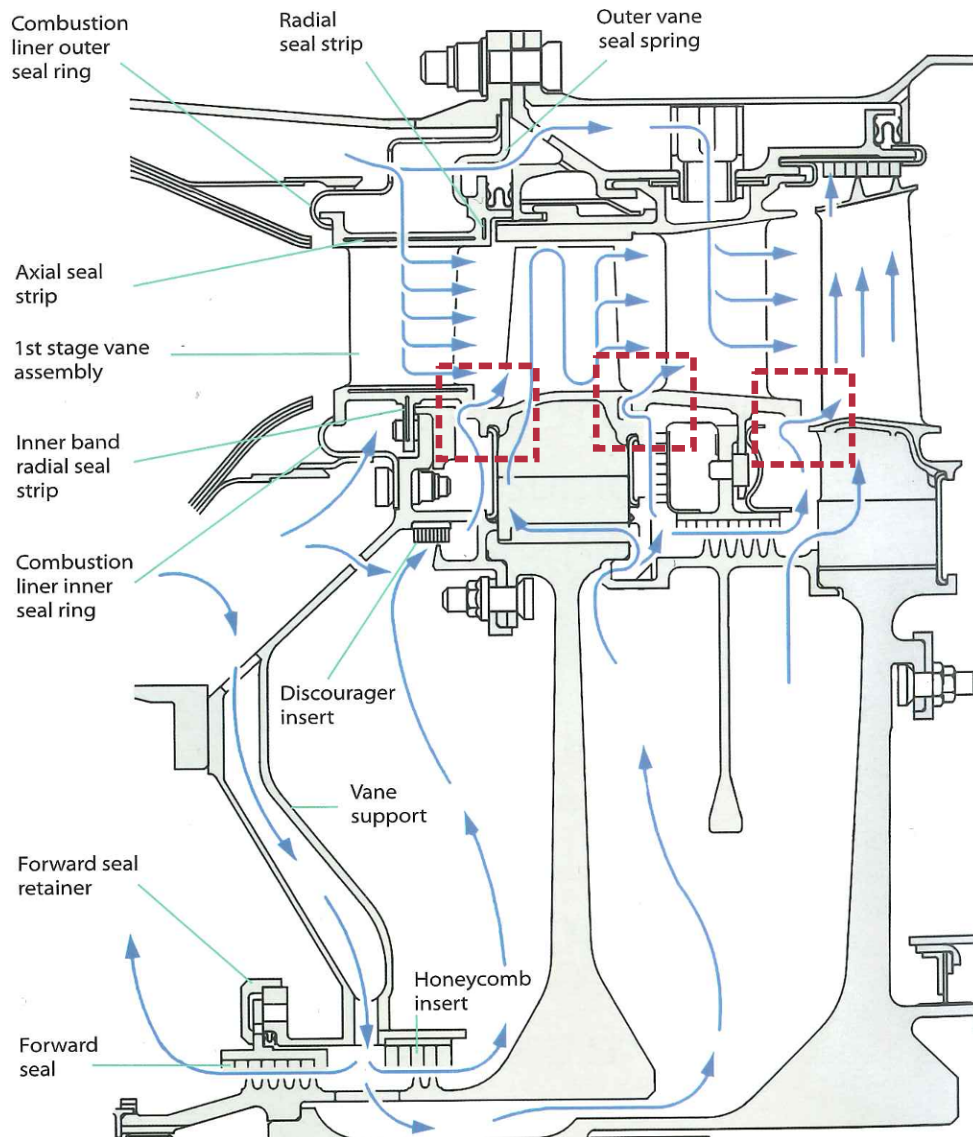
Figure 1.6.: Illustration of the complex cooling circuit in a Rolls-Royce AE 3007 gas turbine engine with purge flow highlighted in red (modified from [153]).

and directed to the turbine section. This air is injected into the wheel space between stationary and rotating parts and serves multiple purposes. Notably, it actively cools the turbine disk, provides cooling air for blade internals and film cooling, and protects the wheel space cavity from hot main flow gas ingestion. An illustration of the internal secondary air system of a Rolls-Royce AE 3007 gas turbine engine is provided in Figure 1.6.

The injection of low-momentum cooling flow affects the local flow field and turbine efficiency. In early work by Hunter and Manwaring [76], the mixing of the low-momentum sealing flow with the main flow was identified as the main source of loss associated to purge flow injection. The cooling

air disturbs the endwall boundary layer to the rotor and modifies also the secondary flow development. McLean et al. [112] stated that even a small amount of purge flow injection (e.g. 1 %) can significantly affect the performance character at the exit of a high-pressure turbine stage. This decrease in efficiency with increasing purge flow was confirmed by Reid et al. [146], who noted a 0.6 p.p. efficiency reduction for a three-stage low pressure turbine. Moreover, Schuepbach et al. [162] measured a 0.6 p.p. efficiency reduction per 0.9 % of purge injection.

Circumferential injection was successfully applied by Girgis et al. [54], who reported a 0.3 p.p. efficiency gain per percent of flow injection when compared to radial injection. Reid et al. [146] measured in a low speed research turbine and noted an approximately equal contribution to efficiency decrease due to purge injection being attributed to enhanced mixing and intensified secondary flows. A larger radial extent of the secondary flow signatures with reduced vorticity albeit increased circulation in the passage vortex while also increased circulation were measured downstream of the rotor [162].

The importance of including secondary air flows in turbine design has been stressed in many studies. The unsteady flow field at the cavity exit due to rotor-stator interactions influences the ingestion and ejection of cavity flows [130], which depends on the rotor position with respect to the stator. The increased geometrical complexity with leakage flows and unsteadiness requires a huge computational effort for simulations. Furthermore, Jakoby et al. [80] noted that large scale rotating structures in wheel space cavities can build up at certain cooling flow rates. These particular structures require full-annular simulations to be resolved, which is not yet computationally feasible during an iterative design process. Relevant work by Schädler et al. [156] involving a combined experimental and computational study demonstrated that effects in the main flow up to 30 % blade span height are measurable due low frequency pressure oscillations inside the cavity. Their full-annular unsteady RANS (Reynolds-averaged Navier-Stokes) simulations captured the experimentally measured low frequency pressure oscillations and showed that spatially distinct cavity ingestion and ejection are related to these characteristics.

The combined effect of endwall contouring and purge flow injection was investigated by Regina et al. [142]. They reported that endwall contouring increases the sensitivity of stage efficiency to purge flow injection and that the beneficial impact is lost for high injection rates. Similarly, Schuepbach et al. [163] measured a 1.2 p.p. efficiency reduction per percentage of purge

injection. In a high-pressure turbine, Rakenius et al. [138] observed a one-third reduction in stage performance sensitivity to purge flow injection for a contoured compared to a flat endwall.

The reported effect of purge flow injection on endwall heat transfer in the literature mainly relates to linear cascades. Blair [21] was among the first to assess the effect of a cooling film upstream of a vane leading edge to be investigated. Later studies by Granser and Schulenberg [59], followed by Roy et al. [152], Burd et al. [31], Oke et al. [126], Oke and Simon [127], Zhang and Jaiswal [182] and Wright et al. [181] also investigated slot coolant ejection upstream of vanes in linear cascades. Among these studies, the common finding was that such slot injection can effectively cool the upstream portion of the endwall as well as the area near the leading edge. The increased momentum of the boundary layer due to the cooling injection also reduces the strength of secondary flows in the passage. Thrift et al. [174] also investigated the effect of the slot orientation on the endwall cooling for a vane in a linear cascade. A substantial improvement in cooling performance for a 45° slot orientation over a 90° orientation was found, with an area-averaged improvement of over 100 %.

The importance of secondary flows in the passage—especially the cross-passage flow migration—on the cooling performance of purge flow on the rotor endwall has been consistently reported in many studies ([53, 170, 171]). The passage vortex sweeps away coolant from the platform, while the area downstream of the local passage vortex is unprotected by the purge flow. Using a high-pressure turbine representative configuration, Lazzi Gazzini et al. [99] showed that purge flow affects the endwall temperature on the platform suction side up to 30 % axial chord extent. While they also reported the strengthening of secondary flows due to purge injection, it played a negligible role in the variation of local heat transfer coefficients.

Rotor Blade Tip Leakage Flows and Designs

The rotor blade tip is of special interest in turbomachinery because tip leakage losses account for approximately one-thirk of total losses [39, 40]. The inevitable gaps between rotating and stationary parts result in a clearance gap above the rotor blade tip. Therefore, controlling the tip gap size is of special interest since it directly reduces leakages. However, due to the massive centrifugal loads on blades as well as thermal expansion and axial movement, it is very difficult to further reduce tip gaps even when using active tip clearance control. For low-pressure turbines, the additional weight

of tip shrouds would significantly increase stress on blade roots and require increased cooling mass flow. Leakage flow on the blade tip also increases the convective heat transfer on the blade, creating an additional heat load that requires active cooling. Blade tips are highly susceptible to structural damage, which can have a severe effect on turbine performance. In the case of damage, the loss of material increases clearance gaps, which further increases leakage flow and heat transfer while intensifying the aforementioned problems. A schematic illustration and smoke visualisation [39] of the pressure-driven tip leakage flow and leakage vortex is provided in Figure 1.7
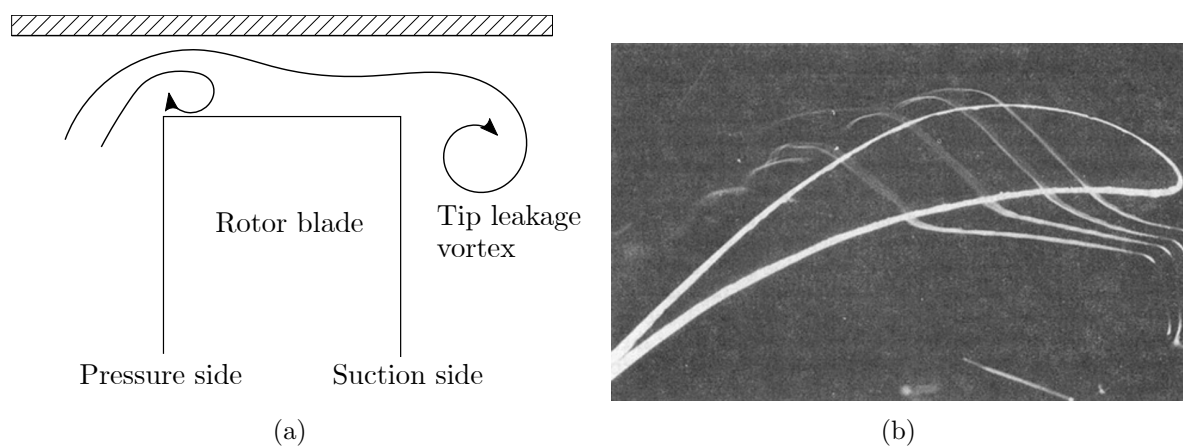
Figure 1.7.: Schematic illustration (a) and smoke visualisation [39] (b) of the over-tip flow and tip leakage vortex.

Aerodynamics and Efficiency

Pressure differences on blades create a leaking flow over the tip that does not contribute to the work output of the turbine and forms a vortex when re-entering the main fluid on the suction side. The loss generated by this leakage flow is due to entropy generation in the tip gap as well as mixing losses with the main flow. From an aerodynamic perspective, the decrease of tip leakage flow—and thus reduction of the efficiency penalty (also called desensitisation of the tip)—must be achieved.

Various concepts and investigations related to tip leakage reduction and the efficiency penalty have been reported in the literature. The most obvious approach—however limited by the thermal and structural complexity of the machines—is the reduction of the blade tip gap between rotor and casing. Early work on the influence of blade tip gap size on turbine efficiency was performed at the National Aeronautics and Space Administration (NASA)

[86, 87, 52, 72, 63, 62], where a linear relationship in efficiency degradation with tip clearance was identified. This trend was confirmed by various studies, with clearances up to 8 % span height. Notably, the high relevance of the amount of turbine reaction to the amount of efficiency degradation was identified. Later work by Kaiser and Bindon [83] quantified the linear relationship as a 1 % and 1.5 % efficiency reduction per 1 % clearance increase for total-to-total and total-to-static efficiency, respectively.

One of the most common geometrical tip modifications is the so-called squealer tip geometry, where the tip has a fence on the outside and a recessed tip cavity. The fence creates a labyrinth-like seal and can either surround the entire blade or only partially surround the pressure or suction side. An inherent advantage of squealer geometries is that if rotor contact occurs with the casing, the tip cooling holes will not become blocked and the internal cooling structures will not be damaged. The benefits of squealer tips have been highlighted by Ameri et al. [11], Willinger and Haselbacher [179], Azad et al. [16], Dey et al. [42] and Kegalj et al. [84], among others. Using CFD, Mischo et al. [116] showed that with appropriate profiling of the cavity recess, total heat transfer can be reduced by 7 % compared to a baseline recess and by 15 % compared to a flat tip.

Various tip platform extensions (or "winglets") were investigated by Harvey and Ramsden [66], Willinger and Haselbacher [179], Dey and Camci [41], among others, and pressure side extensions were found to be highly effective at desensitising tips [41]. Contouring on blade tips [94, 37] and casings [53, 177] has also been reported in recent studies.

The effect of tip coolant ejection on aerodynamic performance was investigated by Rao [139, 140], among others. They found that trench tip coolant ejection reduces the total pressure deficit in the leakage vortex and has a 50 % tip gap reduction. They also investigated the influence of cooling hole location and reported that jets at 61 % and 71 % of the axial chord reduce the leakage vortex size. The highest reduction in pressure deficit was observed at 81 %, and a jet at 91 % of the axial chord did not affect the leakage vortex. Another approach was presented by Behr et al. [18] using coolant injection on the rotor casing. An isentropic stage efficiency improvement of 0.55 p.p. could be achieved by using an appropriate combination of injection mass flow rate and position.

Heat Transfer

Most experimental work on rotor blade tip heat transfer has been conducted on linear cascades due to the inherent complexity of instrumentation and measurements in rotating facilities. Metzger et al. [114] found that heat transfer is reduced when using a deeper tip cavity. In the same study, the effect of the relative motion between the blade and casing was simulated with a moving wall. Notably, the reported heat transfer on the tip was virtually unaffected by the shroud movement. However, Zhu et al. [184] suggested that relative casing motion is an important factor that should not be neglected in future studies due to the significant differences it has on blade tip heat transfer performance. For a cascade test, Nasir et al. [120] reported that while a squealer tip produces slightly higher heat transfer in the close leading edge region, it produces lower heat transfer in the trailing edge when compared to a flat tip. Furthermore, deeper cavity depth reduced heat transfer for the squealer geometry. They also investigated partial squealers (representing fractional burn off) and reported that the suction-side squealer rim is more important for lowering heat transfer on the tip.

Recently, measurements of heat transfer and film cooling for various squealer tip geometries were performed on cascades by Tong et al. [175], Jeong et al. [82], Saul et al. [155], and Wilhelm and Schiffer [178]. Well-designed squealer geometries can reduce the local heat load on the tip, especially with film cooling. However, heat transfer is determined by local flow structures—especially reattachment and impingement—and can vary based on geometry. In a detailed numerical and experimental investigation by Rezasoltani et al. [148], film cooling effectiveness in a three-stage research turbine was investigated for a flat tip and a squealer geometry with either tip hole cooling or compound angle hole cooling on the pressure side using pressure-sensitive paint. They reported that cooling effectiveness tends to be lower with a squealer; however, a larger effective area is covered by the coolant with a squealer. The complex flow structure in the cavity distributes the cooling, while the highest effectiveness is measured near the trailing edge (where the coolant accumulates). By investigating multiple blowing ratios, a monotonically increasing effectiveness with mass flow increase was reported in the same work.

Due to the complex flow field, the design and optimisation of these geometries are almost exclusively performed numerically; as such, there is a strong need for experimental validation of these concepts in terms of

aerodynamics and heat transfer. To reduce the cost and time associated with experimental testing, "rainbow" testing—where a single rotor consists of multiple geometries—has started to be used. To perform aerodynamic plane measurements using these setups, fast-response aerodynamic probes (such as those presented in [56, 75] and [107]) are required to separately resolve the flow field for each rotor passage and hence geometry. Recent publications using rainbow rotor testing in rotating facilities can be found in [148, 94, 34].

Heat Transfer Measurements for Turbomachinery

Measurements in Rotating Facilities

Compared to investigations of linear cascades, the number of studies investigating heat transfer on rotating blades and endwalls remains limited. The nature of performing measurement in a rotating system imposes great challenges for the facilities, instrumentation and the data acquisition process. However, important factors—such as the effect of an unsteady flow field from an upstream stator entering the rotor passage—on local heat transfer can only be considered when measured in representative setups.

One of the first qualitative and quantitative investigations on film cooling performance in a low-speed rotating facility with a cooling hole on the pressure and suction side of a blade was presented by Dring et al. [45] using thermocouples. Later, measurements using thin-film heat flux gauges in shock tunnels were presented by Dunn and Hause [47], Dunn [46], Dunn et al. [48], Guenette et al. [61] and Abhari and Epstein [2]. Double-sided and single-sided heat flux gauges were also used in the subsequent work of Didier et al. [43], Dénos and Paniagua [44], Chana and Jones [35], Tallman et al. [173], Mathison et al. [109] and Mathison et al. [110]. In their work on airfoil heat transfer with different cooling configurations, Nickol et al. [124] found that the overall differences in cooling effectiveness from three investigated cooling configurations were small. This contradicts previous measurements from simplified geometries which stated that, for example, improved cooling from shaped cooling holes over conventional designs and that representative environments of the flow physics are important for measurements. Notably, the fast response time of thin-film heat flux gauges is highly suitable for measurements in short duration experimental facilities and for resolving unsteady heat transfer.

Blair performed full-span heat transfer measurements on the pressure side, suction side and hub endwall of a large-scale turbine rotor passage to investigate the effect of the hub and tip secondary flows [25, 26, 23]. He used blades manufactured from low-conductive urethane foam with an electrically heated stainless steel foil bonded to the surface and embedded miniature thermocouples to measure temperature differences to the main flow and calculate heat transfer. He demonstrated that the hub and tip secondary flows create zones with up to $90\,\%$ higher local heat transfer compared to mid-span values. Thermochromic liquid crystals (TLCs) are widely used for heat transfer measurements in linear cascades due to their excellent spatial resolution. Early studies on rotating surfaces using TLCs were performed by Metzger et al. [115] and Blair et al. [27] in a large-scale low-speed turbine rig. Recently, this technique has been widely used for blade internal cooling investigations [128, 111]. Notably, Waidmann et al. [176] introduced a new rotating facility with a rotating camera for blade internal cooling investigations. Another measurement technique applied in rotating research facilities is pressure-sensitive paint, where film cooling is calculated based on a mass transfer analogy. Such measurements do not require heating and thus have no lateral conduction error, which facilitates the collection of high-resolution spatial data instead of single-point measurements. This technique was widely used in the research facility at Texas A&M University in work on the film-cooled leading edge [7, 8, 9, 10] and rotor endwall cooling [170, 170, 147]. Recently, Lazzi Gazzini et al. [99] presented high-resolution heat transfer measurements collected from a rotor endwall using high-speed infrared thermography with a nickel thin-film heater on the surface to generate heat flux boundary conditions. In their investigation, the measured effect on the Nusselt number from various purge flow injection was within the measurement uncertainty. However, the observed trends indicated a strengthening of secondary flow patterns such as horseshoe and passage vortex from the injection of purge air.

Infrared Thermography

As mentioned in the previous section, traditional techniques used for heat transfer measurements—especially on rotating components—relied on temperature measurements by thermocouples or thin-film sensors, which only provide local measurements. Therefore, spatial resolution is limited or requires an impractical amount of sensors to be installed. As a non-intrusive surface measurement technique, infrared thermography offers a true two-

dimensional surface temperature measurement for high spatial temperature variations. Infrared thermography was initially used by the military after the second world war. However, as the technology evolved, it was applied to a wide range of applications in industry and research, including the field of thermo-fluid dynamics [113]. The evolution and principle of infrared thermography in a thermo-fluid dynamic context and measuring heat transfer is reported by Astarita et al. [12] and Carlomagno and Cardone [33].

In the field of turbomachinery, infrared thermography has mainly been used for investigations in linear cascades [24, 28, 121, 183, 150] and stationary surfaces in rotating facilities [97]. Ekkad et al. [49] and Holgate et al. [73] reported a transient infrared technique to simultaneously measure film cooling effectiveness and heat transfer downstream of cooling holes using a single test. Other studies using a transient technique are reported in [29] and [172].

Measurements on rotating surfaces are challenging due to the very short sensor exposure time for capturing sharp images, which also require extremely sensitive sensors. To the best of the author's knowledge, the only existing study involving heat transfer measurements on rotating surfaces in turbomachinery using infrared thermography was presented by Lazzi Gazzini et al. [99]. The present work extends the use of this technique to highly contoured rotor endwalls and, for the first time, to rotor blade tip heat transfer measurements in a rotating facility.

1.3. Research Objectives

This work contributes to further understanding and improving the aerothermal performance of high-pressure turbines driven by increasing turbine inlet temperatures. The control and accurate prediction of heat transfer and turbine cooling are the basis for pushing the limits of the current design. Using advanced experimental methods in a state of the art rotating axial turbine with an engine representative turbine configuration and extensive numerical methods, the following research objectives are addressed:

- Designing and integrating of a versatile infrared-based heat transfer measurement setup in a rotating test facility to measure heat transfer on rotor endwall and blade tips.

- Evaluation on the influence of advanced three-dimensional endwall contouring extended into the disk cavity on local heat transfer.

- Quantification of the effect of rim seal purge flow variations on the rotor endwall heat transfer coefficient and cooling effectiveness.

- Assessment of the capabilities of numerical simulation tools on predicting rotor endwall heat transfer by validation with experimental data.

- Lower uncertainty in heat transfer prediction to improve life prediction of hot turbine components.

- Experimentally measure and describe the heat load of advanced blade tip geometries and quantify the effect of tip coolant ejection.

- Derive recommendations for gas turbine engineers and practitioners for improved heat transfer designs.

1.4. Thesis Outline

Chapter 1 The first chapter introduces the background and motivation for this research. A short literature review is presented to address the flow structures, secondary flows and heat transfer in axial turbines. Special focus is placed on the effect of cooling flows (e.g. rim seal purge flows and tip cooling ejection) and their influence on aerodynamics and heat transfer. Additionally, an overview of experimental techniques and studies in rotating test facilities is provided.

Chapter 2 This chapter describes details of the axial research test facility used for the experimental work. The bypass injection system and rig modification for the tip cooling injection are presented. The relevant quantities for the investigated turbine operating points are described. This chapter also provides a detailed description of the investigated turbine geometry—especially the endwall design and various blade tip designs.

Chapter 3 The experimental setup and measurement principle for the infrared-based heat transfer measurements are presented. Detailed descriptions of the design and manufacturing of custom made thin-film heating inserts and their associated calibration are provided. The integration of the instrumentation into the turbine facility is discussed along with relevant secondary instrumentation. The data acquisition system is also explained.

Furthermore, the aerodynamic probes used for upstream and downstream rotor flow measurements are described.

Chapter 4 The main data post-processing steps are described and presented in this chapter. An uncertainty analysis of the measurement setup and technique is also presented and supported by results of a repeatability study. Furthermore, the definitions of non-dimensional heat transfer quantities are introduced.

Chapter 5 The numerical setup for the simulation is presented and described, including the simulation domain, grid characteristics and boundary conditions. The approach for deriving heat transfer coefficients from two simulations using different wall boundary conditions is also explained in greater detail. Additionally, this chapter presents results from the convergence assessment and the aerodynamic validation using experimental probe data. Quantitative studies on the influence of surface roughness and non-uniform wall heat flux boundary conditions are also presented.

Chapter 6 This chapter discusses the results of the rotor endwall heat transfer measurements. First, the characteristics of the flow field derived from aerodynamic probe measurements upstream and downstream of the rotor are presented. The characteristic distribution of the heat transfer coefficient and purge cooling effectiveness on the endwall with extended contouring into the disk cavity is introduced for the design purge flow injection rate. The capabilities of steady-state and unsteady time-averaged simulations are examined using the experimental data, while additional flow information is used to link the aerodynamics with the endwall heat transfer patterns. Based on the investigation of two additional purge injection rates, the sensitivity of the heat transfer coefficient and cooling effectiveness are examined. Lastly, the results of turbine off-design operation are compared with the design point and the sensitivity of local heat transfer coefficients to the purge injection rate is discussed.

Chapter 7 The characteristic heat transfer coefficient distribution for the investigated rotor blade tip geometries is presented and discussed. An overview of the aerodynamic influence of different designs on integral turbine efficiency and the rotor exit flow field are presented. The sensitivity of the local heat transfer distribution is also investigated. Furthermore, the changes

in the heat transfer coefficient and local cooling effectiveness for active tip coolant ejection are discussed.

Chapter 8 The conclusions of the presented work and its main achievements and contributions to the scientific community and industry are provided with a concise summary of the thesis. A brief outlook on future work investigations in the field is also presented.

2. Research Facility and Turbine Geometry

2.1. Experimental Test Facility "LISA"

The measurements presented in this work were performed in the rotating axial research turbine facility "LISA"at ETH Zurich. The facility, depicted in Figure 2.1, is a highly modular moderate-speed and low-temperature rig that allows the assembly of both 2-stage and 1.5-stage turbine configurations. An extensive and detailed description of the design for 2-stage turbines is presented by Sell et al. [164], while the modification for the 1.5-stage configuration is provided by Behr et al. [17]. A brief overview and key characteristics are presented in this section.
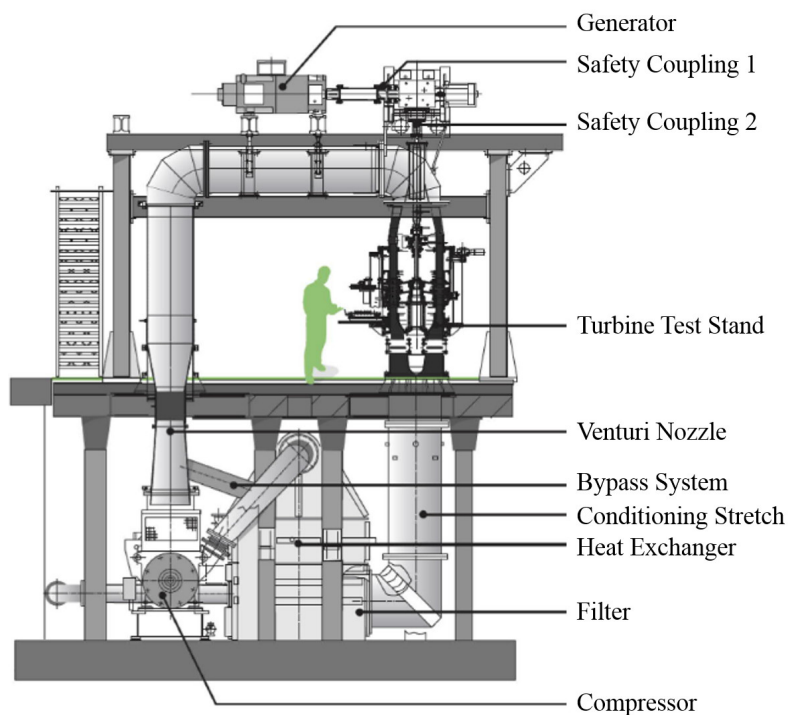
Figure 2.1.: Overview of the axial turbine research facility "LISA" at ETH Zurich.

The quasi-closed air loop of the facility is open to the atmosphere downstream of the turbine section. A radial compressor (750 kW) with a maximum pressure ratio Π_c of 1.5 compresses the air upstream of the turbine section and drives the air in the loop. The compressor pressure ratio and mass flow are controlled by variable inlet guide vanes with a constant rotational speed. A bypass safety system with fast-acting valves is installed to isolate the compressor under emergency stop conditions and to stop airflow to the test section. Upstream of the compressor, a calibrated venturi nozzle measures the main mass flow. After the compressor, a 2-stage water-to-air heat exchanger is used to control the turbine inlet temperature with an accuracy of ± 0.4 K. A 3 m long flow conditioning stretch, with perforated plates, honeycombs and sieves, and a cone contraction are installed upstream of the turbine section to produce a highly uniform flow field. Pitot probes installed on thin struts approximately three axial chords upstream of the test section measure the total inlet pressure. The turbine shaft is connected over an angular reduction gearbox to a DC generator that controls the rotational speed to an accuracy of ± 0.02 % (± 0.5 rpm). The generated power is fed back into the electrical grid. A safety coupling on both sides of the gearbox decouples the turbine or generator from each other in case of a failure.

2.1.1. Turbine Operating Points

The turbine is operated with a constant total-to-static pressure ratio to account for changes in atmospheric pressure between measurement days. Total inlet pressure is measured at 36 % span height on thin struts upstream of the turbine, while static pressure is measured at the hub of the second stator exit. To achieve a turbine pressure ratio Π_{design} of 1.65 with the maximum pressure ratio of the compressor (1.5), the gas is expanded to lower than atmospheric pressure in the turbine. Two rows of de-swirling vanes are installed to recover the pressure back to ambient levels.

Two different turbine operating points were investigated: a design point with a pressure ratio of $\Pi_{design} = 1.65$ and an off-design ($\Pi_{OD} = 1.33$) turbine operation point. Rotational speed was kept constant for both operating points, leading to negative rotor incidence for the off-design case (Section 6.3, Figure 6.21). A summary of the conditions for both operating points is provided in Table 2.1. The flow coefficient Φ and stage loading Ψ profiles of the turbine configuration for both operating points are presented in Figure 2.2.

Table 2.1.: Turbine operating conditions.

	Design point	Off-design	Unit
Pressure ratio	$1.65 \pm 0.4\,\%$	$1.33 \pm 0.4\,\%$	$[-]$
Inlet temperature $T_{o,in}$	328.0 ± 0.4	328.0 ± 0.4	$[K]$
Capacity $\frac{\dot{m}\sqrt{T_{o,in}}}{p_{o,in}}$	$149.8 \pm 0.5\,\%$	$124.0 \pm 0.4\,\%$	$\left[\frac{kg\sqrt{K}}{s\cdot bar}\right]$
Speed $\frac{N}{\sqrt{T_{o,in}}}$	2.49 ± 0.05	2.49 ± 0.05	$\left[\frac{rps}{\sqrt{K}}\right]$
M^{*} (S1ex/Rex/S2ex)	0.53/0.27/0.5	0.43/0.28/0.33	$[-]$
Re^{*} (S1ex/Rex/S2ex)	710k/380k/460k	520k/310k/460k	$[-]$
Flow coefficient ϕ^{*}	0.503	0.400	$[-]$
Stage loading Ψ^{*}	2.35	1.62	$[-]$

$(^{*})$ at midspan

2.1.2. Purge Flow Injection System

To investigate cooling flow effects such as rim seal cavity purge flow or tip coolant ejection, air can be injected into the turbine rig.

Air is bled-off from the main flow upstream of the conditioning stretch and passes through a standard venturi nozzle to measure the bypass mass flow $\dot{m}_{bypass}$. A manually adjusted valve controls the mass flow rate before the auxiliary air is split into 10 tubes connected to the turbine through a distributor (octopus). The tubes are connected to the first stator casing and feed the bypass air into the rotor upstream cavity plenum through tubes in the blades. Figure 2.3 schematically illustrates the bypass injection in the turbine. In the cavity plenum, the bypass air is split into purge flow $\dot{m}_{purge}$ that is injected into the main annulus through the rotor-stator-cavity and leakage air $\dot{m}_{leakage}$ that moves into the drum plenum through a labyrinth seal. Leakage flow is measured with a standard venturi nozzle and ejected into the atmosphere. The control of mass flow is possible as the drum plenum pressure level is (manually) adjusted to zero differential pressure Δp over the rotor downstream seal, suppressing any mass flow exchange with the main flow through this seal.

The purge mass flow is calculated as the difference between the bypass and
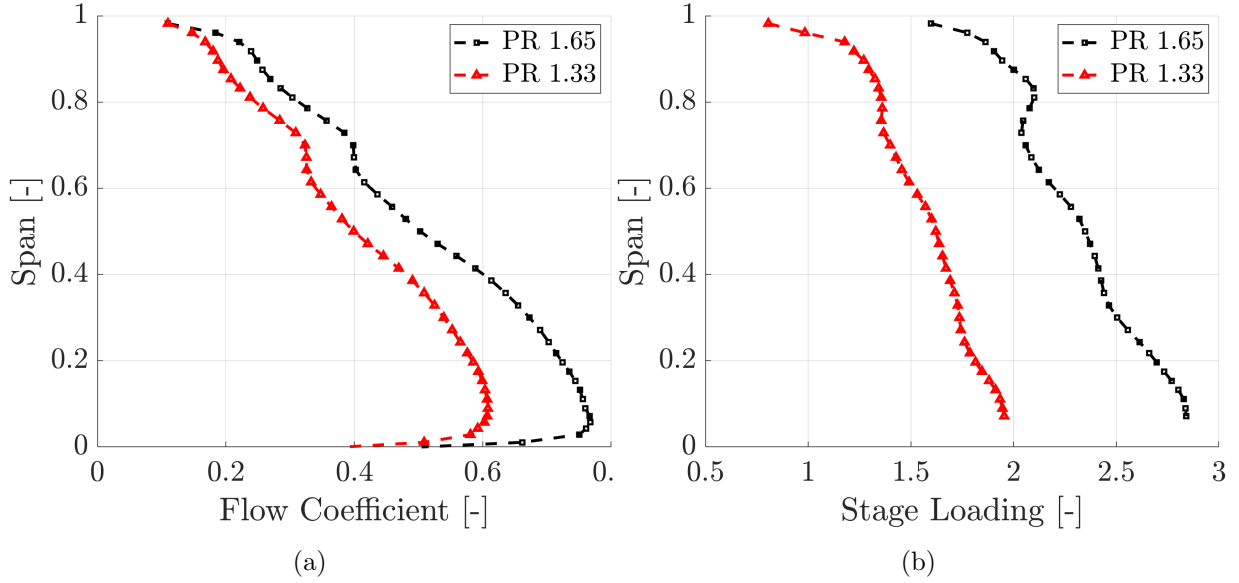
Figure 2.2.: Span-wise profiles of flow coefficient and stage loading for design point and
off-design conditions.

leakage mass flow. For the investigations performed in this work, purge flow injection is defined by the ratio between the purge flow and the main mass flow (Equation 2.1), which is known as the injection rate IR. Measurements were performed for three different injection rates: $IR = 0.0\,\%$, $IR = 0.8\,\%$ (design IR) and $IR = 1.2\,\%$.

$$IR = \frac{\dot{m}_{purge}}{\dot{m}_{main}} \cdot 100 = \frac{\dot{m}_{bypass} - \dot{m}_{leakage}}{\dot{m}_{main}} \cdot 100 \qquad (2.1)$$

The purge flow temperature T_c is measured inside the cavity plenum. As the bypass air is extracted upstream of the turbine section in the loop, the measured purge flow temperature is generally higher than the main flow temperature when injected into the annulus. Despite being known as cooling flow, the influence of the purge flow is measured as a temperature increase on the rotor endwall for these measurements. The described setup was used for the rotor hub endwall heat transfer measurements. The secondary air system was modified (Section 2.1.3) to inject cooled bypass air for hot gas ingestion measurements (Schädler [157]) and was used in the new configuration for rotor blade tip heat transfer measurements.
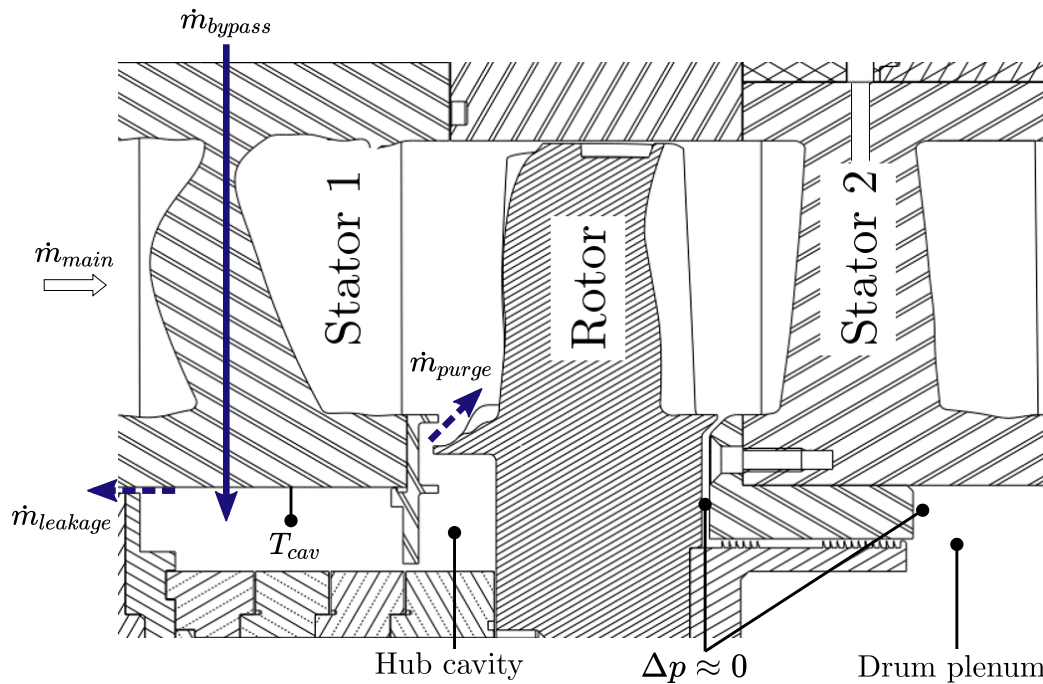
Figure 2.3.: Illustration of the bypass flow injection and purge flow calculation.

2.1.3. Cooled Bypass Injection Modification

After the hub endwall heat transfer studies, the secondary air system of the test rig was modified to inject cooled bypass air. This configuration was used to study tip heat transfer. For this modification, an external cooling loop including a dryer was included to the facility. Figure 2.4 schematically depicts the modifications and illustrates the various air flows.

Compressed air provided by the building infrastructure is first dried to a dew point of approximately $-50\,°\text{C}$ using a dual vessel regeneration adsorption dryer (Ultrapac MSD 0300 UC). The air is cooled using a cryogenic water-cooled chiller (Bitzer K813H/S6F-30.2Y) that can cool down to approximately $-25\,°\text{C}$ at a mass flow rate of $130\,\text{g/s}$. The cooler is switched on and off based on the controller set temperature, with air temperature measured at the exit of the chiller. A control valve downstream of the cooling plant is used to regulate the mass flow, which is measured by a calibrated orifice plate. The cold bypass air is distributed by the flow distributor (octopus) to 10 tubes connected to the stator and fed into the disc cavity. All of the tubing is insulated using low-conductivity insulation to reduce heat transfer to the cooled flow.
To balance the mass flow in the turbine loop, hot air upstream of the flow conditioning stretch bypasses of the turbine and is dumped into the
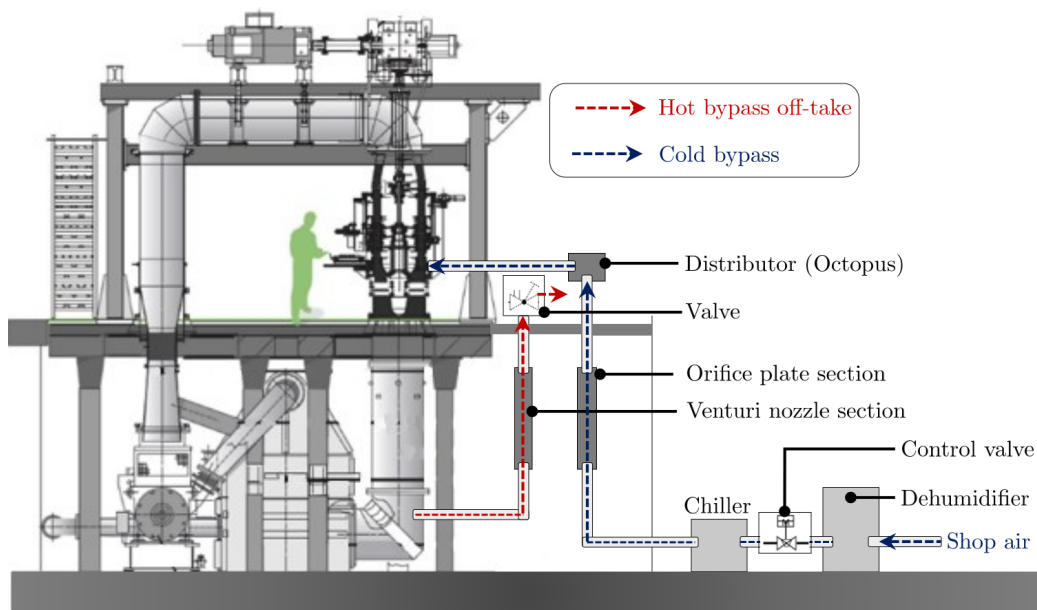
Figure 2.4.: Illustration of test facility modification for cooled bypass injection [157].

atmosphere. The hot off-take air is measured by a venturi nozzle section and controlled by a valve. The cold bypass rate is manually adjusted to the desired injection ratio and the hot off-take air adjusted to the same mass flow.

Despite the insulation of the auxiliary tubing, a considerable amount of heat is transferred to the cooled flow measured as a 40 K to 60 K temperature increase between chiller and rotor cavity. The main heating occurs in the stator passing since these feeding tubes are not insulated.

Two miniature temperature probes were installed on different circumferential positions for the cavity temperature measurements. The probes are manufactured from polyether ether ketone (PEEK) to reduce heat conduction from the probe fixation in the stator segments to the installed Pt100 temperature sensors (Figure 2.5). The cooled bypass air system was extensively tested (for at least 10 hours representing a typical measurement day) with various cooler temperature settings and injection rates to evaluate air flow rate stability and cavity temperatures. Most stable conditions covering injection rates up to $IR = 1.2\%$ (175 g/s) were found for a chiller target temperature of 253 K. Typically, variations below ± 0.3 K for cavity temperature and ± 0.02 p.p. for injection rate were observed during a single measurement day. Values below 2 % relative humidity are measured at the distributor. The thermal inertia of the bypass loop requires approximately 50 min for stable target temperatures to be reached in the cavity.
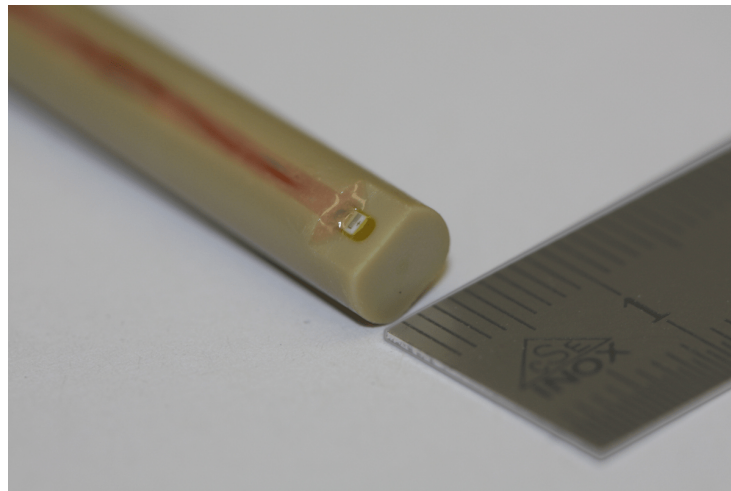
Figure 2.5.: Image of the PEEK cavity temperature probe with an installed Pt100 temperature sensor and ruler for reference.
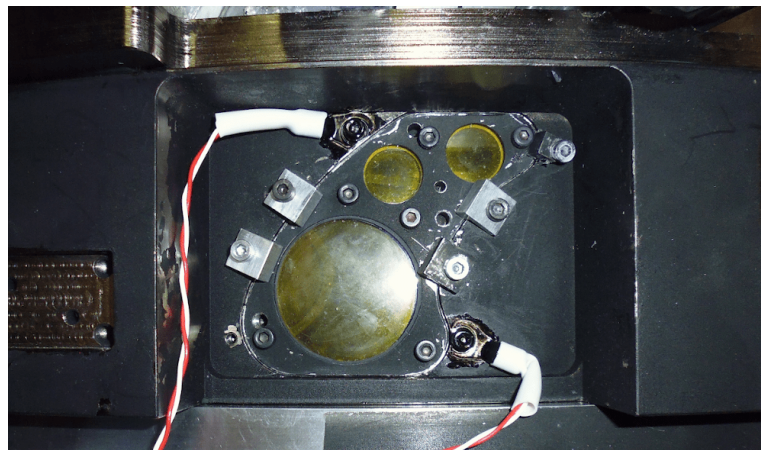
Figure 2.6.: Rotor casing modification for optical access. Installed insert with infrared transparent zinc selenide (ZnSe) windows.

2.1.4. Optical Access for Infrared Measurements

The rotor casing was modified for the required optical access by the infrared-based heat transfer measurements. A recessed opening in the casing could be either equipped with an insert containing infrared transparent windows (Figure 2.6) or a dummy cover for aerodynamic measurements. A rubber gasket between the casing and insert prevents leakages. The rotor casing ring can be attached to the circumferential traversing mechanism of the test rig and facilitates positioning of the measurement window at different relative positions to the upstream stator.

2.1.5. Tip Coolant Injection System

Slight modifications of the turbine rig were made to facilitate the rotor tip coolant integration, whereby the integration of cooled bypass flow is already described in Section 2.1.3. Here, only a brief introduction of the tip coolant path in the turbine is provided. A detailed discussion on the instrumentation for variable blade tip geometries and tip coolant integration for bladed disks is provided in Section 3.4.2.

Two holes were drilled in the bladed rotor disk (blisk) to enable tip coolant supply—one axially to reach into the upstream cavity plenum and one radially to deliver the coolant from the cavity into the tip (Figure 2.7a). The cavity access holes are slightly recessed to either fix a perforated plate with matching holes to supply tip coolant or a sealing plate in the case of no coolant supply. Flow angles in the cavity (derived from preliminary CFD studies) were used to incline the cavity access holes in the direction of flow (Figure 2.7b).
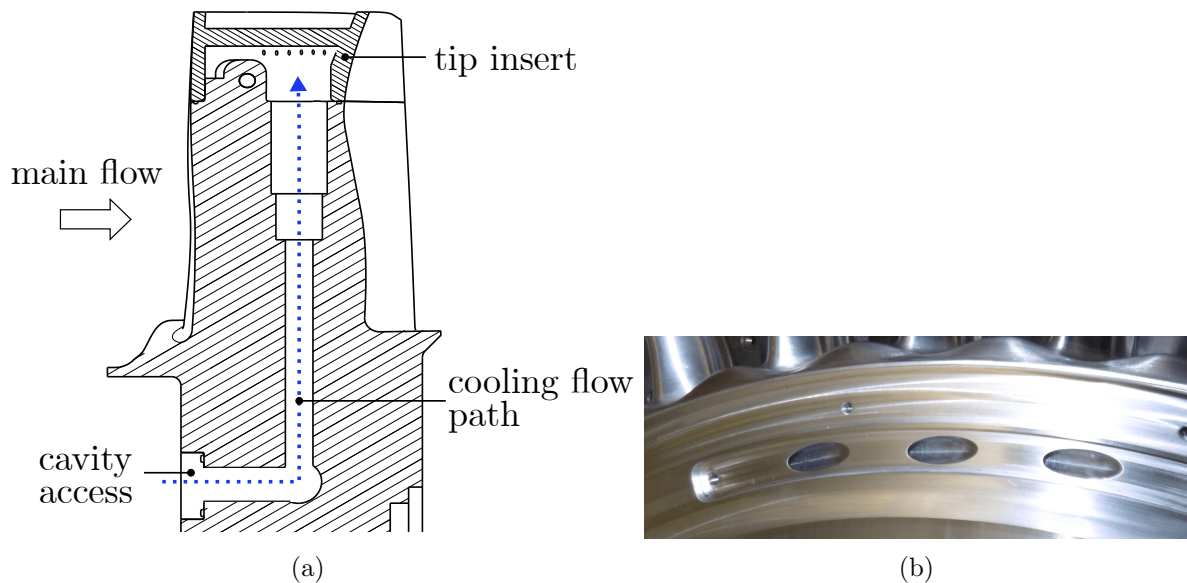
Figure 2.7.: Schematic of the tip coolant supply path in the rotor blisk (a) and close-up image of the inclined cooling access holes in the upstream cavity (b).

The tip coolant mass flow rate is measured using a specially manufactured miniature rotating venturi tube installed in the blade (described in Section 3.5). The non-dimensional tip coolant ejection rate TR is defined similarly to the purge injection rate IR (Equation 2.2). The coolant mass flow measured for one supplied blade (Section 3.5) is multiplied by the rotor
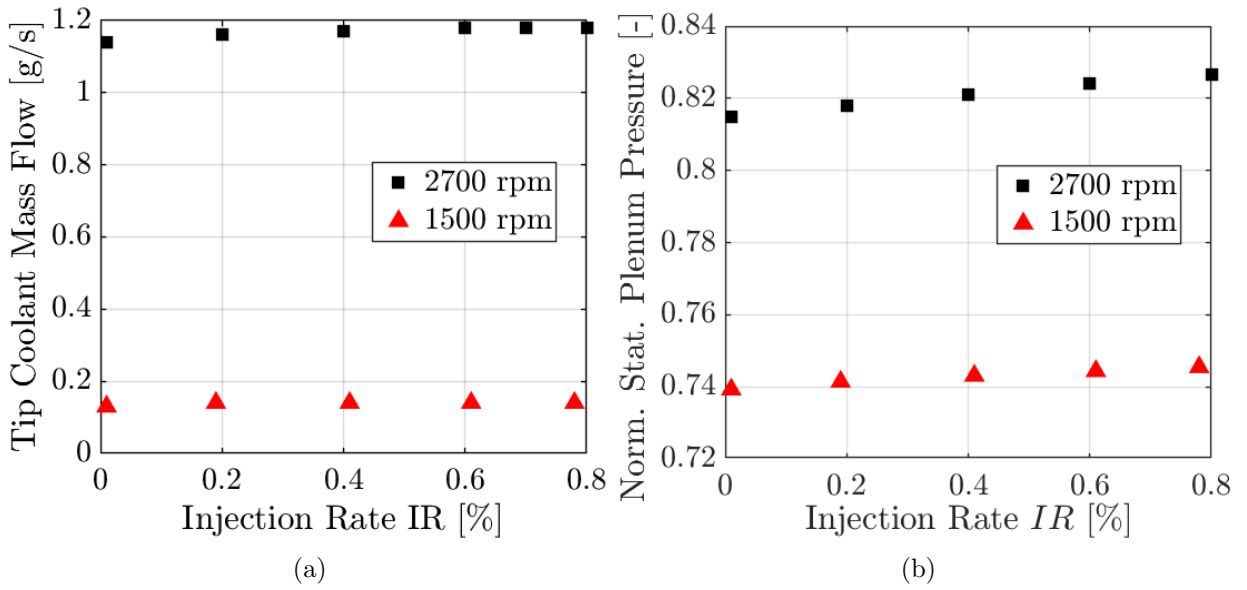
Figure 2.8.: Sensitivity of tip coolant mass flow rate (a) and insert plenum pressure (b) on the purge flow injection rate for two rotational speeds of the turbine.

blade count and divided by the mainstream mass flow.

$$TR = \frac{\dot{m}_{tip,coolant}}{\dot{m}_{main}} \cdot 100 \qquad (2.2)$$

Measurements of the tip coolant mass flow rate (and pressure inside the tip insert) showed very little sensitivity to different bypass flow injection rates into the cavity(Figure 2.8). The main driver for the tip coolant mass flow rate is the rotor pumping effect, which is dependent on the rotational speed (Figure 2.8a). Therefore, the tip coolant ejection rate can only be modified by changing the turbine rotational speed and not by means of cavity pressure (bypass injection rate). The measured tip coolant flow of an individual blade was approximately 1.2 g/s for the design rotational speed and 0.14 g/s for a reduced speed of 1500 rpm. This is equivalent to a tip coolant ejection rate of 0.4 % and 0.1 % if all blades are considered cooled.

Two different tip coolant ejection rates (TR) were investigated—active tip coolant ejection denoted TR_2 and no coolant ejection TR_0—with a closed supply and rotational speed of 2700 rpm. Some common non-dimensional quantities used in tip heat transfer and film cooling studies are estimated and summarised in Table 2.2. The blowing ratio BR is derived from the tip mass flow ratio by dividing the measured mass flow by the respective areas. The reference areas for this calculation are purely geometrical, with

Table 2.2.: Non-dimensional numbers for the investigated turbine conditions.

Quantity		Value
Tip mass flow ratio	$TR = \frac{\dot{m}_c}{\dot{m}_{main}}$	0.4 %
Blowing ratio	$BR = \frac{\rho_c U_c}{\rho_\infty U_\infty}$	1.2
Density ratio	$DR = \frac{\rho_c}{\rho_\infty}$	1.1
Momentum flux ratio	$I = \frac{BR^2}{DR}$	1.3

blockage effects being not considered. Moreover, since no local pressure information on the blade tip surface is available, the exact distribution of tip coolant among the cooling and dust holes is not known. Coolant density was calculated based on the pressure and temperature data measured in the insert plenum.

2.2. Turbine Configuration and Geometry

For this work, a 1.5-stage high pressure turbine representative configuration was tested. The inclusion of a second stator downstream the rotor creates a representative flow field at the exit of the rotor including unsteady potential field interactions. The blade counts of the individual rows were 36, 42 and 36 for stator 1 (S1), rotor (R) and stator 2 (S2), respectively. The main geometrical parameters for all blade rows are summarised in Table 2.3.

Table 2.3.: Mid-span geometrical characteristics of the turbine blades.

	S1	R	S2
Blade count	36	42	36
Aspect ratio (AR)	0.89	1.21	0.83
Solidity σ	1.23	1.06	1.33
Turning [°]		118.7	
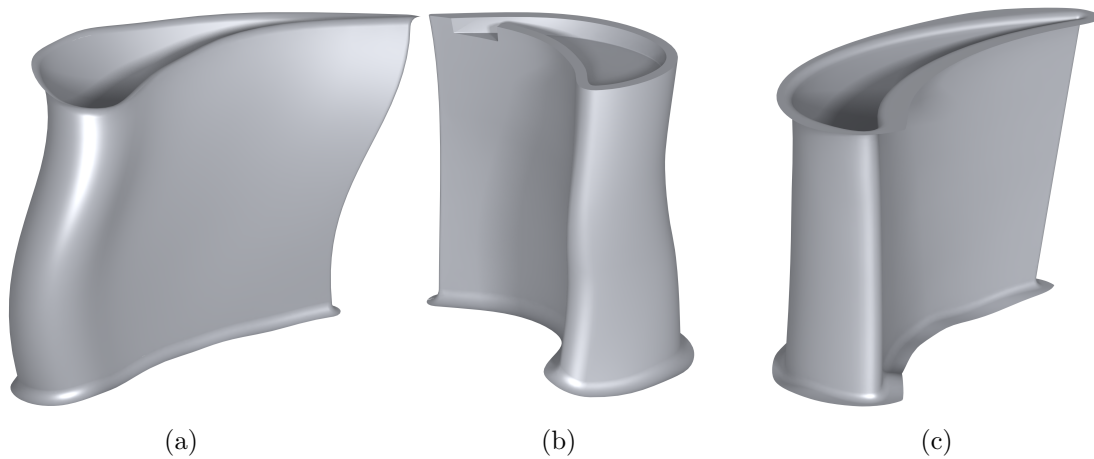
Figure 2.9.: Illustrations of the 3D optimised aerofoils (not to scale). Stator 1 (a), rotor (b) and stator 2 (c).

2.2.1. Blade Designs

All blade rows of the turbine configuration (Figure 2.9) are 3D optimised, including the endwall contouring. The first stator (featuring compound bow and lean) and the second stator were designed for a previous measurement campaign. The key characteristics of this turbine configuration are the re-designed rotor with a substantially reduced blade count ($-22\,\%$) and a modified endwall contouring extending into the disk cavity ([158], [99]). A detailed description of the design intention and optimisation is provided in the next section. Overall, despite the blade count reduction, an integral efficiency improvement of $\Delta\eta_{tt} = 0.37\,\mathrm{p.p.}$ compared to the previous design was measured. A detailed discussion of the achieved aerodynamic performance and the impact on the turbine noise emissions is provided by Schädler et al. [158].

The turbine section has a constant hub and tip radius and a hub-to-tip ratio of 0.825 for all blade rows. The engine-representative nominal tip gap of $1\,\%$ blade span height for the rotor is calculated in relation to a flat tip or the squealer fence.

2.2.2. Cavity Design

The rotor upstream disk cavity sealing arrangement is engine-representative. Two axial sealing lips on the stator side and the extended S-type shape platform of the rotor dipping into the cavity build an overlapping rim seal ($2.1\,\%$ rotor axial chord (c_{ax}) overlap). A schematic cut of the cavity is presented in Figure 2.10. The axial distance of the rotor sealing lip to the
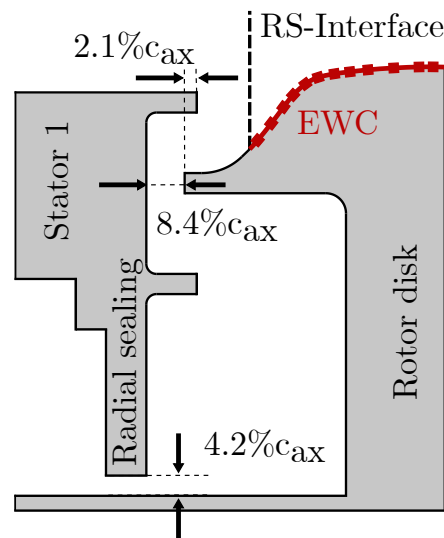
Figure 2.10.: Rotor upstream cavity schematic with indicated rotor-stator (RS) interface and extended endwall contouring (EWC).

stator measures $8.4\,\%$, while the radial slot height measures $12.5\,\%$ of the axial chord. The sealing design intends to reduce hot gas ingestion. A radial sealing ($4.2\,\%$ c_{ax} clearance) separates the larger cavity where the bypass air is injected from the sealing arrangement.

2.2.3. Design Intention and Optimisation of the Rotor and Endwall

The design of the rotor endwall contouring is based on a CFD optimisation cycle performed by the joint industrial partners for this work. The optimisation is purely based on the aerodynamic 1.5-stage efficiency as the target and mass flow as the constraint. The commercial software CAESES® by Friendship Systems AG was used to create the geometries. Only four parameters were used to define the non-axisymmetric endwall contouring of one hill and one trough: amplitude, circumferential propagation, axial position and extent relative to the blade camber line for both hill and trough. This limited design space was intentionally chosen to reduce the geometrical complexity. The endwall was optimised together with the aerofoil by adding this parameter to the converged optimisation setup of the blade.

For the optimisation, the simulation domain included three blade rows and the upstream cavity and a block structured meshes generated with AutoGrid. During the optimisation, only the rotor was re-meshed to save computational cost. To allow extended endwall contouring into the disk cavity, the main flow path was modified to dip into the cavity and the rotor-stator-interface

(RS-Interface) was shifted upstream accordingly (Figure 2.10). Steady-state simulations using TRACE—a specific code for turbomachinery application developed by the Institute of Propulsion Technology at the German Aerospace Center (DLR)—were performed using the shear stress transport model (SST) for turbulence modelling. The design purge flow injection rate (0.8 %) was included and specified as a mass flow boundary condition. AutoOpti—an independent optimisation program code by DLR that uses a genetic algorithm—was used for geometry generation and the surrogate model based on kriging. A total of 89 design parameters were used and approximately 1500 members of the optimisations were required for convergence. A detailed description of the algorithm is provided by Aulich and Siller [15].

2.2.4. Endwall Contouring

All blade rows have non-axisymmetric endwall contouring. The contouring is expressed by the change in radius relative to the nominal hub (or tip) radius and normalised by the span height h_{span} (Equation 2.3). The definition is such that for both the hub and tip endwall, negative contouring Δr is a trough based on the flow annulus and positive Δr a hill.

$$\Delta r = \frac{r - r_{nom,hub}}{h_{span}} \cdot 100 \qquad or \qquad \Delta r = \frac{r_{nom,tip} - r}{h_{span}} \cdot 100 \qquad (2.3)$$

where r : local endwall radius   (m)
         $r_{nom,hub/tip}$: nominal hub/tip endwall radius   (m)
         h_{span} : blade span height   (m)

Stator 1 and 2 Endwall   The first stator has a contoured hub and shroud endwall (see Figure 2.11 (a) and (b)). The general pattern showing two hills—one towards the blade leading edge pressure side and one close to the blade suction side in vicinity of the trailing edge—and an extended trough—spreading from approximately the blade leading edge to half of the axial chord within the blade passage—is similar for hub and tip endwall, with a slightly more pronounced design for the shroud. The maximum values of contouring were $-3.0\,\%$ and $2.5\,\%$ for the through and hill. The second stator features contouring only on the hub endwall (Figure 2.11(c)). The two endwall hills were at very similar locations: 1) close to the leading

(a) Stator 1: tip

Δr [%]

2.5
1.5
0.5
-0.5
-1.5
-2.5
-3.5

(b) Stator 1: hub   (c) Stator 2: hub
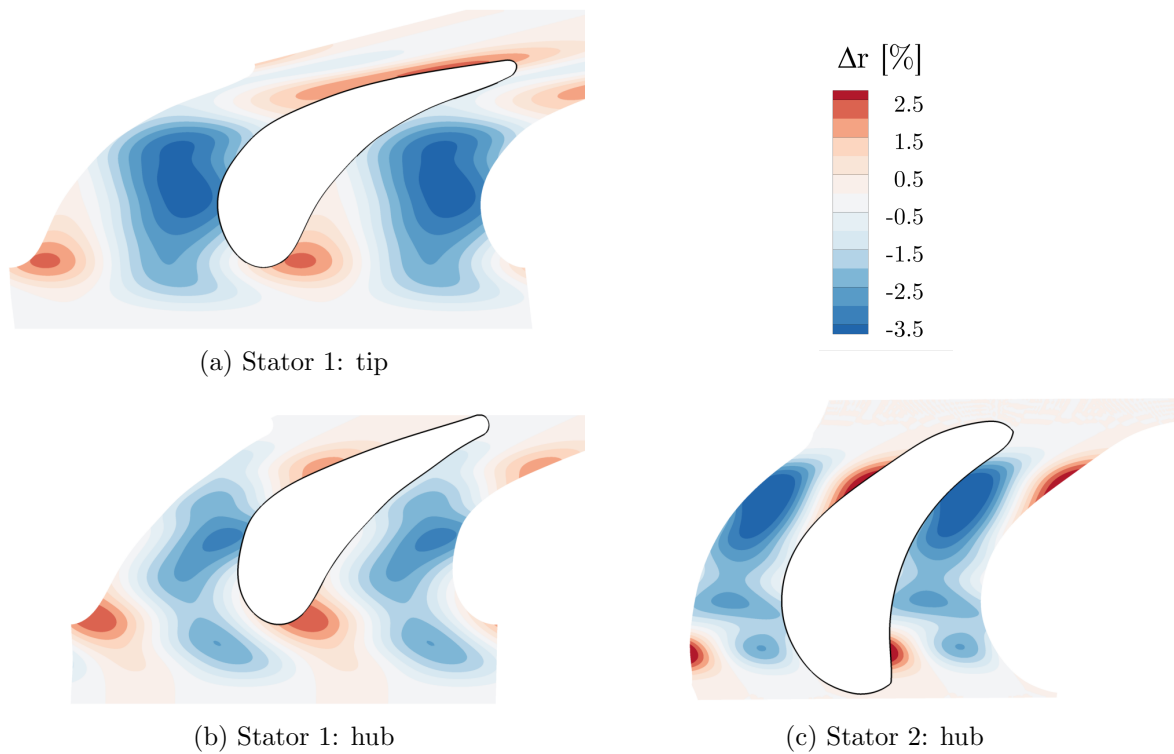
Figure 2.11.: Contouring of the stator 1 hub (a) and tip (b) and stator 2 hub (c) endwall
by percentage of span height.

edge on the pressure side and 2) towards the blade suction side in vicinity
of the trailing edge. The trough is located in the middle of the passage
and extends axially until the pressure side at approximatelly the same axial
position as the second hill. The maximum contouring values were $-4.5\,\%$
and $3.2\,\%$ for the trough and hill, respectively.

Rotor Endwall Contouring Following the parameter restriction mentioned
in the design intention section, the endwall contouring features one distinct
hill and trough (Figure 2.12). The contouring starts $-23\,\%$ c_{ax} upstream
of the leading edge inside the cavity sealing arrangement and below the
nominal hub radius. The integration of platform contouring into the disk
cavity is new in the open literature and only possible due to the integration
of the cavity in the design optimisation. Most of the radius variation on
the endwall is found between the platform start until approximately $50\,\%$
axial chord. The pronounced hill and trough are located at approximetely
the same axial locations as the blade leading edge on the pressure and
suction side of the passage, respectively. This upstream contouring is
different compared to most of the non-axisymmetric endwalls discussed
in the literature. Traditionally, the contouring is found inside the blade
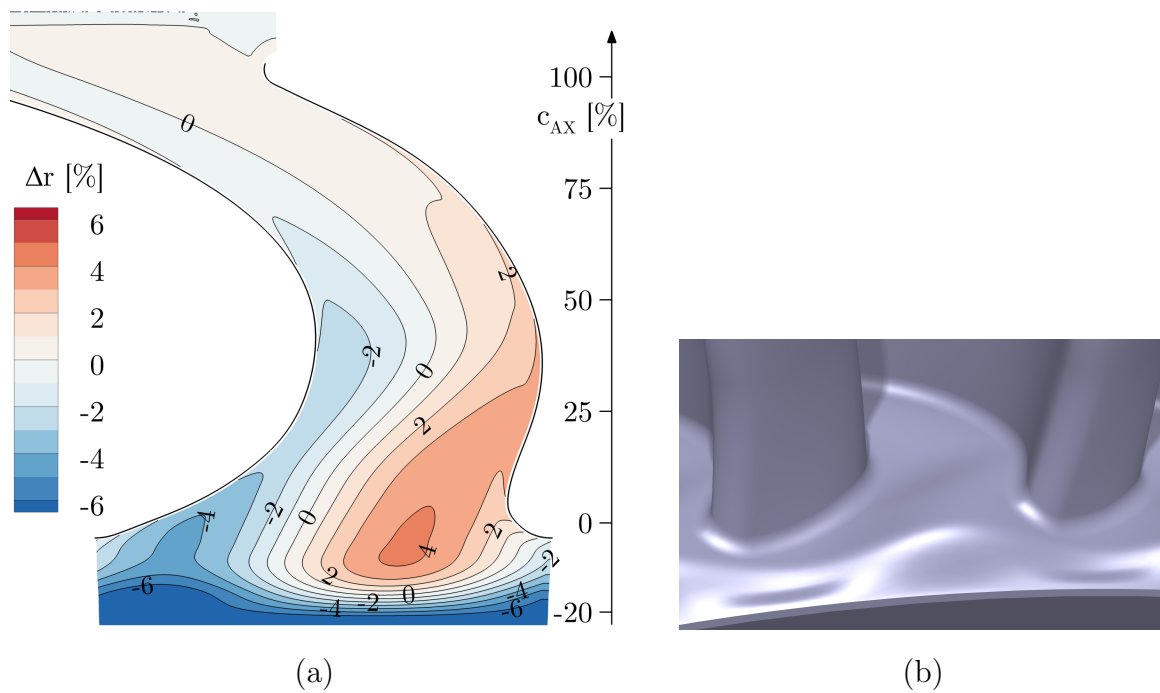
Figure 2.12.: Cavity extended rotor hub endwall contouring. Relative radius difference to nominal hub radius normalised by the blade span (a) and three dimensional CAD rendering (b).

passage to reduce to cross-passage pressure gradients and hence secondary flow strength (see [67], [20], [145] and [144], among others). These designs often result from optimisations without considering wheelspace cavities and rim seal purge air injection, which are unavoidable for high-pressure turbines in real applications.

2.2.5. Rotor Blade Tip Designs

For the rotor blade tip heat transfer investigations, four different tip geometries were installed on the same bladed rotor (blisk) using a rainbow approach. The mechanical integration of tip coolant supply for bladed rotor disks and the integration of the heat transfer measurement setup are discussed in Section 3.4.2. In this part, the individual geometries are briefly introduced and discussed. The coolant supply for the geometries with cooling and purge holes is described in Section 2.1.5 and can also be suppressed by closing the access in the cavity. All designs are shorty described and illustrated in Figure 2.13. All dimensions are given in percentage of the rotor axial chord.
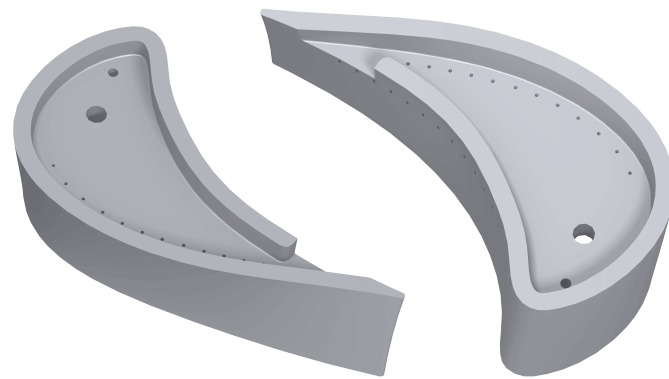
(a) Squealer Geometry
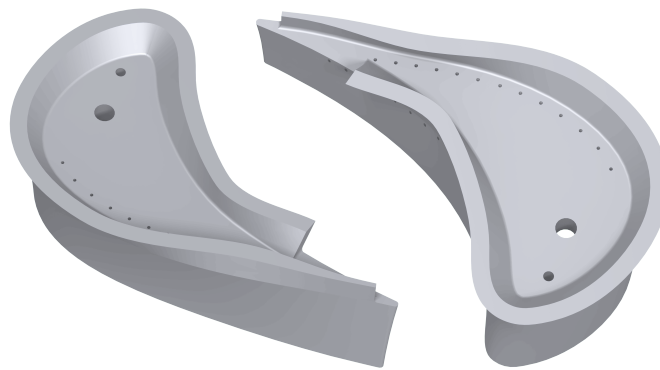
(b) Optimised Squealer Geometry
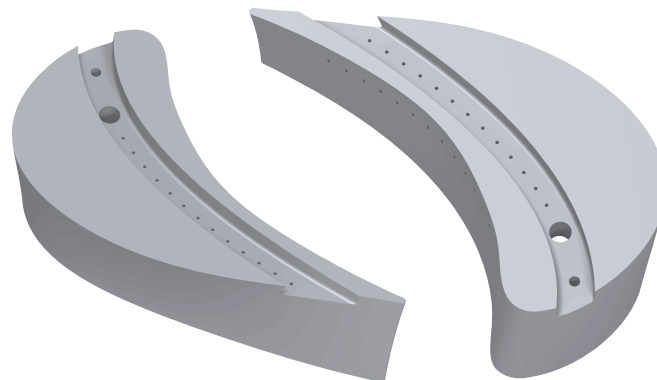
(c) Trench Geometry

(d) Notch Geometry

Figure 2.13.: Rendering of the different rotor blade tip geometries investigated.

Squealer The baseline squealer tip geometry has a fence thickness of 5.2% and a basin/cavity depth of 7.5% c_{ax} (Figure 2.13a). The fence has a cut-out on the pressure side at 77% c_{ax}. The cooling hole pattern consists of two arrays of 13 cooling holes each—placed in the squealer basin close to the suction side fence and on the blade pressure side at 92.4% span height—and two dust holes in the basin. The hole diameters are 1.0%, 3.1% and 6.2% of the axial chord for the cooling holes and two dust holes, respectively. Both cooling hole arrays have equally spaced holes located between 47% to 82% c_{ax} for the basin and 33% to 84% c_{ax} for pressure side locations. The dust holes are placed at 14% and 29% c_{ax} along the blade camber line in the squealer cavity.

Optimised Squealer The optimised squealer design features the same cooling hole arrangement as the baseline squealer tip. However, the main difference is the modified squealer fence geometry. As depicted in Figure 2.13b, the fence is leaned outwards forming a type of "winglet" at the tip and the thickness is reduced towards the trailing edge, which also leads to a slightly larger cut-out. This design intends to reduce the aerodynamic losses associated with tip leakage vortex formation.

Trench The trench tip geometry is a modified flat tip including a slot/trench from the near leading to the trailing edge (Figure 2.13c). The cut-out is approximately 5.8% c_{ax} deep and 10.4% c_{ax} wide and has a reduced curvature compared to the blade camber line. The 13 cooling holes on the pressure side are equivalent to the baseline and optimised squealer geometry. An array of 13 equally spaced cooling holes is placed downstream of the two dust holes centred inside the trench slot. They are placed between 37.1% to 87.7% of the rotor axial chord. The dust holes (3.1% and 6.2% of c_{ax} diameter) are placed at 14% and 29% of the axial chord, respectively.

Notch The notch tip geometry is derived from a flat tip with a cut-out/notch on the suction side (Figure 2.13d). The notch starts at approximately 18.3% of the axial chord and extends up to 82.4% c_{ax} with a constant depth of 8.3% c_{ax}. The maximum width of the cut-out is 6.3% c_{ax}. This design does not include cooling holes or dust holes.

3. Experimental Methods and Instrumentation

This chapter gives an extensive and detailed overview of the heat transfer measurement principle and the instrumentation involved. As outlined in the introduction, results from heat transfer measurements in a rotating facility are rare in the open literature. Moreover, most existing work has been performed using heat flux gauges. However, despite the high temporal resolution for unsteady phenomena, the measurements lack spatial resolution. This work is part of a continuous effort by the Laboratory for Energy Conversion (LEC) at ETH Zurich to enable and develop measurement setups and instrumentation for high-resolution heat transfer measurements in a stationary and rotating frame in a continuously running rotating turbine test facility. The work presented in this thesis builds up on the achievements of Laveau [95] and Lazzi Gazzini [100] by improving and extending the measurement technology for measurements on highly curved rotor hub endwalls and blade tips.

3.1. Background

3.2. Basics of Infrared Thermography

Infrared thermography is the imaging of thermal information of an object through the emitted infrared radiation captured with an infrared-sensitive device. This optical technique is a non-intrusive and truly two-dimensional process. As mentioned in the introduction, its application crosses many disciplines in thermo-fluid dynamics, as well as medicine and military applications.

Every object above absolute zero temperature ($0\,\mathrm{K}$) emits energy as radiation. The amount of radiation emitted by the object is linked to the object's temperature by the fundamental law of physics of Stefan-Boltzmann
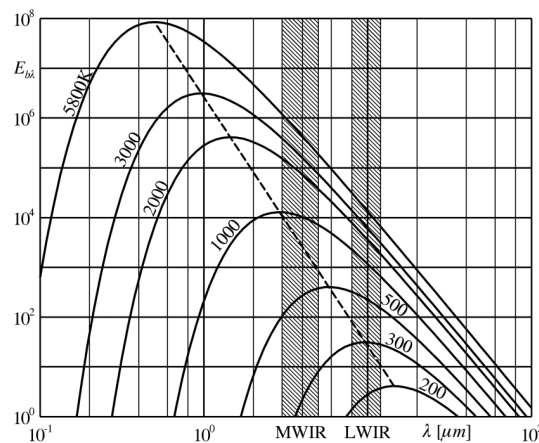
Figure 3.1.: Spectral hemispherical black body emissive power $E_{b\lambda}$ for several absolute temperature values as a function of wavelength λ [13].

(Equation 3.1).

$$E = \sigma \varepsilon T^4 \tag{3.1}$$

The total energy radiated per unit of surface area for all wavelengths per unit of time E is directly proportional to the fourth power of the objects' absolute thermodynamic temperature T. The Stefan-Boltzmann constant σ is equal to $5.670\,373 \times 10^{-8}\,\mathrm{W\,m^{-1}\,K^{-4}}$ and the emissivity ε of a non-ideal black body is <1. The frequency distribution of the radiation is given by Planck's law of black-body radiation and the wavelength of maximum spectral radiance λ_{max} is determined by Wien's displacement law (Equation 3.2).

$$\lambda_{max} = \frac{b}{T} \tag{3.2}$$

The wavelength of maximum radiation is inversely proportional to the object's temperature with b representing the Wien's displacement constant $(2.897\,771\,995 \times 10^{-3}\,\mathrm{m\,K})$. As illustrated in Figure 3.1, the long-wavelength infrared (LWIR) band is of particular interest for thermal measurements at the environmental temperatures used in the research facility as the peak emissive power falls into this wavelength.

3.3. Heat Transfer Measurements in the Rotating Frame of Reference

This section introduces the measurement setup and principle for the infrared base heat transfer measurements in the rotating frame of reference. First,

the general setup in the facility—including a broad overview of the involved instrumentation and components—is presented. Then, the measurement principle for deriving the convective heat transfer coefficient is introduced and described. The last section covers the development, manufacturing and calibration of the custom heat transfer measurement inserts used for the rotor hub and blade tip measurements.

3.3.1. Measurement Setup

The heart of the measurement setup were the custom thin-film surface heater inserts installed on the rotor. The electric current for the heater was provided by a laboratory power supply (Elektro-Automatik EA-PS 3150-4B), with a maximum power output of $600\,\mathrm{W}$ at $150\,\mathrm{V}$ and $4\,\mathrm{A}$, connected to the rotor over a slip-ring. The feeding current was measured by a true-RMS digital multimeter (Uni-T UT803) and logged by the measurement computer. Infrared transparent windows in the rotor casing provided optical access for a high-speed infrared camera to measure the surface temperature of the insert. The camera was connected to and controlled by the measurement computer and mounted on a camera positioning system (Figure 3.2). Resistance temperature detectors (Pt100) were installed inside the heating insert close to the heated surface. They were connected to a wireless rotating telemetry system on the back of the rotor. The data acquisition system was controlled by the measurement computer over a Wi-Fi connection and powered by a laboratory power supply through the second channel of the slip ring. All electrical components were connected to a common ground with the turbine.

The infrared camera was mounted on a vertically adjustable table in front of the optical access (Figure 3.2b). To extend the optical coverage by the infrared camera through the windows (Figure 2.6), multiple acquisitions with different camera angles were performed. Aluminium wedges with angles of $-4.5°$, $4.5°$ and $15°$ were installed below the camera and used to tilt it by the respective angles. Each acquisition consisted of 1000 individually triggered frames.
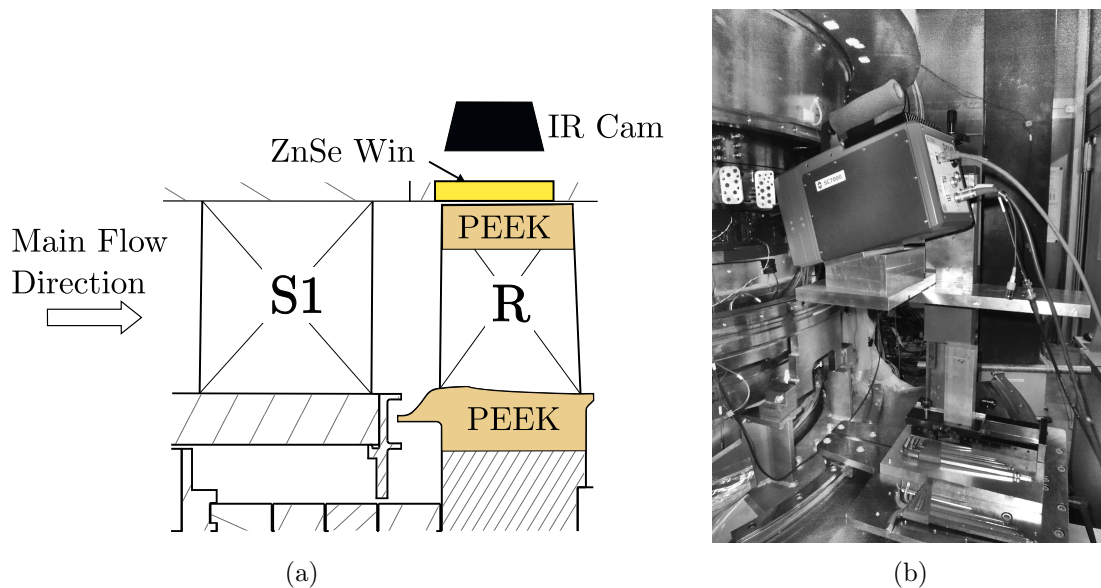
Figure 3.2.: Schematic cut of the turbine illustrating the heat transfer inserts on the rotor hub and tip and the optical access for the infrared camera (a). Image of the camera positioning system outside the turbine with installed wedge for 4.5° camera tilting (b).

High-Speed Infrared Camera

The infrared-based temperature measurement of fast-moving objects at "low" temperatures imposes high requirements on the infrared camera. Using a turbine operating point with a rotational speed of 2700 rpm, the speeds of the surfaces to be measured—based on the nominal hub and tip radius—were approximately 93 m/s and 113 m/s for the hub and tip, respectively. Therefore, a very low sensor integration time was required to capture unblurred images. Conventional uncooled infrared cameras using a micro-bolometer (with a finite mass and typical thermal time constant of 10 ms) are not sensitive enough to enable clear images within the expected temperature range (300 K to 380 K) and exposure time. For this work, a FLIR SC7300L infrared camera with a photon-based detector and a 25 mm optics was used. The mercury cadmium telluride (MCT) camera sensor has a spectral response between 7.7 µm to 9.3 µm and a resolution of 320×256 pixel and was actively cooled by a Stirling cooler to 77 K. The camera was factory calibrated (± 1 K) for two different detector gains ($x1$ and $x3$) with Flir multiNUC for adjustable sensor integration times.

The camera setting used was an integration time of 10 µs and detector gain factor of 3. With the specified speeds of the hub and tip, motions of 0.93 mm and 1.33 mm were achieved for the hub and tip surface, respectively. A
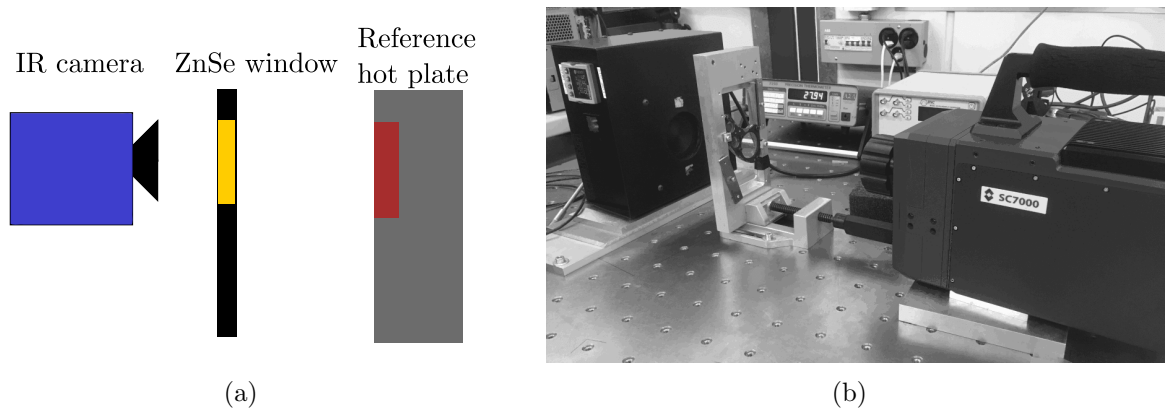
Figure 3.3.: Illustration (a) and image (b) of the infrared camera calibration setup including ZnSe windows and reference grey body hot plate.

specific calibration curve for the camera was derived to account for the transmission losses of the ZnSe-windows. Therefore, a setup using a grey body hot plate (ISOTECH Model 975) and the camera including the ZnSe window in between (representative to the measurement in the turbine) was used (Figure 3.3). The grey body emissivity was specified as >0.95, which was similar to the high-emissivity painting used on the heater surface. The target size was 70 mm in diameter with a specified temperature stability of ±0.2 °C. This calibration was directly used in post-processing to convert the digital camera output to a temperature reading. The calibration setup was based on the suggestions by Ochs et al. [125].

The calibration was performed in two ways. In steps of 10 K, the grey body hot plate was heated up and held constant for 30 min to ensure temperature stability, and reference images with the IR camera settings used in the experiments were taken. In the second step, once the maximum calibration temperature was reached, the transient cool-down of the reference plate was recorded using the IR camera. The reference plate temperature was read out and recorded automatically every 5 s and matched with the camera recordings. The average value from both calibration runs (Figure 3.4a) was taken and a fourth-order polynomial fit used to create the calibration curve for post-processing. The deviation between the averaged calibration curve and the individual readings derived from the heat-up and cool-down measurements was found to be below ±0.5 K, as depicted in Figure 3.4b.
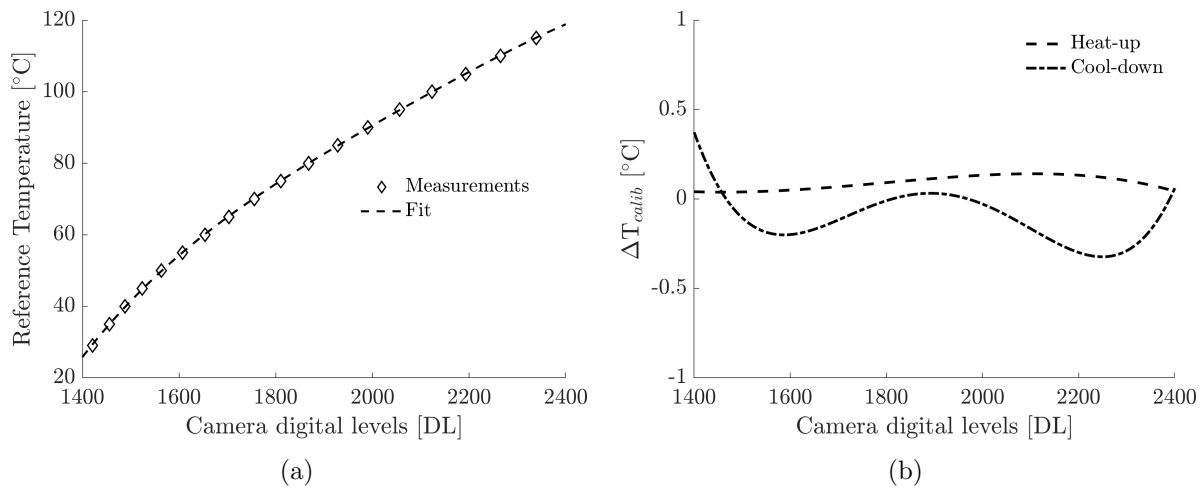
Figure 3.4.: Illustration (a) and image (b) of infrared camera calibration including ZnSe
              windows using a reference grey body hot plate.

Infrared Transparent Windows

For the heat transfer measurements, a steel holder with infrared transparent
windows was inserted in the optical access described in Section 2.1.4. Zinc
selenide (ZnSe), despite being brittle and highly toxic if broken, was the
material of choice for this application due to of its high transmissivity. The
window holder accommodates one central window with an outer diameter of
41 mm and two smaller windows with diameters of 18 mm each. The holder
and windows were re-used from previous measurements performed on the
stator endwall. The windows were coated with an anti-reflection coating
and machined to have the inner and outer surface match the rotor casing
radii. This ensured the avoidance of additional interference when exposed
to the turbine flow field, which was especially important for the rotor tip
heat transfer measurements. The windows were mounted in the holder with
a nitrile rubber gasket to prevent any flow leakage.

3.3.2. Derivation of Heat Transfer Coefficient

The heat transfer coefficient h (HTC) is a very important parameter to
calculate heat transfer between solids and moving fluids in convective
environments (such as gas turbines). The definition of h (as given in
Equation 3.3) is often referred to as Newton's law of cooling. It is very

similar to the thermal conductivity in Fourier's law of heat conduction.

$$h = \frac{\dot{q}''}{T_s - T_\infty} \tag{3.3}$$

where h :   convective heat transfer coefficient   (W/m²/K)
$\dot{q}''$:   heat flux between solid/fluid   (W/m²)
T_s :   solid temperature   (K)
T_∞ :   fluid bulk temperature   (K)

Compared to thermal conductivity, which is a (temperature dependent) material property, the convective heat transfer coefficient also heavily depends on the flow situation (e.g. laminar or turbulent). For engineering applications in the gas turbine industry, the temperature sensitivity of the heat transfer coefficient can often be ignored without introducing significant error.

An extensive review of measurement techniques for the convective heat transfer coefficient is provided by Moreira et al. [119]. For the present work, the convective heat transfer coefficient was assumed to be invariant to temperature and defined as the proportionality factor between the convective heat flux at the wall and the difference in wall temperature T_w and adiabatic wall temperature T_{aw} (Equation 3.4).

$$\dot{q}''_{conv} = h \cdot (T_w - T_{aw}) \tag{3.4}$$

This definition of the heat transfer coefficient has the advantage of being independent of the thermal boundary conditions and the definition of the fluid bulk temperature T_∞, which can be very difficult to define for complex flows such as present in gas turbines. Furthermore, the heat transfer coefficient is only a function of the geometry, flow field and fluid properties [118]. The adiabatic wall temperature is the wall temperature if the wall is in thermal equilibrium with the flow (i.e. zero heat flux is present). In the setup used in this work, the heat flux boundary conditions at the surface were actively set and the wall temperature measured. Using this definition, the heat transfer coefficient can be determined by measuring the wall temperature for multiple known surface heat fluxes, as schematically illustrated in Figure 3.5.

Convective heat flux was calculated from a one-dimensional energy balance
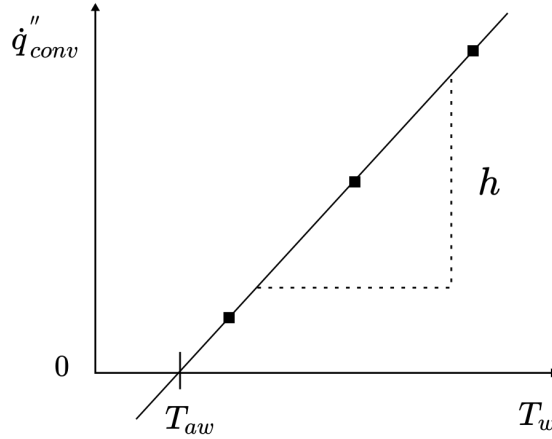
Figure 3.5.: Derivation of the convective heat transfer coefficient h and adiabatic wall temperature T_{aw} from multiple wall temperature measurements with known convective heat flux.
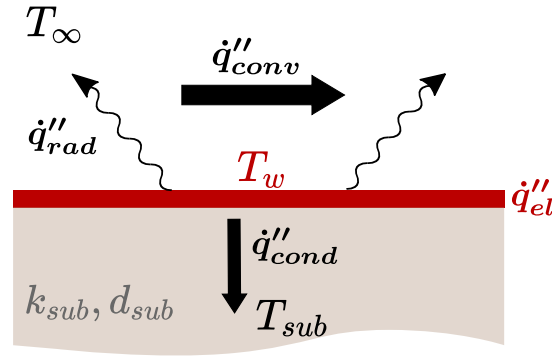
Figure 3.6.: Illustration of heat flux(es) on the measurement setup.

(Equation 3.5) on the wall surface, as illustrated in Figure 3.6.

$$\dot{q}''_{conv} = \dot{q}''_{el} - \dot{q}''_{cond} - \dot{q}''_{rad} \tag{3.5}$$

A thin-film heater installed on the surface of interest generates an electric heat flux $\dot{q}''_{el}$ by resistive (Joule) heating. This heat flux was directly calculated from the supplied power (P_{el}) divided by the surface area (Equation 3.6). A local scaling factor S_q (Section 3.3.3.5) was added to account for local non-uniformities in heat flux generation. Conduction losses $\dot{q}''_{cond}$ were calculated using resistance temperature detectors installed in the substrate and the thermal conductivity k_{sub} (described in Equation 3.7). The radiative heat flux $\dot{q}''_{rad}$ was calculated according to Equation 3.8, with ε being the surface emissivity and σ being the Stefan-Boltzmann constant.
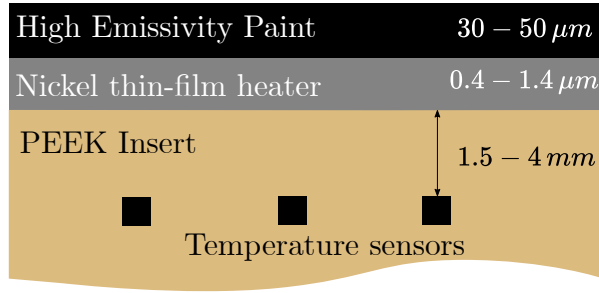
Figure 3.7.: Schematic setup of the thin-film heating inserts (not to scale).

$$\dot{q}''_{el} = S_q(x, y) \cdot \frac{P_{el}}{A_{surf}} \tag{3.6}$$

$$\dot{q}''_{cond} = \frac{k_{sub}}{d_{sub}} \cdot (T_w - T_{sub}) \tag{3.7}$$

$$\dot{q}''_{rad} = \varepsilon\sigma \cdot \left(T_w^4 - T_{t,rel}^4\right) \tag{3.8}$$

A detailed description of the thin-film heating insert manufacturing process, instrumentation and calibration are provided in the next section.

3.3.3. Custom-Made Thin-Film Heating Inserts

The integration of quasi-uniform heat flux boundary conditions in the rotating frame of reference was achieved by using surface thin-film heating inserts. This approach allows the parallel manufacturing of the heat transfer instrumentation and turbine rotor. Also, the calibration and instrumentation of temperature sensors and heat flux uniformity can be performed independently from the rotor. Furthermore, it also allows the easy exchange of potentially malfunctioning instrumentation. The basic setup of the insert was similar for the hub endwall and blade tip heat transfer measurements and is schematically depicted in Figure 3.7. The base material for the insert was PEEK, a high strength (yield stress $\approx$110 MPa) but low-weight and low thermal conductivity semicrystalline thermoplastic polymer (Figure 3.8a). The material has favourable machining properties and is well suited for manufacturing of complex geometries. The detailed mechanical integration of the hub insert and rotor blade tip inserts are discussed in separate Section 3.4.

3.3.3.1. Electroless Nickel Plated Thin Film

Due to the highly curved surface of the rotor endwall geometry (Figure 2.12), the application of commercially available thin-film heating foils was not possible. Previous work presented by Lazzi Gazzini et al. [98] used a physical vapour deposition (PVD) technique to create a thin layer of electrically conductive nickel on a PEEK substrate. It was found that the adhesion of the film depends strongly on film thickness, which limits the design freedom for electrical resistance. Furthermore, local differences in material properties reportedly led to high non-uniformities in the generated heat flux. For this work, electroless nickel plating (also called chemical nickel coating) was used to deposit an even layer of nickel-phospohrus directly onto the PEEK surface (Figure 3.8b). In this process, the film was deposited by the reduction of nickel ions to metallic nickel with a chemical reducing agent. This process offers significant advantages for the coating of complex geometries. The effects of shadowing for PVD or variable layer thickness due to uneven current densities in electroplating were not present. The coating process was performed by Galvotec GmbH, a highly specialised coating company in this field. The specific electrical resistance of chemical nickel films is a function of the phosphorus content [133], while film thickness also likely has an effect. Therefore, high uncertainty in the specific resistance of the layer had to be included in the heater design process. To the best of author's knowledge, the present work represents the first use of custom thin-film heaters based on chemical nickel coating reported in the open literature. Also, the required film thickness (400 nm to 1.4 μm) was much lower than the thickness normally used with this process. The film adhesion strength was qualitatively tested using the scotch-tape method [14] and good adhesion to the PEEK substrate and to the copper pin used for the current connection was observed. This test does not provide a qualitative measure of the adhesion; however, given the concentrated shear stress on the coating, it may be used as a conservative measure of the normal stresses due to the rotation in the facility. Pt100 resistive temperature sensors from IST AG (Type P0K1.161.1E.B.1050) were embedded for substrate temperature measurements. The glue used for their installation has a similar thermal conductivity to the PEEK.

3.3.3.2. Thin-Film Heat Generation and Track Design

The physical principle of heat generation by the thin-film heater is resistive or ohmic heating, which is often also referred to as Joule heating. This is the process in which electric current is converted into heat due to the resistance

(a) Milled PEEK hub insert
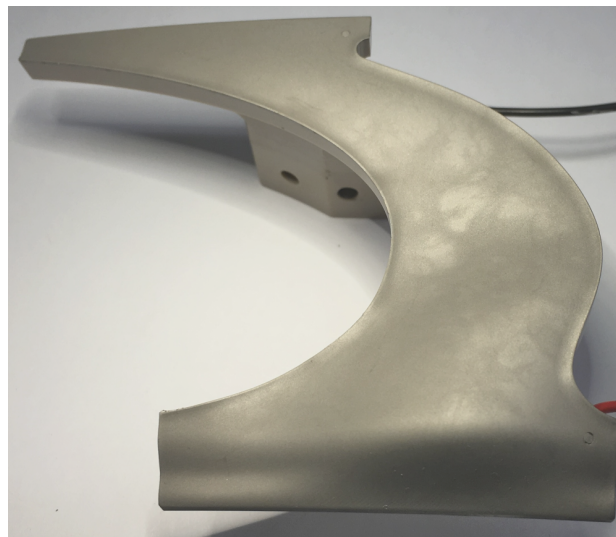
(b) Nickel coated hub insert
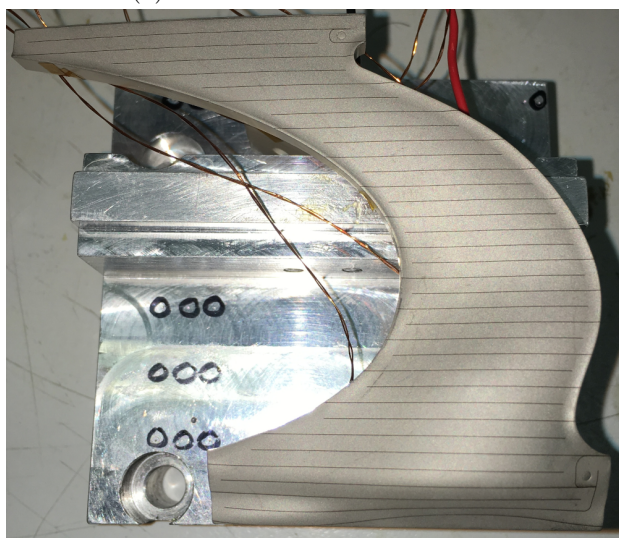
(c) Laser-cut heating track
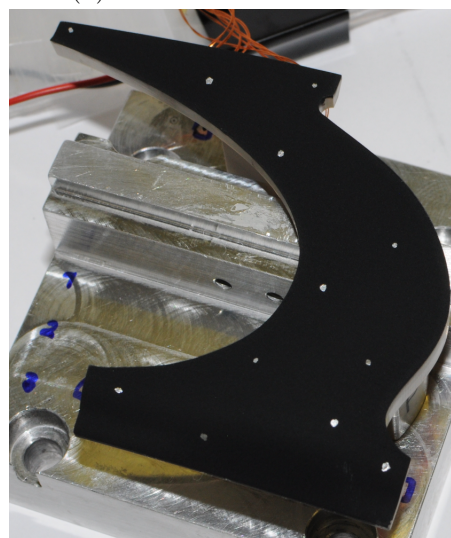
(d) High emissivity painted insert

Figure 3.8.: Major manufacturing steps for the nickel thin-film surface heating inserts.
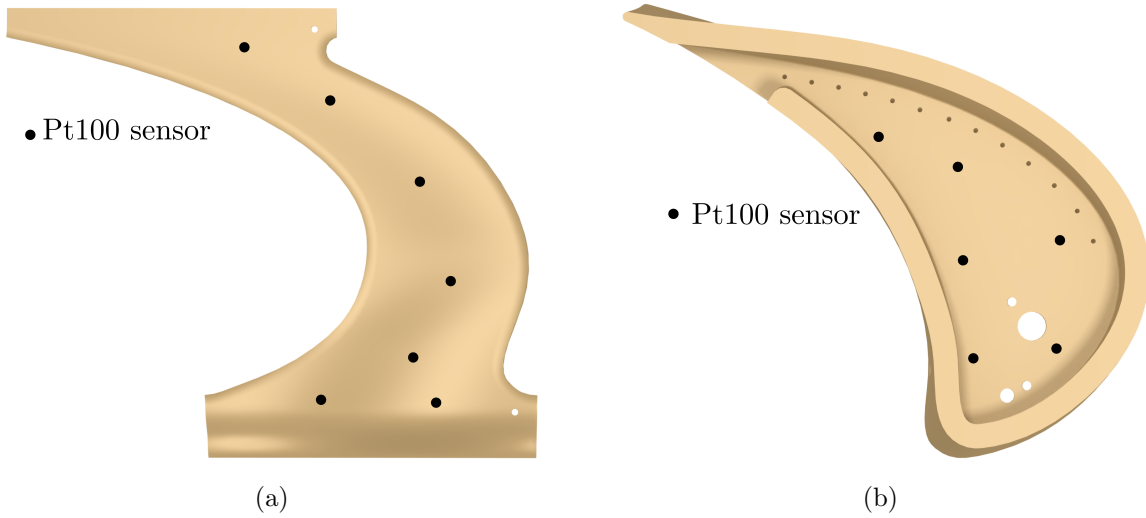
Figure 3.9.: Illustration of the embedded Pt100 temperature sensors for the hub (a) and the squealer tip insert (b).

of the conductor. The electrical power is equal to the voltage drop over the conductor multiplied by the current flowing through. If combined with Ohm's law, electrical power is equal to the voltage drop squared divided by the total resistance (Equation 3.9). Thus, surface specific heat flux is the power divided by the surface area (Equation 3.10).

$$P = U \cdot I = \frac{U^2}{R} \tag{3.9}$$

$$\dot{q}''_{el} = \frac{P_{el}}{A_{surf}} \tag{3.10}$$

The total resistance of a conductor is equivalent to the specific resistance ρ of the material times the length l divided by the cross-sectional area A_{cross} of the conductor (Equation 3.11). In the case of a thin-film heater with a serpentine-like track, cross-sectional area is equal to the layer thickness t times the track width w (Equation 3.12).

$$R = \rho \frac{l}{A_{cross}} \tag{3.11}$$

$$R = \rho \frac{l}{t \cdot w} \tag{3.12}$$

The heater design was based on a constant predefined track width based on experience from previous work and a target electrical heat flux of $10\,\mathrm{kW/m^2}$ at $50\,\mathrm{V}$. The track geometry was designed to cover the maximum possible

area of the insert. Based on the design heat flux and voltage, the total required ohmic resistance (Equation 3.13) could be calculated. The total track length from the design and the total design resistance then define the thickness of the coating (Equation 3.14).

$$R_{design} = \frac{U_{design}^2}{\dot{q}_{el,design}'' A_{surf}} \tag{3.13}$$

$$t_{design} = \rho \frac{l}{R \cdot w} \tag{3.14}$$

Pulsed laser ablation was used to create the heating track by locally removing the nickel layer and creating the electrically connected serpentine-like heating track (Figure 3.8c). This process was suitable due to the high accuracy and the small cutting width of approximately $55\,\mu m$. This relatively simple track design for the hub endwall insert was manufactured using a picosecond Nd:YAG laser coupled with an Aerotech A3200 positioning system using G-code. For the blade tip inserts, where the sensitivity of misalignment due to the cooling holes was higher, the laser ablation of the heating tracks was performed by a specialised company with a more elaborate positioning system.

3.3.3.3. High Emissivity Paint and Surface Roughness

The heating surface was painted with a black coating to increase the emissivity for the infrared measurements (Figure 3.8d). The widely used high-emissivity paint Nextel Velvet-Coating 811-21 by Mankiewicz was directly applied on the nickel surface using compressed air spraying. The total emissivity of the coating is approximately 0.97. Previous studies showed that the emissivity is not significantly sensitive to temperature and stable up to view angles of 60° ([103], [89] and [4]). Additionally to the inserts, all of the aluminium blades and endwalls on the blisk were painted to provide equal roughness on the rotor and to reduce potential reflections for the infrared measurements. Infrared reflective marks were distributed over the insert as reference points for the three-dimensional image reconstruction in post-processing (Section 4.1.1).

The roughness of the painted surface was measured using a Mitutoyo SJ-2010 surface profilometer. Due to the increased surface roughness compared to blank aluminium, the effect of roughness was considered in numerical

Table 3.1.: Surface roughness values measured on the heated surface on the hub and tip
            inserts.

Parameter	Hub endwall	Tip Notch	Tip Trench
Ra $[\mu m]$	6.1 ± 0.4	3.9 ± 0.5	4.6 ± 0.6
Rz $[\mu m]$	37.6 ± 4.2	24.6 ± 2.8	27.6 ± 3.1
Rq $[\mu m]$	7.6 ± 0.5	4.9 ± 0.6	5.7 ± 0.8

modelling and the prediction of heat transfer. Measurements were taken towards the trailing edge of the endwall insert due to the accessibility and reduced curvature of the endwall. For the tip inserts, only the Notch and Trench geometries were measured because the squealer fence blocked access by the profilometer to the heated surface. Table 3.1 summarises typical roughness values measured on the inserts. The reported values are the mean of five measurements with the respective standard deviations.

3.3.3.4. PEEK Material Characterisation

For the calculation of conduction heat flux losses into the substrate, the thermal material properties are important. The manufacturer's stated values of density ρ, specific heat capacity c_p, thermal conductivity k and the derived thermal diffusivity α are presented in Table 3.2. For a rough validation, the same material properties were also measured from material samples of the actual inserts. Accurate measurements of thermal properties are very difficult and involve a great deal of effort. Therefore, the experimental measurements performed in the scope this work serve as a rough validation of manufacturer specifications. A Mettler Toledo DSC1 STARe System was used to measure the thermal heat capacity, while thermal diffusivity was measured using a Netzsch LFA 457 MicroFlash and density was measured using a simple calliper and a Lutro GM-300P scale. The measured values are also reported in Table 3.2. Despite the variance for the heat capacity and diffusivity, the derived thermal conductivity lies within $12\,\%$ of the manufacturer's specification. Due to higher confidence in the manufacturer's specifications, their values of material properties were used for this work.

Table 3.2.: Thermal properties of PEEK.

	$\rho \left[\frac{kg}{m^3}\right]$	$c_p \left[\frac{J}{kgK}\right]$	$k \left[\frac{W}{mK}\right]$	$\alpha \left[\frac{mm^2}{s}\right]$
Specification	1310	1340	0.25	0.142**
Measurements	1300	994*	0.28**	0.221*

*Measurement difficult with high uncertainty

**Derived quantity

3.3.3.5. Calibration

In addition to the high-speed infrared camera, the custom-made heat transfer inserts represent the core of the measurement setup and require careful calibration. This section describes the different calibrations performed for the inserts and presents the calibration results.

Temperature Sensors   The insert-embedded Pt100 temperature sensors were calibrated together with the rotating data acquisition system in a temperature-controlled oven. This calibration was necessary because the installation of the sensors in the platform may have altered the sensors' characteristics and because each measurement channel of the data acquisition board was tuned for maximum sensitivity in the expected temperature range. The calibration oven temperature was changed in steps of 10 °C to 20 °C within the sensor calibration range. The oven reference temperature was measured by two RTD's located near the instrumented inserts and the measured temperature spread of this two measurements was generally found to be below ±0.5 K. The calibration of each sensor was calculated as the first-order polynomial fit through the data. The standard error of the fit (RMSE) was generally below 0.15 K with an R-square above 0.99. Figure 3.10a illustrates typical calibration curves for the Pt100 temperature sensors, while Figure 3.10b presents typical (absolute) errors between the calibration measurements and fit. The sensitivities achieved were approximately 34 mV/K for the hub endwall insert and between 66 mV/K to 93 mV/K for the tip inserts, depending on the individual sensors and the best achievable gain setting on the acquisition board.

Heater Resistance   The heating power of the surface film heater—and thus the generated heat flux—was calculated in the experiments based on
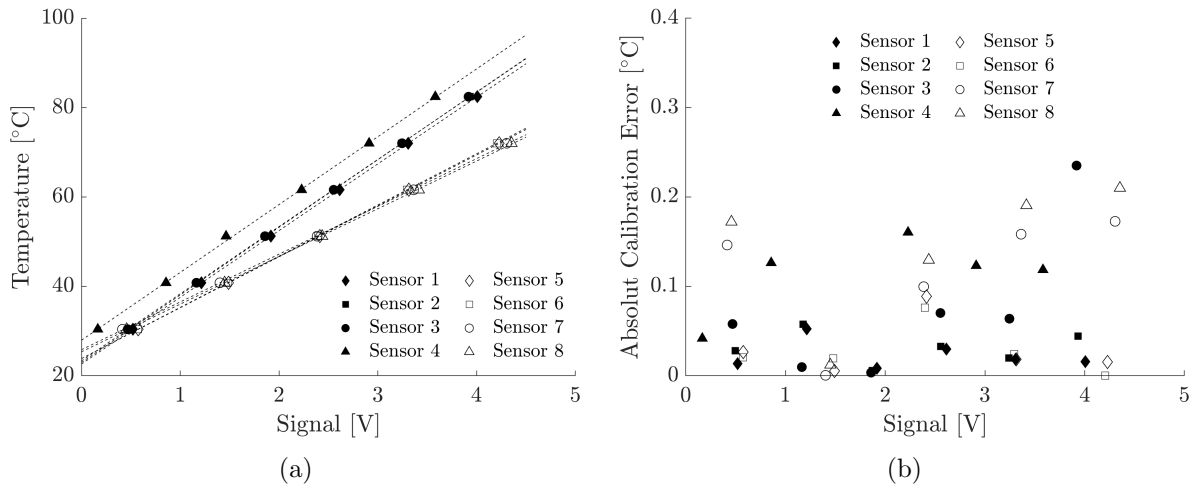
Figure 3.10.: Calibration fit (a) and error (b) for a representative sample of Pt100 temperature sensors used for the conduction heat flux calculation.

Table 3.3.: Heating surface resistance and sensitivity to temperature.

	Hub	Tip			
		Squealer	Opt. Squealer	Trench	Notch
Sensitivity $[\Omega/K]$	0.103	0.083	0.030	0.018	0.017
$\alpha \left[\times 10^{-4} \; ^\circ C^{-1}\right]$	2.0	3.6	1.3	1.7	1.7
R at $50\,^\circ C$ $[\Omega]$	510.5	235.4	225.5	105.5	95.2

the total resistance of the heater and the current supplied. Since the nickel thin-film heater itself may change its electrical resistance with changing temperature, the total resistance was measured and calibrated for different temperatures. The calibration was performed in the same temperature-controlled oven as the temperature sensors and the total insert resistance was measured using a Fluke 175 true-RMS digital multimeter at different temperatures.

Table 3.3 summarises the key temperature calibration variables for all inserts. For all heating inserts, the temperature sensitivity of total electrical resistance was found to be close to or below $0.1\,\Omega/K$. This translates to temperature coefficients α more than an order of magnitude below typical values of Pt100 resistive temperature detectors.

Surface Heat Flux Non-Uniformity The described heat flux generation based on the conductor resistance (Section 3.3.2) is an integral (averaged)
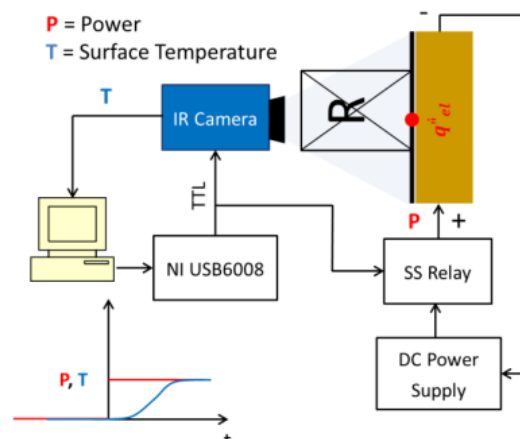
Figure 3.11.: Schematic illustration of the calibration setup for the surface heat flux correction ([98]).

value over the surface. The locally generated heat flux may not be uniform for the heater due to material impurities or current concentrations. To account for this effect, a local correction factor $S_q(x, y, z)$ was introduced, which locally scaled the average heat flux generation. This process was based on the work of Lazzi Gazzini et al. [98] and is briefly outlined here.

For the calibration, the transient thermal response of the heater surface is measured to a step-wise change in applied power. In the setup (schematically depicted in Figure 3.11) the heater was connected to a laboratory power supply with a solid-state relay in between. A multifunctional I/0 device was controlled by the measurement computer and used to create the trigger signal for image acquisition and the switching of the relay. The transient temperature rise on the heater surface was recorded by the camera while a true-RMS multimeter recorded the current fed to the heater. This test was performed for different heating levels representing to the use for the measurements in the turbine.

A rise in the surface temperature of a homogenous, semi-infinite solid with a step-wise change in surface heat flux is theoretically described by Equation 3.15 [180].

$$\Delta T(t) = T(t) - T_0 = \frac{2 \cdot \dot{q}_{el}''}{e} \cdot \sqrt{\frac{t - t_0}{\pi}} \tag{3.15}$$

where T_0 is the initial surface temperature, $\dot{q}_{el}''$ is the heat flux and e is the thermal effusivity of the substrate. The assumptions for this relationship to

hold are:

- One-dimensionality

- Heat flux source at the free surface of the solid and in perfect thermal contact

- An initial homogenous substrate temperature

- Homogenous and isotropic solid

Surface temperature rise is linearly dependent on the square root of time (Equation 3.16). Hence, local heat flux generation can be calculated by Equation 3.17.

$$\Delta T(t) = p_1 \cdot \sqrt{t - t_0} \tag{3.16}$$

$$\dot{q}''_{el} = \frac{e \cdot \sqrt{\pi}}{2} \cdot p_1 \tag{3.17}$$

The transient temperature rise was evaluated for each pixel and mapped onto a surface mesh of the heater geometry using the infrared markers (Section 4.1.1). The linear fit between the square root of time and temperature increase (parameter p_1 in Equation 3.16) was evaluated based on this data (Figure 3.12). The start of the linear fit region was chosen to be twice the estimated thermal diffusivity time constant τ of the high-emissivity coating based on a thermal diffusivity α for paint coatings [137] and the estimated paint layer thickness t (Equation 3.18).

$$\tau \approx \frac{t^2}{\alpha} \tag{3.18}$$

For regions with high heat flux generation, such as heating track turns with local current concentration (point B in Figure 3.13), lateral conduction occurs after some time and led to a decreased temperature rise. This was observed as a deviation of the expected linearity between the temperature rise and the square root of time (Figure 3.12). The considered signal range for the linear fit of the data was iteratively decreased for each point until a normalised root mean square error of the fit below 0.008 was reached. A point-by-point scaling factor S_q was calculated for each point on the endwall as the ratio of the locally generated heat flux and the average heat flux of
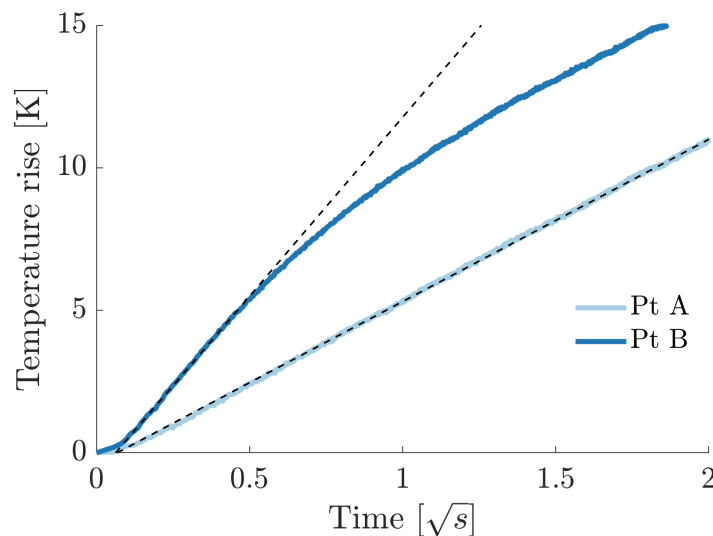
Figure 3.12.: Temperature response on a step-wise heat flux change of the surface heater (Point A and B illustrated in Figure 3.13a).

the endwall (Equation 3.19).

$$S_q(x, y, z) = \frac{\dot{q}_{el}''(x, y, z)}{\bar{\dot{q}}_{el}''} \qquad (3.19)$$

The scaling factor of the local electric heat flux used in post-processing (Equation 3.6) was averaged from all heating steps that were calibrated for. Typical standard deviations found between scaling factors for different power levels were below 0.03, or 2.5 % of the averaged value (Figure 3.13b). In general, the chemical deposited thin-film heaters showed a very high uniformity in heat flux generation excluding the track turn areas with current concentrations. The non-uniform heat flux generation observed for the physical vapour deposited heater presented by Lazzi Gazzini et al. [98] with correction factors up to 3 could be eliminated with the new coating technique. Variations of the scaling factor S_q on the main heater area were typically below ± 15 %. The scaling factor distribution of the hub endwall and the four tip measurement inserts are depicted in Figure 3.13.

(a) Hub endwall

(b) Hub endwall standard deviation

(c) Squealer

(d) Optimized Squealer

(e) Trench

(f) Notch
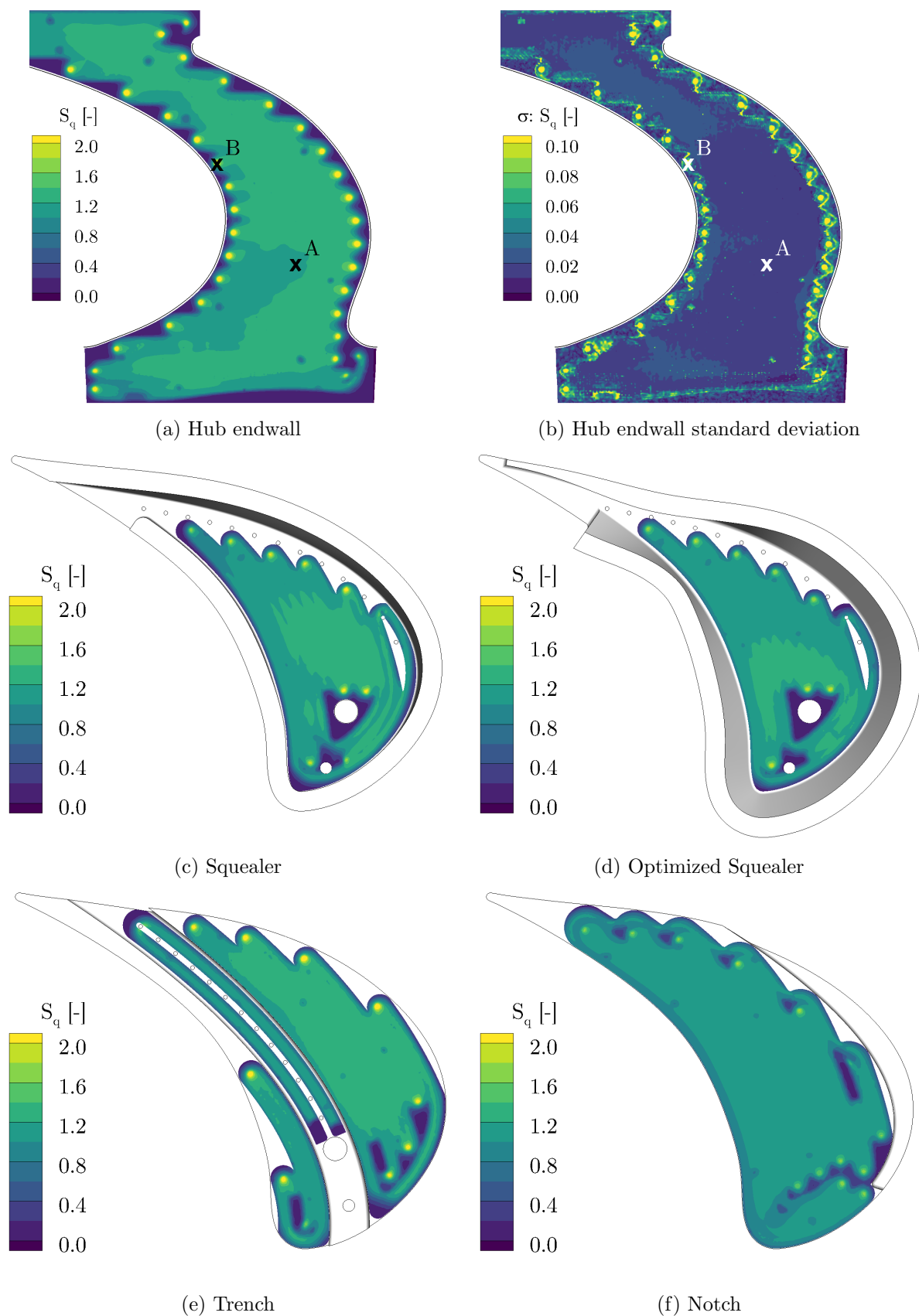
Figure 3.13.: Distributions of the average heat flux scaling factor S_q on the rotor hub endwall (a), blade tip inserts (c)-(f) and standard deviation for the hub (b).

3.4. Rotor Integration of Heat Transfer Measurement Inserts

Besides the manufacturing and calibration of the custom heat transfer inserts, their integration on the rotor is crucial for measurements in a rotating facility. The mechanical integrity of the system must be given to prevent damage to the test rig due to foreign object damage in the flow path or increased vibration due to imbalances. The hub platform integration process was similar to the work presented by Lazzi Gazzini [100]. Therefore, only a numerical assessment regarding the increased weight due to the reduced blade count and cavity design was performed. To the best of the author's knowledge, the integration of variable blade tip inserts for infrared-based heat transfer measurements—including pressure and temperature sensors as well as tip coolant ejection for bladed disk rotors—has not been published in the open literature. Details of the integration for both concepts are presented in this section. Three identical inserts were always installed next to each other on the rotor to provide instrumentation redundancy in case of failure.

3.4.1. Hub Endwall Platform Inserts

The rotor hub inserts had two extrusions fitting into counter pockets in the rotor blisk. The precisely machined fit between the parts restrained the circumferential bending and torsional movement of the insert. An M5 shoulder fitting screw inserted from the front fixed the inserts against radial displacement (Figure 3.14 and 3.15a) and carried the main load. Two additional M3 screws were mounted from the back side of the blisk to fix the rear portion of the insert. The 0.25 mm gaps between the aluminium blisk blades and the inserts needed for installation were filled with epoxy glue to create a smooth surface connection (Figure 3.15b).

3.4.1.1. Numerical Structural Analysis

A numerical structural investigation was performed using Ansys 18.2 to assess the stress and deformation of the platform. For this setup, the full rotor—including all sub-components such as the hub endwall platforms, fixation screws and cavity ring—were included and modelled. Bonded surface contacts were applied where the screws were fixed to the platform and between the rotor and the screws. The gap between the rotor fillet and the

(a)   (b)
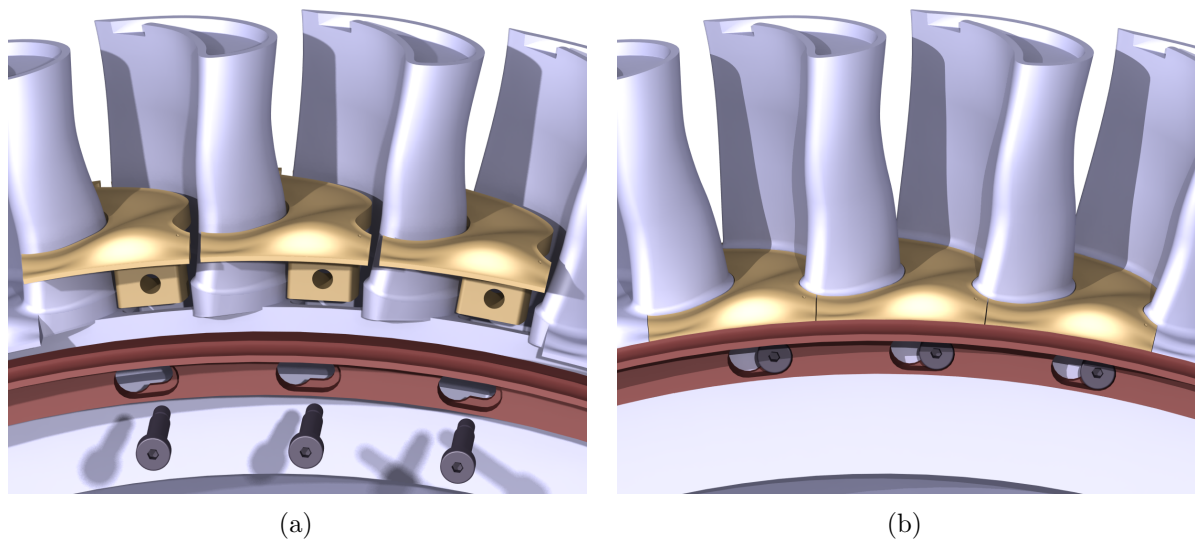
Figure 3.14.: Illustration of the hub heat transfer platform integration into the rotor blisk.
Exposed view (a) and assembled view (b).

(a)   (b)
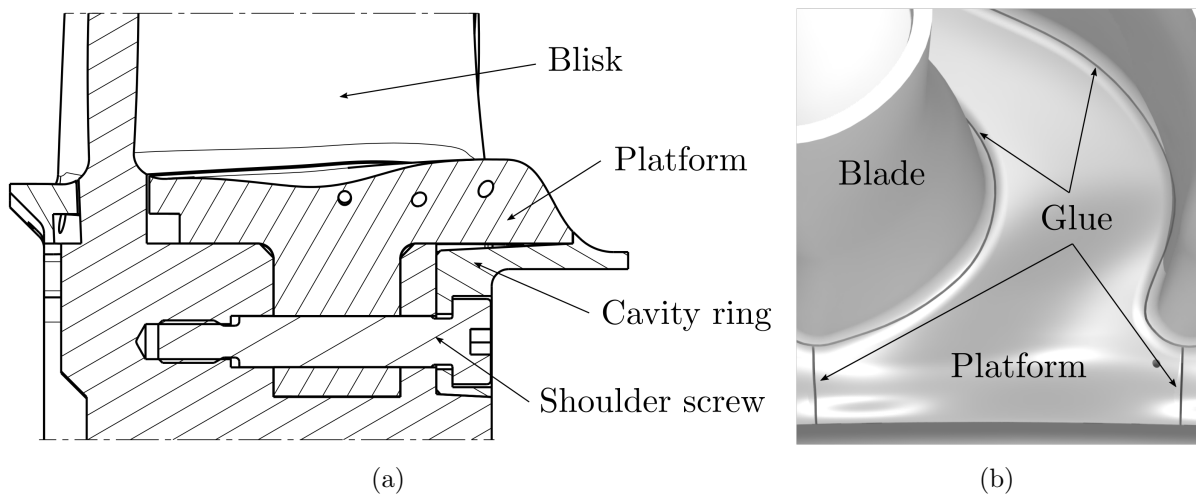
Figure 3.15.: Axial cut of the hub endwall heating platform integration and fixation on
the rotor blisk (a). Shoulder screws fix platform in place from the front (two
additional screws in the back portion are not shown). Illustration of glue
filled gap between insert and blisk (b).

hub platforms, which was filled with glue for the experiments, was modelled as frictionless contact. Therefore, the predicted results are considered conservative. The gap between the individual platforms, at the front and back end, are however implemented as bonded surfaces representative of the real experimental setup with the glue applied. The ambient temperature was set to 55 °C and the platforms were assumed to have a uniform temperature of 80 °C. Simulations were performed for the design rotational speed of 2700 rpm as well as for 3000 rpm to represent over-speed conditions (i.e. during start-up). In total, 4.3 million mesh nodes were used for the geometrical discretisation. Appropriate materials with values derived from the respective suppliers were used for the different components.

Stress Assessment

The equivalent (Van-Mises) stress levels are depicted in Figure 3.16 for the nominal rotational speed of 2700 rpm and an elevated platform temperature of 80 °C. The stress levels observed on the platform were well below the material yield strength of PEEK, with a local maximum of 16 % of yield strength. Stress concentrations were found around the fixation holes in the platform extrusions and at the radius between the endwall and extrusion. A radial fixation of the platform by the upstream cavity ring (Figure 3.15a) would have reduced the stress but could not be implemented due to machining restrictions. Nevertheless, the observed stress levels were far below the material yield strength and offer a safety factor of more than 6. For the over-speed condition, the maximum equivalent stress and principal stress increased by 11 % and 22 %, respectively, which still offered a safety factor well above 4.5. Also, the loads on the fixation screws and rotor were well below their material limits for safe operation—even in rotor over-speed conditions predicted by the finite element (FEM) simulations.

3.4.1.2. Deformation Assessment

Besides the material stresses, the total deformation of the hub endwall inserts was analysed. The centrifugal force due to rotor rotation led to a deformation of the inserts. The predicted total deformation for nominal operation speed is depicted in Figure 3.17 and normalised with the nominal tip gap of 0.7 mm. The front part of the insert exhibited the highest local deformation (up to 40 % of the nominal tip gap). This was expected due to the overhang and mass concentration of the endwall to the fixation of

Equivalent stress
[% Yield strength]

Max. priniciple stress
[% Yield strength]
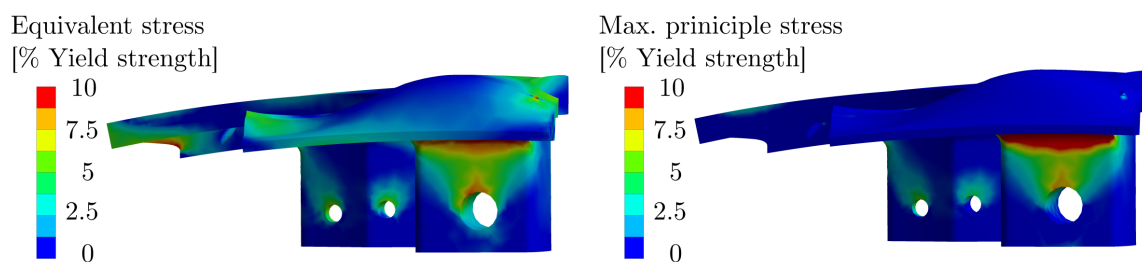
Figure 3.16.: Predicted equivalent (a) and maximum principal stresses (b) on the hub endwall insert for the designed rotational speed and heated platform to (80 °C).

Total Deformation
[% Tip gap]
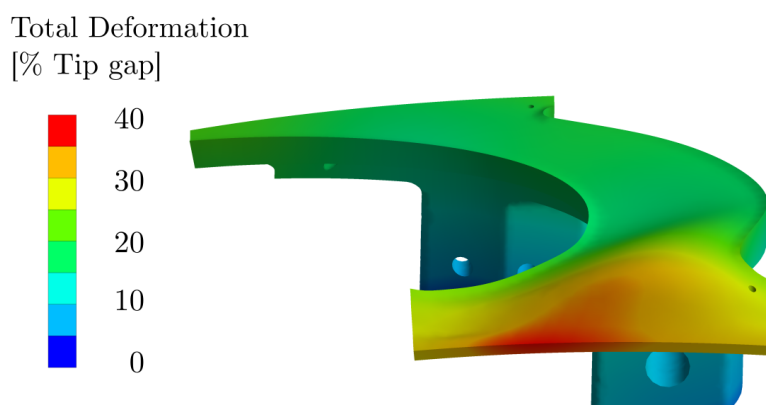
Figure 3.17.: Predicted total deformation for the hub endwall insert by FEM for the designed rotational speed and heated platform (80 °C).

the insert. Since the front portion of the insert was not fixed in the radial direction by the exchangeable cavity ring, a large deformation was present. This deformation introduced a geometrical step between the cavity ring and insert, which may locally disturb the flow field and hence the heat transfer. The friction between inserts and cavity ring was not modelled in the simulation, which would slightly reduce the maximum deformation in the experiment. During over-speed, the maximum deformation increased by 23 %, however, this point was not relevant for the heat transfer measurements.

3.4.2. Variable Blade Tip Inserts

The previously developed and tested heat transfer setup on the rotor endwall had to be integrated on the rotor tip. Moreover, the task involved integrating tip cooling in an existing bladed disk rotor and creating a versatile concept to test multiple geometries on a single rotor. This rainbow approach
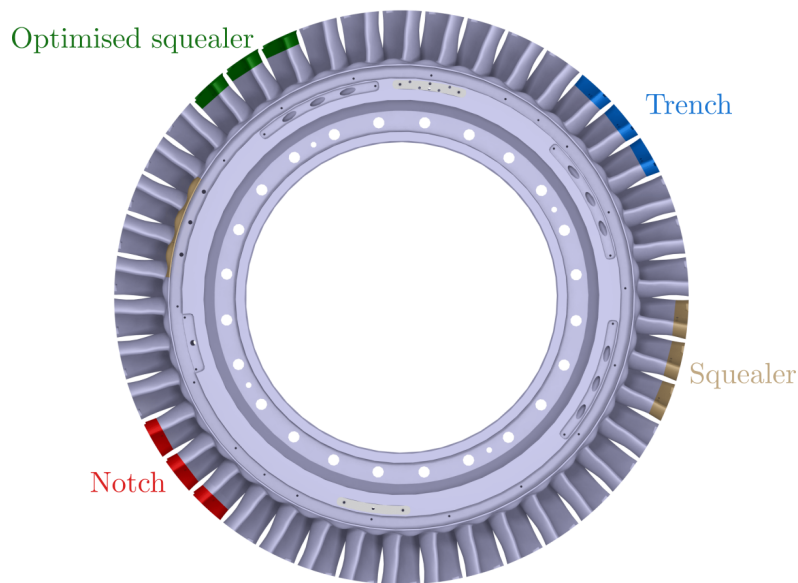
Figure 3.18.: Illustration of the rainbow rotor with four integrated blade tip design inserts.

enabled cost- and time-efficient experimental testing for the design study. The concept of variable blade tip inserts for combined aerothermal measurements is discussed in this section and facilitated the integration of the four aforementioned blade tip geometries (Section 2.2.5) on the bladed disk rotor (Figure 3.18) with only minor modifications. This section presents the insert design and assembly, the experimental testing and numerical investigation for the mechanical integration as well as the aerodynamic validation.

Insert Design and Assembly

For the integration of a tip insert, the rotor blade on the blisk was split into the main blade section and the insert (Figure 3.19a). The insert covered the last 30 % of the blade span. This approach has the following advantages for instrumentation and manufacturing:

- The tip insert can be instrumented and calibrated separately from the rotor

- An existing rotor blisk can be used and modified to accommodate inserts

- Blade tip coolant can be integrated in to a blisk by using conventional machining for the blade internal coolant supply channel
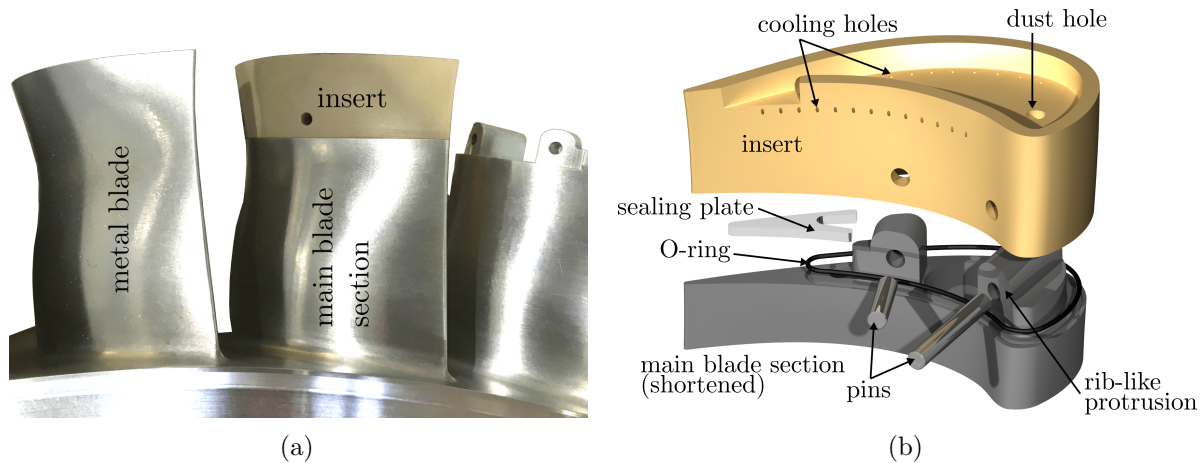
Figure 3.19.: Comparison of a metal blade to an instrumented blade with a tip insert (a)
and schematic illustration of the tip insert fixation (b).

The inserts were manufactured using the same high strength but low-
conductivity material as the hub inserts (PEEK). To allow blade tip coolant
ejection, the inserts had a hollow plenum to supply the cooling and dust
holes.

The assembly and fixation of the insert on the main blade section are illus-
trated in Figure 3.19b. Two pins at approximately 25 % and 55 % of the
blade camber line were used to fix the insert in radial direction. For this
purpose, the main blade section had two rib-like protrusions on the joint
face to hold the pins and the centrifugal load. The shape and tight fit to
the insert ensured precise alignment between the main blade surface and
the insert. The pin angles were the best compromise between maximum
contact area on the insert and accessibility for installation and removal.
After installation, epoxy glue was applied to secure the pin and to smooth
the flow-exposed surface. For the instrumentation wires, a separated channel
for coolant supply was drilled behind the trailing edge protrusion to the
rear of the blisk where the data acquisition system was mounted. To reduce
parasitic leakage of cooling flow between the main blade section and the
insert, a 0.7 mm sealing O-ring was installed in between the joint surfaces.
To achieve this, the trailing edge part of the insert plenum was closed with
an aluminium sealing plate (Figure 3.19b).

These tight manufacturing tolerances resulted in a firm fit between the main
blade section and the insert. Epoxy glue was used to level the transition
between the metal and insert blade profile. A step below $\pm 50\,\mu\text{m}$ was
measured before glue application using a surface profilometer (Figure 3.20).
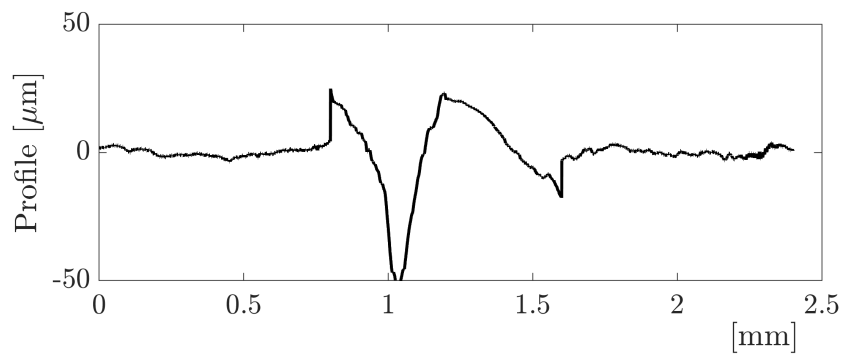
Figure 3.20.: Surface profile over the joint between a metal blade and insert before glue application.

Mechanical Integrity of Insert Fixation

In a rotating test facility (such as the facility used for this work) the mechanical integrity of instrumentation is crucial for safe operation. For the tip inserts, forces due to rotation and plenum overpressure were the main loads to be maintained by the fixation. Bending forces due to blade loading were carried by the protrusions of the main blade section.

Preliminary experimental tests using a representative test assembly in terms of the blade geometry, fixation and material (Figure 3.21) with additional ribs for clamping were performed. Tensile tests were performed at the Institute of Virtual Manufacturing at ETH Zurich using a ZwickRoell Model BZ1-MMRMOSO.ST02 with a maximum force of 30 kN and a thermally controlled specimen chamber ($-80\,°C$ to $250\,°C$). Tests were performed with two different load ramping rates ($2\,N/s$ and $5\,N/s$) up to a maximum force of $1200\,N$ (approximately equivalent to a safety factor of 2.4) at an elevated temperature of $55\,°C$. Additionally, also a 6-hour hold test was performed with a constant load of $1200\,N$. All tests confirmed the mechanical integrity of the insert and fixation with no signs of damage or cracks.

In addition to experimental mechanical integrity tests the setup, FEM simulations using Ansys 18.2 were conducted primarily to assess the maximal deformation of the inserts during operation. The actual blade tip geometries were used for the investigation, including a reduced main blade section (cut at $52\,\%$ span) and the two fixation pins. Bonded contacts between the pins and the blade main section and frictionless contact to the insert were defined. The load was applied by defining the desired rotational speed and fixed support for the main blade section. Material properties were
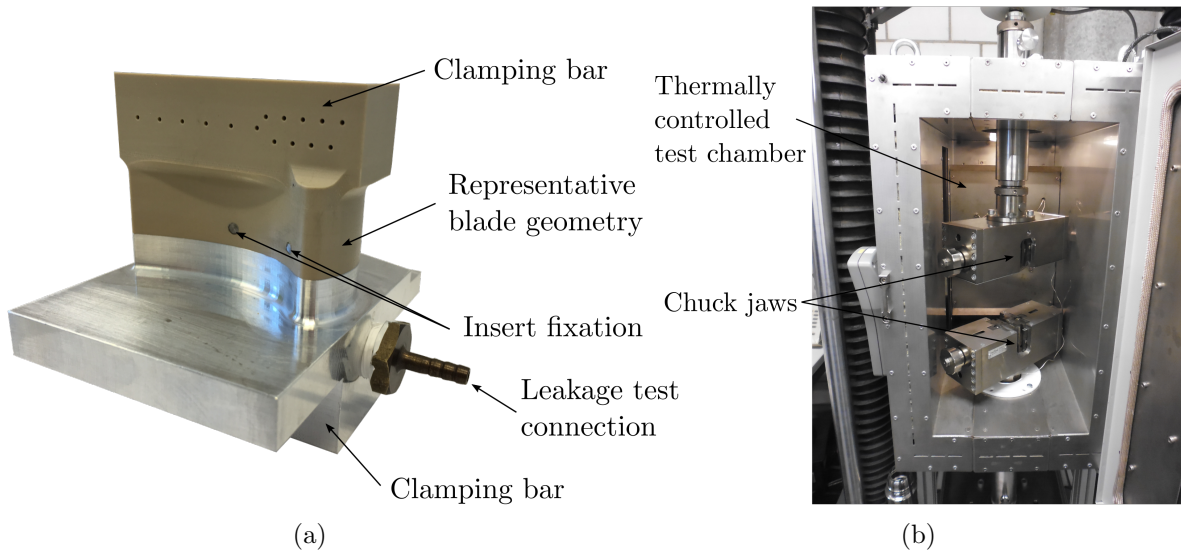
Figure 3.21.: Blade tip insert test assembly for tensile and leakage tests (a). Tensile test machine with a thermally controlled chamber (b).

defined and assigned to the parts according to the experiments and material data sheets. The additional weight of the thin-film nickel layer and the copper contact pins present in the experiments was estimated and accounted for by an artificially increased density of the PEEK in the model. The estimations were based on experience from an early prototype and were quite accurate (e.g. an approximately 1.5 % lower weight was estimated than later measured for the squealer geometry).

Adaptive mesh refinement was used to reduce the mesh node count and computational time. After two refinement steps, changes were generally below 1 % for maximum equivalent stress and below 5 % for total deformation. The convergence of the results with adaptive meshing was further confirmed by a manual mesh refinement study for the baseline squealer geometry. As depicted in Figure 3.22a, the stress levels were comparable to the results with high manual refinement. The maximum predicted deformation was not very sensitive to the mesh refinement (Figure 3.22b) and was well within the profile tolerance from the rotor manufacturing ($\pm 50\,\mu m$).

To assess the potential of rubbing at the casing, the total deformation of the insert with the given fixation was investigated (for all geometries). The total deformation in percentage of the nominal tip gap at the designed rotational speed of 2700 rpm is depicted in Figure 3.23 with a scale factor of 40. The qualitative and quantitative results are very similar for
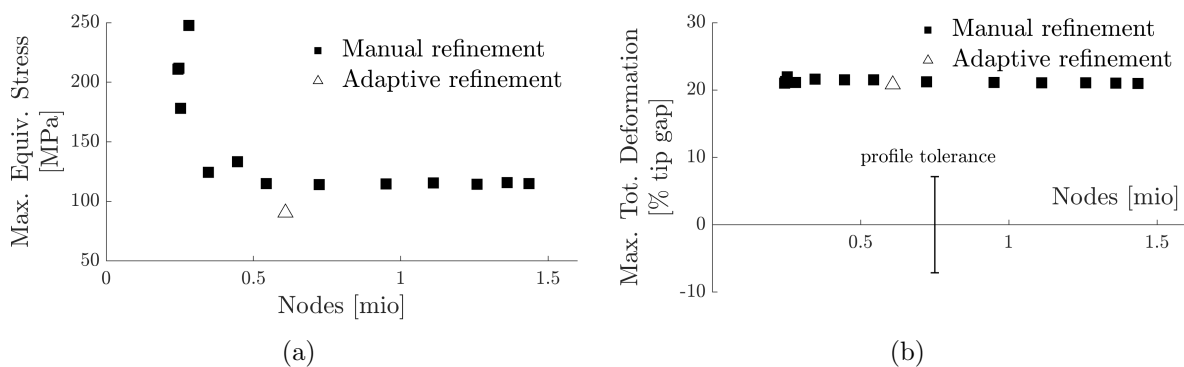
Figure 3.22.: Manual and automatic adaptive mesh refinement study on equivalent stress and total deformation.

all investigated tip geometries. The predicted deformations were below the manufacturing tolerance around the pin fixation area up to 65 % of the axial chord. Driven by the limited fixation towards the trailing edge, this region exhibits the largest predicted deformation—up to 21 % of the nominal tip gap for the design rotational speed and increasing to 25 % for over speed conditions during start-up (3000 rpm). The influence of this deformation—which presents a closing the tip gap—on the tip leakage flows and the turbine flow field could not be predicted *a priori*. However, since the deformations between different geometries are comparable, the results between designs on a rainbow rotor should be comparable. The effect of trailing edge deformation with this kind of insert fixation could potentially be compensated for by including these preliminary results into the design process and adjust the insert manufacturing.

In tip cooling studies, the leakproofness of the inserts is of high relevance and parasitic leakages between the main blade section and the insert should be avoided. Preliminary tests with the representative test assembly (Figure 3.21b) showed that relevant leakage was present without the installation of a sealing O-ring. The leakage with installed sealing was tested and measured using the tensile test machine with applied overpressure in the insert plenum. The resulting leakage rates as a function of plenum overpressure with an applied tensile load of 500 N—representative for nominal rotational speed—are depicted in Figure 3.24. The maximum blade specific leakage rate at 950 mbar overpressure was determined to be 1.2×10^{-10} g/s, which was approximately four orders of magnitude below the expected cooling flow rate.
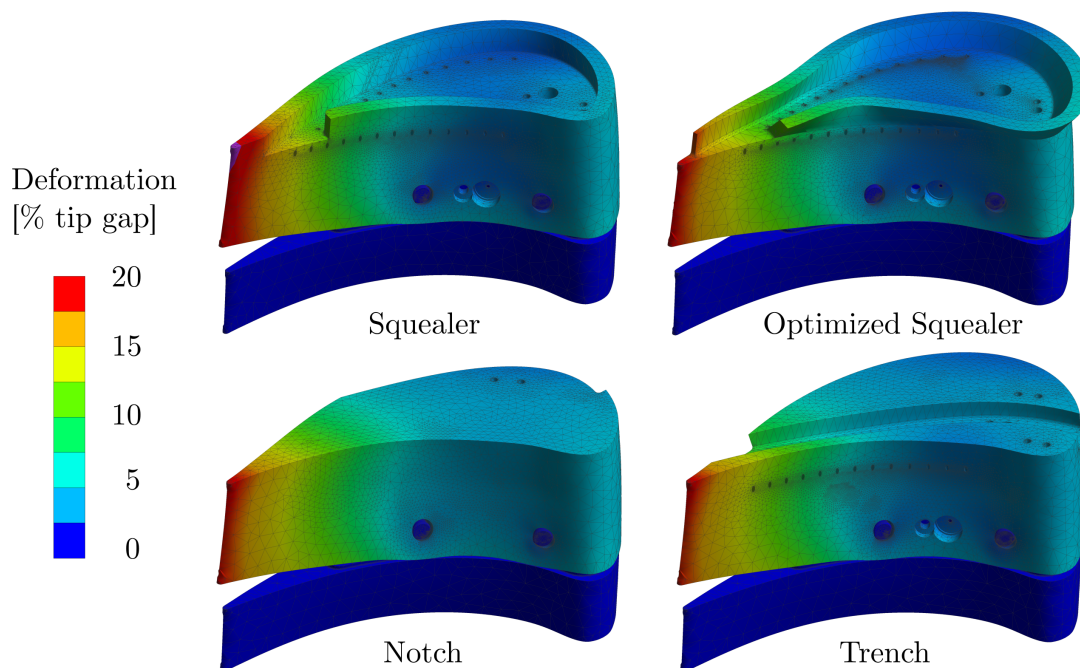
Figure 3.23.: Predicted total deformation (percentage of the nominal tip gap) by FE
              simulations for blade tip inserts under the designed rotational speed of
              2700 rpm (scale factor 40).
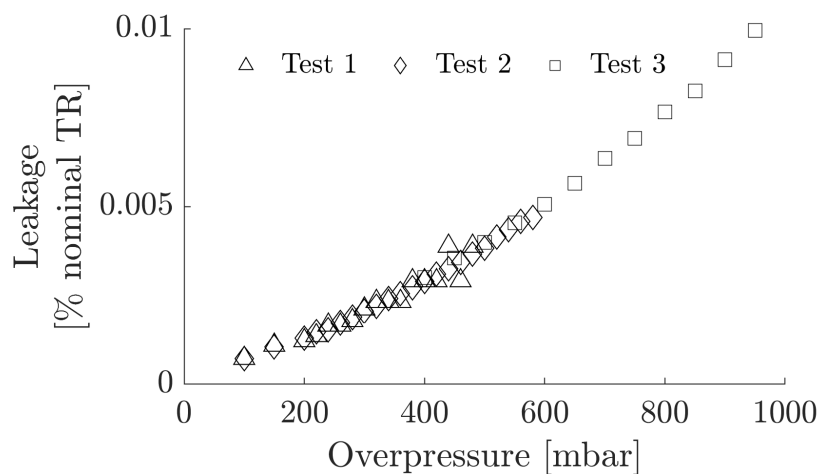
Figure 3.24.: Parasitic leakage (in percentage of the nominal tip coolant ejection rate TR_2)
              as a function of overpressure with 500 N tensile load applied.

Aerodynamic Validation

The variable blade tip instrumentation was also validated from an aerodynamic perspective by using fast-response probes and flow field measurements downstream of the rotor. The baseline squealer tip geometry was identical to the reference geometry of the aluminium blisk and was used for the aerodynamic validation. For this study, tip cooling supply to the instrumented tip was disabled (Section 2.1.5) to have similar flow conditions between the metal reference and the insert. Due to time and cost constraints, no special insert without cooling holes could be used for the validation. However, it was anticipated that the presence of "passive" cooling holes does not alter the local flow field more than the measurement resolution. The time-resolved flow field data was separated for each rotor passage and analysed for the three instrumented blades and all metal reference blades separately.

The circumferentially averaged relative total pressure and yaw angle profiles are presented in Figures 3.25 and Figure 3.26, respectively. The mean value of all the reference metal blade passages is plotted together with the mean value of the three instrumented blades. Additionally, the maximum and minimum blade-to-blade variations for the metal reference blades is shown. Considering the probe uncertainty and blade-to-blade variations of the rotor, the influence of the tip inserts on the flow field were concluded to be minimal. For both investigated flow quantities, the differences between the metal reference and instrumented blades were below the measurement uncertainty of the probe.

Instrumentation

All installed tip inserts for each geometry were equipped with a custom made thin film heater designed to maximise the heated surface area. Figure 3.27 shows the heating tracks for the four investigated geometries before being painted with high-emissivity paint. The profile-shaped surface posed a major challenge creating heating tracks with as few turns as possible (leading to local overheating), maximum coverage and accessibility for the electrical connection pins to the insert plenum. The cooling holes towards the suction side were bypassed in the design. However, as shown by Gottschlich [58], the chemical coating process would also allow coating of the inside of cooling holes, thereby reducing local overheating due to the track width reductions for heating patterns running over the holes. For the trench design, the three tracks on each surface were connected in series within in the blade plenum to extend to covered surface.

(a)   (b)
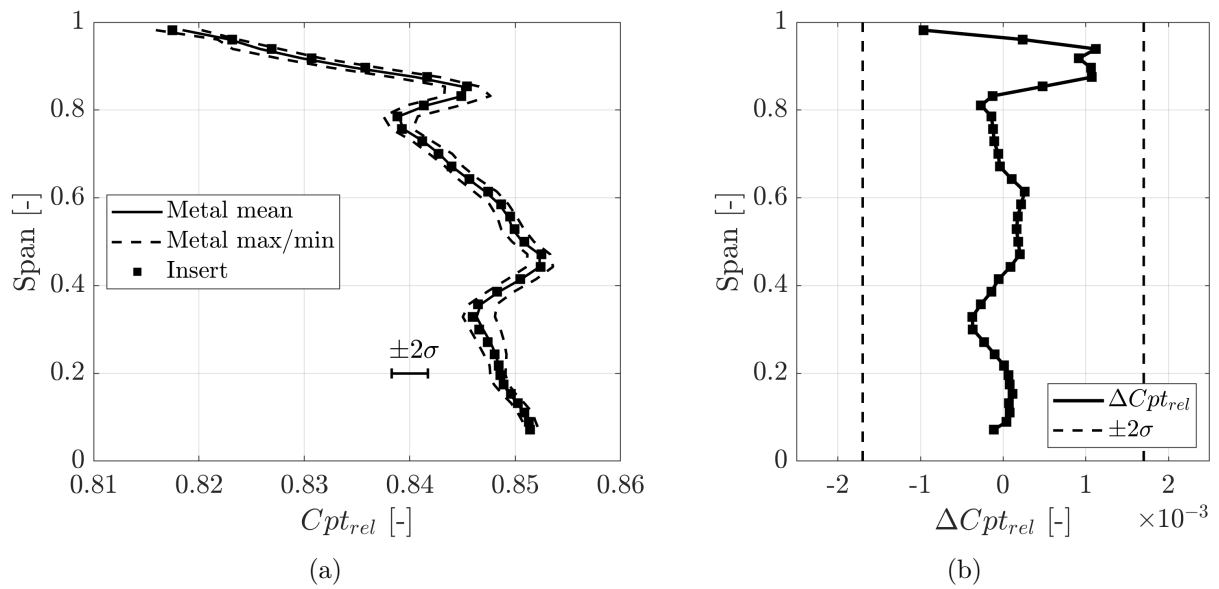
Figure 3.25.: Circumferentially mass averaged normalized relative total pressure profiles:
Metal blade and insert profiles (a) and absolute difference (b).

(a)   (b)
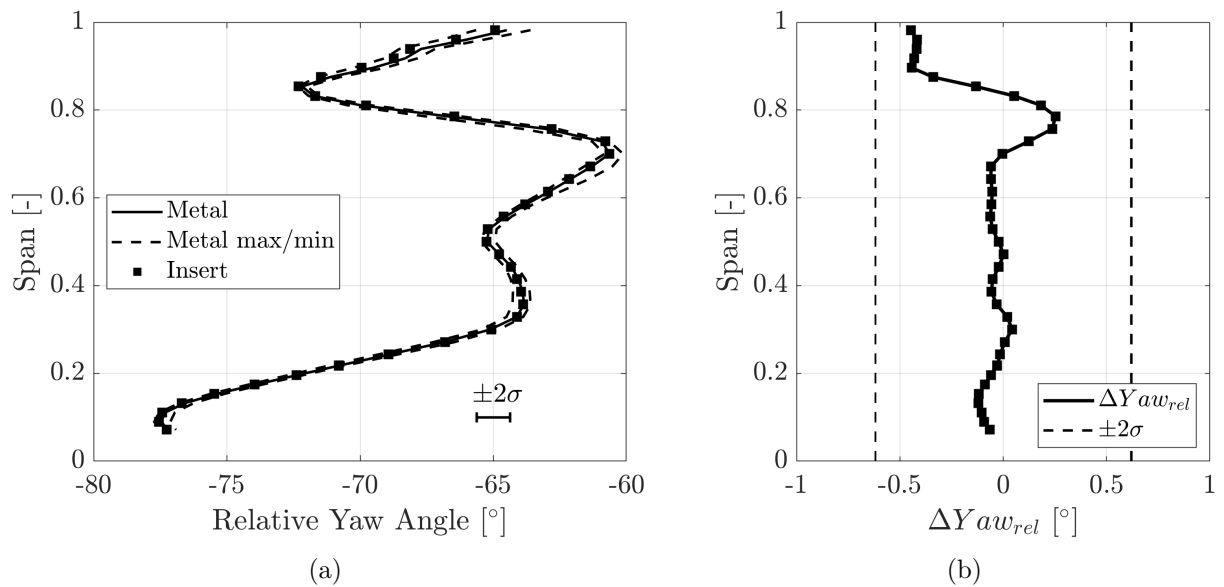
Figure 3.26.: Circumferentially mass-averaged relative yaw angle profiles: Metal blade and
insert profiles (a) and absolute difference (b).

(a) Squealer

(b) Optimized Squealer

(c) Trench

(d) Notch
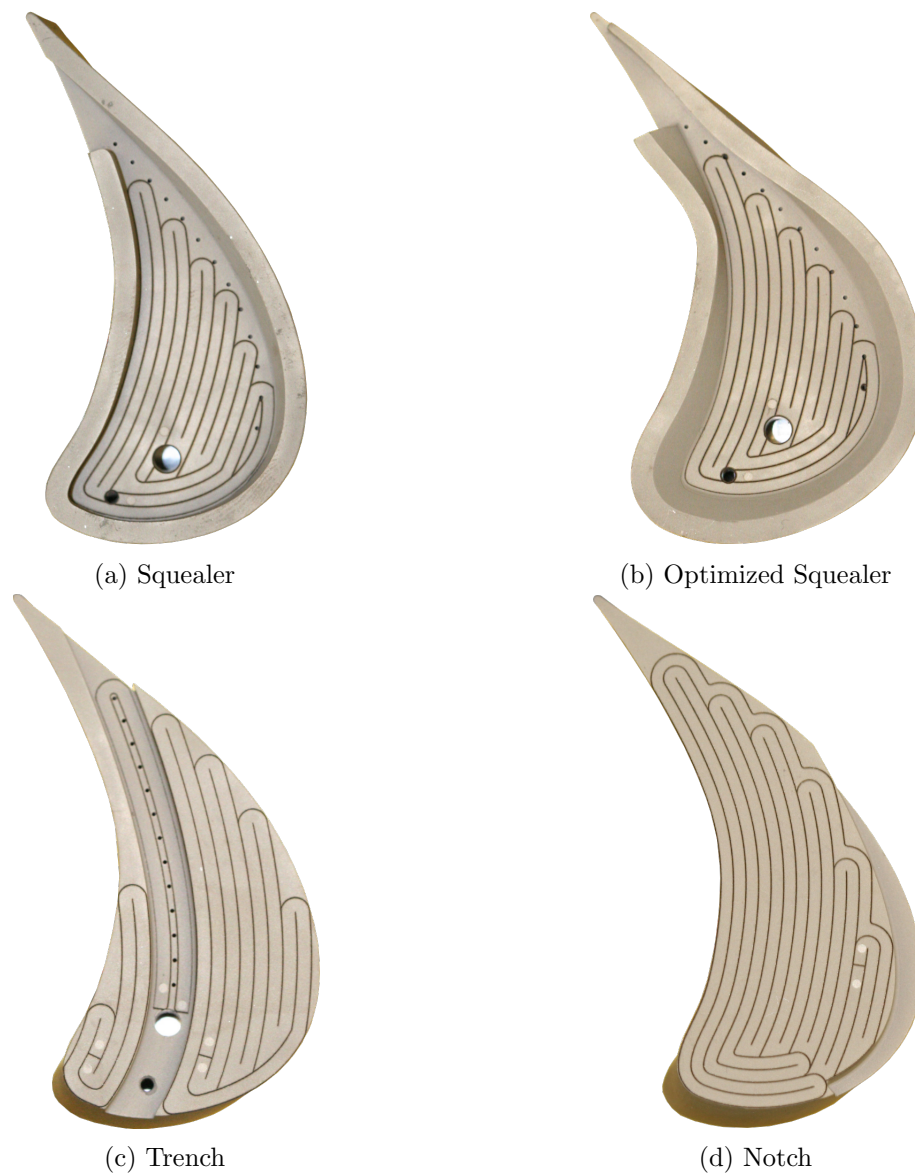
Figure 3.27.: Custom surface heating tracks on the studied blade tip geometries.

Temperature sensors (Pt100) were glued onto the rear surface inside the insert plenum and evenly distributed for substrate temperature measurement (conduction correction). The optimised squealer and trench design were further equipped with a fast-response pressure sensor to measure the pressure within the plenum.

3.4.3. Rotor Balancing

Notably, the instrumentation and rotating data acquisition system led to an imbalance in the rotor. Despite the high tolerance of the research rig to turbine vibrations, the uncompensated imbalance from the installed

instrumentation would have been too high for a save operation. Therefore, the imbalance was quantified and balanced at MTU Aero Engines AG and final levels of 630 g mm and 580 g mm were achieved for the hub and tip measurements, respectively. These values were below quality grade $G\,6.3$ according to ISO 1940 for rotor balance quality requirements.

3.5. Tip Coolant Mass Flow Measurements

Since the tip coolant for each supplied blade branches off from the rotor upstream cavity plenum (Section 2.1.5), additional instrumentation to measure the mass flow had to be developed. A miniature venturi flow meter—which can be integrated into the blade coolant supply channel to measure mass flow rate by means of the differential pressure over a contraction—was manufactured and calibrated for this purpose. The design of the venturi was based on, but not exactly according to, the ISO 5167-4 standard due to its small size and the limited space available (Figure 3.28). The diameter ratio for the differential pressure measurement was $\beta = 0.82$ and the half angles of the convergent and divergent sections were 11.5°. An outside thread on the venturi was used for the mounting in the coolant supply channel. Two piezoresistive pressure sensors were used for the pressure measurements. These were installed in pockets and connected to the venturi annulus by a small hole of 0.5 mm in diameter. The instrument was manufactured out of aluminium (AlSi10Mg) as one piece by selective laser melting (SLM) to create the internal geometry and then using conventional machining for the sensor pockets and mounting thread.
The instrumentation was calibrated using a mass flow controller with a thermal mass flow meter (Bronkhorst F-201AC-FAC) as a reference.
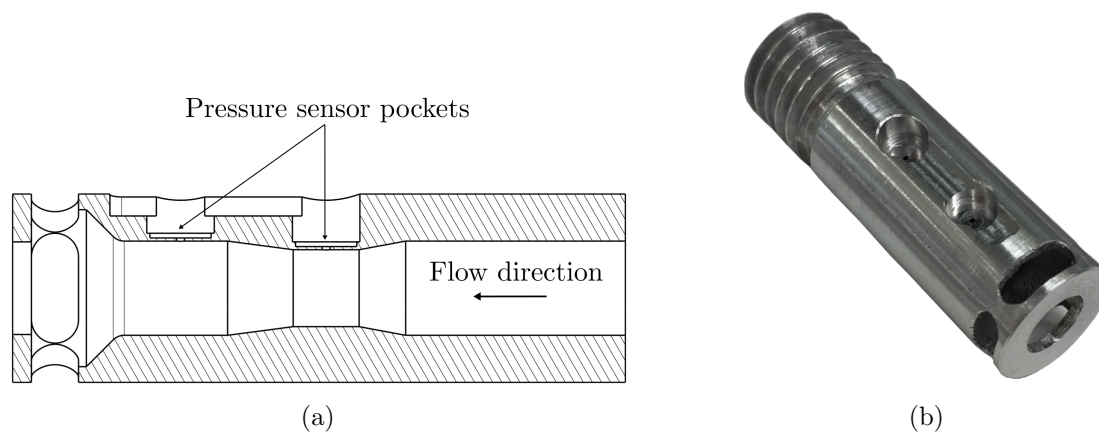
Figure 3.28.: Schematic cut (a) and image (b) of the miniature venturi mass flow meter installed in the blade for tip coolant mass flow measurements.

3.6. Rotating Data Acquisition System

A wireless rotating data acquisition system specifically developed for the Laboratory for Energy Conversion was used to acquire data from the installed sensors on the rotor and control of the surface heaters in the turbine.

3.6.1. Telemetry Modules

The wireless data acquisition (DAQ) boards (Figure 3.29a) developed by LimmatScientific AG and Ilpra SA represent the heart of the onboard telemetry system. These were specifically designed for turbomachinery applications and made to withstand accelerations of up to $15\,000\,g$. Each board had four analogue input channels to connect either four Pt100 temperature sensors or two piezoresistive pressure sensors (or heat flux gauges). The current supply for each channel was individually adjustable and was set to $1\,mA$ for the temperature sensors. Each analogue channel had two individually programmable amplifiers (x1 to x128) and a voltage offset to increase the sensor signal sensitivity and signal-to-noise ratio. After a high-resolution analog-to-digital converter ($0\,V$ to $5\,V$), the data was logged at 16-bit resolution. The sampling frequency was freely programmable at a maximum of $200\,kHz$. Embedded flash memory was used for the short-term data storage (maximum $8\,s$ at full resolution) and then transferred to a micro SD card. A maximum of eight boards could be stacked on top of each other. For this work, stacks of two to three boards were used (Figure 3.29b). Stacking the boards connected the trigger signal and multiplexer signals of all boards used to control the surface heaters. All sensor signals were fed through the

<div align="center">(a)   (b)</div>
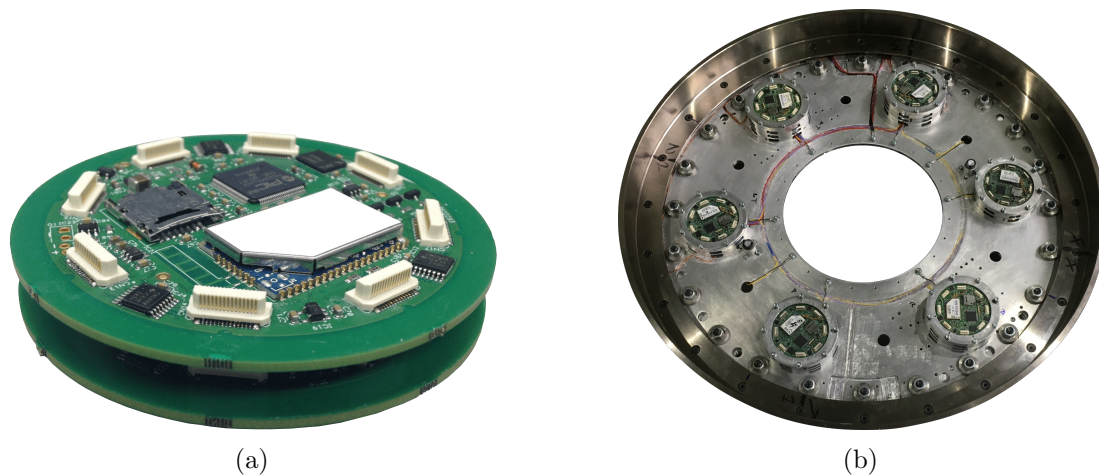
Figure 3.29.: Close-up view of two stacked rotating data acquisition (DAQ) boards (a). Installed stacking towers on the carrier disk at the rear of the rotor blisk (b).

board connectors in one stack. Each stack was mounted on an interface board that all the sensors were connected through to distribute the signals to the boards. All boards were equipped with a Wi-Fi chip for communication and connectivity to a wireless network and could be addressed individually to set preferences. The trigger signal was set by a photo-resistive diode using a fixed mounted fixed in the turbine.

The same acquisition system was also used for blade vibration measurements in a radial compressor facility [38] and unsteady blade surface pressure measurements on axial turbine blades [141]. A general overview of the system capabilities was provided by Mansour et al. [108].

3.6.2. Turbine Integration

The data acquisition system was integrated on a board carrier disk mounted at the rear of the rotor (Figure 3.29b). High-strength aluminium cages were used to fix the board stacks on the carrier disk using eight screws secured with counter nuts. All sensor and heater cabling was fed from the rotor blisk onto the disk and routed to the corresponding interface boards. The power for the DAQ boards and surface heater inserts in the rotating system was transferred through a two channel slip ring. The in-house designed slip ring had two brass contact rings mounted on the rotor shaft separated by insulating rings made from Ertacetal. Two spring-loaded carbon brushes for each channel were mounted at a 90° angle on a movable arm mounted on a carriage to create electrical contact. The carriage was pneumatically actuated to move between the connected state and retreated brushes for

assembly/disassembly of the turbine.

3.7. Aerodynamic Measurement Setup

3.7.1. Aerodynamic Flow Probes

Aerodynamic probe measurements were performed at various planes using in-house built miniature pneumatic and fast-response probes. A short description is provided in the following section. While all probes were developed and manufactured in-house, they are commercially available through the company Limmat Scientific AG.

The miniaturised pneumatic five hole probe (5HP) with a cobra-shaped head (Figure 3.30a) had a tip diameter of only 0.9 mm. The head geometry featured a quadratic pyramid with 45° inclined surfaces and a flat top. The probe head was approximately five diameters away from the probe shaft to reduce flow disturbances.

(a) 5 HP   (b) FRAP
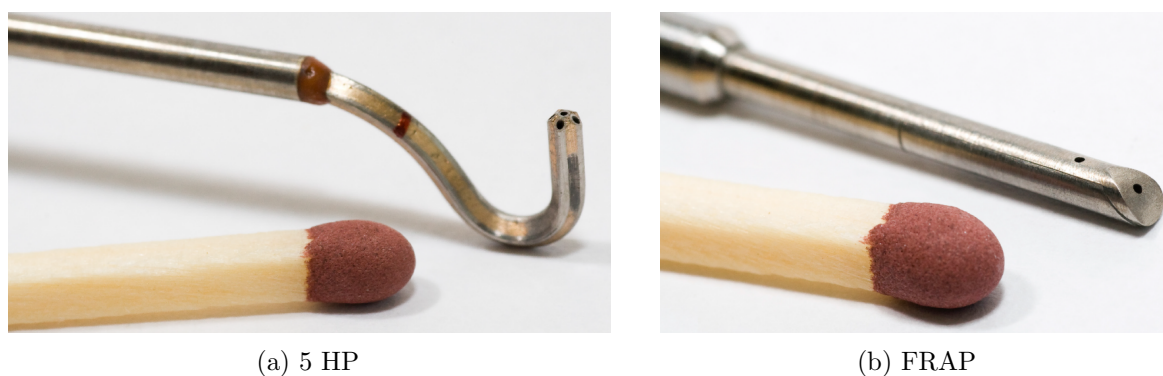
Figure 3.30.: Close-up images of the aerodynamic probe heads with a matchstick for reference. Pneumatic five hole probe (5HP) and fast response probe (FRAP).

Fast-response aerodynamic probe (FRAP) technology was developed in the Laboratory for Energy Conversion nearly three decades ago. The stem-shaped probe had a tip diameter of 1.8 mm and two integrated piezoresistive pressure transducers. The cavity between the probe holes and pressure sensor limits the frequency bandwidth of the probe to 48 kHz (tested in a shock tube facility). Unsteady data were acquired at each measurement point for two seconds with a sampling rate of 200 kHz and simultaneous turbine shaft trigger recording. This trigger was important for data post-processing and data averaging. It allowed the extraction of flow field data for specific blade

passings. This is necessary for evaluating the aerodynamic measurements of the different geometries in rainbow rotor designs (multiple designs on one rotor separately).

The probe was operated in a virtual four-sensor mode to derive the three-dimensional flow properties with only two physical sensors as described in [134] and [135]. Details on the latest probe design used in this work were provided by Schlienger [159], while fundamentals on the probe and sensory technology were provided by Gossweiler [57] and Kupferschmied [88].

To derive stage efficiencies in the rainbow rotor setup, unsteady temperature measurements were made using the fast-response entropy probe (FENT). The FENT probe was developed by Mansour [107] at ETH Zurich and has a stem-like tip of 1.8 mm in diameter. A pair of thin-film gauges installed at the tip was used for unsteady temperature measurements and a piezoresistive sensor (similar to FRAP) was used to measure the unsteady pressure. Simultaneous measurement of time-resolved total pressure and total temperature allowed us to derive a time-resolved entropy rise with reference to the turbine inlet.

Typically, all probes are calibrated before and after each measurement campaign. A static temperature and pressure calibration of the FRAP sensors was performed in a fully automated facility. The aerodynamic calibration was performed in a free jet facility with an axisymmetric uniform velocity profile. The probes were mounted in a traversing system controlling the axial probe position to the free jet and the probe yaw angle. The whole traversing system could be rotated to vary pitch angles. Typically, the probes are calibrated for $\pm 25°$ yaw and $\pm 20°$ pitch angles in 2° steps at representative Mach numbers for each measurement plane in the facility.

Non-Deterministic Unsteady Pressure Fluctuations

The unsteady pressure signal $p(t)$ recorded with the fast-response aerodynamic probes was decomposed according to Porreca et al. [136] into a mean value $\overline{p}$, a periodic signal $\tilde{p}(t)$ and a random part $p'(t)$. The random part of the pressure fluctuation can be calculated after the phase-lock averaging of the data. Using this decomposition, the level of flow unsteadiness was determined by the root mean square value of the random pressure signal.

$$p(t) = \overline{p} + \tilde{p}(t) + p'(t) \tag{3.20}$$
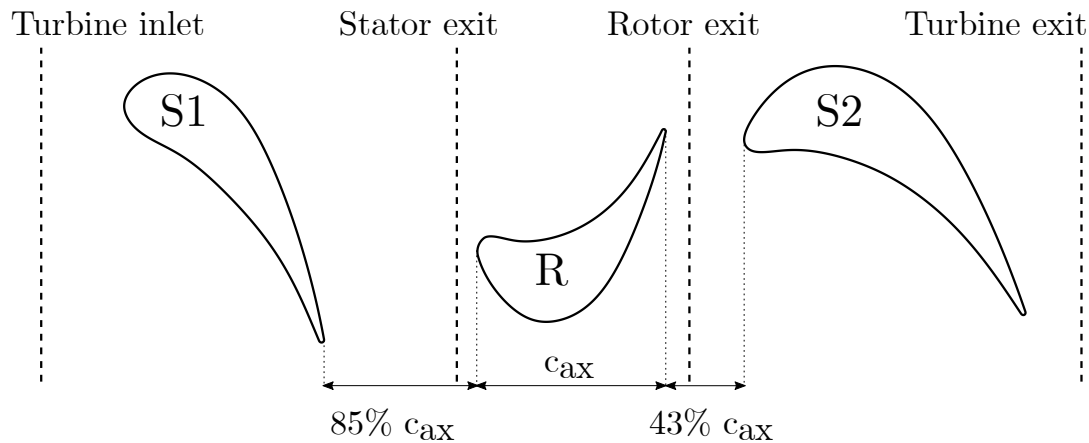
Figure 3.31.: Illustration of the aerodynamic probe measurement planes of the 1.5-stage turbine configuration.

3.7.2. Probe Measurement Planes

For this work, focused on rotor hub and tip heat transfer, measurements were performed on planes upstream and downstream of the rotor (Figure 3.31). Probe measurements for the turbine inlet conditions approximately 60 % upstream of the first stator row were performed in a previous project. This data was used to set inlet boundary conditions for the numerical simulations. The rotor inlet flow field was measured using pneumatic 5HP and FRAP probes. The measurement plane was inclined by 7° from tip to hub (approximately 11 % of rotor axial chord upstream of the rotor leading edge at mid-span). This allowed the probe to be traversed radially into the rotor-stator cavity for extended measurements below nominal hub radius. The measurement grid consisted of 49 radial points clustered towards the endwalls and at the cavity-main flow interface to resolve velocity gradients as well as 41 points in the circumferential direction to cover one stator pitch (10°).

The measurement plane for the rotor exit flow field was located approximately 12 % axial chord downstream of the rotor trailing edge. The measurement grid consisted of 38 points in the radial direction with a clustering toward the hub and tip endwall and 41 equally spaced circumferential points to cover one stator pitch (10°).

3.7.3. Uncertainty Probe Measurements

A detailed study following the *Guide to the expression of Uncertainty in Measurements* (GUM) [32] was presented by Behr [19] for the FRAP and

Table 3.4.: Expanded uncertainty for the pneumatic and fast response aerodynamic probe.

Probe	Parameter	Stator exit $M = 0.25$	Rotor exit $M = 0.5$
5HP	Yaw angle φ	$\pm\,0.7\,\%$	$\pm\,0.5\,\%$
	Total pressure p_t	$\pm\,1.9\,\%$	$\pm\,0.7\,\%$
	Static pressure p_s	$\pm\,2.2\,\%$	$\pm\,0.9\,\%$
FRAP	Yaw angle φ	$\pm\,1.3\,\%$	$\pm\,0.5\,\%$
	Total pressure p_t	$\pm\,2.8\,\%$	$\pm\,1.0\,\%$
	Static pressure p_s	$\pm\,3.7\,\%$	$\pm\,1.2\,\%$

pneumatic probe. The GUM provides a standardised method to derive and express measurement uncertainties. The derived uncertainties for the probes were evaluated with a coverage factor of $k = 2$, which is equivalent to a confidence level of $\approx 95\,\%$ for normally distributed results. The reported uncertainties were derived by Lenherr [102] and are reported for the two representative Mach numbers behind the first stator and the rotor, respectively (Table 3.4). Total and static pressure uncertainty was expressed as a percentage of the local dynamic head, while uncertainties in flow angles were expressed as a percentage of the respective calibration range.

4. Image Processing and Data Reduction

This chapter describes the image post-processing required to derive heat transfer quantities from infrared measurements on the rotor hub and tip. The limited optical access, multi-angle image acquisition and inherent jitter in the acquisition highlight the need for extensive post-processing. Furthermore, the geometrical reconstruction of 2D images on three-dimensional surfaces is described. Thereafter, an uncertainty analysis of the measurement technique is presented and the heat transfer quantities used in the results section are defined.

4.1. Structure of Post-Processing

The post-processing of measurement data involved considerable image processing and data reduction to derive local heat transfer coefficients and cooling effectiveness values from the acquired measurement data. In a preliminary step, all of the required instrumentation calibrations (described in Section 3) were performed and processed. This also includes the geometrical image reconstruction for infrared reference markers on the heating inserts (described in Section 4.1.1).

Image processing includes the following steps: (1) All individual frames of each acquisition are registered to account for trigger jitter and then averaged (discussed in Section 4.1.2); (2) The averaged images are projected on a three-dimensional mesh representing the heater surface using infrared reference markers; (3) In the case of the rotor hub endwall, where multiple camera angles were used to extend the optical coverage, the data from all angles for each heating step are combined.

The auxiliary measurement data (e.g. the current delivered to the inserts and the temperature data of the embedded Pt100 sensors) were averaged for each heating step. Combined with the surface temperature data, the heat fluxes (according to Section 3.3.2 and Equations 3.5 to 3.8) were calculated.

Thereafter, the heat transfer coefficient and adiabatic wall temperatures were derived using the data from all heating steps.

4.1.1. Geometrical Image Reconstruction for Infrared Reference Markers

Optical measurement techniques facilitate high-resolution measurements on surfaces but do not contain any (direct) positional information (for the measured surface). The (arbitrary) three-dimensional information of the object is represented by a two-dimensional image from the projection on the camera sensor. A geometrical reconstruction of the image is thus required to relate each camera pixel's information to a geometrical location on the object under investigation. Image reconstruction of the infrared temperature data on the investigated geometry was performed by a geometrical transformation calculated from multiple points with known image and real-word coordinates. To achieve this, infrared reflective markers were manually applied on the heating surface. To reconstruct the 3D coordinates of these reference markers in the CAD system, the direct linear transformation (DLT) method was used (see below).

The measurement inserts were placed on a precisely manufactured jig with specific geometrical features such as corners and edges with precisely known positions in the CAD reference system (Figure 4.1). Isometric images of the jig with mounted measurement inserts were taken using a digital single-lens reflex camera (DSLR). These images were then used to reconstruct the reference marker 3D coordinates. Therefore, multiple pairs of image coordinates (u, v) and their respective CAD coordinates (x, y, z) were used to calculate the projection matrix using the direct linear transformation. This process was performed for three to four images from different perspectives for each insert. The resulting coordinates from all images were averaged to obtain the final coordinates.

Direct Linear Transformation

The DLT method was used to calculate transformations as originally reported by Abdel-Aziz and Karara [1]. To represent projective transformations, homogenous coordinates were used. This method uses control points with known coordinates in the image frame $u = (u, v, 1)$ and 3D world $x = (x, y, z, 1)$ to calculate a mapping between the two. Homogenous coordinates allowed the mapping $(u' = Px)$ to have the form of a 3×4 projection matrix

P (Equation 4.1).

$$\lambda \begin{pmatrix} u \\ v \\ 1 \end{pmatrix} = \begin{pmatrix} u' \\ v' \\ w' \end{pmatrix} = \begin{pmatrix} P_{1,1} & P_{1,2} & P_{1,3} & P_{1,4} \\ P_{2,1} & P_{2,2} & P_{2,3} & P_{2,4} \\ P_{3,1} & P_{3,2} & P_{3,3} & P_{3,4} \end{pmatrix} \cdot \begin{pmatrix} x \\ y \\ z \\ 1 \end{pmatrix} \qquad (4.1)$$

The transformation can be expressed as the vector product $u' \times Px = 0$, where only two equations are linearly independent. In the DLT algorithm, it is standard practise to ignore the dependent equations. Using the vector product, the equation can be transformed to a form $Ap = 0$ with 12 unknowns p_i being the elements of the transformation matrix P. Since each pair of coordinates gives two equations, a minimum of six reference points is required. Having n pairs of points (more than the minimum) extends matrix A (as described in Equation 4.2) to a dimension of $(2n \times 12)$.

$$\begin{pmatrix} x_1 & y_1 & z_1 & 1 & 0 & 0 & 0 & 0 & -u_1 x_1 & -u_1 y_1 & -u_1 z_1 & -u_1 \\ & \vdots & & & & \vdots & & & & \vdots & & \\ x_n & y_n & z_n & 1 & 0 & 0 & 0 & 0 & -u_n x_n & -u_n y_n & -u_n z_n & -u_n \\ 0 & 0 & 0 & 0 & x_1 & y_1 & z_1 & 1 & -v_1 x_1 & -v_1 y_1 & -v_1 z_1 & -v_1 \\ & \vdots & & & & \vdots & & & & \vdots & & \\ 0 & 0 & 0 & 0 & x_n & y_n & z_n & 1 & -v_n x_n & -v_n y_n & -v_n z_n & -v_n \end{pmatrix} \begin{pmatrix} P_{1,1} \\ \vdots \\ P_{1,4} \\ \vdots \\ P_{3,4} \end{pmatrix} = 0$$

$$(4.2)$$

This overdetermined system of equations was solved using a singular value decomposition (Equation 4.3) where each column of V represents a solution to $Ap = 0$.

$$A = U \cdot \Sigma \cdot V^T \qquad (4.3)$$

The eigenvector v_i with the smallest eigenvalue is the projection with the smallest projection error and can be reshaped to build the projection matrix P. Arbitrary 3D coordinates (x, y, z) were transformed into the image space by using the transformation matrix P (Equation 4.4).

$$\begin{pmatrix} u' \\ v' \\ w' \end{pmatrix} = P \begin{pmatrix} x \\ y \\ z \\ 1 \end{pmatrix} \qquad (4.4)$$

(a)   (b)
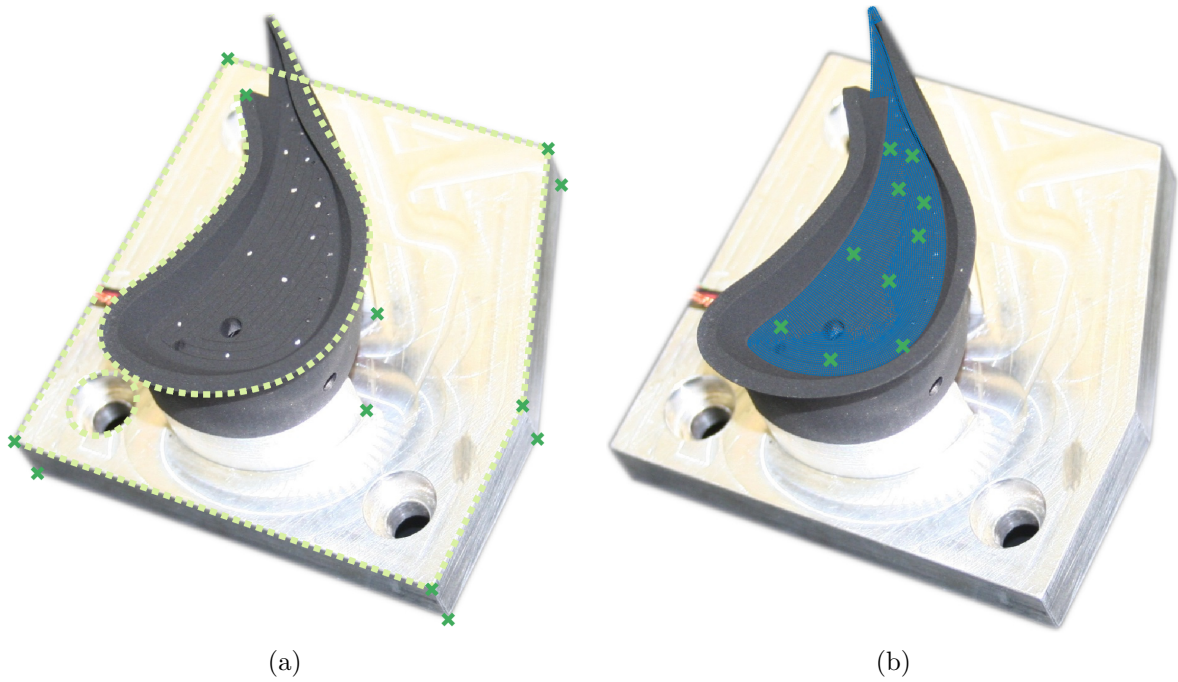
Figure 4.1.: Illustration of the coordinate reconstruction for the infrared markers. Projected reference geometry points to evaluate transformation (a) and projected surface mesh for IR marker interpolation (b).

To preserve the scaling, the image coordinates (u', v', w') were scaled according to Equation 4.5 to return the homogenous image coordinates $(u, v, 1)$.

$$\begin{pmatrix} u \\ v \\ 1 \end{pmatrix} = \frac{1}{w'} \begin{pmatrix} u' \\ v' \\ w' \end{pmatrix} \tag{4.5}$$

4.1.2. Image Registration

For each image acquisition, 1000 individually triggered images were recorded and subsequently averaged to reduce measurement noise. As explained in Section 3.3.1, the image acquisition of the infrared camera was triggered by a reflective mark on the turbine shaft and a photodetector. The analogue signal output of the photodetector and the infrared camera itself introduce jitter in the trigger signal (beyond the rotational stability of the turbine), thereby resulting in the misalignment of individual frames of an image sequence. Therefore, all frames must be registered to reduce the blurring introduced by the averaging of unaligned frames. Figure 4.2 illustrates the effect of a jitter-induced blur for the hub and tip measurements as well as

(a) Unregistered mean hub

(b) Registered mean hub

(c) Unregistered mean tip

(d) Registered mean tip
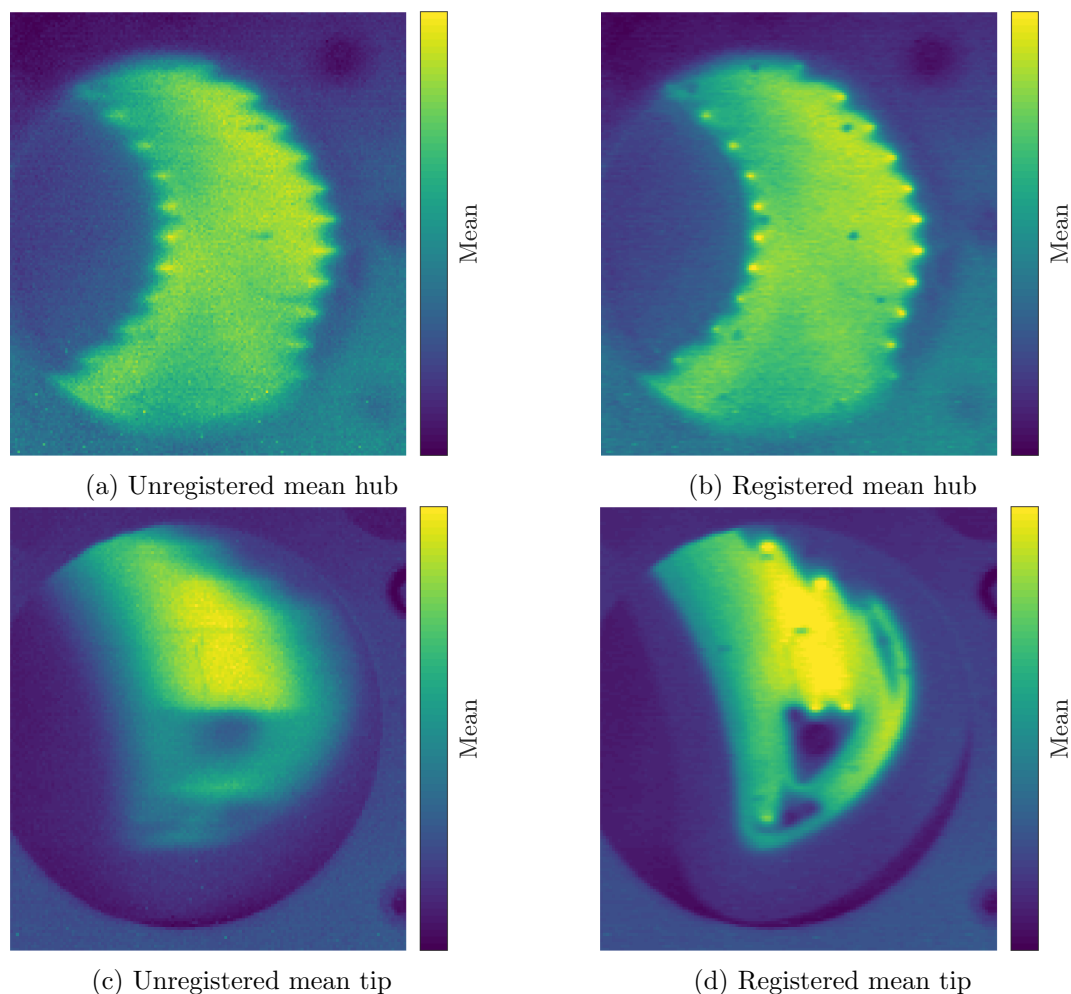
Figure 4.2.: Illustration of the trigger jitter-induced blur (a) and (c) for the averaged image sequence with unregistered frames. The resulting averaged data after registration for the hub (b) and tip (d). The increased jitter for the tip measurements (c) is clearly visible compared to the hub (a).

the results of the frame registration process.

The image registration was based on the Matlab inbuilt *imregister* function, which is an intensity-based registration algorithm. It calculates a translation matrix for the moving frame compared to a fixed reference. Based on the setup used, it is known that only lateral translations occur due to the rotor rotation. The intensity-based registration was limited on a sub-window of the image as illustrated in Figure 4.3a where the moving rotor and also strong intensity gradients were also visible to facilitate the process.

The registration was performed in two steps. First, the registration was performed for all frames by taking the first frame of the image sequence as
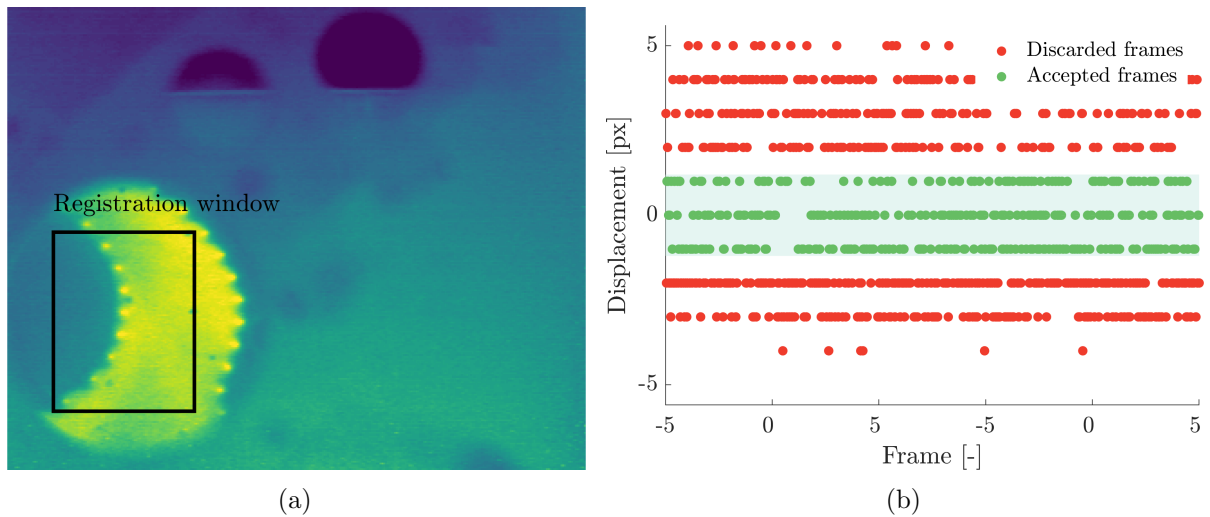
Figure 4.3.: Sub-window for the image registration process (a) and an illustration of frame
           jitter (in pixel) for a sequence of 1000 acquired images (b). Only frames within
           ±1 pixel shift were used for averaging.

a reference to find the mean position of the rotor within the acquisition. In
the second step, the frame shifts with respect to this reference position were
calculated. Generally, approximately 35 % of the frames for the hub and
10 % for the tip study fell within the ±1 pixel shift limit to be considered
in the averaging process (Figure 4.3b). The increased trigger jitter for
tip measurements is explained by (a) the increased object speed ($\approx$20 %)
compared to the hub, leading to an equal increase in object motion and
(b) the shaft trigger signal electronics being changed, which introduced
increased jitter in the analogue signal.

The impact of the frame registration procedure on the subsequent frame
averaging is illustrated in Figure 4.4. Around the track turning points, where
the highest temperature gradients were present, the standard deviations of
the temperature data for each pixel was the most significant. The maximum
values of standard deviations were reduced by a factor of 2.3.

4.1.3. Image Projection and Averaging

Image projections were performed to determine the three-dimensional tem-
perature on the investigated surfaces. This process was similar to the process
described in Section 4.1.1. The silver marks were distinguishable in the
infrared image due to their different emissivity and hence reduced tempera-
ture signal on the heated surface (Figure 4.5a). The two-dimensional image
coordinates of the reference marks were matched with the corresponding,
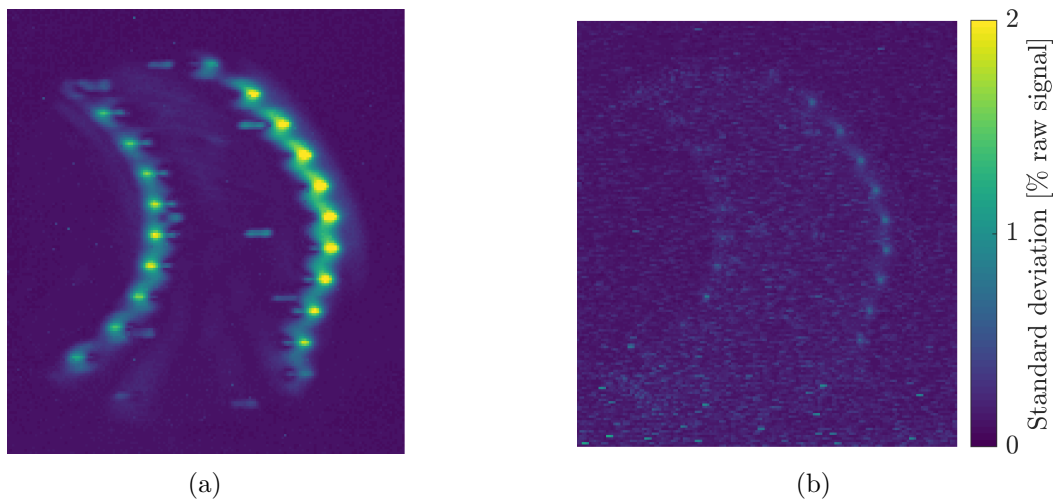
Figure 4.4.: Standard deviation of the raw infrared image data from one acquisition (1000 images) before (a) and after (b) image registration.

(a) IR image   (b) Reference marks   (c) Projected temperature information on geometry
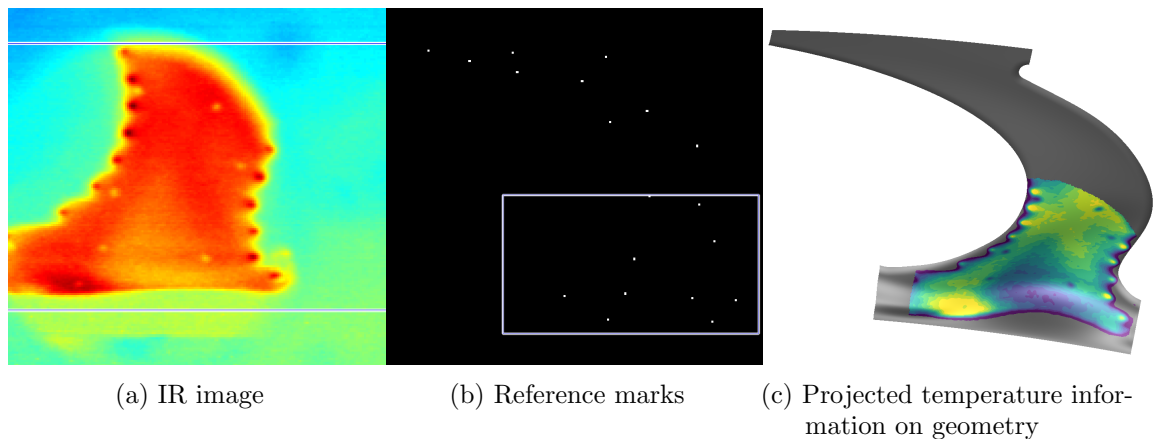
Figure 4.5.: Infrared image projection onto the three-dimensional geometry using the reference infrared markers.

previously determined, real world coordinates and used to calculate the projection of the surface mesh onto the image, where the temperature information was interpolated onto the mesh.

Following the temperature distribution interpolation on the surface mesh for all camera angles, the data were averaged for regions covered by more than one camera angle. A slight temperature variation between the different camera angles could be observed. However, the observed differences were generally below the camera accuracy of $\pm 1\,\mathrm{K}$ and may have also been introduced by variations in the turbine inlet temperature. The typical times between different camera angle acquisitions were 5 to 10 minutes due to the manual repositioning of the camera.

4.1.4. Conduction Modelling and Correction

For steady-state measurements in a continuously running facility, the conduction losses through the insert substrate from the generated heat flux cannot be neglected. As mentioned in the Section 3.3, Pt100 resistance temperature sensors were embedded in the heater insert (hub) or glued onto the rear surface for the rotor tip inserts. Temperature measurements had to be manually triggered since the rotating data acquisition system was not designed for continuous data recording.

For each temperature sensor location, the closest point in a normal direction on the heater surface was calculated and the surface temperature was extracted. Infrared temperature acquisition data were combined with the sensor data based on timestamp information. Moreover, using the one-dimensional normal conduction assumption, the conduction heat flux was calculated based on the temperature difference, conductivity and thickness of the substrate. Due to some sensor losses and acquisition difficulties, only a limited number of data points from the embedded sensors were available for each heating step and measurement day. Therefore, data available from all measurements were collected and averaged to provide a single conduction heat flux for each heating step. The error introduced due to this simplification is accounted for in the uncertainty analysis.

4.2. Definition of Heat Transfer Quantities

The derived heat transfer quantities of adiabatic wall temperature and heat transfer coefficient are presented in a non-dimensional format. These representations facilitate the application of these results to other test cases or geometries.

4.2.1. Nusselt Number

The Nusselt number was used to express the heat transfer coefficient h in a non-dimensional form by using the axial chord length c_{ax} and conductivity of air k_{air} at mid-span (rotor inlet) (defined in Equation 4.6). According to the dimensional analysis, the Nusselt number Nu is a (globally) scaled expression for the heat transfer coefficient h. In the scope of this work, the

terms Nusselt number and heat transfer coefficient are used interchangeably.

$$Nu = \frac{h \cdot c_{ax}}{k_{air}} \qquad (4.6)$$

where h :   convective heat transfer coefficient $(W/(m^2 K))$
           c_{ax} :   axial chord length at mid-span (m)
           k_{air} :   conductivity of air at mid-span $(W/(mK))$

The effect of purge flow variation on the heat transfer coefficient was studied by using the relative change in Nusselt number compared to the reference injection rate of 0.8% as described in Equation 4.7.

$$\Delta Nu = \frac{Nu - Nu_{IR0.8\%}}{Nu_{IR0.8\%}} \cdot 100 \qquad (4.7)$$

4.2.2. Cooling Effectiveness

The adiabatic wall temperature T_{aw} is presented in the form of a cooling effectiveness according to Equation 4.8. This representation is equivalent to the definition used for film cooling studies and it is suitable for comparing experimental results with CFD predictions—even for a mismatch in purge flow or cavity temperature.

$$\eta = \frac{T_{aw} - T_{ref}}{T_c - T_{ref}} \qquad (4.8)$$

where T_{aw} :   adiabatic wall temperature   (K)
           T_{ref} :   reference flow temperature   (K)
           T_c :   cavity flow temperature   (K)

This definition uses a reference main flow temperature T_{ref} and the cavity flow temperature T_c. Compared to simplified experiments with linear cascades, where the environment—and thus the reference temperatures—are well defined, the definition and accessibility in rotating experiments are more complicated.

The coolant reference temperature T_c is defined as the temperature measured next to the bypass flow injection into the upstream cavity (described in Section 2.1.2 and illustrated in Figure 2.3). Between this measurement location and the ejection as purge flow or tip coolant, the bypass air absorbs heat from the cavity walls and, for the tip, from the internal channel of

the blade. Therefore, even for the most ideal cooling scenario, effectiveness values below 1 were expected.

The reference flow temperature T_{ref} was defined differently for the hub endwall and the blade tip investigation. For the hub endwall study, the relative total temperature at the rotor inlet (mid-span height) was used. This temperature was measured during the experimental campaign using the fast-response aerodynamic probe. For the blade tip investigation, probe measurements at the rotor upstream measurement plane were not possible due to the upstream extended tip geometry of the optimised squealer interfering with the measurement plane. Therefore, the turbine inlet temperature was used as a reference.

Despite the difficulties of defining reference temperatures for cooling effectiveness compared to bench experiments in simple environments, the introduced definition is considered an appropriate nondimensionalisation for the adiabatic wall temperature.

4.3. Uncertainty Analysis and Repeatability

This section discusses the uncertainty analysis performed for the setup and the measurement technique used for heat transfer measurements. Moreover, the various sources of uncertainty and the procedure for calculation are presented. The results of a repeatability study are presented in Section 4.3.2.

4.3.1. Uncertainty Estimation

A general uncertainty assessment of the heat transfer coefficient and adiabatic wall temperature derived from the measurements was performed according to the procedure described by Moffat [117]. Using this method of sequential perturbation, the propagation of uncertainties from all sources to the final values can be estimated using the data reduction program.

From the derivation of the heat transfer coefficient and adiabatic wall temperature (outlined in Section 3.3.2) the main factors contributing to uncertainty include:

- Determination of the surface temperature

- Determination of the heat flux generated by the heater

- Determination of the conduction losses through the substrate

The individual components of these factors are addressed in the paragraphs that follow.

Error in Surface Temperature   The main sources of error in measured surface temperatures include the accuracy of the infrared camera, the associated calibration and the image post-processing. The camera was factory calibrated to a specification of $\pm 1\,\mathrm{K}$, which is a high level of accuracy for an infrared camera. The variations in the calibrations performed to account for the transmissivity of the ZnSe window used in the experimental setup were observed to be below the accuracy of the camera. The average surface temperature variation observed in the frame (averaged after registration) and from different camera angles were well below the camera specification. Therefore, no additional uncertainty based on the post-processing of surface temperature images was included. Thus, the main source of error was the accuracy and calibration of the infrared camera.

Error in Generated Electric Heat Flux   The heat flux generated by the electric surface heater was calculated based on the electrical current supplied, the heater resistance and the local scaling factor S_q.
The vendor specified accuracy for DC current measurements in the range used was $\pm 0.8\,\%$ of the measured value plus $0.3\,\mathrm{mA}$. Current fluctuations between the different images combined for each heating step were below the stated accuracy of the measurement device. The error induced by the heater resistance was calculated based on the resistance temperature calibration and average temperature difference between the lowest and highest heating steps. Due to the low temperature sensitivity of the thin-film resistance, the typical resistance error was calculated to be well below $1.0\,\%$. However, the error associated with the local heat flux correction factor was approximately $2.5\,\%$ (standard deviation between the calibrated heating steps).
Notably, the error in generated electric heat flux calculation was predominately driven by the error in the correction factor derivation.

Error in Conduction Heat Flux   Sources of errors in the calculation of conduction heat flux include the spatially averaged conduction calculation for each heating step, the material properties of the substrate and the temperature measurements. The point-wise evaluated conduction heat flux at each temperature sensor locations was averaged to create a single value in the post-processing stage (as described in Section 4.1.4). Notably, non-uniformity of the calculated conduction across the heaters represents up to
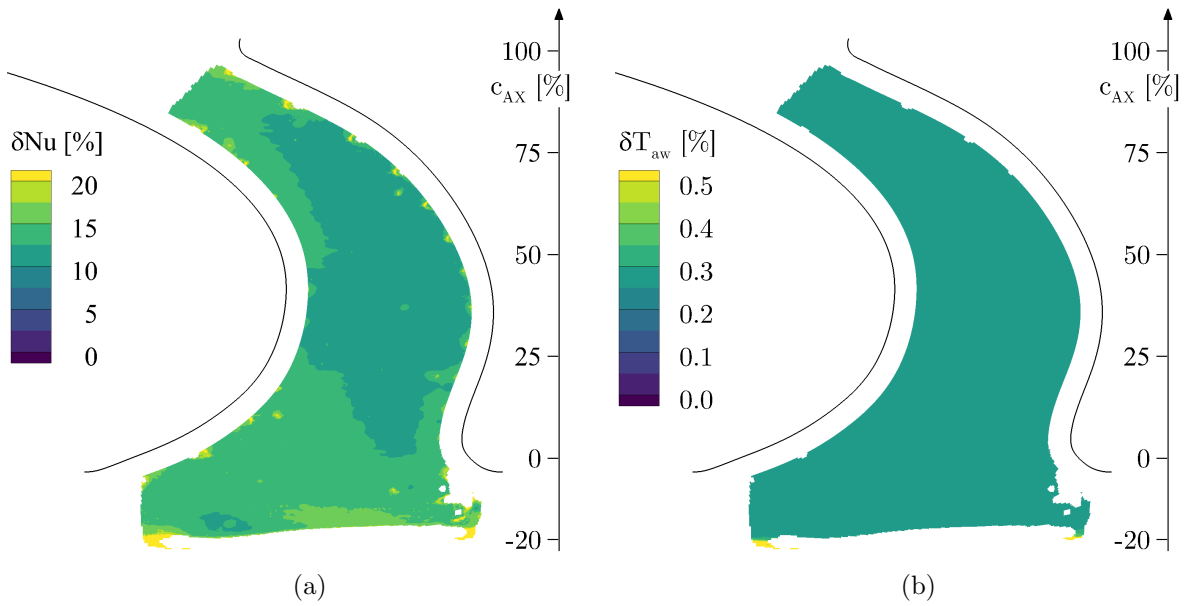
Figure 4.6.: Endwall-resolved overall uncertainty in Nusselt number (a) and adiabatic wall temperature (b).

double the average value. In the uncertainty derivation based on the perturbation method, the error in conduction were varied by 100 %. Therefore, the temperature sensor calibration and material property uncertainties were not considered.

Measurement Uncertainty

Using the method from Moffat [117], all of the aforementioned variables were successively altered by the corresponding error in the post-processing routine. For the surface temperature, 50 iterations with randomly perturbed temperatures within the associated error were performed. The uncertainty contribution on Nusselt number and adiabatic wall temperature from the surface temperature error is calculated as twice the standard deviation in 50 iterations.

Overall, the platform-averaged uncertainties for Nusselt number and adiabatic wall temperature were 13.3 % and 0.3 %, respectively. The platform-resolved uncertainty distributions are depicted in Figure 4.6.

Individual contributions to the overall uncertainty in Nusselt number and adiabatic wall temperature are provided in Table 4.1. For both derived heat transfer quantities, the contributions of errors in surface temperature T_s and in the conduction heat flux dominate the overall uncertainty over the contribution of scaling factor or heating current measurement errors. The

Table 4.1.: Relative contributions to the uncertainty in Nusselt number and adiabatic wall temperature.

	δT_s [%]	$\delta \dot{q}_{cond}$ [%]	δS_q [%]	δI [%]
Nusselt number				
Pressure ratio 1.65	30.3	65.0	3.3	1.4
Pressure ratio 1.33	28.4	66.2	5.3	0.0
Adiabatic wall temperature				
Pressure ratio 1.65	71.5	28.4	0.0	0.1
Pressure ratio 1.33	87.0	13.0	0.0	0.0

main driver for Nusselt number uncertainty is the error in conductive losses for the measurement setup used.

4.3.1.1. Cooling Effectiveness

The cooling effectiveness used to represent adiabatic wall temperature is a derived quantity. Therefore, uncertainty was evaluated according to the the law of error propagation (Equation 4.9).

$$\delta \eta = \sqrt{\left(\frac{\partial \eta}{\partial T_{ad}} \delta T_{ad} \right)^2 + \left(\frac{\partial \eta}{\partial T_{t,rel}} \delta T_{t,rel} \right)^2 + \left(\frac{\partial \eta}{\partial T_c} \delta T_c \right)^2} \qquad (4.9)$$

As observed in Equations 4.10 to 4.12, uncertainty in the adiabatic wall temperature will drive overall cooling effectiveness uncertainty because the partial derivative of the cooling effectiveness has the term $(T_c - T_{t,rel})$ without power in the denominator.

$$\frac{\partial \eta}{\partial T_{ad}} = \frac{1}{T_c - T_{t,rel}} \qquad (4.10)$$

$$\frac{\partial \eta}{\partial T_{t,rel}} = \frac{T_{ad} - T_c}{(T_c - T_{t,rel})^2} \qquad (4.11)$$

$$\frac{\partial \eta}{\partial T_c} = \frac{T_{t,rel} - T_{ad}}{(T_c - T_{t,rel})^2} \qquad (4.12)$$

Based on these terms, it is also evident that the small temperature difference achieved in the test facility between "coolant"/purge and main flow is unfavourable for highly accurate cooling effectiveness measurements. A high delta temperature significantly reduces the uncertainty contributions of all involved temperatures. With an adiabatic wall temperature uncertainty of $\pm 0.88\,\mathrm{K}$ (as derived in the previous section) the contribution of this term on the overall cooling effectiveness is dominant ($>73\,\%$).

The overall uncertainty of cooling effectiveness was estimated at ± 0.09 when averaged over the platform (in absolute value). This value covers the entire range of measured adiabatic wall temperatures and only changes by up to ± 0.002 depending on the adiabatic temperature.

4.3.2. Repeatability Study

In addition to the uncertainty analysis presented above, repeatability measurements were performed for the hub endwall and the rotor blade tip investigation. Due to the limited time available in the experimental facility and the duration of the measurements, only one turbine operating point was measured twice.

Rotor Hub Endwall Measurements

Repeatability measurements were performed for the turbine design pressure ratio and $0.8\,\%$ purge flow injection with 27 days in between. Furthermore, the turbine configuration was disassembled and assembled within this period to exchange some instrumentation.

The absolute value of the relative difference in derived Nusselt number between the two measurements is depicted in Figure 4.7. The endwall resolved and laterally averaged results indicate that the differences were below $\pm 3\,\%$, especially in the region after the blade leading edge. In the more upstream region, slightly higher values (within $5\,\%$ and $8\,\%$) of differences were found. However, this also falls well within the estimated measurement uncertainty. At the platform start, discrepancies above $10\,\%$ were found. The results for this region should be viewed with caution (see explanation in Section 6.1.2).

Rotor Blade Tip Measurements

To study rotor blade tip heat transfer, a repeatability investigation of the Notch tip geometry was performed at the turbine design operating point
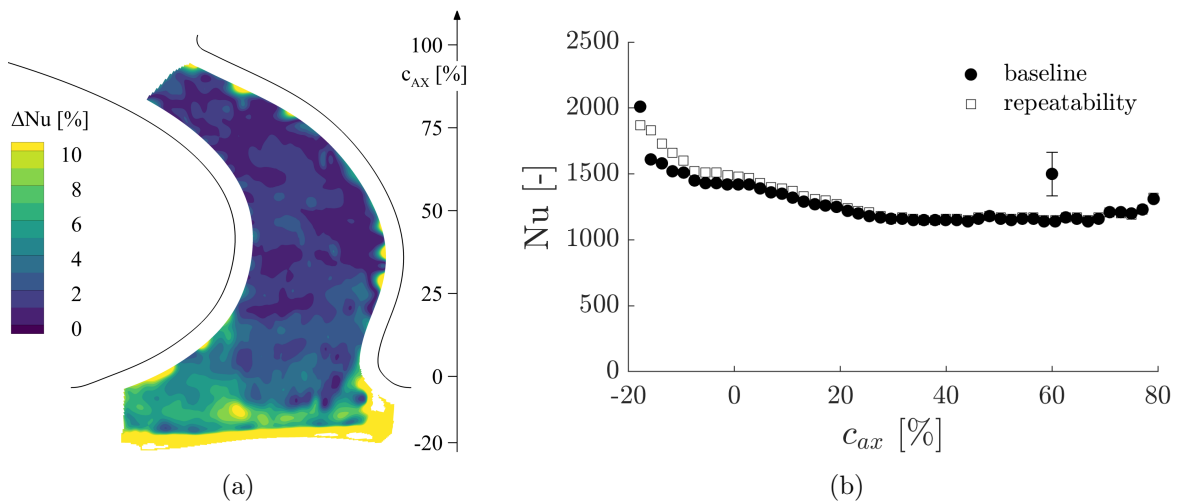
Figure 4.7.: Endwall-resolved absolute difference between two measurements at the same operating conditions on different days (a) and laterally averaged comparison (b).

over two consecutive days. The relative Nusselt number difference as well as the absolute adiabatic wall temperature difference between the measurement days are depicted in Figure 4.8. The good repeatability of the measurement setup and technique is evident in the results, with an averaged Nusselt number difference of 2.5 % and adiabatic wall temperature difference of 0.2 K.

The two repeatability measurements demonstrated the capability of the measurement setup and technique, which had an indicated precision well below the level of measurement uncertainty.
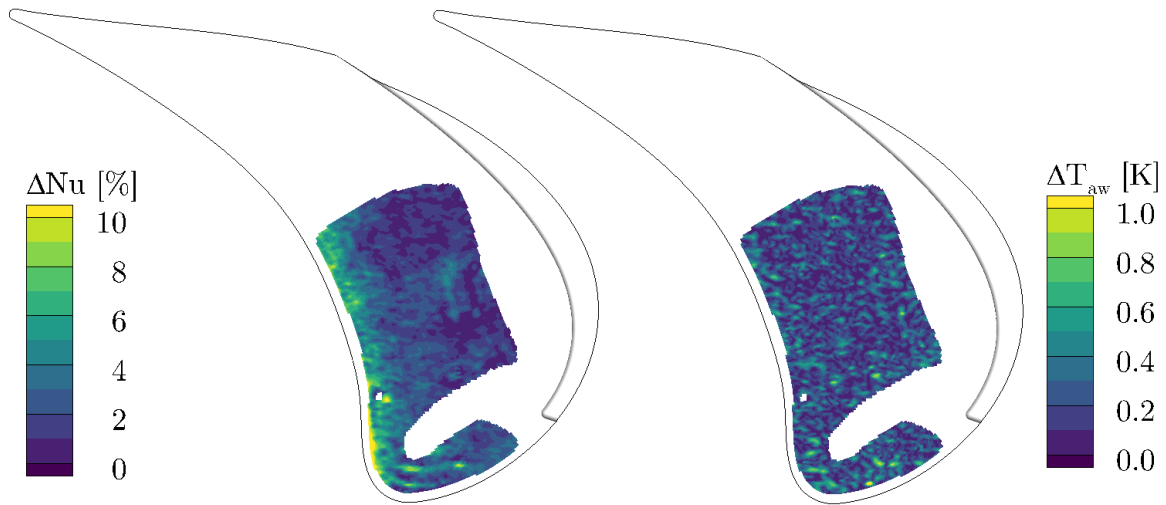
Figure 4.8.: Repeatability of Nusselt number (left) and adiabatic wall temperature (right) expressed as absolute difference for the Notch tip geometry from two different measurement days.

4.4. Influence of Stator-Rotor-Relative Position

In the measurement setup, surface temperatures on the rotating rotor were measured using a stationary infrared camera. Hence, the unsteady time-dependent heat transfer on the rotor endwall or blade tip could not be resolved. Instead, surface temperatures were measured for a specific relative position of the rotor to the upstream stator. This relative position was determined by the position of the optical access for the camera, which could be rotated around the turbine axis as described in Section 2.1.4. The thermal response time of the measurement insert was expected to suppress unsteady effects. Therefore, this measurement technique was expected to measure a time-averaged instead of instantaneous heat transfer, while the relative position of the rotor to the stator is irrelevant for the data acquisition.

To confirm this approach and assess the influence of the rotor position relative to the stator trailing edge, measurements of rotor hub endwall heat transfer were performed for three different positions (Figure 4.9). These different positions were achieved by the circumferential movement of the rotor casing with the optical access and camera traversing system. The camera recording trigger signal was offset accordingly to capture the same part of the endwall as for the default position. This default position was aligned such that the rotor leading edge of the pressure side blade of the measurement insert was aligned along the trailing edge metal blade angle of the stator at mid-span.
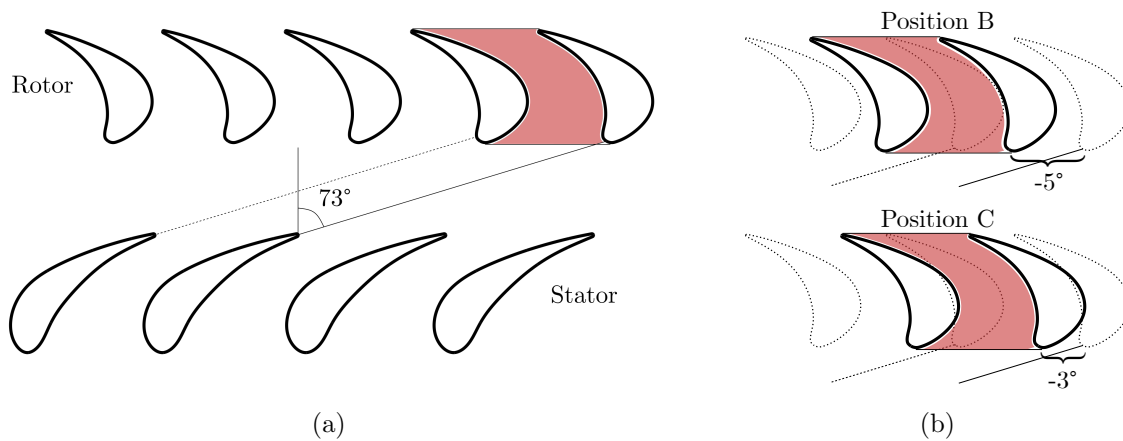
Figure 4.9.: Illustration of stator-to-rotor relative position for measurements (a). Rotor offset positions of $-5°$ and $-3°$ (b).

Trigger delays of $309\,\mu s$ and $185\,\mu s$—corresponding to approximately $-5°$ and $-3°$ of rotor rotation (as illustrated in Figure 4.9b)—were investigated.

The relative change in local Nusselt number for both positions compared to the nominal position (Equation 4.13) are depicted in Figure 4.10. The general differences observed in the passage were well below $\pm 5\,\%$. Furthermore, no distinct local differences were observed which could be attributed to the well-known secondary flow structure signatures. The greatest differences were observed between the platform start and the rotor leading edge.

$$\Delta Nu = \frac{Nu_{posB/C} - Nu_{ref,pos}}{Nu_{ref,pos}} \cdot 100 \qquad (4.13)$$

Changes in the local heat transfer coefficient between the investigated positions were well below the level of measurement uncertainty. Therefore, it was concluded that either the unsteady heat transfer effects were too low to be resolved with this measurement setup or the thermal response time of the surface too long so that the setup measures a time averaged heat transfer. Notably, the relative position of the rotor to the upstream stator was not relevant for the measurements. For a comparison with numerical predictions, unsteady CFD results should be time-averaged instead of phase-averaged to compare with the measurements.
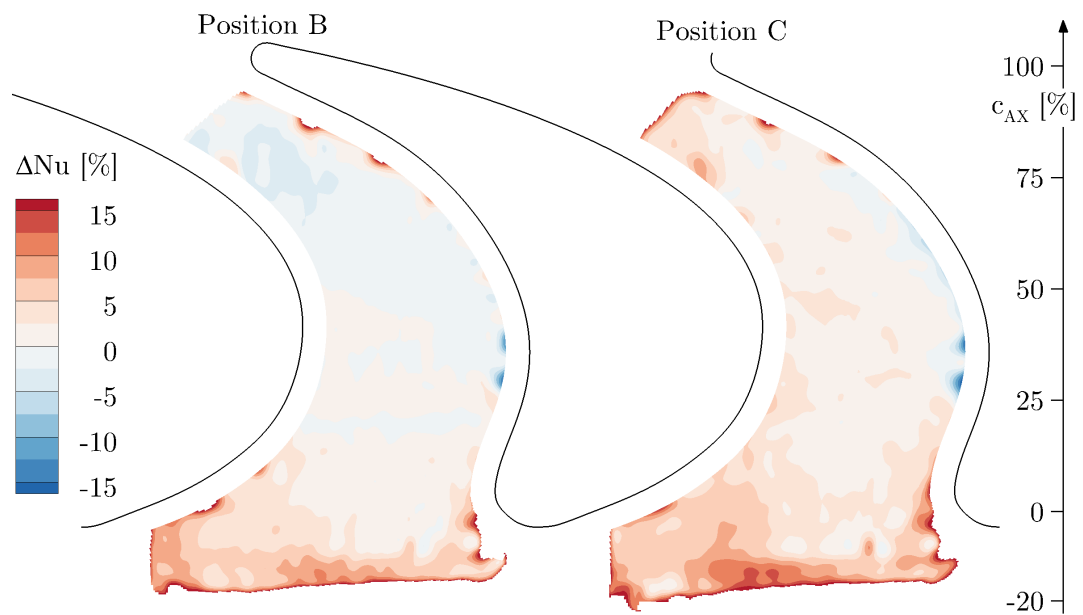
Figure 4.10.: Relative difference in local heat transfer distributions (Equation 4.13) for stator-to-rotor relative positions B and C (Figure 4.9).

5. Numerical Setup

Complementing numerical investigations to the experimental rotor hub heat transfer measurements were performed for the described turbine geometry. The computational modelling provided additional information and insights on the flow field details that were not accessible by aerodynamic probe measurements, especially in the rotating frame and inside the cavity. Furthermore, the quality of numerical predictions of steady-state and (numerically more expensive) unsteady simulations on the endwall heat transfer coefficient and cooling effectiveness was evaluated using the experimental data as a reference.

This section describes the details of the numerical setup, the aerodynamic validation of the simulations and discusses the influence of roughness modelling and heat flux boundary conditions on the endwall heat transfer coefficient.

5.1. Numerical Setup and Solver

5.1.1. Numerical Domain and Grid

The experimental geometry described for the rotor hub endwall study (see Section 2.2) was used for the numerical investigation. Only two geometry simplifications were introduced to reduce the meshing complexity: a) the purge flow injection into the rotor upstream cavity was modelled as an axial inflow (see Figure 5.1) and b) the squealer cut-out at the blade tip was not open. The non-representative squealer modelling was judged to have no relevance for the investigations on the hub endwall. Also, the impact of the axial purge flow injection was assumed to not affect the flow field after the conditioning of the radial sealing arm in the cavity.

 The numerical domain included all blade rows of the 1.5-stage turbine, including the upstream and downstream hub cavities. Separate structured grids were created for each blade row. Due to the cavity extended endwall contouring, the rotor upstream cavity was meshed together with the rotor. Figure 5.2 illustrates a close-up view of the mesh between the cavity the
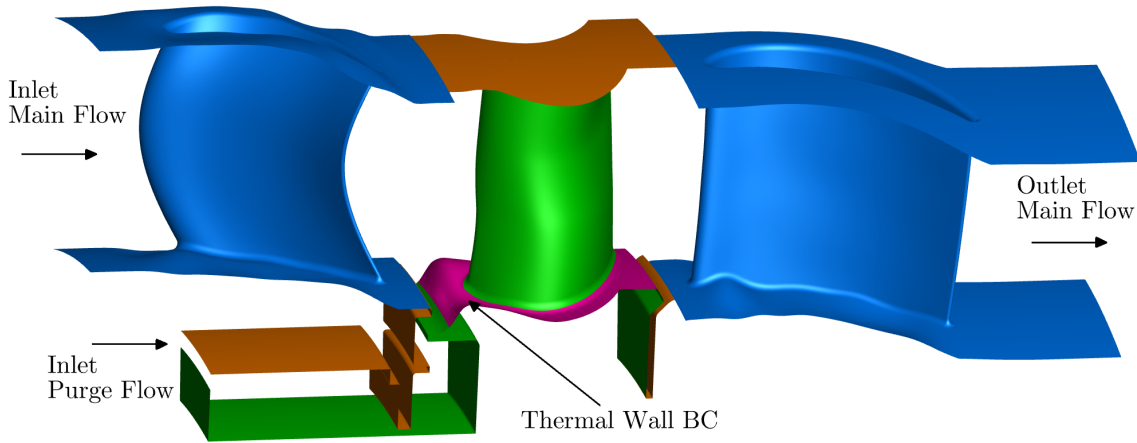
Figure 5.1.: CFD domain with indicated inlet and outlet flows. Wall colours according to boundary conditions: stationary (blue), counter-rotating (orange), rotating (green) and rotating with thermal BC (pink).

Table 5.1.: Mesh statistics and quality.

	Stator 1	Rotor (incl. cavity)	Stator 2
Nodes radial	117	125	103
Nodes cicumferential	69	68	69
Nodes total (1 pitch) [million]	2.2	7.2	2.4
Max. Expansion Factor	5	(118*) 6	3
Aspect Ratio	308	3717*	359

(*) only in tip squealer region

and main flow. The structured grid was created during a student project at MTU Aero Engines [101] and was provided for this work within the framework of the joint industrial project. The high-density grids had a total of 2.2, 7.2 and 2.4 million nodes per blade pitch for the stator 1, rotor (including cavities) and stator 2, respectively. With this resolution, an average value of 1.4 was achieved for the non-dimensional near wall spacing y^+ (Figure 5.3). Table 5.1 provides a summary of the mesh statistics.

5.1.2. Boundary Conditions

Experimental probe measurement data from previous measurements in the same turbine were taken and applied as turbine inlet boundary conditions
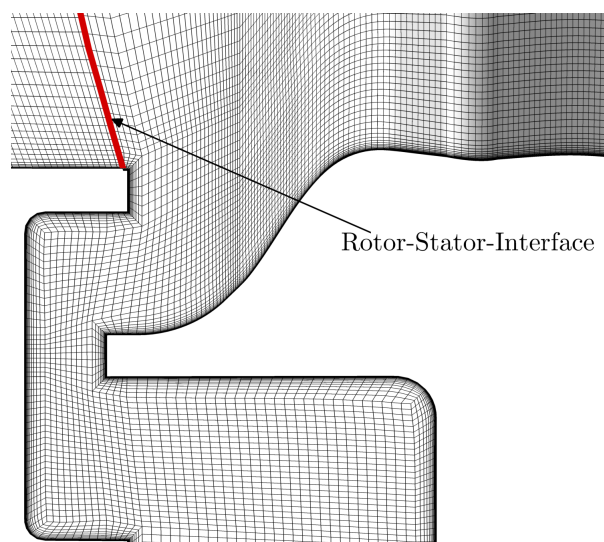
Figure 5.2.: Mesh detail of the upstream cavity connected to the rotor domain and indicated rotor-stator-interface location.
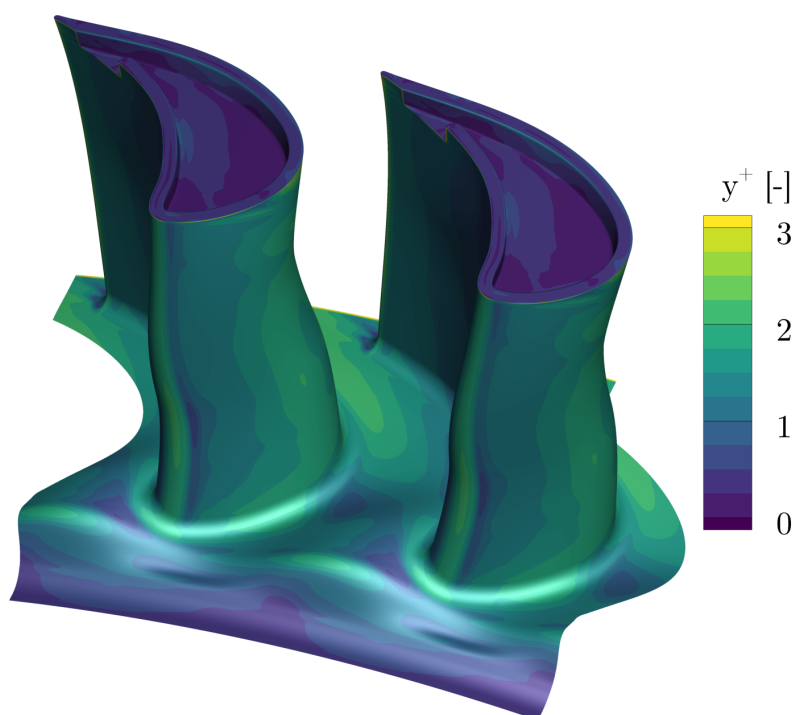
Figure 5.3.: Non-dimensional wall distance y^+ distribution on the rotor.

in the simulation. Profiles of total pressure, total temperature, turbulence intensity and eddy length scale, as well as the velocity components were specified. Average static pressure and radial equilibrium were set at the turbine outlet. The purge flow boundary conditions were set as a specified mass flow according to the injection ratio and defined static temperature of 325.8 K (average measured cavity temperature for 0.8 % and 1.2 % injection). For simplicity, the specified temperature was kept constant for all investigated purge flow injection rates.

No-slip conditions were specified for all walls. The stationary walls in the rotating domain (e.g. rotor shroud wall and stator-sided cavity walls) were assigned counter-rotating velocities (Figure 5.1). To account for the experimental surface roughness introduced in the experiments by the high emissivity paint, wall roughness was applied on the rotor surfaces. Values of 6 µm for the geometric roughness height of the rotor domain and an equivalent sand grain roughness of 20 µm for the surface were used. The influence of surface roughness and sensitivity on the equivalent sand grain roughness of the numerical predictions is discussed in Section 5.3.1.

Wall heat transfer was modelled as adiabatic for all walls in the adiabatic simulations. In the case of diabatic simulations (Section 5.1.4), constant heat flux boundary conditions were applied solely on the rotor hub endwall (Figure 5.1). A heat flux of $20\,\mathrm{kW/m^2}$ was set, which was found to provide stable simulations in previous investigations. A study using experimental representative non-uniform heat flux boundary conditions introduced by the actual heating track is presented in Section 5.3.2.

5.1.3. Solver

All simulations were performed on the high-performance computing cluster "Euler", which is managed by ETH Zurich, using the commercially available solver CFX version 18.2 from Ansys. Turbulence was modelled using the shear stress transport (SST) turbulence model with the activated gamma theta turbulence transition model. For the steady-state simulation, the stage mixing plane approach between stationary and rotating domains conserving total pressure was used. These results were also used as initial conditions for the unsteady calculations. Due to the unfavourable blade count ratio (6-7-6) of this turbine geometry, a sector of 60° would need to be simulated for unsteady calculations to conserve circumferential periodicity at the stator-rotor interface. To reduce the numerical effort, only one pitch

per row using the transient blade row model with profile transformation was used for the unsteady simulations. Time transformation would have been favourable since it conserves frequencies; however, it was numerically less stable for the investigated setup.

The profile transformation method scales the flow profiles at the transient blade row interface and maintains pitch-wise periodicity. This only spatial but not temporal scaling leads to a frequency shift, where the dominant blade passing frequency in both the stationary and rotating frame of reference is the rotor blade passing frequency. The pitch ratio of 1.166 for the investigated geometry using one pitch per row was close to unity and thus suitable for this approach. The time step was set to 100 steps per stator blade passing period, which is equivalent to a 0.1° rotation per time step as well as three coefficient loops. Both values were based on experience from the industrial partners. The unsteady results were time averaged over six stator periods (60°).

5.1.4. Heat Transfer Calculation

The convective heat transfer coefficient at the rotor hub endwall was calculated based on two parallel simulations with different wall boundary conditions. The wall temperature and heat flux data from a simulation with adiabatic wall boundary conditions and a diabatic simulation with a predefined wall heat flux $\dot{q}''$ were combined to derive the local heat transfer coefficient h (Equation 5.1) based on the linear relationship used for the experiments (Equation 3.4). Both simulations were performed using the same solver parameters.

$$h = \frac{\dot{q}''_{wall}}{T_{w,diabatic} - T_{w,adiabatic}} \tag{5.1}$$

5.2. Convergence and Experimental Validation

5.2.1. Simulation Convergence

The simulation convergence was monitored and estimated using numerical residuals, calculating correlations of periodic signals and comparing local changes while advancing the unsteady simulation in time. The root-mean-square residuals were found to be in the order of 10^{-5} for the mass flow and

10^{-4} for the momentum, respectively for both steady-state and unsteady simulations.

The periodic convergence of the transient simulation was additionally evaluated using the correlation coefficient of the unsteady data at monitoring points between two subsequent periods according to the method of Clark and Grover [36]. This introduces a specific measure of the (expected) periodic convergence on unsteady variables (see illustrated pressure fluctuations of the monitoring points at the rotor inlet plane in Figure 5.4(a)). The correlation coefficient (CC) for period P is defined as described in Equation 5.2. N is the number of time steps per period and $p^{'}$ is the mean corrected fluctuation of the investigated variable.

$$CC(P) = \frac{\dfrac{1}{N} \sum\limits_{0}^{N-1} p^{'}(n-1)p^{'}((n-1)-N)}{\dfrac{1}{N} \left[\sum\limits_{0}^{N-1} p^{'2}(n+1) \sum\limits_{0}^{N-1} p^{'2}((n+1)-N) \right]^{1/2}} \qquad (5.2)$$

A correlation coefficient CC of 1 would indicate perfect periodic convergence at the specific location. For the pressure signal of two consecutive rotor blade passings, general cross-correlation values above 0.99 were found (Figure 5.4(b)). The pressure signal downstream of the rotor at 85 % span achieved lover levels of convergence. Regarding the hub heat transfer investigations, the level of convergence at this location was considered sufficient.

Acceptable levels of convergence of the hub endwall temperatures—and hence the heat transfer coefficient and cooling effectiveness—were more difficult to reach than for the flow field. In particular, the region in the vicinity of the purge flow injection on the endwall was considered challenging to converge. For the convergence assessment, relative changes of the unsteady time-averaged Nusselt number and cooling effectiveness values over six consecutive stator periods (60°) were compared to the previous periods (Figure 5.5). The local changes in Nusselt number were ±10 % after 24 simulated periods, which is below the level of measurement uncertainty. The platform averaged change in Nusselt number of the full endwall was calculated as 1.7 %. Moreover, the local change in cooling effectiveness was below ±0.1. Overall, it was determined that unsteadiness in the vicinity of the cavity for the investigated geometry was imposing challenges to heat transfer convergence and required large amounts of simulation time for
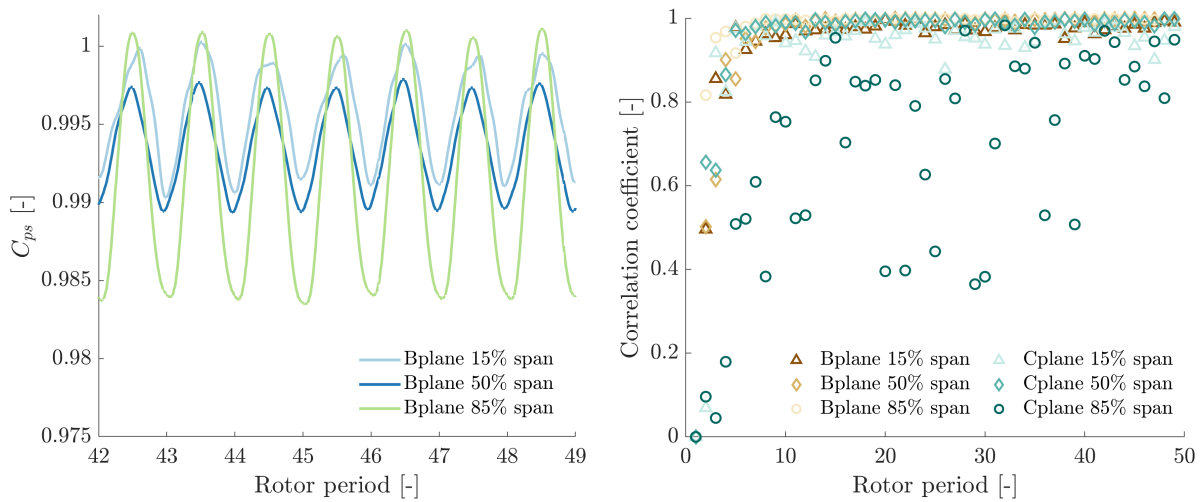
Figure 5.4.: Illustration of the periodic pressure fluctuation of monitoring points at the rotor inlet plane (a). Correlation coefficient as convergence history for the unsteady pressure at different monitoring points (b).

acceptable convergence.

5.2.2. Experimental Validation

Validation of the flow field with experimental data was necessary to infer the correctness of the simulation. The available high-resolution probe measurement data at inter-stage traversing planes for the investigated configuration served as basis for this validation. Correct prediction of the turbine flow field with complex secondary flows was required to accurately predict rotor hub endwall heat transfer, especially for turbine representative geometries and setups as used for this work.

The (aerodynamic) experimental validation was performed for the flow field upstream and downstream of the rotor. Validation and discussion of the simulation setup and solver for rotor endwall heat transfer predictions are integral aspects of this work and discussed in the results (see Section 6.1.4 for greater detail).

The circumferentially time- and mass-averaged flow field validation of the steady-state and unsteady time-averaged simulation at the rotor inlet measurement plane is depicted in Figure 5.6. For both simulations, the profiles match well with the measurement data. In the main flow region above $0\,\%$ span, non-dimensional pressure was slightly overestimated by a maximum of $1\,\%$. The loss region at $60\,\%$ span was not captured in the circumferentially averaged data. The total pressure reduction in the vicinity of the cavity was

P: 6   P: 12

P: 18   P: 24

(a)   (b)

(c)   (d)

ΔNu [%]
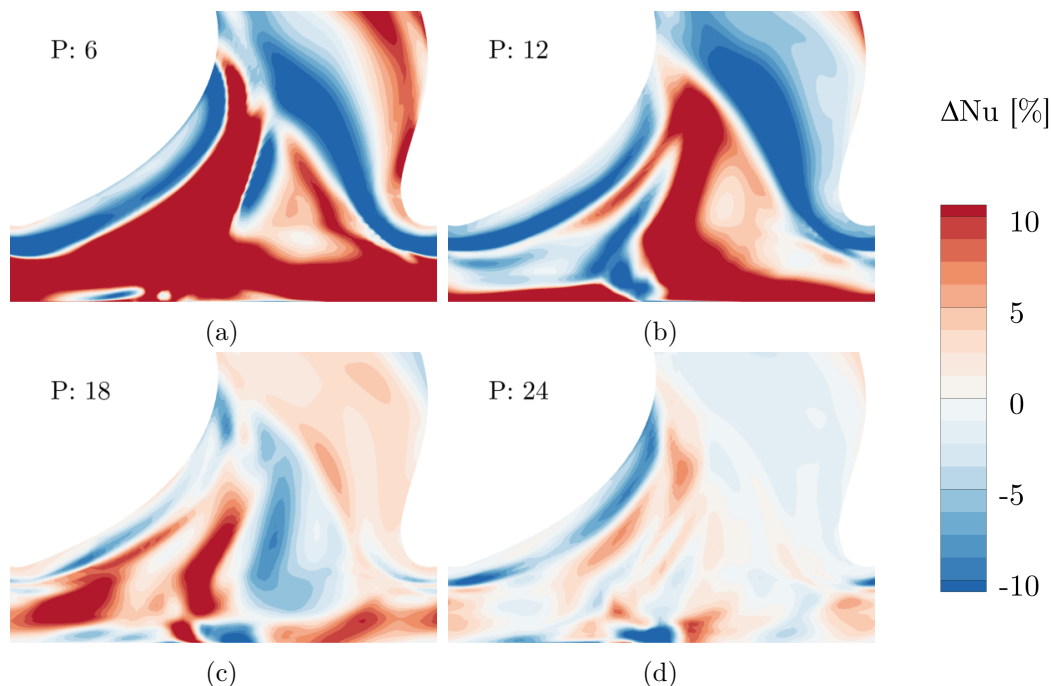
Figure 5.5.: Convergence of rotor hub Nusselt number distribution. The relative difference for the time-averaged values between six consecutive periods.

well captured. Inside the cavity, the total pressure was up to 3.8% lower at -3% span for the simulations.

The absolute yaw angle profile was qualitatively well predicted in the simulations. A nearly constant offset by 2.5% in absolute yaw angle between CFD and measurements was found between 10% to 90% span. It remains unknown whether this systematic deviation was introduced by the simulation or associated with the probe measurements.

A comparison of the time-averaged—yet circumferentially resolved—total pressure in the stationary frame is depicted in Figure 5.7 for the unsteady simulations and experiments. Due to the profile transformation approach of the simulation, the data were scaled to one rotor pitch in the simulations instead of one stator pitch given in the experiments. A good agreement of the span-wise distribution of the main total pressure loss regions from the hub passage vortex, the (inclined) blade wake and the tip secondary flows was achieved.

Figure 5.8 presents the circumferentially time- and mass-averaged total pressure and yaw angle profiles downstream of the rotor. A good agreement up to 80% span was found for both flow quantities between simulations and measurements. The prediction of the unsteady simulation was closer to the measurements than the steady-state simulation, with deviations below
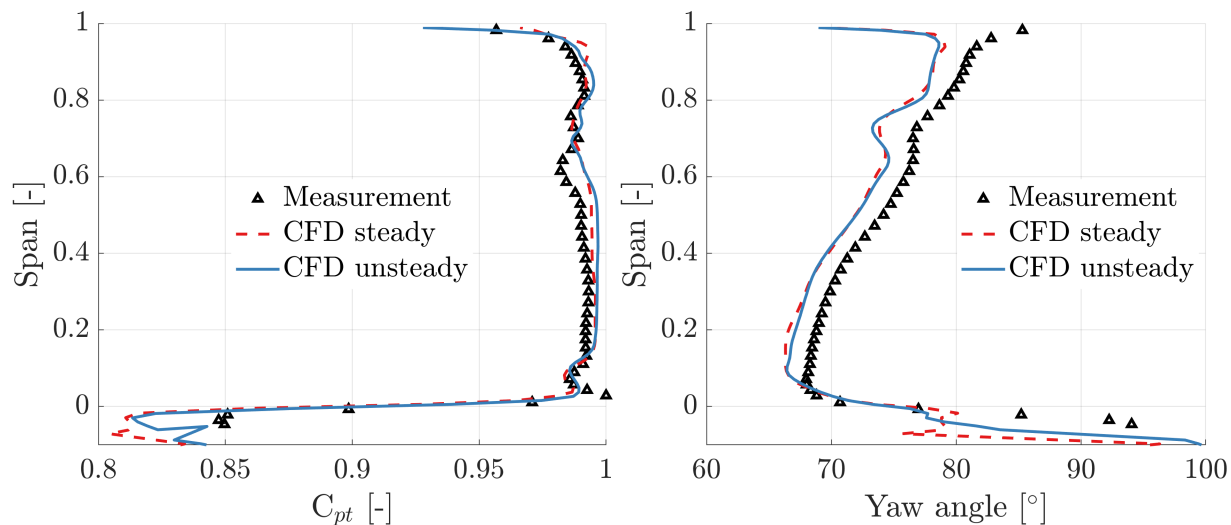
Figure 5.6.: Comparison of the mass- and time-averaged flow profiles for non-dimensional total pressure (left) and absolute flow yaw angle (right) at the exit of the first stator between probe measurements (FRAP) and simulations for IR 0.8%.

(a) Measurements

(b) Simulation (unsteady)
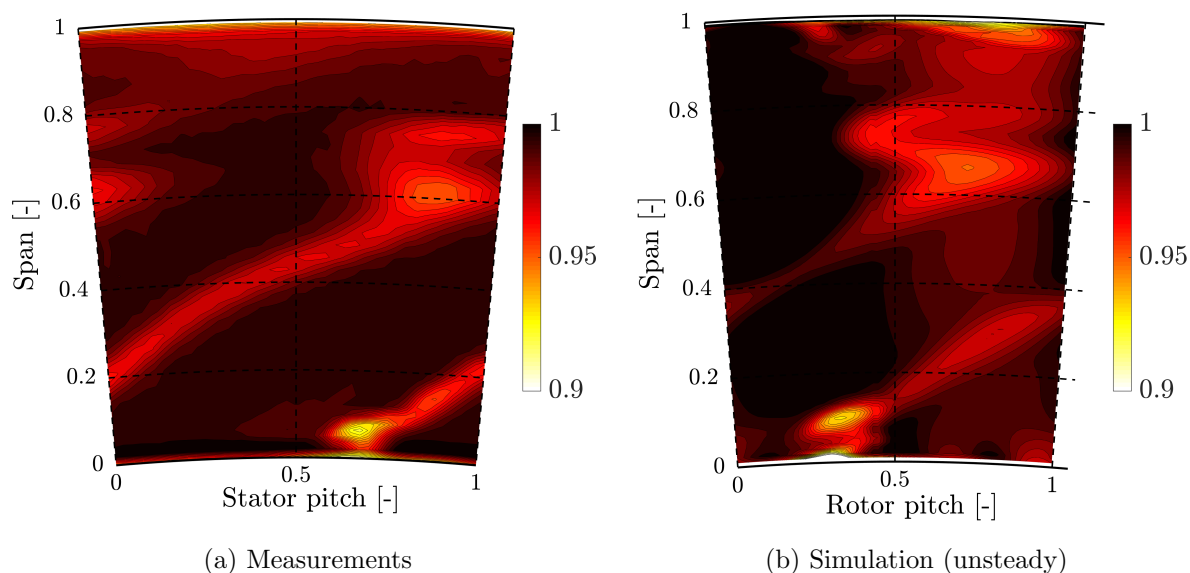
Figure 5.7.: Comparison of the time-averaged normalised total pressure C_{pt} in the stator frame of reference at the rotor inlet plane for 0.8 % purge flow injection between FRAP measurements (a) and unsteady simulations (b).
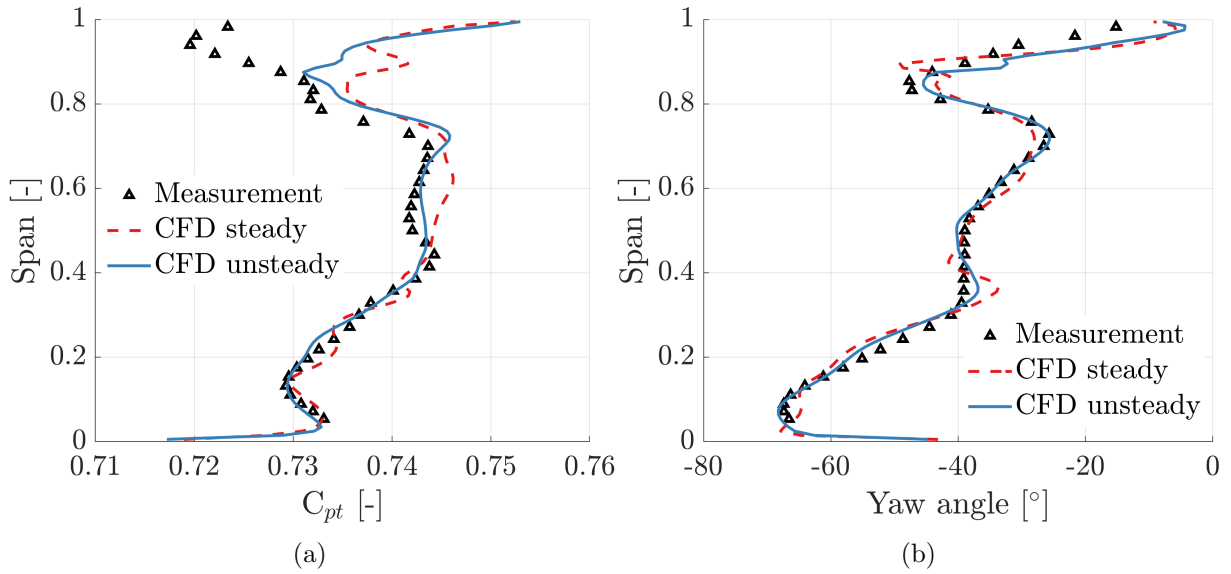
Figure 5.8.: Comparison of the mass- and time-averaged flow profiles for the non-dimensional total pressure (a) and absolute flow yaw angle (b) at the exit of the rotor between probe measurements (5HP) and simulations for IR 0.8 %.

± 0.5 %. In the tip region above 80 % span, both simulations over-predicted the total pressure. A potential explanation for this is the not fully representative modelling of the blade tip. However, this region was judged to be irrelevant for the hub endwall investigation. The absolute yaw angle downstream was accurately predicted by both steady-state and unsteady simulations. Apart from the region between 20 % and 35 % span—where the simulations over- and underestimate the turning by $-3°$ and $2°$, respectively—the absolute difference in yaw angle was below $\pm 1°$.

5.3. Investigation of Simulation Parameters

5.3.1. Influence of Surface Roughness

To account for the surface roughness of the high-emissivity paint (Section 3.3.3.3) used in the experiments, the simulations were also performed with modelled surface roughness.

Previous investigations by Blair [22] showed that surface roughness can greatly enhance local heat transfer (>100 %) compared to smooth walls. Moreover, a study by Lutum et al. [104] highlighted the need for surface roughness modelling for comparing numerical predictions with heat transfer
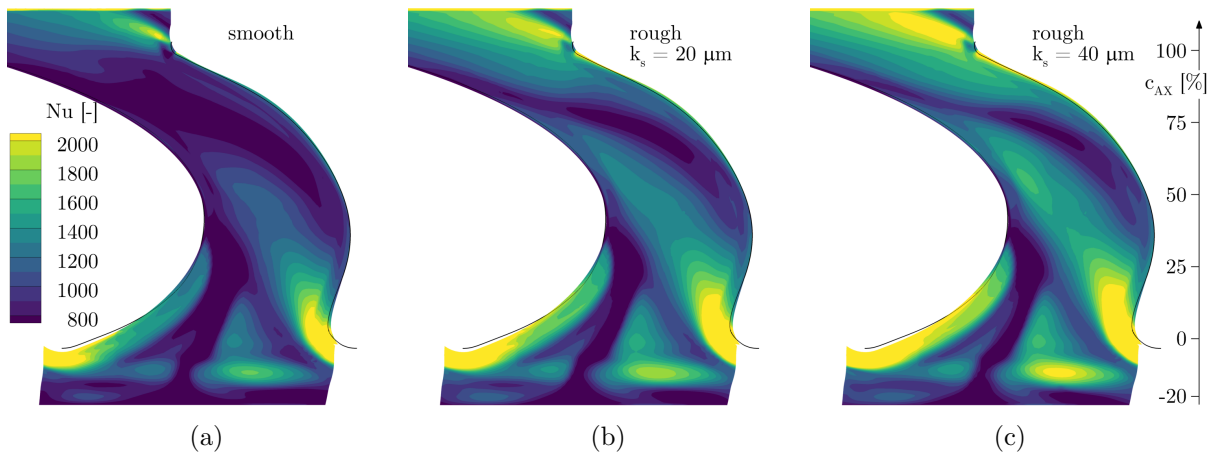
Figure 5.9.: Hub endwall heat transfer maps for different wall roughness values. Smooth walls (a) compared to rough walls with equivalent surface roughness values k_s of 20 µm (b) and 40 µm (c).

measurements on rough walls. Details of the implementation of the roughness model in CFX were discussed by these authors based on an equivalent sand grain roughness parameter k_s. The derivation of typical roughness parameters from measurements such as the arithmetic means of the profile deviations (Ra) or peak-to-peak profile heights (Rz) is not straightforward. However, some simple estimations have been proposed by Adams et al. [3] and others.

To evaluate the influence of surface roughness on the hub endwall heat transfer coefficient, steady-state simulations for two different equivalent sand grain roughness values (20 µm and 40 µm) were compared against smooth walls. The geometric roughness was maintained at 6 µm for both simulations, which was determined to be a representative value.
The endwall-resolved Nusselt number distributions for all three cases are depicted in Figure 5.9. Local heat transfer patterns do not appear to change with surface roughness. However, the levels of heat transfer increase with increased surface roughness.
On laterally averaged values, the case with k_s =20 µm had approximately 10 % to 20 % higher heat transfer levels at up to 80 % axial chord. In the throat region (between 80 % and 100 % of the axial chord), values up to 40 % higher than with smooth walls were observed. This confirms that surface roughness modelling for heat transfer is especially important in regions with highly accelerated flows, such as in the blade throat area. The differences between 20 µm and 40 µm surface roughness k_s showed a similar trend. In the flow acceleration region, the higher roughness increased heat transfer
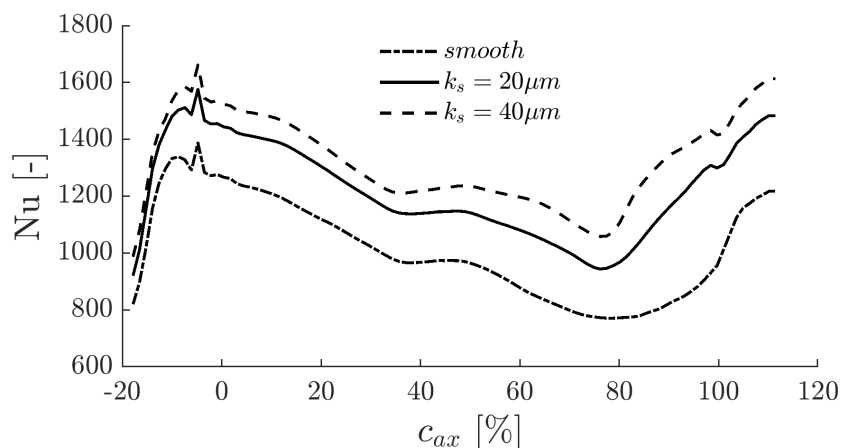
Figure 5.10.: Comparison of laterally averaged Nusselt values for smooth walls and two values for equivalent surface roughness.

by approximately 15 %, otherwise the differences were between 5 % to 10 % relative to the $k_s =$ 20 µm case.

5.3.2. Non-Uniform Heat Flux Boundary Conditions

In the experimental setup, non-uniform heat flux boundary conditions were imposed by the thin-film heater due to local current concentrations (Section 3.3.3.5). However, for the simulations described in Section 5.1.2, uniform heat flux boundary conditions were specified for the heat transfer calculation. This section presents the influence of experimentally representative and non-uniform heat flux boundary conditions on the heat transfer coefficient derived from steady-state simulations. Due to time restrictions, this study was limited to steady-state calculations.
For this, the experimentally derived map of the non-uniformity correction factor S_q was imported in Ansys CFX as a user function and used to scale the constant heat flux imposed by the ideal simulation (Figure 5.11).

The Nusselt number distributions for both boundary conditions are depicted in Figure 5.12. It is apparent that the non-uniform heat flux boundary conditions with locally increased heat flux at the heating track turns led to locally increased heat transfer coefficients. The phenomena were most pronounced around the blade leading edge region and in the blade throat on the pressure side. These were the regions where—due to the flow direction or the formation of secondary flows structures—a new thermal boundary layer was formed. A similar effect was also observed in the experiments. However, this data region was masked and not considered for the analysis.
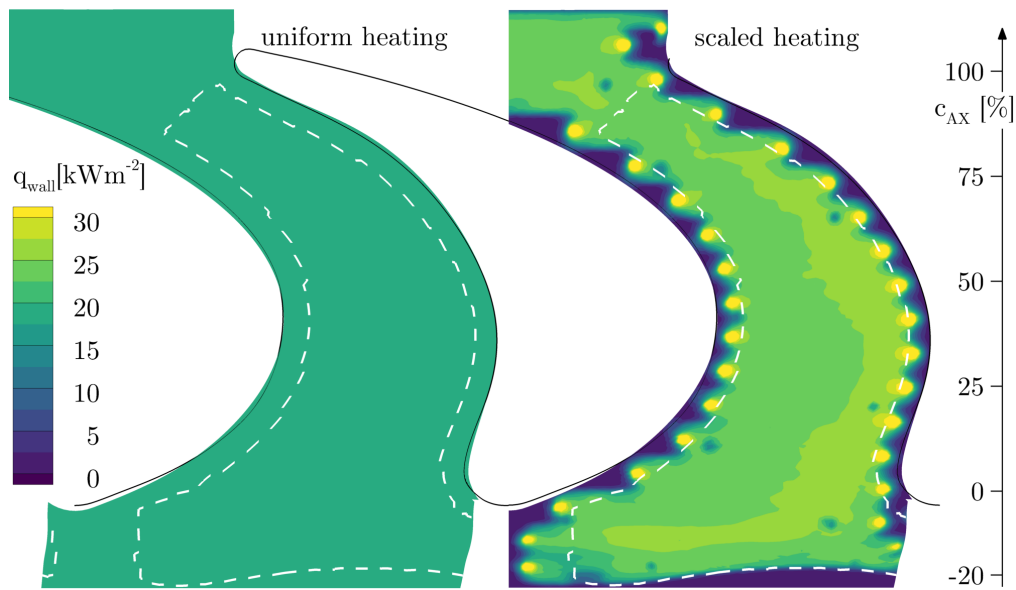
Figure 5.11.: Endwall heat flux boundary conditions for the uniform (left) and non-uniform scaled (right) simulation.

Therefore, for the quantitative comparison of the two simulations, only the region indicated by the dashed lines (Figure 5.12) were considered.

Figure 5.13 shows the local relative difference between uniform and non-uniform heating and the laterally averaged Nusselt numbers for both simulations. Apart from the differences close to the blade fillet (not considered here), the maximum difference was observed at the upstream face of the endwall hill (up to $30\,\%\ c_{ax}$). A physical explanation for this was not readily available and it was suspected that this may be due to the poor capturing of the unsteady interaction between the main flow and cavity by the steady-state simulation. The increased heat transfer coefficient at the throat pressure side due to the newly formed thermal boundary layer extends into the passage following the cross-passage flow direction and causes up to a $20\,\%$ increase in local Nusselt number. For the main part of the platform, a $5\,\%$ to $8\,\%$ offset in Nusselt number was observed. The laterally averaged profiles in Figure 5.13(b) illustrate the qualitative similarity in heat transfer and the quantitative offset observed.

5.3.3. Simulation Parameters

For the final simulations presented in this work, a setup with an equivalent roughness value k_s of $20\,\mu\text{m}$ and uniform heat flux boundary conditions were used. The chosen roughness value was expected to accurately represent experimental surface conditions. Uniform heat flux boundary conditions
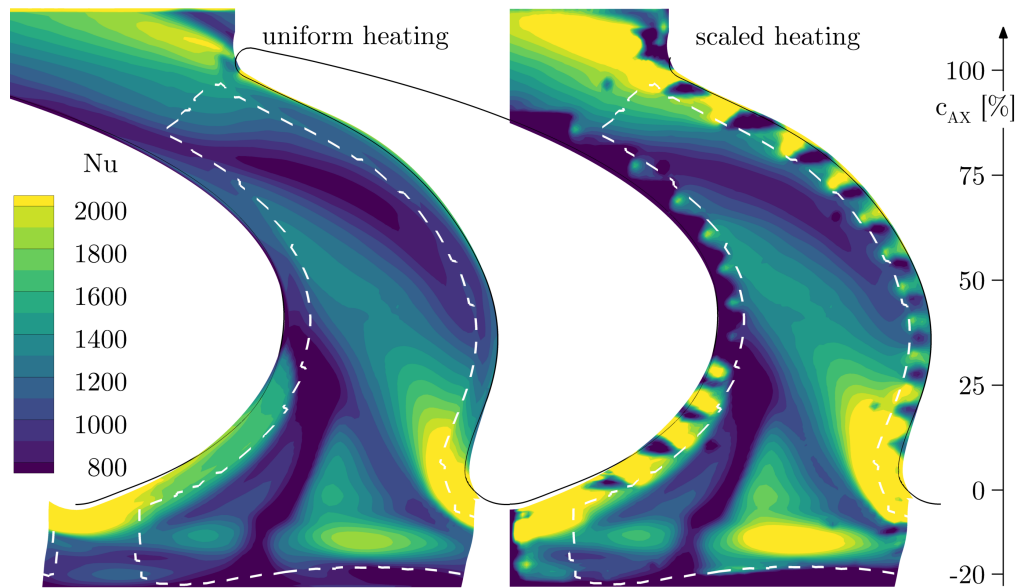
Figure 5.12.: Comparison of endwall Nusselt number distribution for uniform platform
heating (left) and experimentally representative locally scaled heating (right).
Dashed white lines indicate the visible data range in experiments.
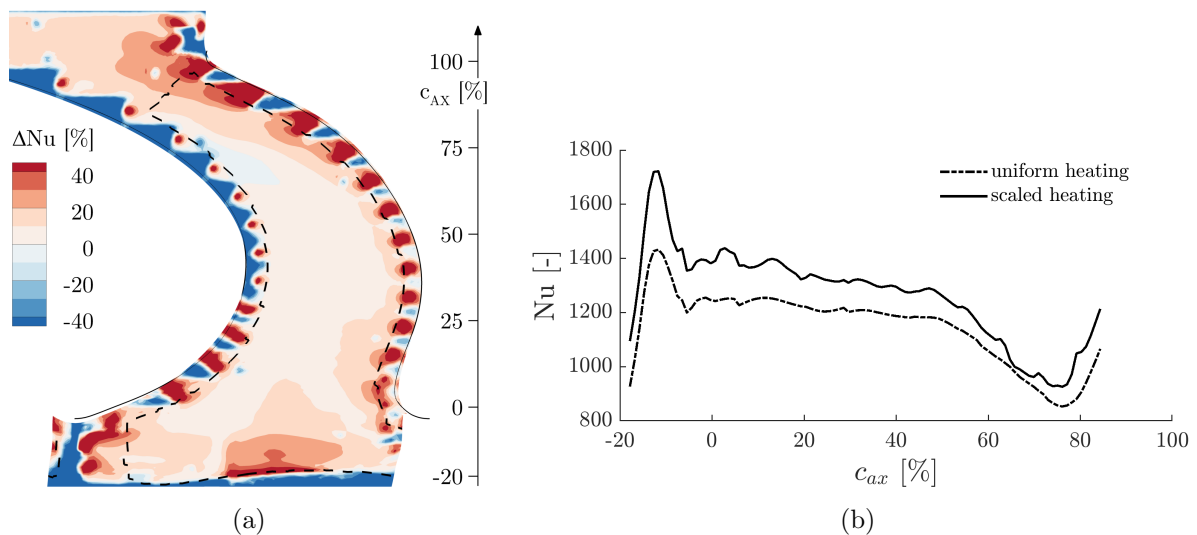
Figure 5.13.: Absolute difference in local Nusselt number between uniform and scaled
heating (a). Laterally averaged Nusselt number comparison on experimental
data range (b).

were chosen due to the increased data availability at regions close to the endwall fillet.

However, the investigation with non-uniform, experimentally representative heat flux boundary conditions showed that an impact on the derived heat transfer coefficient was visible in the vicinity of the non-uniformities. The benefit of representative boundary conditions was counterbalanced by a reduced area with valid heat transfer results. Simulations of this type may be used in the future to verify (where possible) heater designs to ensure valid experimental boundary conditions for the regions of interest with quasi-iso-energetic measurement setups.

6. Purge Flow Effects on Rotor Hub Endwall Heat Transfer

This chapter presents the combined aerothermal investigation of a highly loaded axial turbine configuration under representative purge flow conditions. Experimental data were acquired using fast-response aerodynamic probes to measure the unsteady flow field upstream and downstream of the rotor as well as the infrared-based heat transfer measurement setup for rotor endwall heat transfer measurements. The unique combination of spatially- and time-resolved flow field measurements together with high-resolution endwall heat transfer measurements in a rotating system provides insights into the complex interactions in high-pressure turbines with purge flow injection. The aerodynamically optimised highly loaded rotor blade design with extended endwall contouring into the disk cavity presents a turbine design with great interaction between the main flow and purge flow.

In highly efficient modern gas turbines, purge flow injection is essential to provide rotor disk cooling and sealing the cavity from high-temperature main flow gases. The increased thermal efficiency of these machines due to higher main flow temperatures is contradicted by penalties due to increased cooling requirements, and therefore reduced work generating main flow and increased aerodynamic losses from the interaction of main flow and coolant. Therefore, the engineer's target is to reduce the cooling requirement while maintaining a sufficient sealing of the cavity and minimising negative impact from the main flow interaction. For many years, cascade measurements have been performed assessing the impact of rotor upstream slot injection or endwall contouring on endwall heat transfer. However, time-resolved flow field measurements in rotating facilities have also indicated that the interaction between main flow and purge flow is highly unsteady and that purge flow entrainment on the endwall hub platform is more jet-like rather than a uniform slot injection. This highlights the need for heat transfer measurements on rotor endwalls in rotating facilities under engine representative unsteady flow conditions.

Section 6.1 presents flow field and hub endwall heat transfer characteristics

for the designed turbine pressure ratio of 1.65 and a purge flow injection of 0.8 % of the main turbine mass flow. Additionally, a comparison between experimental measurements and numerical predictions is included and used to link the observed heat transfer patterns with aerodynamics. In Section 6.2, the impact of purge flow variations on local endwall heat transfer and sensitivity are discussed based on the experimental data and predictions. Section 6.3 provides information related to endwall heat transfer for turbine off-design operation.

6.1. Aerothermal Characteristics of a Highly Loaded Axial Turbine Under Design Purge Flow Conditions

This section introduces and discusses the aerodynamic flow field and rotor hub endwall heat transfer characteristics of the investigated turbine geometry at design conditions.

6.1.1. Aerodynamic Flow Field

The aerodynamic flow field was described by the yaw angle and non-dimensional total pressure at measurement planes upstream and downstream of the rotor (Section 3.7.2). The upstream stator introduced significant disturbances in the flow field approaching the rotor. The time-averaged flow yaw angle and non-dimensional total pressure coefficient upstream of the rotor are depicted as circumferentially mass-averaged profiles and contours in Figure 6.1 and Figure 6.2, respectively. Deficits in the total pressure profile at approximately 7 %, 61 % and 75 % indicated the radial location of the stator secondary flow structures. In the contour plot, the inclined wake of the stator blade is visible. Furthermore, the pressure deficit from the hub secondary flow structures was very compact (compared to the tip).

The rotor exit flow field is illustrated in the relative frame of reference for relative flow yaw angle (Figure 6.3) and non-dimensional total pressure (Figure 6.4) as circumferentially mass- and time-averaged profile and time-averaged contour. The flow overturning in the hub and tip region from the secondary flows is visible in the yaw angle profile. The contour plot revealed that the flow was over-turned for a large portion of the hub region (up to 20 % span). The relative total pressure contour (Figure 6.4(b)) reveals the

Figure 6.1.: Circumferentially time- and mass-averaged flow profile (a) and time-averaged contour (b) of relative flow yaw angle at the stator 1 exit with $0.8\,\%$ purge flow injection.
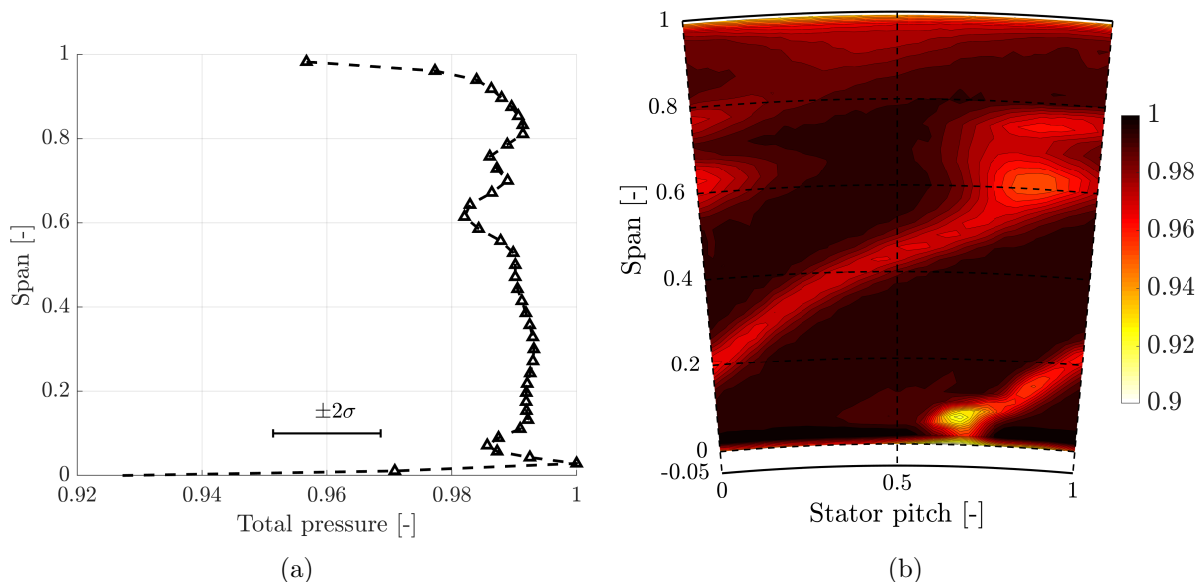
Figure 6.2.: Circumferentially time- and mass-averaged flow profile (a) and time-averaged contour (b) of total pressure at the stator 1 exit with $0.8\,\%$ purge flow injection.
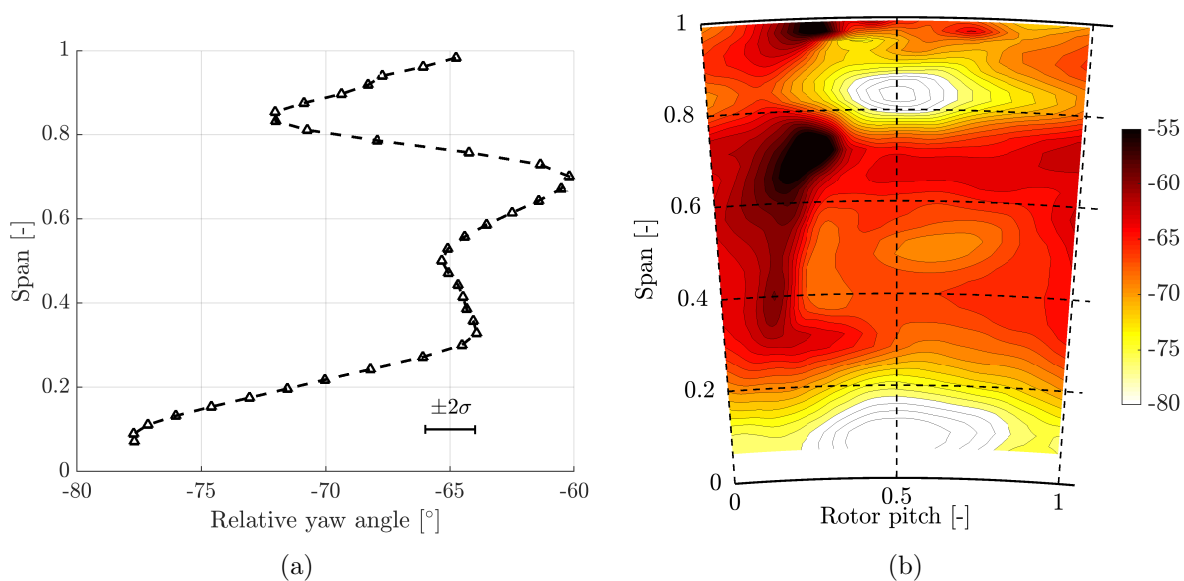
Figure 6.3.: Circumferentially time- and mass-averaged flow profile (a) and time-averaged contour (b) of relative flow yaw angle at the rotor exit with 0.8 % purge flow injection.

pressure deficit in the secondary flow structures and the rotor wake. The rotor hub secondary flow structures lifted off of the endwall and are found at approximately 20 % span at the rotor exit.

The time-resolved pressure unsteadiness (Section 3.7.1, Equation 3.20) acquired by the FRAP probe presented various interesting features close to the rotor upstream cavity. As depicted in Figure 6.5(a) for a radial location at 5 % span, high unsteadiness in pressure was observed around the 0.6 stator pitch position. This high unsteadiness was driven by the stator secondary flows such as the blade wake and passage vortex region (flow contour shown in Figure 6.2). The unsteadiness at this radial location was largely driven by the stator flow structures and showed little influence from the rotor blade passing, since this feature remained constant in space over the rotor blade passing. Further into the cavity at −5 % span (depicted in Figure 6.5(b)), the rotor blade passing drives the pressure unsteadiness. The regions of highest unsteadiness in the flow field are stationary with the rotor and thus inclined in space for the representation in the stator fixed system. This highlights the need for investigations of purge flow injection in rotating facilities.
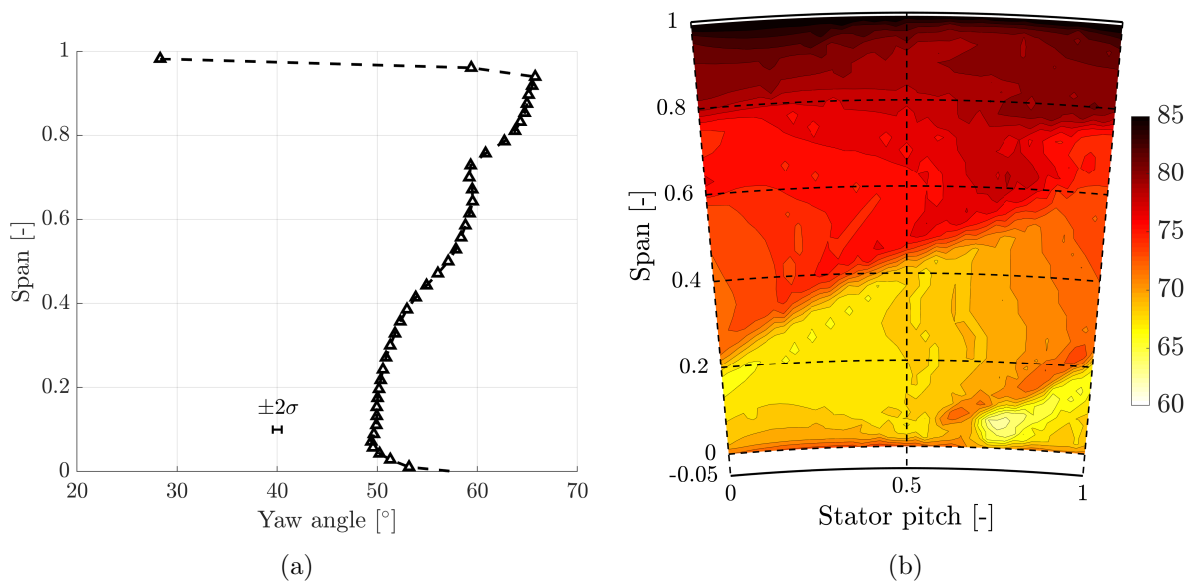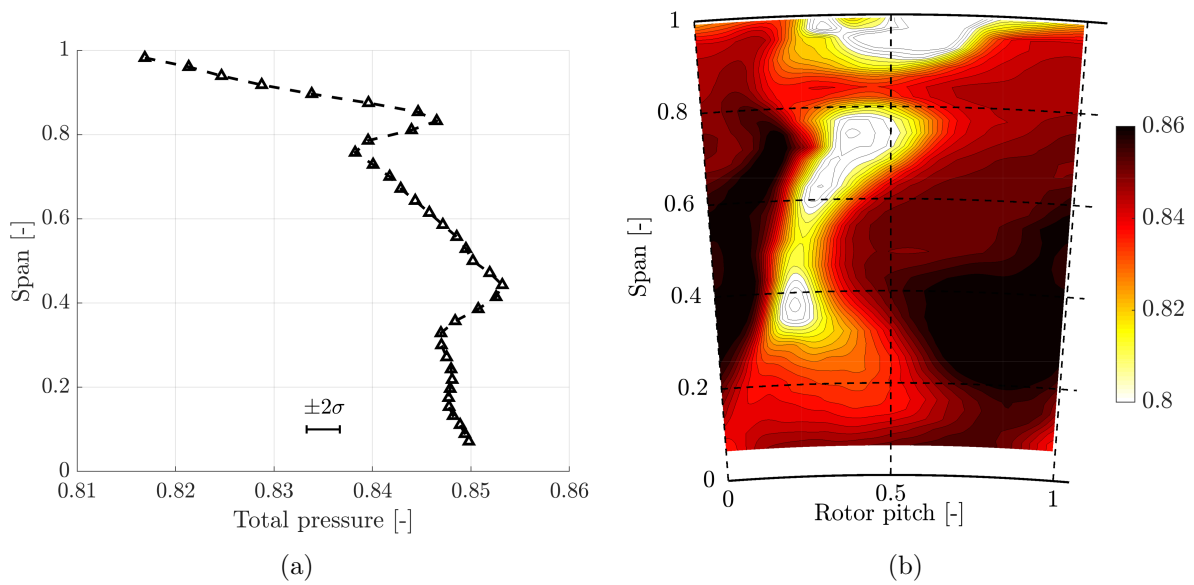
Figure 6.4.: Circumferentially time- and mass-averaged flow profile (a) and time-averaged contour (b) of total pressure at the rotor exit with 0.8 % purge flow injection.
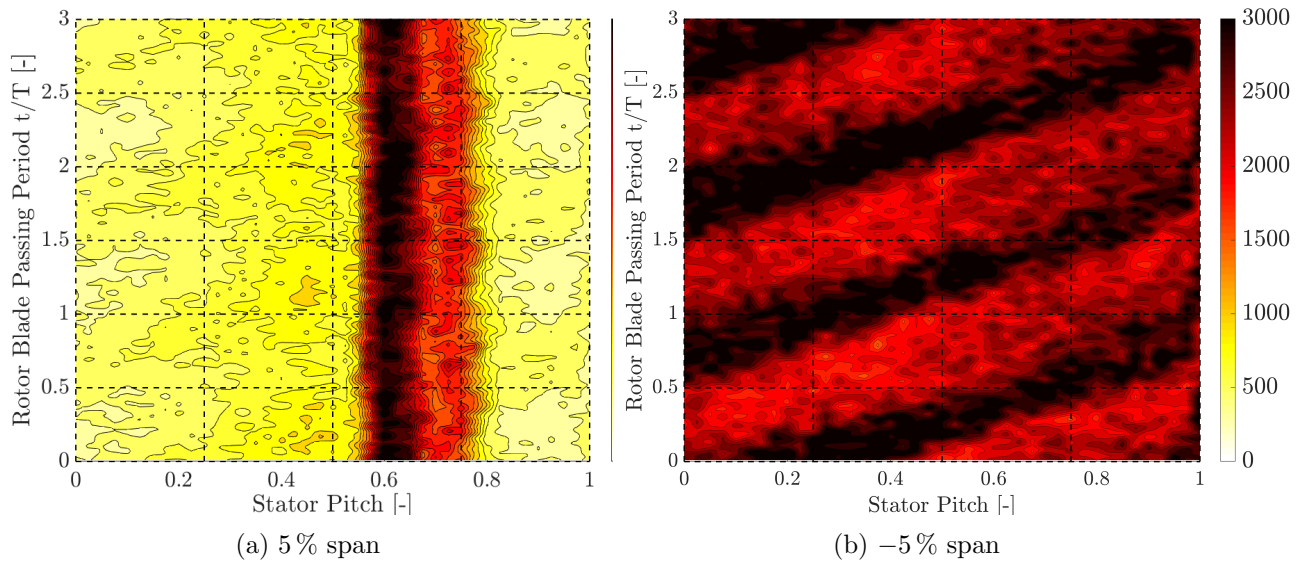
(a) 5 % span

(b) −5 % span

Figure 6.5.: Space-time plot of pressure unsteadiness in the stationary frame of reference at 5 % (a) and −5 % (b) span position at the rotor inlet plane.
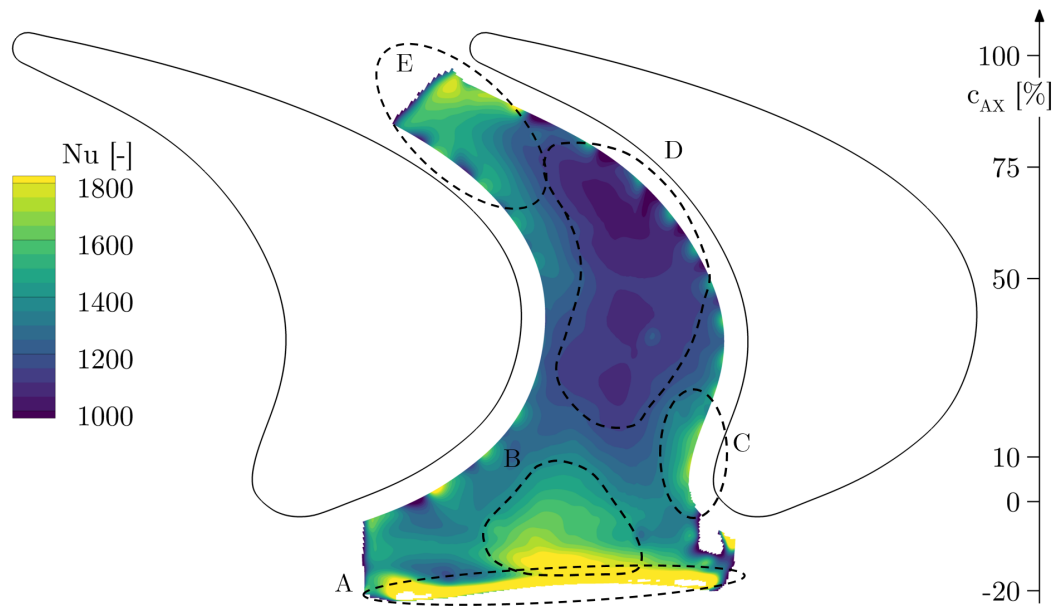
Figure 6.6.: Local Nusselt number distribution for design point pressure ratio and 0.8% purge flow injection.

6.1.2. Rotor Hub Endwall Heat Transfer Coefficient with Cavity Extended Endwall Contouring

The local endwall heat transfer coefficient distribution, presented as a non-dimensional Nusselt number (Equation 4.6), for the design operating point with a pressure ratio of 1.65 and 0.8 % purge flow injection is presented in Figure 6.6. Multiple interesting regions are highlighted and marked as zones A to E.

At the very start of the heated portion of the endwall platform (region A), a small stripe of high heat transfer levels (Nu >2000) was found. Similar findings were reported in [99] and [96] using a comparable setup. Notably, several factors are thought to cause a high heat transfer at this location. Due to the heating of the platform surface, a new thermal boundary layer was formed at the start of the platform that possibly resulted in high heat transfer rates. Furthermore, the potential radial displacement of the platform by centrifugal load (as described in Section 3.4.1.2 predicted by FEM simulations) may have introduced a forward facing step causing local flow recirculation and enhanced heat transfer. The third factor that may have contributed to these results is lateral conduction taking place from the platform into the upstream cavity ring (Figure 3.15a) not accounted for in the post-processing. This region was not considered in further analyses.

The region marked B in Figure 6.6 was found to coincide with the upstream endwall contouring hill (see Figure 2.12). This feature of increased heat transfer levels in the middle of the passage is specific to this cavity extended endwall contouring and has not been reported in the literature for flat or conventional non-axisymmetric endwall contouring [105, 129]. With the endwall contouring exceeding the nominal hub radius of the upstream stator and the steep drop into the cavity, the accelerated main flow may impinge on the forward face of the endwall hill and thus increase heat transfer levels. A trace of the forming horse-shoe vortex pressure side leg with increased heat transfer is marked in region C. The increased mixing of the vortex leg increased the endwall heat transfer before the vortex migration through the passage to the suction side of the adjacent blade.

Between approximately 10 % and 75 % of axial chord, an extended region with lower heat transfer was found (marked D). Downstream of the horse-shoe vortex migration and build up of hub passage vortex, low-momentum fluid is present in the vicinity of the endwall.

Towards the blade throat region (E), the flow in the passage was accelerated, leading to a decreased boundary layer thickness and increased local heat transfer.

6.1.3. Purge Flow Endwall Cooling Effectiveness

Apart from its main task of preventing hot gas ingestion into the wheel space cavity and providing cooling air to the rotor disk and blades, purge flow can also have a direct cooling effect on the hub endwall. This effect of the purge air on wall temperature was studied using the film cooling effectiveness η. This non-dimensional number describes how effective the cooling of the purge on the wall is (see Section 4.2.2 for a more detailed definition and the utilised reference temperatures). Compared to most studies on cooling effectiveness, the injected purge flow in this particular setup is at higher temperature than the main flow and thus heats the endwall. This is due to the bypass setup described in Section 2.1.2, where bypass air is extracted upstream of the turbine inlet and injected as purge flow into the turbine. Using Equation 4.8, the heating of the endwall is translated into an equivalent cooling, therefore it is simply referred to as cooling. Due to the small temperature difference present, also the density ratio between main and cooling flow is close to unity.

The cooling effectiveness for the nominal operating point on the rotor hub

endwall is depicted in Figure 6.7. The results indicate that the measured cooling effectiveness of the purge flow for the investigated rotor hub endwall contouring is highly localised. The upstream portion of the endwall platform that extended into the disk cavity (below the nominal stator hub radius) exhibited the strongest cooling effect, which is expected due to its immersion in the cavity flow. A trace of decreasing cooling effectiveness (dashed line A in Figure 6.7) was found starting from the endwall trough (Figure 2.12) at the platform start along the blade suction side up to 35 % of the axial chord.
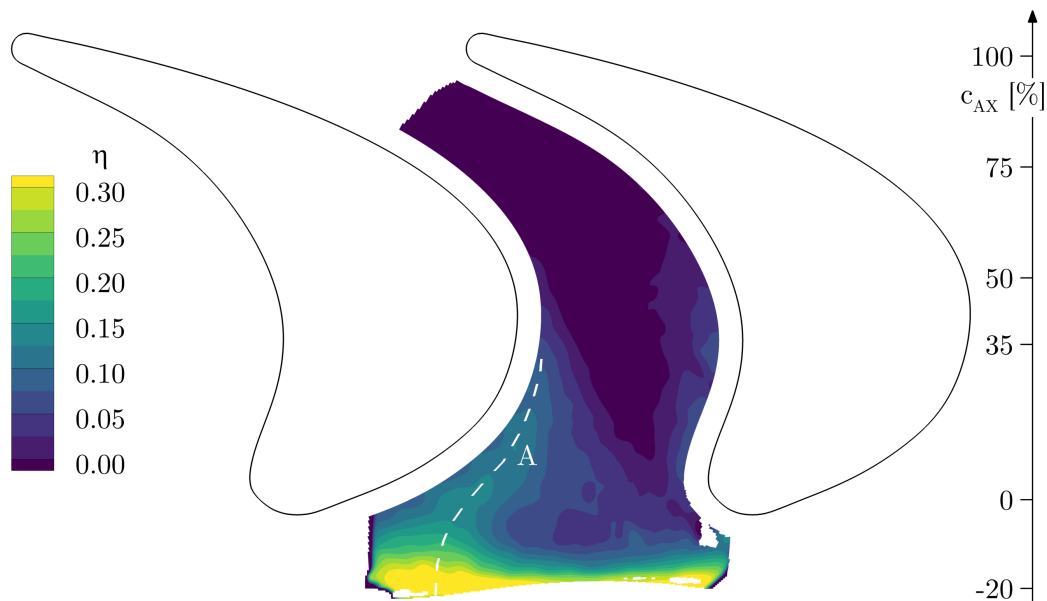
Figure 6.7.: Cooling effectiveness distribution for the designed point pressure ratio and 0.8 % purge flow injection.

In Figure 6.8, the extracted cooling effectiveness values along this line are plotted against the axial chord. A rapid decrease in effectiveness from 0.35 (at the most upstream point) to 0.15 (at −5 % of the axial chord) was observed. The general values found in this region and the curve of decreasing effectiveness are in line with results reported in the literature for single cooling hole studies on a flat plate [70, 160]. This local concentration of cooling effectiveness, which is correlated with the presence of purge flow, also indicates a jet-like purge flow injection into the main flow. This behaviour of jet formation—instead of a slot "waterfall"-like injection of purge flow—was described by previous studies in rotating facilities [81, 143]. The interaction between the main flow and the potential field of the rotor and endwall contouring seems to determine the location of purge flow injection into the main flow, which is "stationary" in the rotor frame of reference. The

dominance of rotor effects in the cavity is also shown in the space- and time-resolved plot of flow unsteadiness (Figure 6.5(b)) from the unsteady probe measurements.
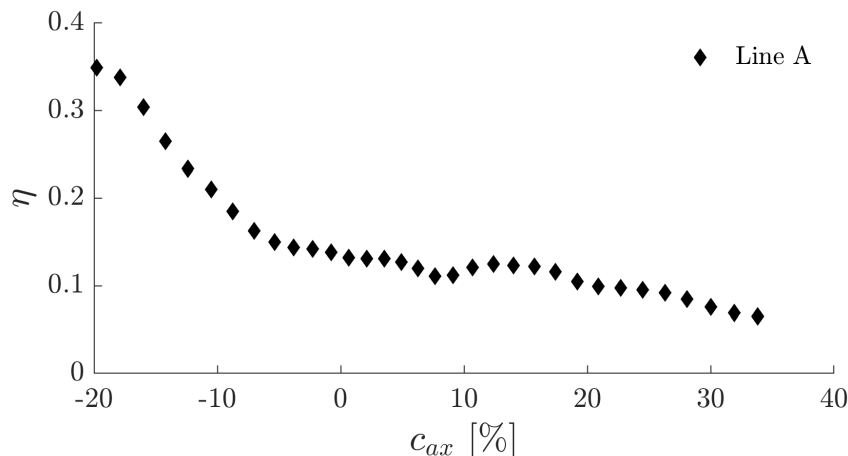
Figure 6.8.: Cooling effectiveness along the purge flow path A indicated in Figure 6.7.

6.1.4. Validation and Comparison of Numerical Predictions with Experiments

Numerical tools are widely established for the design and analysis of gas turbine designs and components in industry. As discussed in the introduction, the results from numerical predictions can provide highly valuable information for the design and analysis process of advanced components at lower cost compared to experiments. Compared to experimental measurements, where data acquisition can be limited due to poor accessibility and/or rotating parts, CFD simulations provide information on the entire simulated flow field. This section discusses the comparison of experimental rotor hub endwall heat transfer measurements with steady-state and transient time averaged numerical predictions. A general validation of the numerical simulations, including convergence assessments and an aerodynamic comparison with the experimental probe measurements, is presented in Chapter 5. The results were compared for the turbine design pressure ratio of 1.65 and a purge flow injection of $0.8\,\%$ of the main flow.

Due to the steadily increasing availability of computational power and advancements in numerical codes to efficiently handle highly parallel simulations, steady-state RANS simulations are well established in the industry. However, the computational resources required for unsteady simulations remain high and must be well justified. This section provides indications

for engineers regarding where additional effort and cost are well justified for endwall heat transfer predictions.

6.1.4.1. Laterally Averaged Comparison

Laterally averaged results represent a good start for analysing and comparing heat transfer results. Despite their inherent drawback of disregarding local phenomena (discussed in more detail in Section 6.2), the reduced complexity simplifies data analysis and is widely used in the industry. Figure 6.9 presents the laterally averaged Nusselt number for the experiments and predictions. Both, steady-state and time-averaged simulations, showed a peak in the heat transfer coefficient at approximately $\approx -13\,\%$ of the axial chord, whereby the peak values were $23\,\%$ higher for the unsteady simulation. Both simulations predicted decreased heat transfer levels further upstream of this peak, where the experimental measurements showed an increase that led to the maximum at the platform beginning (discussed in Section 6.1.2). A sharp decrease following the peak values was observed for all results further downstream. Moreover, both numerical simulations were found to be within the level of measurement uncertainty until $60\,\%$ of the axial chord. The steady-state prediction showed nearly constant Nusselt number levels between $0\,\%$ and $50\,\%$ c_{ax}. In contrast, the time-averaged unsteady results closely followed the measurements and showed a slight reduction with two plateaus. Towards the throat region, neither the time-averaged nor the steady-state simulations predicted the experimentally measured increase in heat transfer. However, the time-averaged results were in better agreement with the experiments. The effect of under-predicted heat transfer by CFD for accelerating flows was also found in [104] and explained by the reduction in roughness Reynolds number not being resolved in the solver roughness model.

Regarding the cooling effectiveness presented in Figure 6.9(b), both simulations showed discrepancies to the measurements, especially at the start of the platform. At the very start of the platform, where the time-averaged simulation and experiments began with very similar cooling effectiveness values (around 0.3), the steady-state simulations overestimated cooling effectiveness by nearly a factor of two (value approaching 0.6). The strong decline in cooling effectiveness observed at the platform start was not as distinct in both simulations. However, the rate of decrease in effectiveness between $0\,\%$ to $80\,\%$ was very comparable to the experiments for the un-
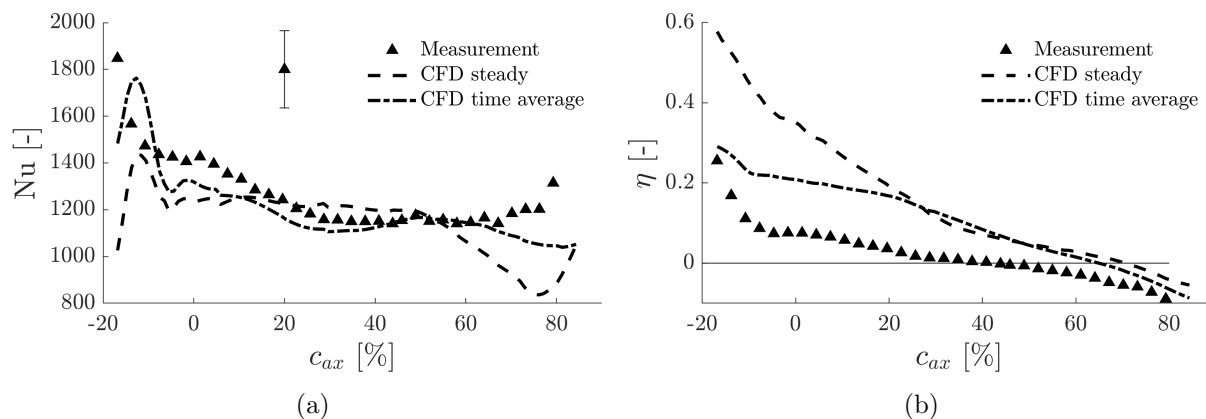
Figure 6.9.: Comparison of lateral averaged Nusselt number (a) and cooling effectiveness (b) between experiments and steady-state and unsteady time averaged simulations.

steady time-averaged simulation (with a slight offset). For the steady-state predictions, this decline rate was reached at approximately $30\,\%$ c_{as}. Based on the laterally averaged results, a reduced mixing between purge flow and main flow was anticipated for the steady-state predictions due to the higher effectiveness and slower decrease through the passage.

The definition used for the cooling effectiveness does not include a correction to account for the temperature decrease in the turbine passage due to the rotor work extraction, therefore effectiveness values go below zero towards the blade throat.

6.1.4.2. Endwall-Resolved Comparison

The high-resolution experimental heat transfer data also allowed a local endwall-resolved comparison with the two numerical approaches. The local Nusselt number distributions are presented in Figure 6.10 using a common colour range for easier comparison. The general patterns of heat transfer coefficient distribution between steady-state and time-averaged simulations were very similar and highlight most of the key features also observed in the experiments (see Section 6.1.2). Upstream of the endwall hill, a region of high heat transfer levels was found that extends in a triangular pattern into the passage. Furthermore, a high Nusselt number region (upstream the rotor leading edge and extended towards the pressure side) caused by the horse-shoe vortex formation is visible. These two distinctive features for this specific endwall design were found to be well captured by the steady-state and unsteady-time averaged simulations.

A band of very high heat transfer observed at the start of the platform was not predicted by either of the simulations, which further indicates that this region was affected by the measurement setup. Both simulations predicted a trace of increased heat transfer downstream of the cross-passage migration path of the pressure side horse shoe vortex leg, which was slightly weaker in the time-averaged simulation. The experiments did not capture this increase—especially in the middle of the passage, where low heat transfer coefficients were measured. This indicated that this secondary flow structure detached earlier from the endwall in the experiments.

The experimentally measured Nusselt number increase observed towards the blade throat was not predicted by either simulation (see Figure 6.9(a) for the laterally averaged data). Generally, it was found that the numerical predictions showed higher spatial peak-to-peak variations in Nusselt number (up to 50 %) when compared to the measurements. Steady-state simulations seem the overestimate these variations since the periodic fluctuations of the upstream flow structures and interactions with the local flow field were suppressed.
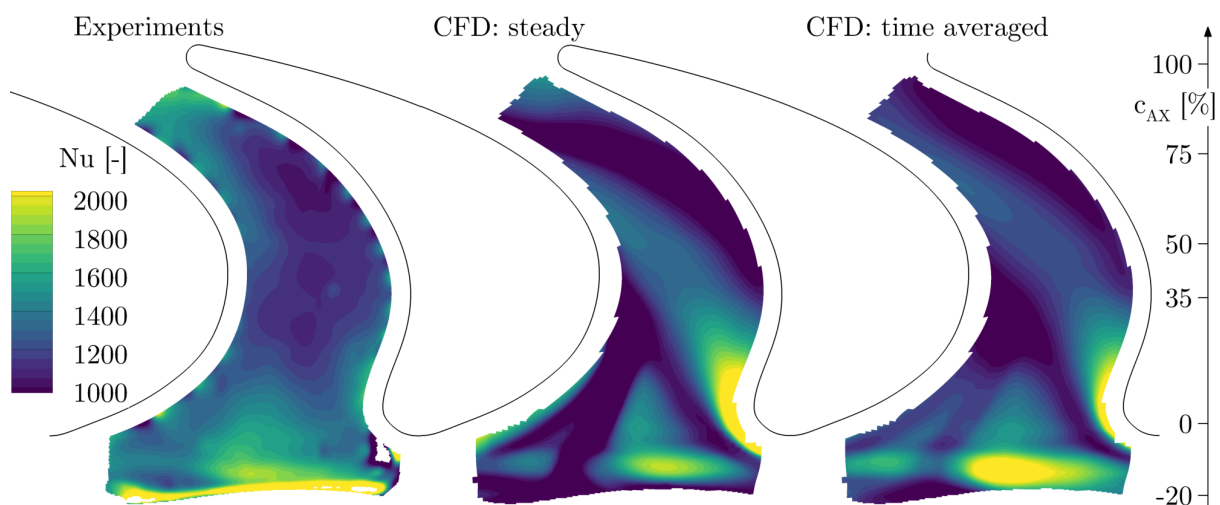
Figure 6.10.: Local hub endwall Nusselt number comparison between measurements, steady-state and unsteady time-averaged CFD simulations.

The cooling effectiveness distribution, which is mainly driven by the hub endwall adiabatic wall temperature, was significantly more dependent on the simulation setup than the heat transfer coefficient (Figure 6.11). An adapted scaling of the colour bar was applied in the figure to enhance the readability of the distributions and emphasize the cooling pattern.
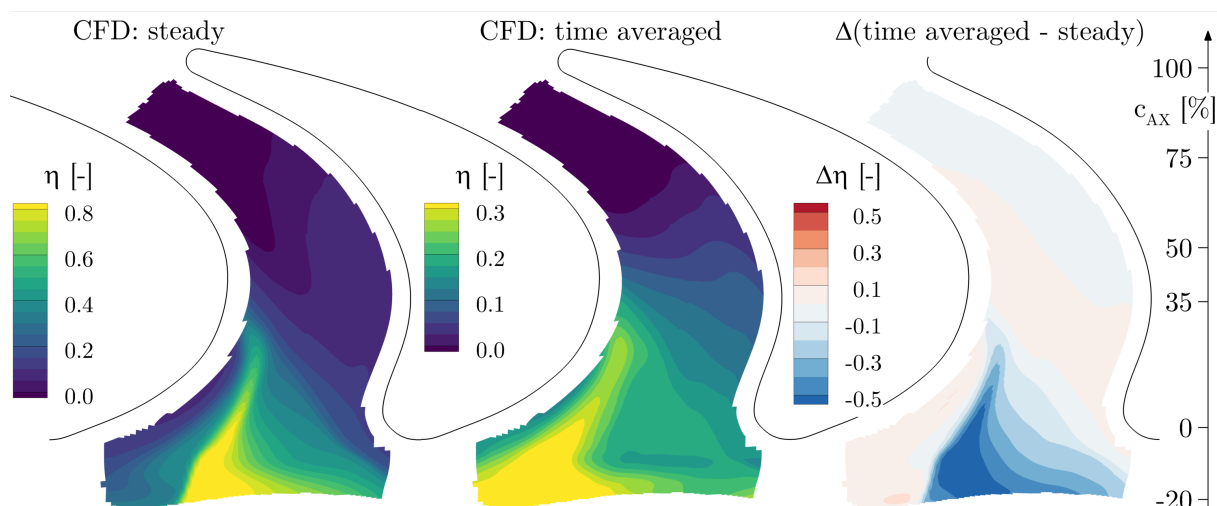
Figure 6.11.: Local rotor hub cooling effectiveness comparison between steady-state and unsteady time-averaged CFD simulations (different scales on colour bars) and absolute difference.

As previously indicated in the laterally averaged comparison (Figure 6.9(b)), the steady-state simulation predicted much higher cooling effectiveness at the beginning of the endwall platform (up to approximately $\approx 35\,\%$ axial chord). This indicates that suppression of the unsteady main flow cavity interaction is greatly reducing the mixing process and resulted in an overestimated local cooling effect of the purge flow on the endwall. The overall pattern between the two simulations were similar. A streak of highest cooling effectiveness extends from the cavity into the platform towards the blade suction side at $30\,\%\ c_{as}$. However, the purge flow is entering the platform closer the contouring hill and more axially for the steady-state simulation compared to the more suction side aligned trace for the time-averaged predictions.

The comparison of both simulations with the experiments is presented in Figure 6.12. Despite the slight over-prediction of the endwall cooling effect, the unsteady simulation predicted the experimentally observed cooling pattern reasonably well. The steady-state simulation greatly over-predict the endwall area affected by the purge flow. These results indicate that unsteady simulations are required to predict the effect of mixing between main and purge flow and predict the cooling effect of purge flow on the endwall.

The presented comparison emphasises the need for unsteady simulations to predict rotor hub endwall heat transfer—especially under purge flow or cooling flow injection. The reduction in flow field complexity in steady state simulations with suppressed flow unsteadiness impacted the prediction accuracy for rotor hub endwall heat transfer. The inherently unsteady character
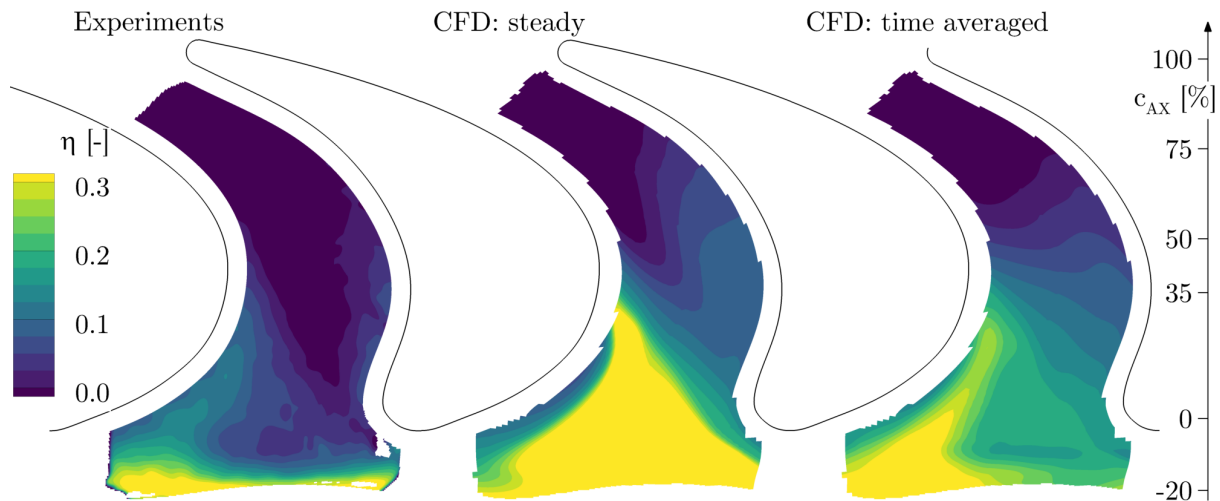
Figure 6.12.: Local rotor hub cooling effectiveness comparison between measurements (a), steady state (b) and unsteady time averaged (c) CFD simulations.

of turbine flows with cavities and purge flow injection must be included in numerical predictions. Steady-state simulations may over-predict the rotor hub endwall cooling effectiveness by more than a factor of two and could also over-predict the peak-to-peak variation of the heat transfer coefficient. Time-averaged unsteady predictions were used for all further investigations in this work.

6.1.5. Linking of Aerodynamics and Rotor Endwall Heat Transfer

Numerical predictions facilitate the investigation of endwall heat transfer and its link with aerodynamics in greater detail. As shown in the previous section, time-averaged results from unsteady simulations agree reasonably well with the experimental results regarding the endwall heat transfer coefficient and cooling effectiveness distribution. These results were used to investigate the flow field in detail and link the observed heat transfer patterns with turbine aerodynamics.

Wall streamlines, which are derived from the wall shear stress vector due to zero velocity at the walls, were used to study the flow field near the hub endwall. In linear cascade measurements, oil film visualisations are often used to experimentally determine near wall flow patterns. The saddle point of the boundary layer roll-up and formation of the horse shoe vortex
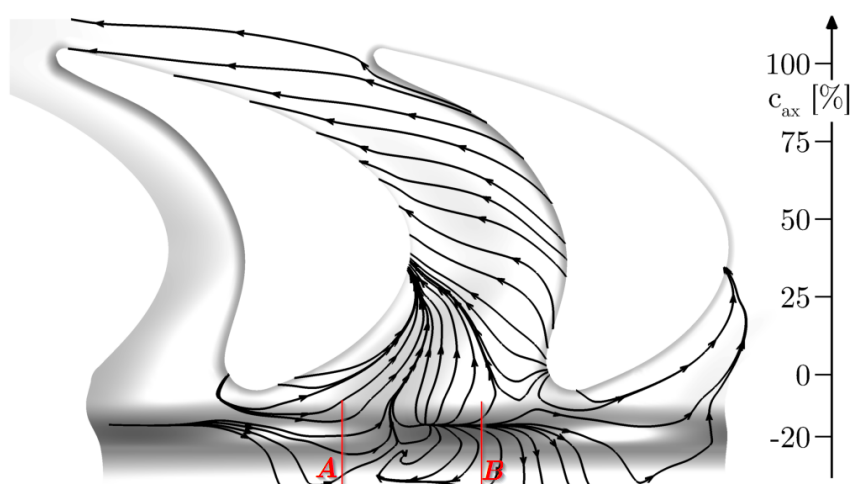
Figure 6.13.: Rotor hub endwall surface streamlines derived from the wall shear stress vector.

upstream the rotor leading edge are visible in Figure 6.13, with the separation line along the pressure side horse shoe vortex leg migration located towards the suction side. Inside the passage, surface streamlines illustrate the pressure-induced cross-passage flow from the blade pressure side towards the suction side building the hub passage vortex. Upstream of the endwall hill at approximately $-20\,\%$ of the axial chord, a flow attachment line was identified with streamlines being deflected into the cavity. This flow attachment line coincides with the peak location of the high heat transfer region introduced in Section 6.1.2 (marked as region B in Figure 6.6).

The local pressure distribution depicted in Figure 6.14(a) highlights a local maximum at this location. A potential field was formed by the hill of the endwall contouring in the vicinity of the hub region which combined with the rotor leading edge potential field.

The local stagnation line at the endwall hill was found to be from high-momentum main flow impinging on the endwall above the nominal hub radius. This is well illustrated in Figure 6.15(a), where the projected streamlines on an iso-pitch slice along line B (indicated in Figure 6.13) are depicted. Part of the main flow impinging on the endwall hill was deflected into the upper cavity and merges with the purge flow in a rim seal vortex structure. The remaining portion of the main flow accelerated over the endwall hill into the rotor passage.

This particular endwall design—with a pronounced hill upstream of the rotor

(a)   (b)
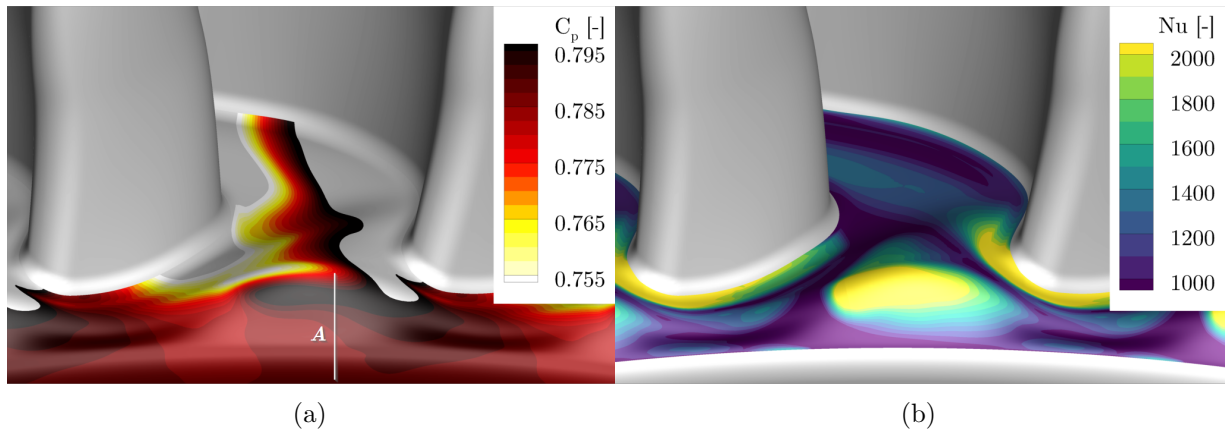
Figure 6.14.: Distribution of local non-dimensional pressure (a) and Nusselt number (b) on
the front portion of the rotor hub endwall.

(a) 60 % pitch   (b) 20 % pitch
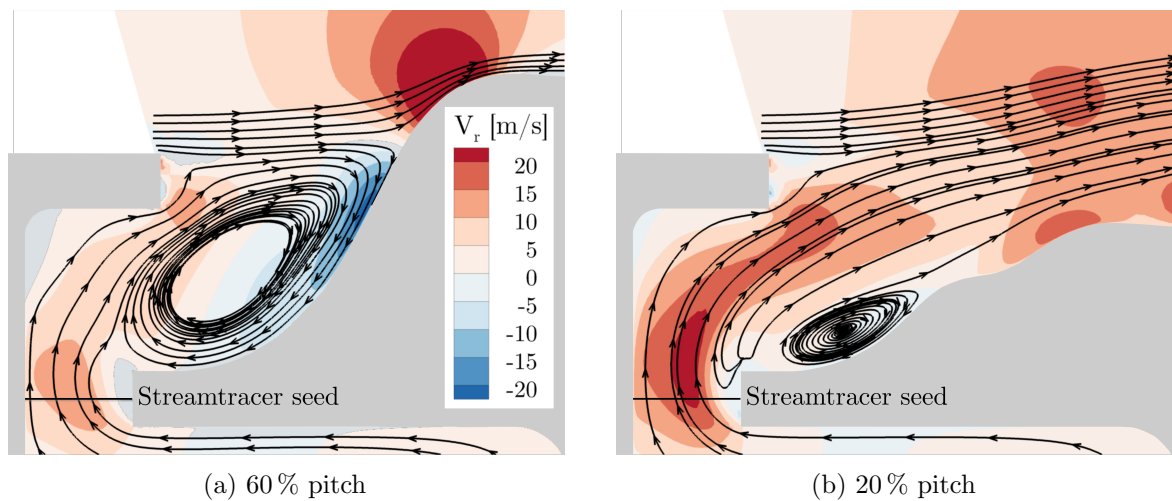
Figure 6.15.: Projections of streamlines on constant rotor pitch planes through the rotor
flow domain showing radial velocity contours. The planes at 60 % rotor pitch
(a) and 20 % rotor pitch (b) are indicated in Figure 6.13.
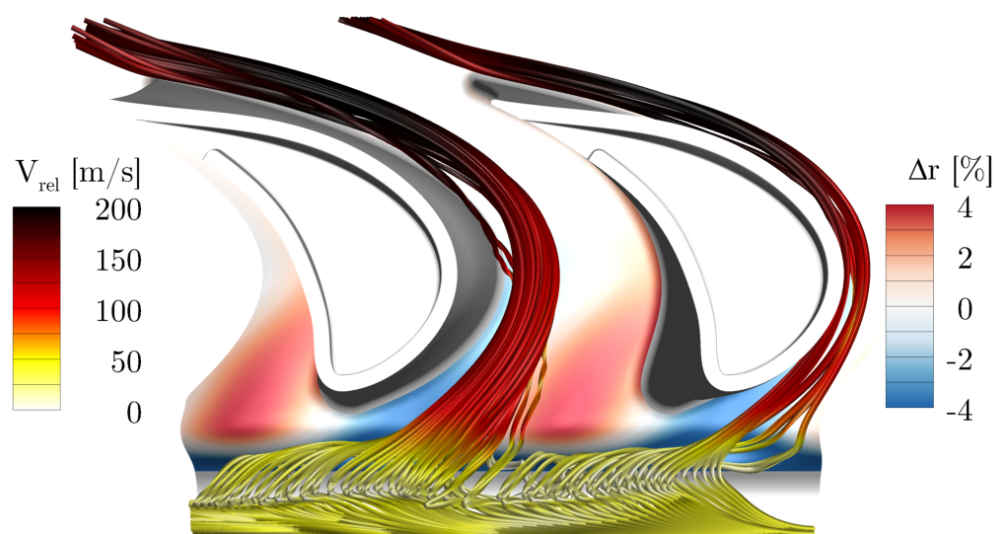
Figure 6.16.: Purge flow streamlines seeded in the cavity with their indicated velocity in the rotor relative system. The rotor endwall is showing contouring relative to the nominal hub radius.

blades and extended contouring into the cavity—caused a local heat transfer coefficient maximum of the same order as that observed at the location of horse shoe vortex formation. Furthermore, the interaction between purge flow and the main flow was enhanced due to the deflection of the main flow into the upper cavity.

This cavity rim vortex (Figure 6.15(a)) was the dominating flow structure in the upper part of the rim seal cavity. Figure 6.16 illustrates this structure with purge flow streamlines. Stream tracers were seeded at the plane where the rotor-sided sealing lip was closest to the stator side (6.15(a)). A colour map illustrates the relative velocity of the streamlines and the endwall contouring relative to the nominal hub radius (Equation 2.3). The formation of the cavity rim vortex upstream of the endwall hill was preventing purge flow from entering the platform at this location. The purge flow left the cavity as a jet-like flow between the blade suction side and the endwall hill. The streamlines presented in Figure 6.15(b) were projected onto an iso-pitch slice through this region to illustrate the situation. The radial momentum of the sealing flow was high enough to radially displace the main flow and enter the platform. This jet-like purge flow injection on the platform also explains the locally high cooling effectiveness towards the blade suction side in the experiments and numerical predictions. The axial extent is limited by the cross-passage flow and the migration of the pressure side horse-shoe vortex that detaches the purge flow from the endwall.

6.2. Sensitivity of Rotor Hub Endwall Heat Transfer to Purge Flow Variations

This section presents the influence of purge flow variations on the local rotor hub endwall heat transfer distribution for the designed pressure ratio of 1.65. In addition to the nominal purge flow injection rate of 0.8 %, a high purge flow case with 1.2 % and a zero purge flow (0.0 %) case were investigated.

6.2.1. Heat Transfer Coefficient Sensitivity on Purge Flow Variation

Laterally averaged values for all injection rates are presented in Figure 6.17. All purge flow rates showed the typical strong decrease of heat transfer at the start of the platform, which was similar to the heat transfer decay on a flat plate with a turbulent boundary layer. The decay was stabilized at approximately ± 5 % of the axial chord before heat transfer levels further decreased up to 30 % c_{ax}. A slight increase towards the blade throat area was measured for all purge flow rates. Interestingly, the laterally averaged heat transfer levels for the nominal 0.8 % purge flow injection were the lowest until 30 % of the axial chord. Previous studies [131, 151] reported the general trend of increasing heat transfer at the platform start with higher purge flow injection, which is in contradiction to the measured results for this investigated geometry. On a laterally averaged basis, the measured differences were relatively small and fell within the measurement uncertainty. However, since the lateral averaging neglects local differences, endwall-resolved data must be considered for a more detailed investigation. Local data on relative changes in Nusselt number compared to the 0.8 % reference case (defined in Equation 4.7) are analysed in the following section.

Figure 6.18 depicts the local distributions of relative changes in heat transfer for both investigated off-design purge flow rates relative to the reference of 0.8 %. For both injection rates (0.0 % and 1.2 %), changes in local heat transfer up to and above ± 20 % were observed on the endwall, which were well above the measurement uncertainty. However, significant changes were only observed at the start of the platform for up to 30 % of the axial chord for both cases. This implies that the direct impact of purge flow injection on endwall heat transfer is limited by the cross-passage flows and horse-shoe
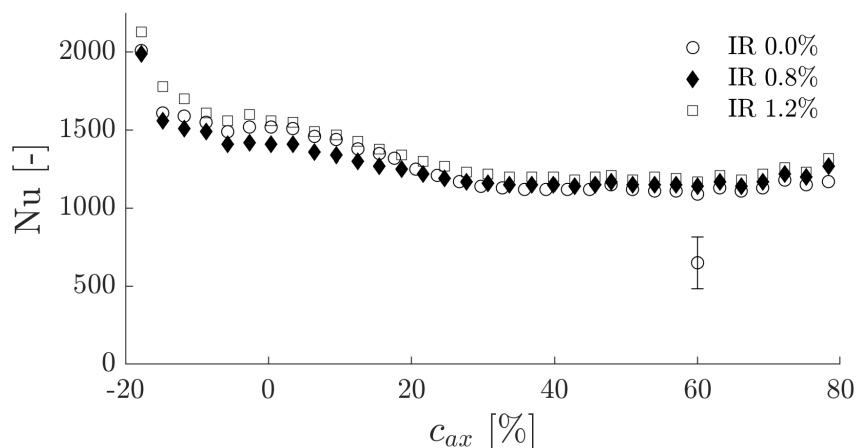
Figure 6.17.: Laterally averaged hub endwall Nusselt numbers for all measured purge flow injection rates (0.0 %, 0.8 % and 1.2 %) at a design pressure ratio of 1.65.

vortex migration where the purge flow is mixed into the secondary flow structures and detached from the endwall. Areas further downstream were found virtually unaffected by variations in the purge flow.

With zero purge flow injection, a distinct increase in heat transfer was observed between the blade suction side and the endwall hill extending up to approximately 25 % of the axial chord. This implies that in the absence of the purge air spilled onto the platform at this location—as illustrated in the previous section for the design purge flow rate—the high-speed and high-momentum main flow fluid present enhanced the local heat transfer. A small increase in heat transfer was also observed for the pressure side leg of the horse-shoe vortex close to the leading edge and at the start of the migration. In the middle of the passage, and towards the throat area, the heat transfer levels were generally lower for the zero purge injection case; however, the differences were within the measurement uncertainty.

6.2.2. Cooling Effectiveness Sensitivity on Purge Flow Variation

The variation of the purge flow injection rate was also expected to change cooling effectiveness on the hub endwall. Figure 6.19 shows the local cooling effectiveness for nominal (0.8 %) and high (1.2 %) purge air injection. Both results showed very similar qualitative patterns in cooling distribution. The highest effectiveness was found at the platform start, located approximately at the endwall trough location following along the suction side until
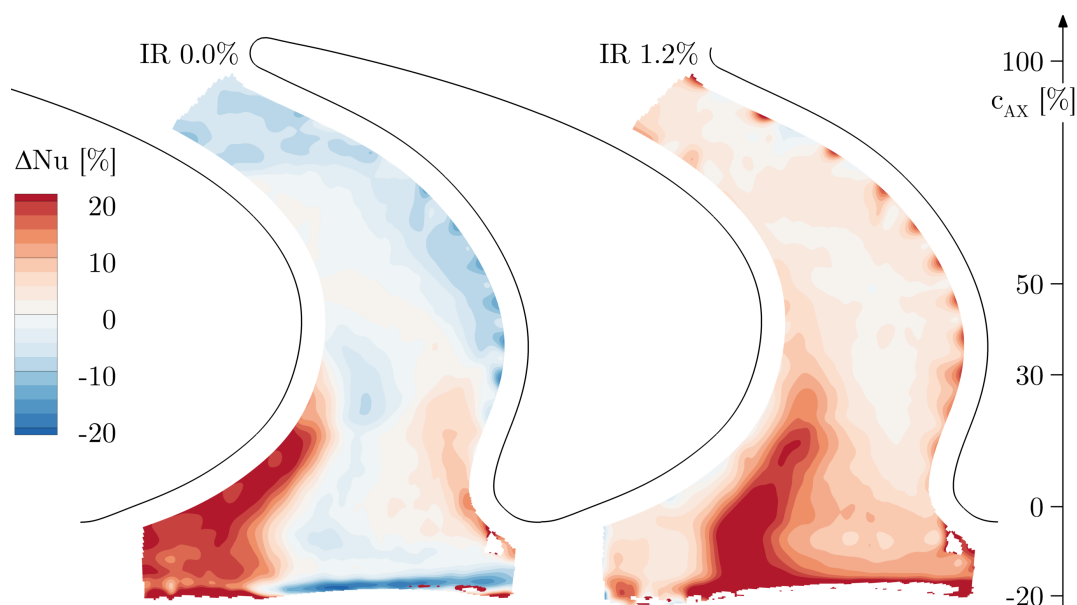
Figure 6.18.: Relative Nusselt number difference for the design pressure ratio compared to the reference purge flow rate (IR 0.8 %) for 0.0 % and 1.2 % purge flow injection.

approximately 30 % axial chord.

The systematic offset between the two injection cases—as illustrated by the absolute difference ($\approx$0.07) in Figure 6.20—over the entire platform was within the measurement uncertainty and may have been introduced by the turbine operating point. At the purge entrainment location (indicated by a dashed white line A in Figure 6.19), the local increase in cooling effectiveness was above the measurement uncertainty. Peak effectiveness at the platform start increased from 0.33 to 0.47 for the high purge flow case and then dropped to a rate similar to the 0.8 % case.

Based on these results it is concluded that the potential of purge flow injection for cooling of the rotor hub endwall is limited. The cavity extended endwall contouring effectively controls the location of purge flow jet entrainment on the platform and leads to a very localised cooling effect on the endwall. For an efficient cooling of the endwall distinct cooling holes distributed on the endwall—especially downstream of the horse-shoe vortex migration line—are needed.
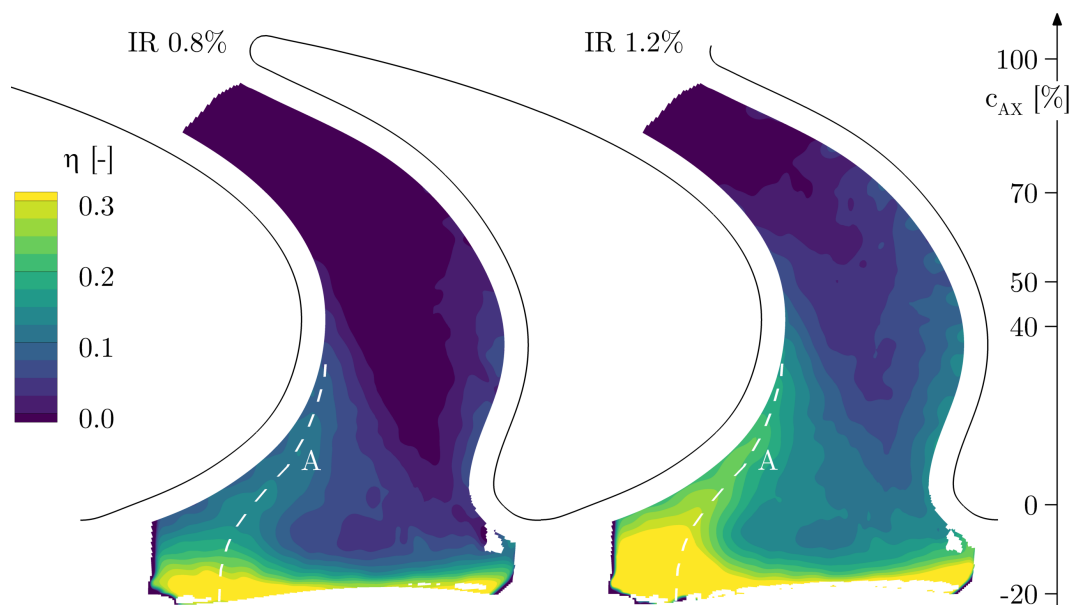
Figure 6.19.: Purge flow cooling effectiveness η for the design pressure ratio 1.65 and 0.8 % and 1.2 % injection.
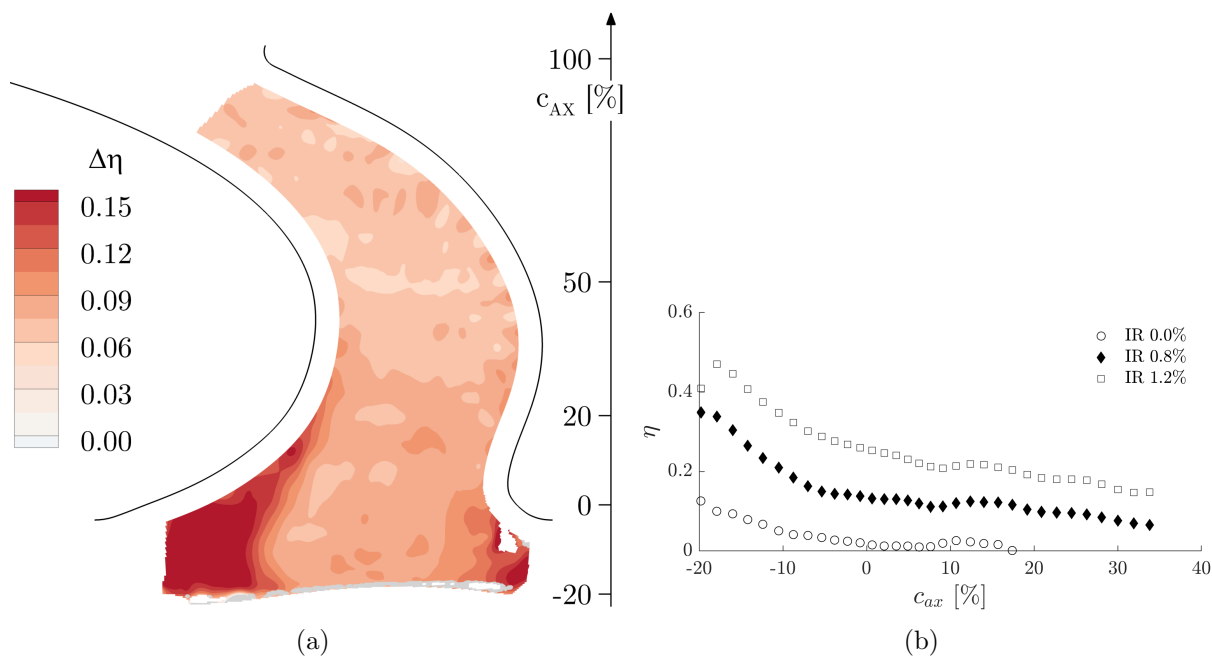
Figure 6.20.: Absolute difference in cooling effectiveness for the design point between 1.2 % and 0.8 % purge flow injection (a). Cooling effectiveness along line A (Figure 6.19) for all purge flow injection rates (b).

6.3. Heat Transfer at Turbine Off-Design Conditions

Traditionally, stationary gas turbines were often operated at a very specific operating point to provide base-load power. However, the increased penetration of highly volatile renewables in the power market changes the operating characteristics for these stationary turbines. High flexibility in output power and fast ramp-up speeds increase the need for efficient off-design turbine operation. Similar to aircraft engines, stationary gas turbines can be consistently operated under off-design conditions.

This section presents the effect of a reduced pressure ratio on the rotor hub endwall heat transfer distribution and the sensitivity on purge flow variations under this off-design condition. Complementary to measurements at the design pressure ratio of 1.65, a second operating point with a reduced total to static pressure ratio of 1.33—but with the same rotational speed—was investigated for three purge flow injection rates of 0.0 %, 0.8 % and 1.2 % of the respective main turbine mass flow.

6.3.1. Influence of Turbine Pressure Ratio on Endwall Heat Transfer

The effects of reduced pressure ratio but constant turbine speed is investigated for the design purge flow injection rate of 0.8 %.

Aerodynamic Implications

The effects of reduced pressure ratio with 0.8 % purge flow injection were investigated experimentally by two turbine operating points (described in Section 2.1.1). The reduction in pressure ratio while maintaining the rotational speed led to a reduced turbine mass flow (and hence reduced rotor inlet Mach and Reynolds number). Due to the fixed rotational speed, the reduced rotor inlet Mach number translated into a change in relative rotor inlet yaw angle, resulting in a negative flow incidence on the rotor (Equation 6.1). The span-wise distribution of incidence angle change for the off-design condition is depicted in Figure 6.21. The flow incidence angle gradually decreased from tip to hub and was approximately $-9°$ close to the nominal hub radius.

$$i = \beta_{PR1.33} - \beta_{PR1.65} \tag{6.1}$$
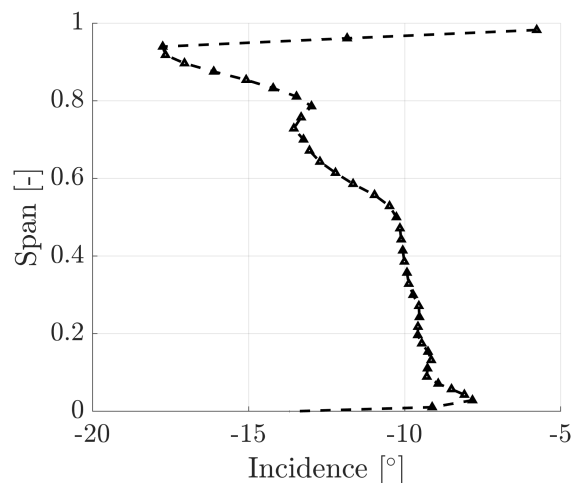
Figure 6.21.: Radial profile of flow incidence at the rotor inlet for off-design compared to design point conditions.

A span-wise comparison of basic turbine quantities such as flow coefficient Φ and stage loading Ψ for the two operating points is provided in Section 2.1.1 and Figure 2.2. As indicated in the profiles, both flow coefficient and stage loading were reduced for the off-design conditions. Stage loading was considerably lower for the off-design operating point with an average -33% reduction in loading being nearly constant over the span. The average reduction in flow coefficient was found to be approximately -25%. The stage—and hence the blade—loading is one of the dominant factors determining the strength of secondary flow structures formed in the blade passage as outlined in the introduction.

Heat Transfer Coefficient

The endwall-resolved Nusselt number distribution for both operating points is depicted in Figure 6.22. A qualitative comparison revealed that the main features of the heat transfer coefficient distributions are similar for both cases. The highest heat transfer coefficients were observed at the impingement location at the upstream endwall hill face. For the off-design point, no signature of the horse shoe vortex around the pressure side leading edge was observed in the data set. It is speculated that the reduced inlet Reynolds number leads to weaker and smaller vortex formation around the leading edge, which is not captured by the measurement setup. Besides the peak values found at the location of main flow impingement, the heat
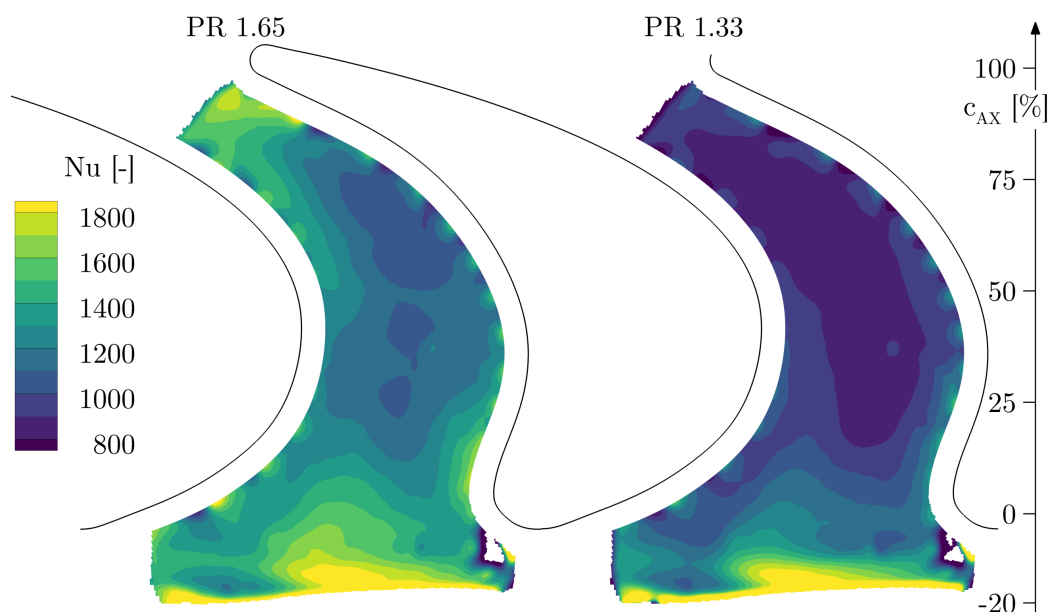
Figure 6.22.: Local Nusselt number distribution for design point (a) and off-design (b) pressure ratio and 0.8 % purge flow injection.

transfer levels were generally found to be lower in absolute terms for off-design operation.

This is illustrated in Figure 6.23(a), which depicts the laterally averaged Nusselt number. From the platform start until $-10\,\%$ of the axial chord, similar Nusselt number values were measured for both pressure ratios. From $-5\,\%$ to $75\,\%$ c_{ax} (the main part of the platform), a nearly constant absolute offset in Nusselt number of 270 ± 35 was observed. These differences increased in the throat region since no increase in laterally averaged heat transfer coefficient was measured for the lower pressure ratio.

The platform heat transfer coefficient was mainly expected to change based on the reduced Reynolds number for the off-design operating point. Figure 6.23(b) depicts the Stanton number ratio of both operating points according to Equation 6.3. An average value of 0.79 was observed on the platform between $0\,\%$ to $75\,\%$ of axial chord. This result is congruent with the correlation observed by Holman [74] for the estimation of Stanton number via Reynold's analogy using skin friction (Equation 6.2).

$$St_x = 0.332Re_x^{-1/2}Pr^{-2/3} \qquad Re_x < 5x10^5 \qquad (6.2)$$

The predicted Stanton number ratio derived from this correlation using the
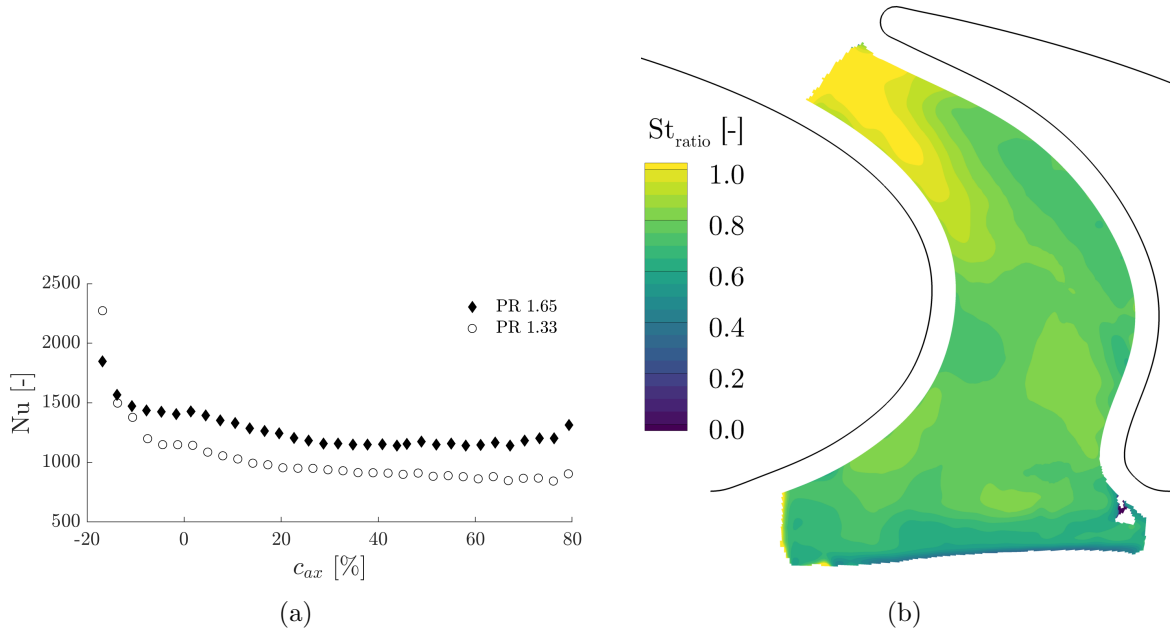
Figure 6.23.: Laterally averaged Nusselt number distributions for both turbine pressure ratios (a). Stanton number ratio between the two pressure ratios (b).

inlet relative Reynolds numbers is approximately 0.78 (Equation 6.3).

$$St_{ratio} = \frac{St_{1.65}}{St_{1.33}} \approx \left(\frac{Re_{1.65}}{Re_{1.33}}\right)^{-1/2} = 0.7836 \tag{6.3}$$

Cooling Effectiveness

The local cooling effectiveness of the purge flow was evaluated for both pressure ratios (Figure 6.24). Notably, for the reduced mass flow operating point, higher endwall cooling effectiveness for the same fractional mass flow injection was generally observed. The systematic offset between the two operating points is found to be 0.3 ± 0.04 extracted from line A in Figure 6.24. It is speculated that this offset and the increased cooling effectiveness at part load condition is attributed to the measurement uncertainty at this point. The small temperature difference measured over the platform and the different thermal situation in the cavity affecting the reference temperature may be the key driver for this. The trend of higher cooling effectiveness emerging from the cavity along the blade suction side was similar for both operating points. The profile depicted in Figure 6.25 illustrates the absolute differences in endwall cooling effectiveness relative to the last measurement point in axial direction for both operating points along the peak of cooling
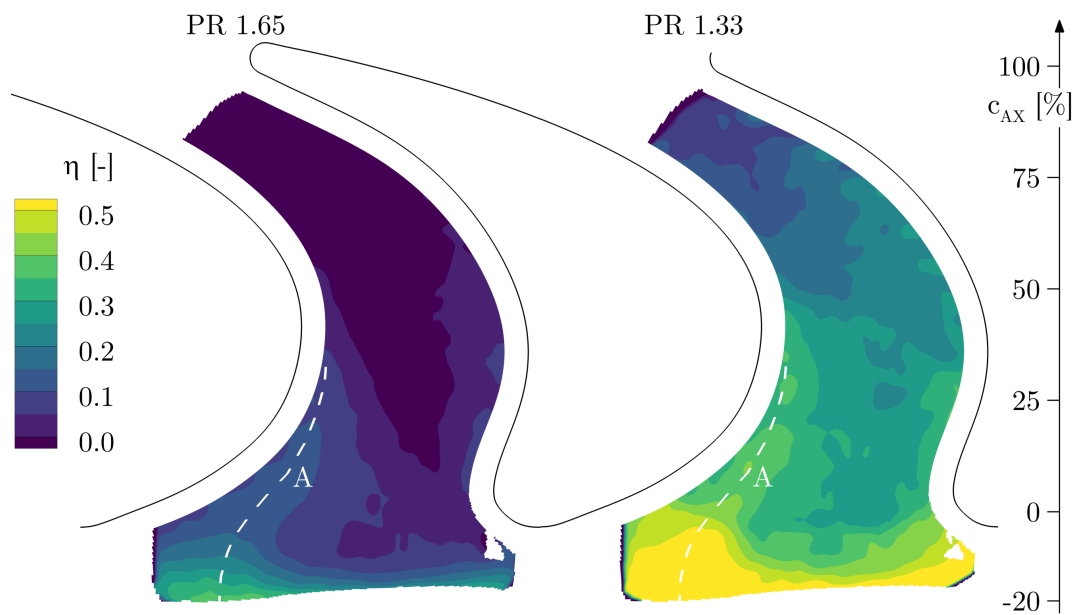
Figure 6.24.: Local cooling effectiveness for the design point (PR 1.65) and off-design (PR 1.33) pressure ratio and 0.8 % purge flow injection.

effectiveness (line A) illustrated in Figure 6.24. This illustration without the systematic offset depicts the similarity of the cooling pattern between the two operating points. At the off-design point, up to 50 % increased cooling effectiveness was measured upstream of the rotor leading edge at 0 % c_{ax} below the nominal hub radius. Further downstream the levels and rate of decreases are comparable.
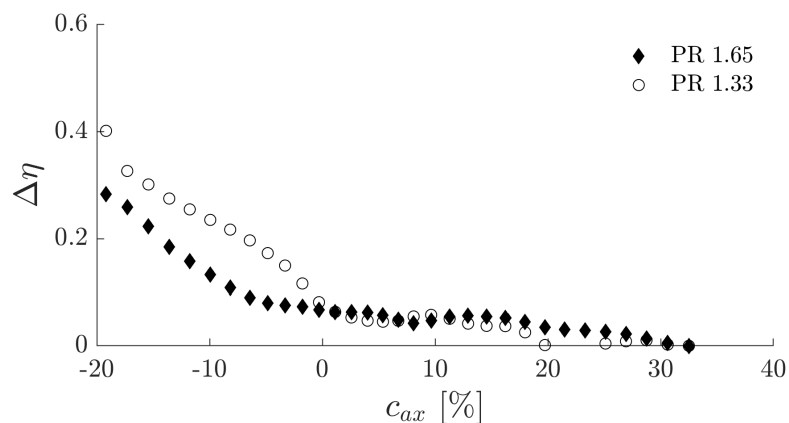
Figure 6.25.: Absolute decrease in cooling effectiveness along line A indicated in Figure 6.24.

This comparison of the two presented operating points with different turbine pressure ratios and rotor inlet Reynolds numbers highlighted the impact of off-design turbine operation on rotor endwall heat transfer characteristics.

The qualitative patterns of the local heat transfer coefficient and cooling effectiveness with injected purge flow remain similar. Both were dominated by the specific hub platform geometry with cavity extended endwall contouring, which led to a characteristic zone of enhanced heat transfer at the upstream face of the endwall hill and promoted jet-like purge flow entrainment on the platform over the endwall trough along the blade suction side. Except for the discussed feature at the endwall hill, the absolute levels of Nusselt number on the endwall were higher for higher Reynolds numbers. The local Stanton number ratio between the two operating points was nearly constant over a wide range on the endwall. The derived ratio accurately matched with estimations based on skin friction and Reynold's analogy. A systematic offset in cooling effectiveness was measured with higher values for the low Reynolds number case and attributed to limitations of the measurement setup with small temperature difference over the platform. However, very similar patterns of cooling flow distribution on the platform for both operating points were found, indicating the relevance of the specific endwall contouring on the purge flow ejection location.

6.3.2. Purge Flow Sensitivity of Endwall Heat Transfer at Turbine Off-Design Pressure Ratio

This section describes the results of a purge flow sensitivity study of the endwall heat transfer coefficient and cooling effectiveness at the turbine off-design pressure ratio of 1.33. Similar to previous investigations, three purge flow injection rates (0.0 %, 0.8 % and 1.2 %) were experimentally measured in the research facility.

Heat Transfer Coefficient

Laterally averaged profiles of Nusselt number for the different purge injection rates are depicted in Figure 6.26. Similar to the design pressure ratio, a strong decrease in heat transfer after the start of the platform was visible for all injection rates. However, at this operating point the laterally averaged heat transfer coefficient consistently increased for higher injection rates. From $-20\,\%$ to $-5\,\%$ axial chord the values for $0.8\,\%$ were very similar to the $1.2\,\%$ injection case and further downstream from $40\,\%$ to $80\,\%$ c_{ax} similar to $0.0\,\%$ purge injection. However, the differences are small in a laterally averaged assessment between all of the three investigated injection rates.
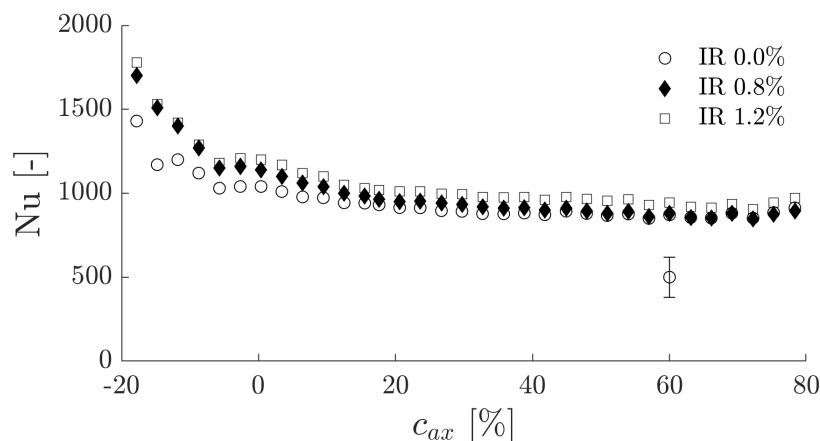
Figure 6.26.: Laterally averaged hub endwall Nusselt numbers for all measured purge flow injection rates (0.0 %, 0.8 % and 1.2 %) at off-design pressure ratio of 1.33.

The distributions of local Nusselt number change (Equation 4.7) for 0.0 % and 1.2 % of purge flow injection compared to 0.8 % are presented in Figure 6.27. Local variations exceeding values of ±20 % when comparing the two cases with the baseline were observed. Since these changes were very localised and restricted in space, the laterally averaged analysis did not provide a sufficient understanding of the sensitivity.

The case with zero active purge flow injection revealed a streak with reduced heat transfer levels from the platform beginning until 40 % of the axial chord. The location was in-between the blade suction side and the endwall hill, similar to the streak of increased heat transfer coefficient observed for the 1.2 % injection case at the design point pressure ratio. Furthermore, identical to the observation with a pressure ratio of 1.65, a slight increase in the pressure side horse-shoe vortex and a subsequent signature in increased heat transfer was observed. However, this change was well within the measurement uncertainty.

With an increase purge injection of 1.2 %, a distinct trace—however slightly shifted towards the blade suction side compared to the 0.0 % case—but of enhanced Nusselt number (>20 %) was observed. Compared to the design pressure ratio case, this signature extends axially up to approximately 40 % of the axial chord.

These local changes in Nusselt number significantly above the measurement uncertainty were not observed in the laterally averaged comparison and highlight again the need for and benefit of high-resolution heat transfer measurements to expand the knowledge and understanding of endwall heat transfer.
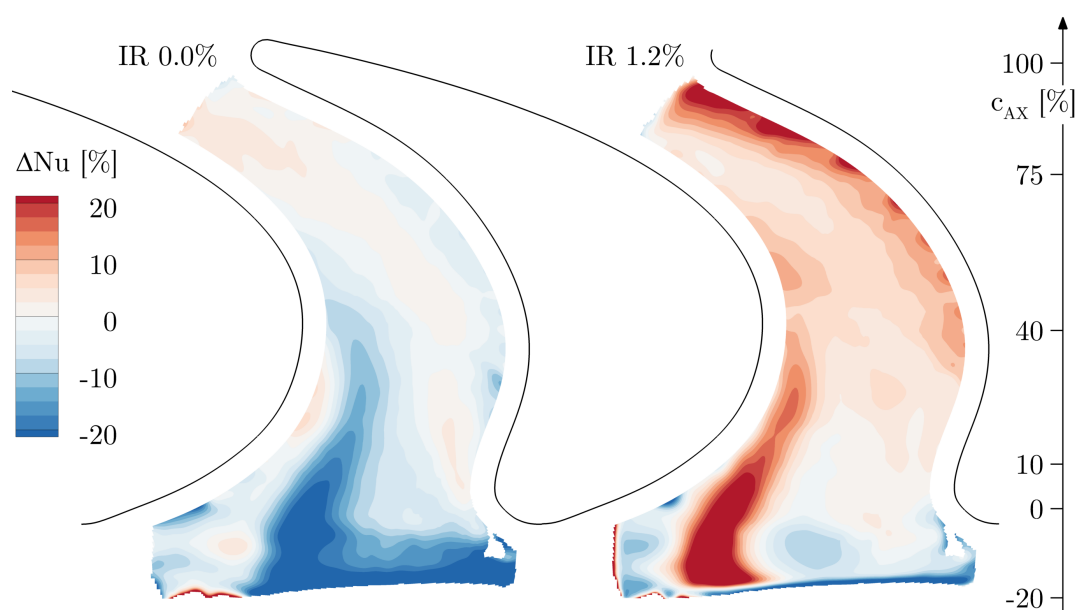
Figure 6.27.: Relative Nusselt number difference compared to the reference purge flow rate (IR 0.8 %) for low (IR 0.0 %) and high (IR 1.2 %) purge flow injection.

Cooling Effectiveness

For part-load conditions and 0.8 % purge flow injection, a similar dependence of adiabatic effectiveness as for the design point pressure ratio was observed. The distribution depicted in Figure 6.28 shows high cooling effectiveness at the platform start and extending from the endwall trough into the passage towards the suction side. However, the axial extension was lower and only up to approximately 20 % of the axial chord. Notably, the absolute levels were slightly higher for the off-design compared to the design point.

For the high injection case of 1.2 %, the location of high cooling effectiveness—and thus purge jet location—was less visible. The region of maximum η shifted towards the leading edge, which could have been caused by the higher momentum of the purge jet and thus the lower deflection and deeper penetration into the main flow.
The enhanced mixing of purge and main flow above the platform could also explain the higher effectiveness for 1.2 % purge from 20 % to 75 % of the axial chord. The potential main flow temperature decrease in vicinity of the endwall due to the stronger mixing with the purge flow may have caused this axially extended cooling effect measured for 1.2 % purge flow injection.

The comparison of endwall cooling effectiveness from 0.8 % and 1.2 % purge
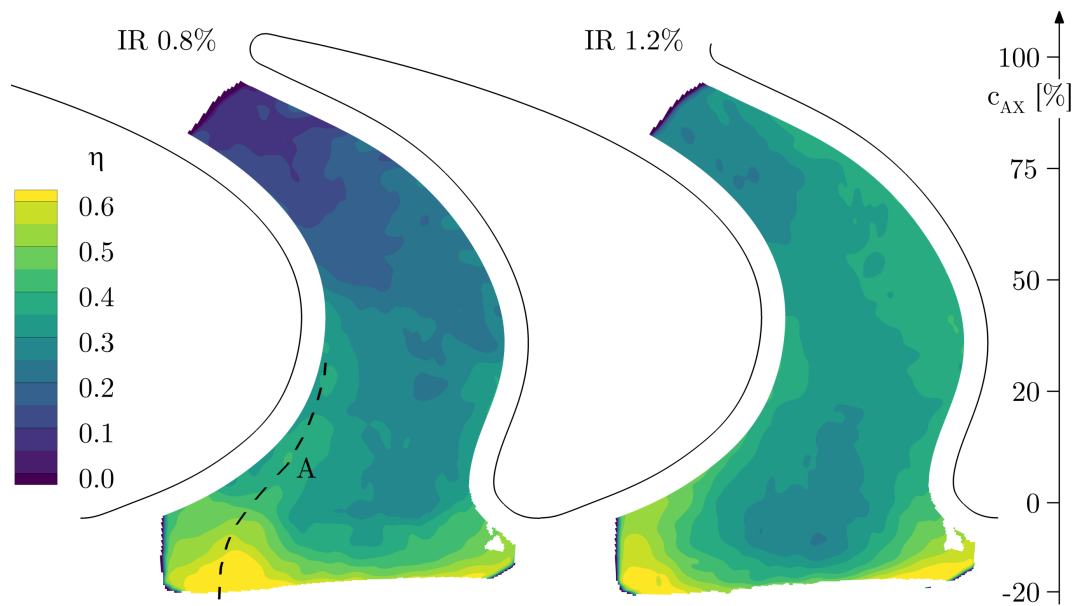
Figure 6.28.: Purge flow cooling effectiveness η for the part load condition with $0.8\,\%$ injection and $1.2\,\%$ injection.

flow injection is presented as absolute difference in Figure 6.29. Notably, the differences in cooling effectiveness between the two injection rates were clearly visible. In a triangular region around the endwall contouring trough a higher cooling effectiveness was measured for the $0.8\,\%$ purge flow injection. Contrary, the high purge injection rate of $1.2\,\%$ beneficially cooled the endwall region downstream of $50\,\%$ of the axial chord length.
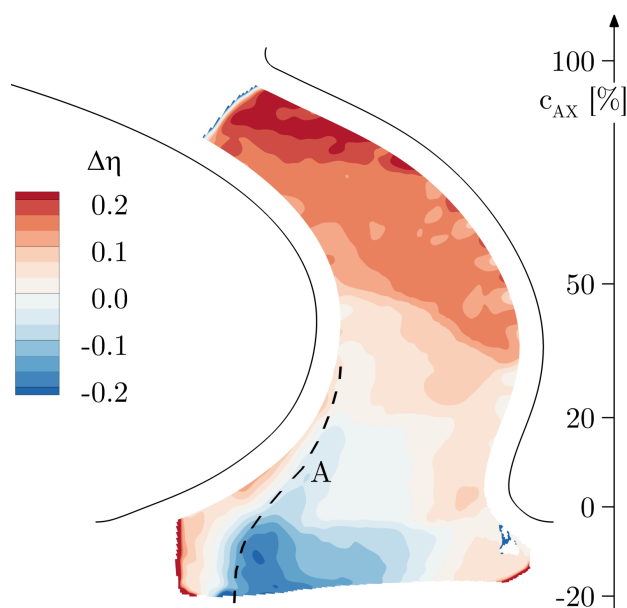
Figure 6.29.: Absolute difference in cooling effectiveness for part-load between $1.2\,\%$ and $0.8\,\%$ purge flow injection.

6.4. Discussion on Rotor Hub Endwall Heat Transfer

The progress in turbine cooling and thus the operation of turbine components in the hot gas path exceeding their normal material temperature limits has put the thermal issues of the components in the spot light of development. The fundamental aim in the design is to achieve the highest possible thermal efficiency while maintaining acceptable component life time. The thermomechanical and cooling design of the components has to be such that acceptable thermal loads and stresses are achieved.

For a safe operation of the components the cooling has to be adequate throughout the operational envelope of the engine. The design of the cooling system, however, can only be optimised for a specific turbine operating point. Therefore, during transient or off-design operation the cooling is overdesigned or temperature hot spots may occur leading to increased thermal stresses or corrosion. Accurate predictions of heat transfer and cooling are needed to reduce the cooling requirements and improve the turbine efficiency and component life time. This is achieved by reduced uncertainty in numerical predictions and better understanding of the interaction of cooling flow and main flow interactions.

The investigated rotor endwall design with upstream contouring extending into the cavity revealed important takeaways for designers. The upstream contouring led to a controlled purge flow injection onto the platform and the main flow. The jet-like characteristic of the purge is maintained over a wide range of injection rates and could be used to modify the secondary flow formation such as the suction side horse-shoe vortex. On the other hand, the high velocity main flow impingement on the endwall hill leads to a spot like region with particularly high heat transfer on the platform, which has to be cooled adequately.

Furthermore, the results clearly showed the need for (a) including secondary flows during the design phase and (b) great care to be taken on the modelling of hot gas mixing from cooling flows. It was found that CFD predictions tend to overestimate the cooling effect of the purge flow on the hub endwall.

7. Heat Transfer of Highly Loaded Turbine Blade Tip Geometries

Economic and environmental pressure placed on gas turbine manufacturers and operators drive continuous investigations aimed at reducing and optimising the cost and efficiency of turbines. Reducing the blade count of rotors (and stators) not only reduces manufacturing costs of engines but subsequently reduces maintenance costs for the operator or owner. The weight reduction due to fewer blades may be partially counterbalanced by increased individual blade weights. However, the reduced flow-exposed surfaces can reduce the cooling air requirement and thus improve thermal efficiency. To maintain the power output, the reduced blade count results in increased blade loading. This generally strengthens secondary flow structures in the passages and is therefore associated with aerodynamic losses. Thus, due to the high thermal load and difficulties related to cooling, the rotor blade tip region is of special interest for improvements.

Very little high-resolution data regarding the aerodynamics and heat transfer of highly loaded turbine blade tips based on measurements from rotating facilities are available in the open literature. The instrumentation developed within this work for infrared-based heat transfer measurements on rotor blade tips and the fast-response aerodynamic probes enabled combined aerothermal measurements and provided a unique data set on local heat transfer for different blade tip designs.

7.1. Aerodynamics and Heat Transfer Characteristics of Highly Loaded Turbine Blade Tip Geometries

This section introduces the effect of the different rotor blade tip geometries on the aerodynamic flow field at the rotor exit and the local distribution of the heat transfer coefficient. The designers face a trade-off between aerodynamic and thermal load optimisation. The aerodynamic comparison

between the investigated rotor blade tip designs is based on the design pressure turbine operating point without active tip coolant ejection. This facilitates a fair comparison, since the notch tip geometry featured no cooling holes (see Section 2.2.5).

7.1.1. Aerodynamic Influence of Tip Geometry Variations

This section presents a brief overview of the aerodynamic flow field and integral turbine efficiency for the investigated rotor blade tip geometries. Fast-response aerodynamic probe technology allowed to measure the flow field behind a rainbow rotor with multiple different geometries and individual flow field analysis behind specific rotor blades. In the data post-processing, the flow field behind the central blade of each group with the same geometry was extracted and used for the analysis. For the flow field evaluation, data were acquired using the fast-response aerodynamic probe (FRAP). For efficiency, the fast-response entropy probe (FENT) was used.

The integral (time- and mass-averaged) 1-stage and 1.5-stage efficiencies for the different geometries were evaluated against the baseline squealer design and are presented in Figure 7.1. The three investigated tip geometries were found to show positive improvements for both the 1- and 1.5-stage integral efficiency. The analysis presented in [157] showed that the sensitivity of integral efficiency decreased due to a mass flow redistribution. A span-wise local efficiency deterioration of approximately 5.7 % was observed for the notch tip between 80 % and 100 % blade span. However, due to the mass flow redistribution away from this loss-affected region, the integral mass-averaged efficiency was found to be positive. The one-stage efficiency improvements were 0.11 p.p. for the optimised squealer, 0.06 p.p. for the trench and 0.03 p.p. for the notch. Since the tip secondary flow structures propagate downstream through the second stator, the 1.5-stage efficiency was also investigated. The optimised squealer geometry showed the largest efficiency improvement with and increase of 0.30 p.p. over 0.21 p.p. for the trench and 0.14 p.p. for the notch tip.

A more detailed view on the effect of the different blade tip geometries on the flow field and potential losses is provided in Figure 7.2. This figure depicts the time-averaged non-dimensional total pressure distribution at the rotor exit of the central blade for each tip geometry in the rotor's frame of reference. The data is plotted for the top 40 % of the blade span,
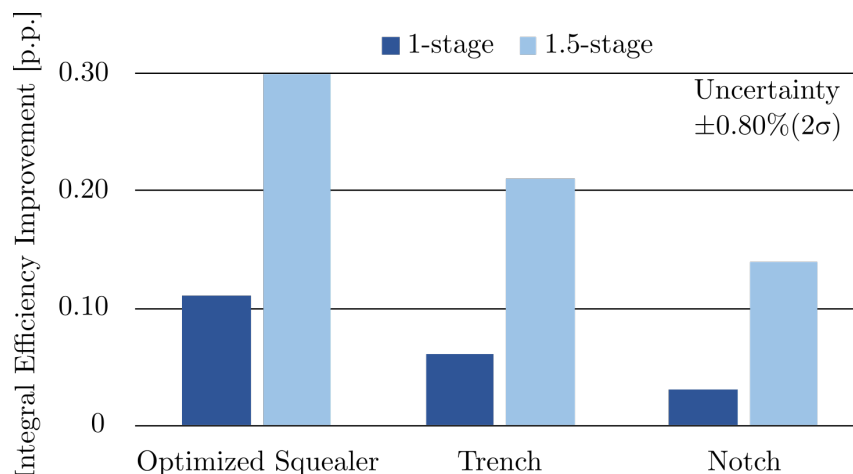
Figure 7.1.: Mass- and time-averaged temperature-based integral 1-stage and 1.5-stage efficiency improvements over the baseline squealer in percentage points (p.p.).

where relevant differences in the flow field were observed. For the optimised squealer, a slight increase in total pressure between 60% to 80% span at 0.5 rotor pitch was observed when compared to the baseline squealer. The total pressure deficit in this location is attributed to the trailing edge shed vortex and tip passage vortex. In the flow field above 80% span, which is dominated by the tip leakage vortex, only a minor increase in total pressure was observed. Changes in the relative total pressure for the trench tip compared to the baseline squealer were relatively small, consistent with the previously observed low integral efficiency change. However, despite the same integral efficiency improvement for the notch tip, the local flow field revealed distinct changes in the total pressure distribution at the rotor exit. The low-pressure region related to the tip leakage vortex was significantly enlarged (top 20% span), whereas the total pressure in the region of the passage and trailing edge shed vortex improved over 2%.

This analysis of the aerodynamic flow field revealed that the local flow field changes for the optimised squealer and trench tip designs were moderate downstream of the rotor when compared to the reference baseline squealer. The highest sensitivity in the flow structures was observed for the notch geometry. All geometries showed an improvement in integral efficiency, which was intended in their design. The increased impact in 1.5-stage efficiency over 1-stage efficiency indicates that the interaction between rotor secondary flows and downstream stators is important for exploiting the improvements of rotor tip geometries.
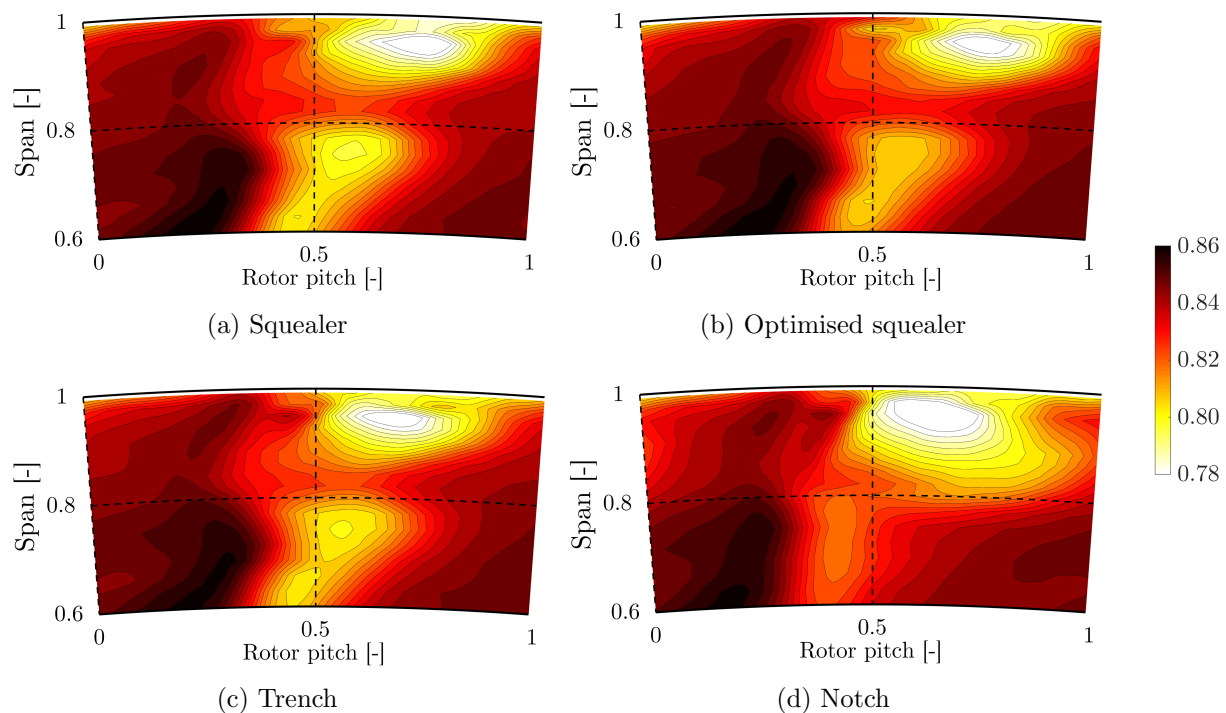
Figure 7.2.: Rotor downstream dimensionless relative total pressure for all tip geometries without active tip coolant ejection.

7.1.2. Characteristic Heat Transfer Coefficient Distribution

In this section, the distribution of local heat transfer coefficients for all investigated blade tip geometries is presented and discussed. The direct comparison between the different geometries, except for the two squealer type tips, is difficult due to their very different designs. However, a detailed overview of the measured Nusselt number distribution for each design may serve for designers as a reference data set for future tip geometries. Notably, the comparisons were performed without active tip coolant ejection. Hence, the tip coolant supply in the rotor upstream cavity was sealed. As a result, the uncooled notch geometry could also be included in the analysis.

The local distributions of the Nusselt number for the design point pressure ratio are depicted in Figure 7.3 for all geometries using the same scaling. Due to the different heating track designs required for each geometry, the available data range differs among the tips. Notably, the discussion focuses only on the depicted areas with available data. The squealer type geometries were generally found to have lower peak heat transfer coefficients in the recess cavity compared to the trench and notch designs.

The optimised squealer showed a region of enhanced heat transfer in the basin close to the pressure side squealer rim. While a similar pattern was observed for the baseline squealer geometry, it is shifted more towards the blade camber line. It is speculated that this region with increased heat transfer coefficient is associated with the reattachment of the leakage flow entering the squealer cavity over the pressure side fence. Observed peak levels of Nusselt number were approximately 1800, with slightly higher values for the baseline geometry. The shift of flow reattachment towards the pressure side for the optimised squealer is explained by the inclined fence. The winglet-like fence geometry shifts the flow detachment towards the pressure side, resulting in a shifted flow reattachment inside the cavity. Bot notch and trench geometries showed increased heat transfer coefficients along the pressure side edge of the tip. Notably, this is attributed to flow reattachment after entering the tip gap. Peak Nusselt numbers in the experimentally covered regions were well above 2200. These increased values are explained by the smaller effective tip gap present for these two geometries compared to the recess in the squealer basin. A gradual decrease in heat transfer coefficient towards the suction side was observed for the notch tip. On the trench tip, a more pronounced plateau of reduced heat transfer was observed on the suction side of the tip.

7.1.2.1. Sensitivity to Turbine Pressure Ratio

The same geometries were investigated for the off-design turbine operating point with a reduced pressure ratio of 1.33 instead of 1.65. As discussed in Section 6.3.1, the flow enters the rotor with negative incidence (approximately $-17°$ at 90% span) due to the constant rotational speed. For aircraft engines—and more recently also stationary power applications—part-load performance is of major interest. Thus, adequate designs for reliable operation regarding heat transfer at such operating points is crucial.

The sensitivity of the local heat transfer coefficient to the operating point is depicted in Figure 7.4, illustrating the patterns of relative change in Nusselt number compared to the design point. For the optimised squealer, both a decrease and an increase in local heat transfer coefficient were measured for the off-design point. Downstream of the large dust hole towards the suction side, local increases in heat transfer of up to 45% were observed. Towards the pressure side squealer fence—where increased levels of heat transfer due to the flow reattachment were present at the the design point—heat transfer was reduced by approximately 35%. A similar pattern was identified for
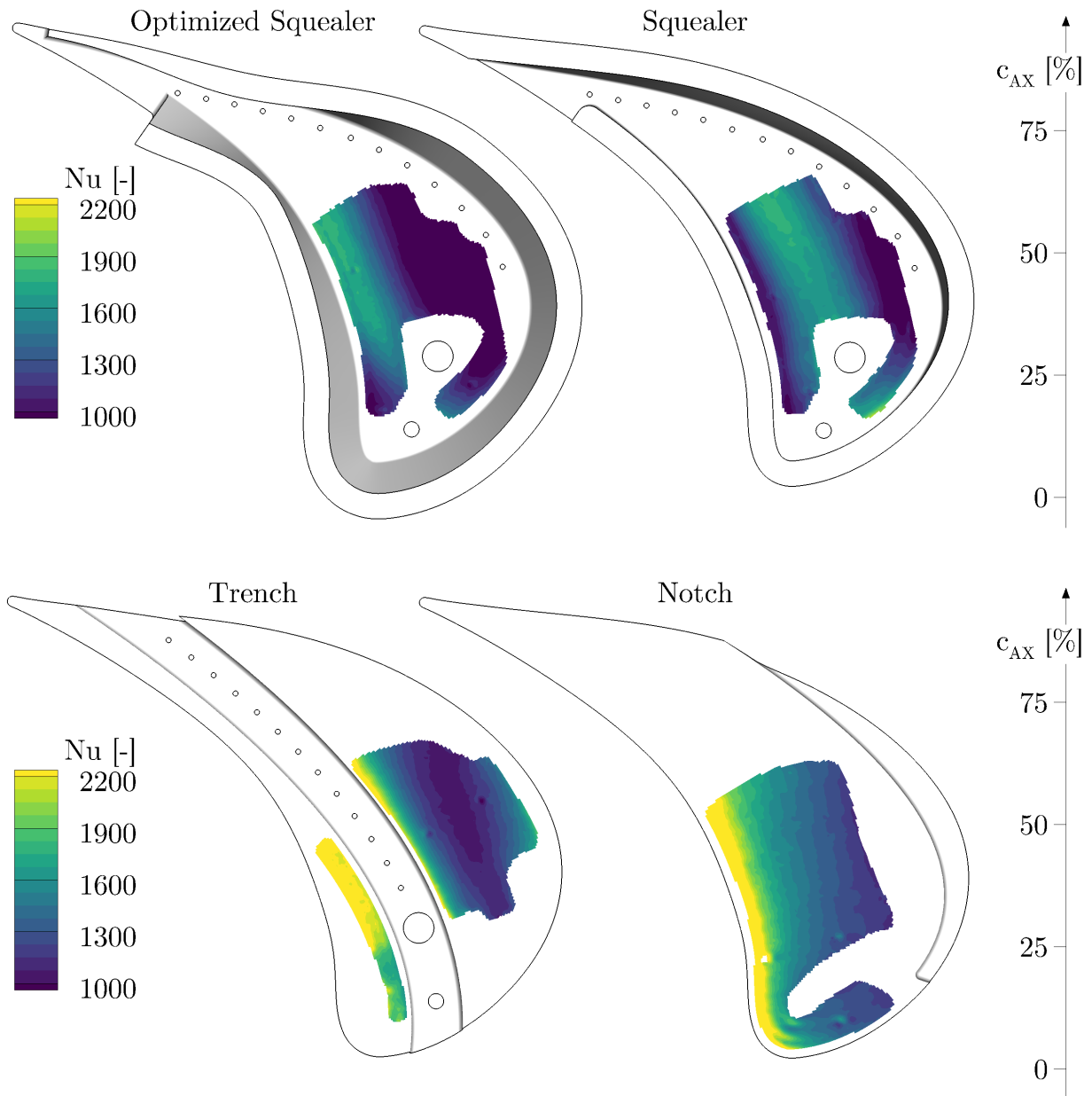
Figure 7.3.: Characteristic Nusselt number distribution at design pressure ratio without active cooling ejection for all investigated rotor blade tip geometries.

the baseline squealer design. However, both patterns with locally reduced and enhanced heat transfer were shifted towards the suction side. The heat transfer reduction was comparable to the optimised squealer, while the peak increase in the observed area was below 30 %.

In contrast, both the trench and notch tips essentially showed a nearly exclusive reduction in Nusselt number for the off-design operating point. The highest reductions of up to −45 % were located for both geometries close to the pressure side edge of the tip, thus indicating again the reduced strength of the leakage flow reattachment on the tip. Interestingly, the trench cut reduced the heat transfer sensitivity on the suction side of the trench tip when compared to the notch tip.

A more integral assessment of the sensitivity was performed based on the area-averaged heat transfer coefficient. A direct comparison between the different geometries—except for both squealer tips to some extent—was not possible due to the different tip areas covered for each geometry. The averaged heat transfer coefficients for both operating points and the sensitivity are depicted in Figure 7.5. As expected, for all investigated tip geometries, the averaged heat transfer coefficient was reduced for the off-design conditions. However, the relative amount of reduction varied considerably. The highest sensitivity was found for the notch tip, with an averaged reduction of nearly 40 %. For the baseline squealer and trench geometry, the decrease was very similar (−19.8 % and −19.2 %). With only −12.5 % reduction in averaged heat transfer coefficient, the optimised squealer had the lowest integral sensitivity.

For designers, a low sensitivity to turbine operating conditions may be preferable to reduce the cost of experimental and numerical investigations. However, great care must be taken when reducing the data complexity to evaluate this sensitivity. Despite having the lowest averaged sensitivity, the optimised squealer tip exhibited local increases in heat transfer coefficient of up to 45 %.
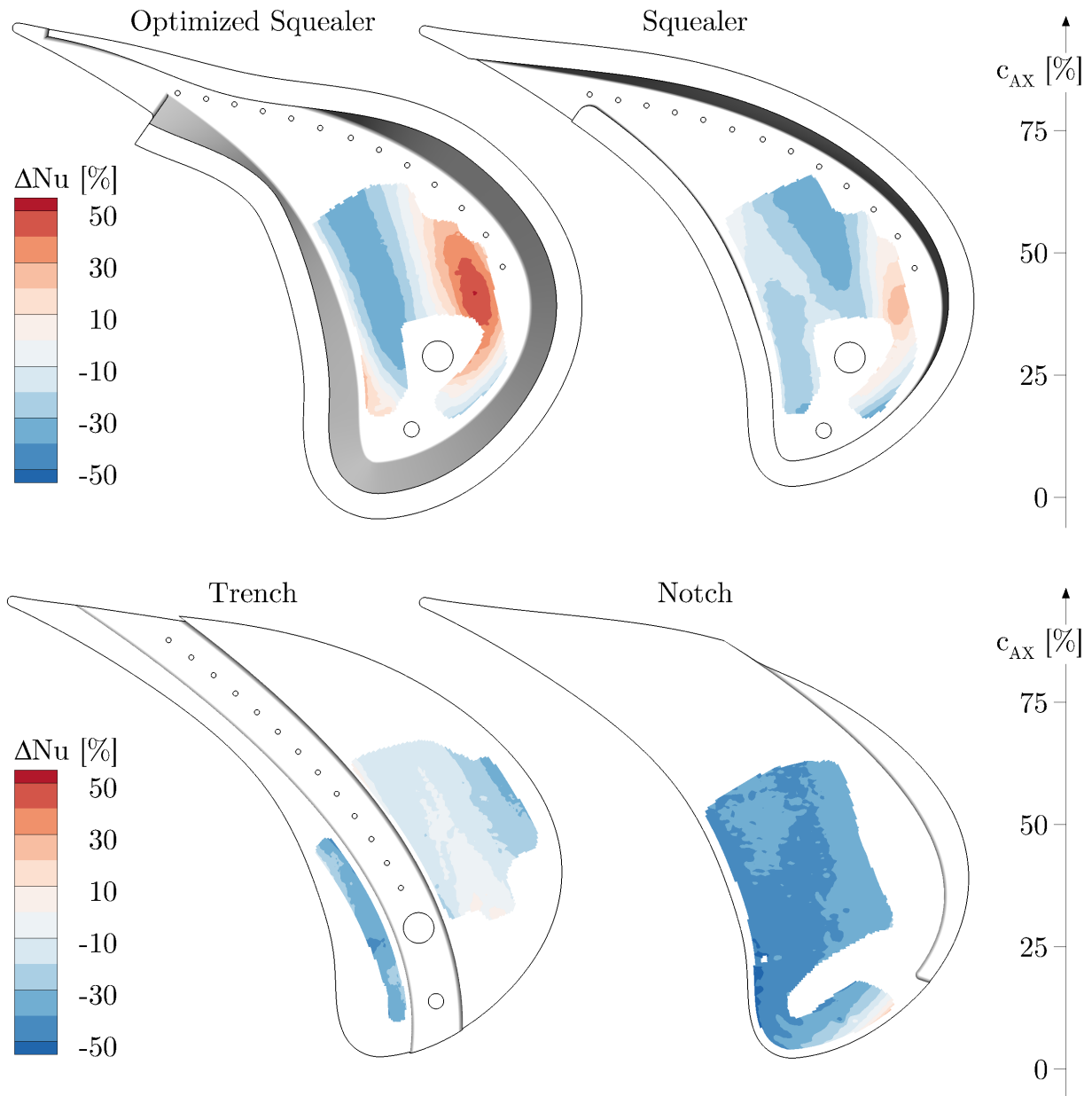
Figure 7.4.: Relative change in local Nusselt number for the off-design compared to the design turbine pressure ratio.
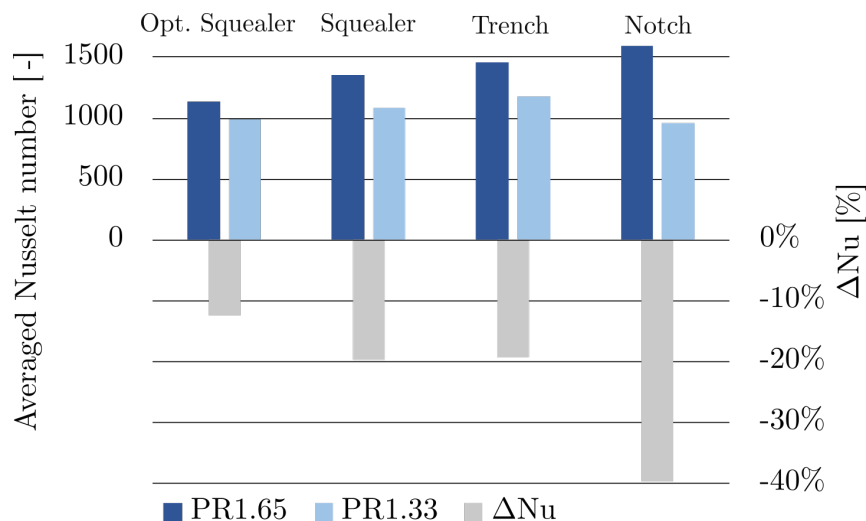
Figure 7.5.: Area-averaged Nusselt number for design point and off-design turbine pressure ratio and the relative change for all geometries.

7.2. Effect of Coolant Ejection on Blade Tip Heat Transfer

Based on the instrumentation introduced in Section 3.4.2 for the tip heat transfer measurements, active tip coolant supply was integrated into the bladed disk rotor. The tip coolant was supplied from the rotor upstream hub cavity and fed through a bore hole through the blade into a tip plenum, to which all cooling and dust holes were connected. In this section, the impact of active tip coolant ejection on the heat transfer coefficient and adiabatic wall temperature is discussed for each geometry in terms of cooling effectiveness.

7.2.1. Squealer Tip

The effect of active tip coolant ejection on the local heat transfer for the squealer tip geometry is depicted in Figure 7.6. The observed band of enhanced heat transfer attributed to the reattachment of the leakage flow in the tip cavity is shifted towards the squealer fence with active tip cooling ejection. The earlier flow attachment inside the basin is speculated to be driven by a blockage effect of the coolant ejected through the two dust holes. This change in local flow pattern led to a significant increase in local Nusselt number towards the pressure side fence (Figure 7.7). The increase in heat transfer coefficient measured was above 50 % in this region, with peak values of up to 80 %. This local increase is particularly critical, since for the
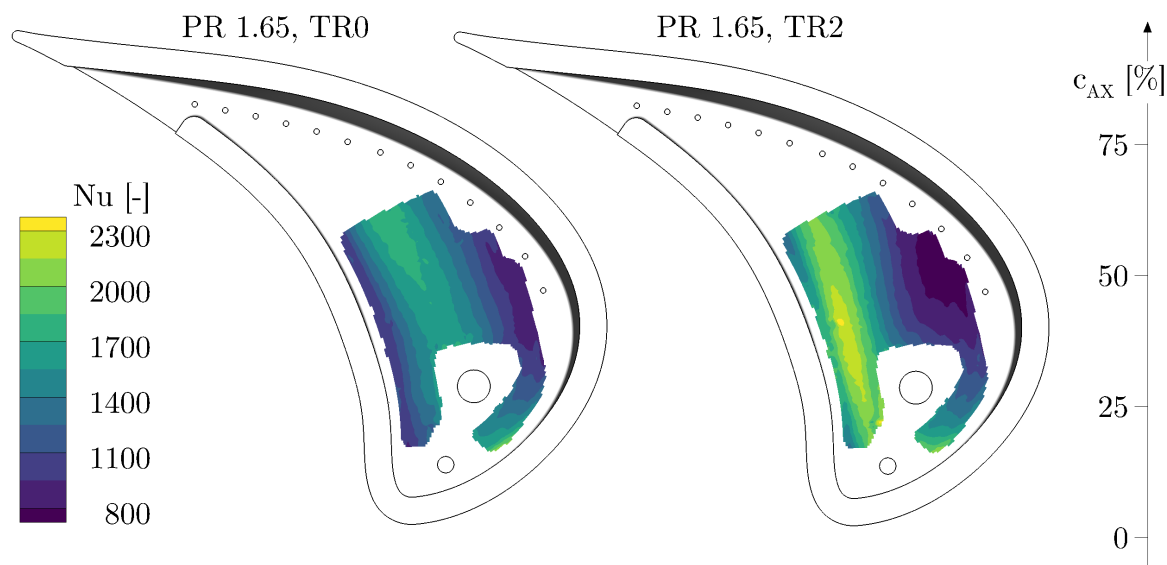
Figure 7.6.: Local Nusselt number distribution in the basin of the squealer blade tip geometry without (TR0) and with active tip coolant ejection (TR2).

design investigated no cooling holes are in the vicinity to reduce the heat load in this area. For the whole depicted tip surface, an average increase of 9.2 % was calculated for the heat transfer coefficient with active tip cooling. The cooling effectiveness depicted in Figure 7.6 was highest downstream of the large dust hole. This only weak signature of the tip coolant inside the squealer cavity is attributed to the complex flow structures and enhanced mixing created in the basin.

7.2.2. Optimised squealer

Similar to the baseline squealer geometry, a shift of the enhanced heat transfer region by flow reattachment towards the pressure side of the squealer fence was observed for the optimised squealer with active tip coolant ejection (Figure 7.8). However, the more distinct region where increased heat transfer was observed with tip coolant ejection was located towards the suction side squealer rim (Figure 7.9). Peak values were lower compared to the baseline squealer, however they were 45 % higher than the uncooled reference. It can only be speculated that this effect is driven by an interaction between the coolant jet from the dust hole with the tip leakage flow. Similar to the baseline squealer, the highest values of cooling effectiveness were observed in a downstream-extending stripe after the two dust holes.
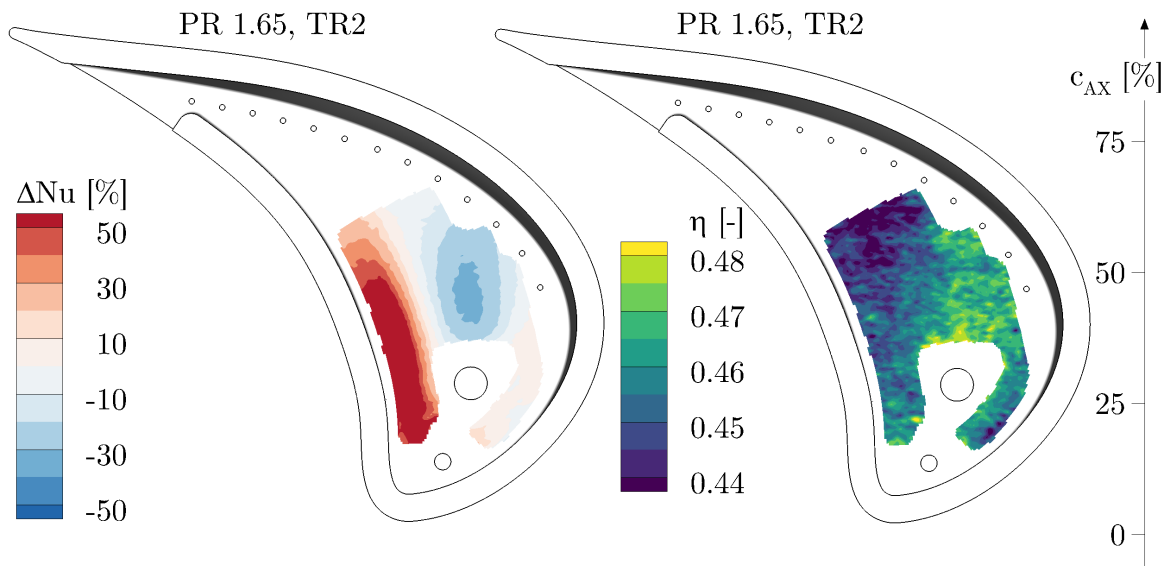
Figure 7.7.: Relative change in local Nusselt number for active tip coolant ejection compared to no cooling and tip cooling effectiveness for the baseline squealer.
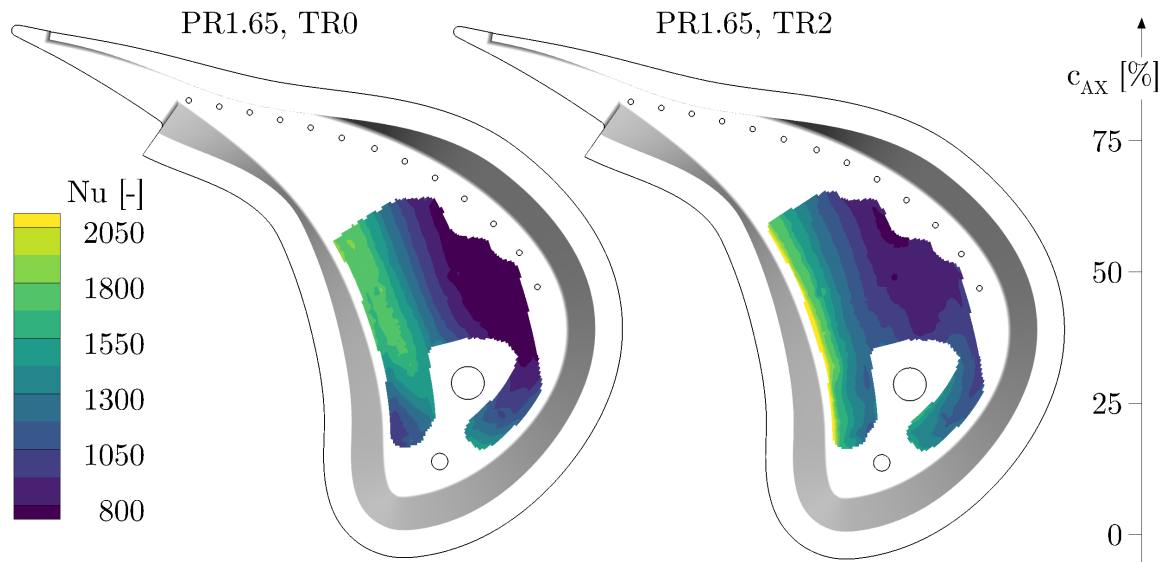
Figure 7.8.: Local distribution of Nusselt number in the basin of the optimised squealer blade tip geometry without (TR0) and with active tip coolant ejection (TR2).
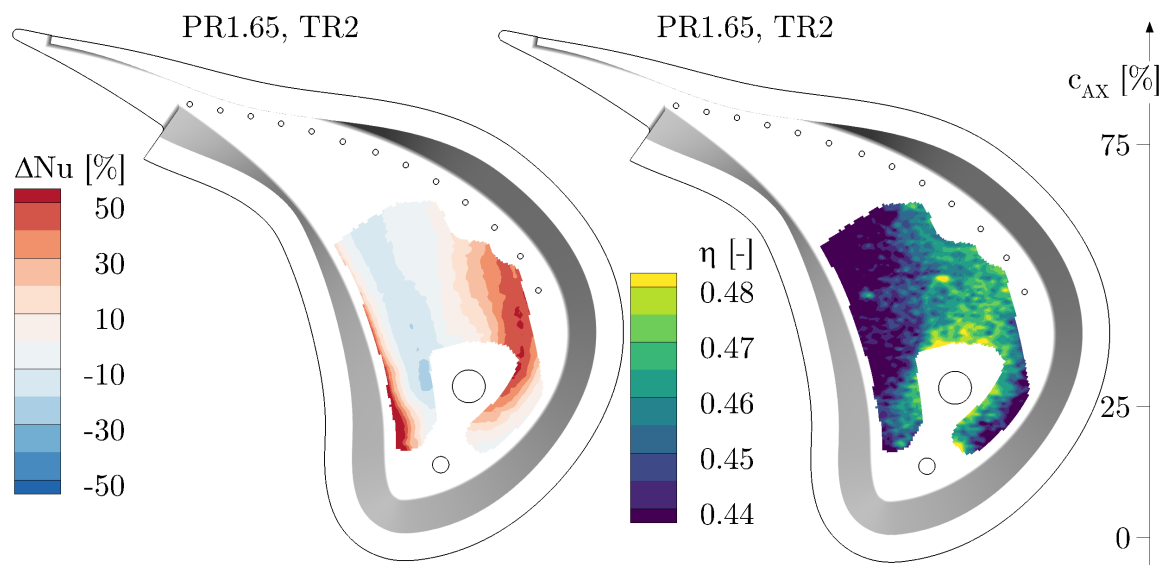
Figure 7.9.: Relative change in local Nusselt number for active tip coolant ejection compared to no cooling and tip cooling effectiveness for the optimised squealer.

7.2.3. Trench

The heat transfer pattern for the trench tip design was very similar for tip coolant ejection (TR2) and close tip coolant supply (TR0). As depicted in Figure 7.10, the characteristic pattern of increased heat transfer coefficient from the leakage flow attachment in the vicinity of the blade pressure side edge as well as after the trench slot was visible for both conditions. On the suction side flat part, slightly higher Nusselt numbers were observed with active tip coolant ejection.

This difference is more clearly visible in Figure 7.11, where the relative difference between the two operating points is plotted. A general increase of approximately 7 % to 10 % was observed in the vicinity of the trench slot on the suction side surface. A distinct trace with up to 20 % enhanced heat transfer coefficient was observed near the dust hole. It is suspected that this could be explained by the coolant jet of the dust hole. As depicted in Figure 7.11, the cooling efficiency for the trench tip design showed a distinct trace extending from the dust hole location downstream onto the suction side tip part. This indicates that a large portion of coolant is ejected through this relatively large dust hole and swept away from the trench slot onto the tip suction side. Therefore, this enhanced heat transfer may be explained by the reattachment and impingement of the cooling jet on the tip.
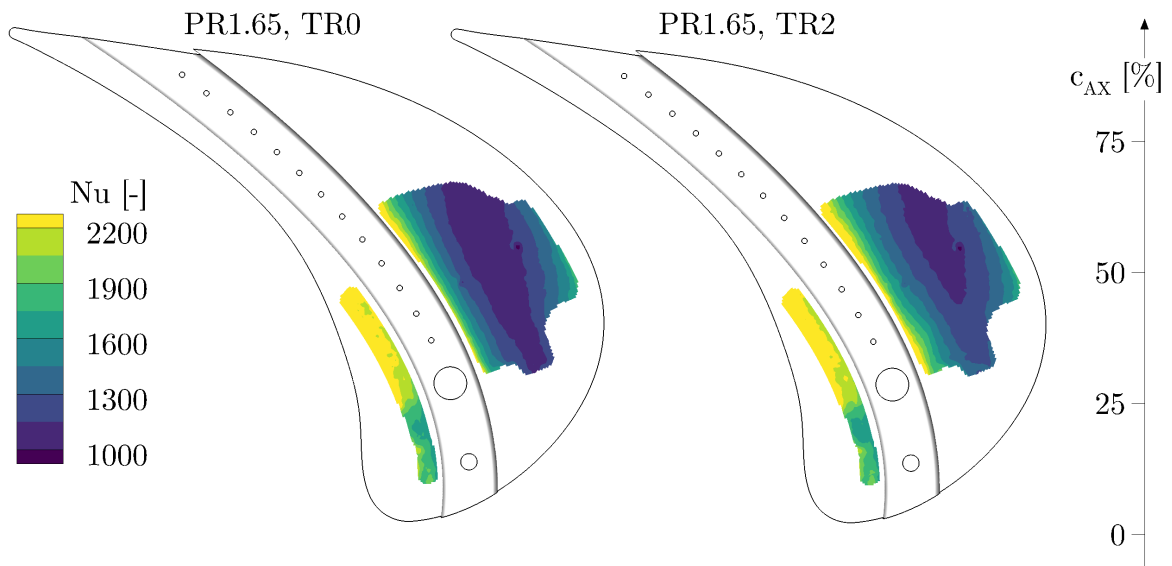
Figure 7.10.: Local distribution of Nusselt number in the basin of the trench blade tip geometry without (TR0) and with active tip coolant ejection (TR2).
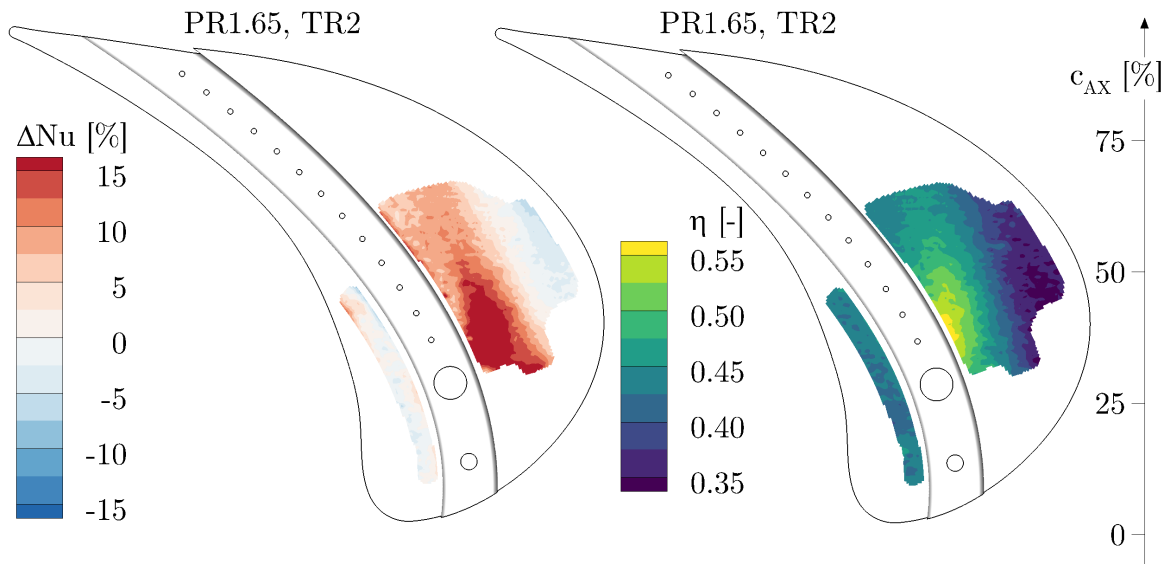
Figure 7.11.: Relative change in local Nusselt number for active tip coolant ejection compared to no cooling and tip cooling effectiveness for the trench tip geometry.

7.3. Discussion on Rotor Tip Heat Transfer

The rotor blade tip region is very difficult to cool and exhibits among the highest heat load in gas turbines. Furthermore, as the tip leakage losses contribute substantially to the overall losses in the turbine, geometrical deterioration from partial burn-off or corrosion heavily impacts the overall turbine performance or vibrations due to imbalances.

The rotor blade tip geometries investigated in this work were either derived from a squealer type tip (baseline and optimised squealer) or flat tip (trench and notch). For all geometries, the flow reattachment on the tip was identified as the region with highest local heat transfer coefficients. The lowest absolute heat transfer levels were measured for both squealer type geometries, which showed also a more uniform distribution over the tip. However, both squealer tip geometries were identified to be more sensitive to variations in the turbine operating point. Even for a 30 % reduced turbine loading, local increases in heat transfer coefficient up to 50 % were measured for the optimised squealer tip. For the trench and also notch tip, a reduction in local and also averaged heat transfer coefficient was measured with reduced loading. Notably, the trench cut was found to desensitise the suction side part of the blade tip to the turbine operating condition.

The effect of tip coolant ejection on the trench tip design was in peak magnitude higher compared to the squealer tip geometries. However, it was spatially more confined, especially around the coolant jet from the dust holes. It was anticipated that the more complex flow recirculation in the squealer cavity led to enhanced mixing of coolant and leakage flow and therefore led to a more distributed cooling effect for this type of geometry. The squealer rim fence was not included in the measurement setup for this work. More detailed investigations regarding the heat load of this particular part of squealer tip geometries has to be performed since cooling is difficult and the fence prone to thermal degradation. This again would change the thermal loads and aerodynamic performance compared to the design case.

8. Summary and Conclusions

This work presents experimental heat transfer measurements with numerical investigations of novel high-pressure turbine geometries under cooling flows. When combined with advanced manufacturing techniques, numerical optimisation tools extend the possible design space for modern turbine geometries. In gas turbines, increasing turbine inlet temperature remains the main driver for efficiency improvements. Adequate cooling, especially in the high-pressure section, is not only essential for safe operation but also required to extend the life-time of parts. The efficient use of cooling air and its interaction with the main turbine flow field requires a profound understanding of the aerothermal effects.

Within the work of this thesis, an infrared-based measurement setup for heat transfer measurements on complex geometries in rotating facilities has been improved and successfully applied in an axial turbine research facility. High-resolution heat transfer measurements were performed on the rotor hub endwall with cavity extended endwall contouring, and were combined with high-resolution aerodynamic probe measurements. The acquired data were used to validate steady-state and unsteady numerical simulations for endwall heat transfer predictions and to asses their capabilities. The influence of varying purge flow injection on the heat transfer coefficient and endwall cooling effectiveness was studied in detail. The modular measurement setup was successfully used to perform cost- and time-efficient measurements using various blade tip designs on a single rainbow rotor setup. A unique data set of heat transfer measurements for novel rotor blade tip geometries with and without tip coolant ejection has been acquired.

8.1. Conclusions

The following conclusions were drawn from the aerodynamic probe and heat transfer measurements of a highly loaded high-pressure representative turbine under different purge and tip cooling flow conditions complemented by computational fluid dynamics simulations:

(1) **Modular Instrumentation and Measurement Setup for Infrared based Heat Transfer Measurements on Rotating Components.**

   – A direct chemical nickel thin-film coating was demonstrated to be a reliable and versatile technique for manufacturing custom-made surface heaters.

   – High-resolution heat transfer measurements on complex surfaces (e.g. highly contoured endwalls or rotor blade tip geometries) are possible with averaged uncertainties below 14 % and repeatability error below 8 % for the heat transfer coefficient.

   – Conductive heat flux losses into the instrumentation insert are the main driver of heat transfer coefficient uncertainty in the steady-state measurement setup accounting for up to 65 %.

(2) **Rotor Endwall Heat Transfer with Extended Endwall Contouring into the Disk Cavity.**

   – Highly optimised rotor endwall geometries extending into the disk cavity can introduce regions of enhanced heat transfer on the rotor platform that were described in the open literature for flat or conventional non-axisymmetric endwall contouring in the blade passage.

   – Rotor blade upstream and cavity extended endwall contouring can introduce regions of increased heat transfer due to high momentum flow impingement.

   – The modulated interaction between main flow and disk cavity purge flow promotes local and jet-like purge flow ejection from the cavity. This leads to a limited cooling effect of the purge on the endwall but also emphasises the need for including secondary flows and cavities during the design process.

   – The effect of purge flow variations on endwall heat transfer must be locally analysed since the interpretation with reduced complexity (e.g. laterally averaged profiles) may underestimate the local effects.

   – The extent of cooling on the hub endwall from purge flow injection was identified to be limited to the front portion of the platform. The cross-passage migration of the pressure side horse-shoe vortex and build up of the passage vortex detach the purge flow away from the endwall.

(3) **Numerical Predictions of Rotor Endwall Heat Transfer.**

    – A two-part simulation setup with adiabatic and constant heat flux boundary conditions is suitable to predict rotor endwall heat transfer coefficients.

    – Steady-state and unsteady time-averaged simulations predict the local heat transfer coefficient on a rotor with extended endwall contouring into the disk cavity within $15\,\%$ when compared to experiments. These simulations capture the characteristic high heat transfer coefficient region upstream of the endwall hill.

    – Unsteady simulations are required to capture the mixing between main and purge flow and predict the cooling effectiveness on the endwall. The suppression of the unsteady interaction between the main flow and purge flow near the cavity in steady-state predictions leaded to a greatly overestimated cooling effect of purge flow.

    – Care must be taken for the convergence of heat transfer estimates in the near cavity region due to the unsteady flow nature, which was found to increase simulation time by more than a factor of 5 (in reference to a sufficient aerodynamic convergence).

    – For the design process but also the validation of complex and integrated turbine geometries using automatic optimisation tools, cavities and secondary flows must be included to account for their effect on the main flow and geometry.

(4) **Heat Transfer of Highly Loaded Turbine Blade Tip Geometries.**

    – Tip leakage flow reattachment in the cavity basin for squealer type tip geometries or on the blade tip was identified as the main driver for peak heat transfer coefficients on the rotor blade tip.

    – Peak and average heat transfer coefficients were reduced for the baseline and optimised squealer case compared to the blade tip with a trench and a notch.

    – Local Nusselt number increases of up to $47\,\%$ were observed for the optimised squealer under the turbine off-design operating point. The highest reduction ($-40\,\%$) in average Nusselt number under the off-design point was found for the notch tip design.

    – Active tip coolant ejection leads to a shift of the leakage flow attachment point in the squealer cavity towards the pressure side due to

blockage and a local strengthening of the heat transfer coefficient.

Main Contributions

This work provides the following contributions to the turbomachinery field and scientific community:

- Development and substantial improvement of an infrared-based measurement setup for high-resolution heat transfer measurements on complex geometries in moderate-speed rotating facilities. The thin-film surface heating instrumentation can also be applied outside the field of turbomachinery where the heating of custom and complex surfaces is required.

- Experimental investigation of heat transfer on a rotor endwall geometry with extended contouring into the disk cavity under various purge flow injection rates were performed highlighting the relevance of purge flow variations on local hub endwall heat transfer.

- High-resolution heat transfer data on a rotor endwall from a rotating facility were provided for the validation of CFD tools and their numerical predictions. It was shown that numerical predictions tend to underestimate the mixing of purge and main flow and therefore overestimate the cooling effectiveness on the endwall platform.

- Upstream cavity extended rotor endwall contouring was introduced and showed the potential to control the purge flow ejection into the main flow path.

- To the best of the author's knowledge, this study provides the first high-resolution, thin-film heater-based heat transfer measurements on rotor blade tips in a rotating facility using optical high-speed infrared temperature measurements. A unique dataset of high-resolution heat transfer coefficient and cooling effectiveness distributions for novel tip geometries was acquired.

- Various squealer type and flat rotor blade tip type geometries were compared based on their aerothermal performance. Despite generally higher absolute values and gradients in heat transfer coefficients and spatially contained cooling effectiveness, a desensitising effect on heat transfer variations regarding operating conditions was found for a trench tip geometry.

8.2. Summary

8.2.1. Instrumentation and Measurement Setup

In the present work, a highly versatile instrumentation and measurement setup has been developed and substantially improved for optical infrared-based heat transfer measurements in rotating systems on complex surfaces. The manufacturing of custom made thin-film surface heaters using a chemically deposited Nickel layer on a PEEK substrate was possible for very complex geometries (e.g. highly contoured endwalls and blade tip desings). High uniformity of surface heat flux generation was achieved using this new coating technique, where pulsed laser ablation was used for cutting a heating track into the coating. The mechanical integrity and robustness of the instrumentation installed in the rotating research facility have been demonstrated after over 120 turbine start-ups and resonance crossings and a total of nearly 1000 hours of turbine operation. Furthermore, the versatility of the insert-based instrumentation has been demonstrated by its integration for rotor hub endwall heat transfer measurements as well as four different rotor blade tip geometry inserts in a rainbow design rotor. Successful high-resolution measurements of rotor hub endwall and rotor blade tip heat transfer were performed.

8.2.2. Numerical Predictions of Hub Endwall Heat Transfer

Numerical simulations using the commercial solver CFD from Ansys for heat transfer and cooling effectiveness predictions were performed in addition to experimental measurements. Steady-state and unsteady time-averaged simulations (using the profile transformation approach to reduce the computational cost due to the unfavourable blade count ratio of the turbine) were compared to the experimental results. For the derivation of the local heat transfer coefficient, the results of two simulations—one with adiabatic and one with uniform heat flux wall boundary conditions—were combined using Newton's law of cooling. It was shown that convergence of the heat transfer coefficient in the vicinity of the rotor upstream cavity is difficult to reach due to the highly unsteady flow structures present. The required simulation run time and subsequent numerical cost were found to be up to 5x more compared to the aerodynamic convergence in the main flow field. Heat transfer coefficient predictions were found to be within $\pm 15\,\%$ of the

experimental measurements and the characteristic patterns of the investigated geometry were well predicted. The experimentally measured increase in heat transfer in the blade throat region was not captured in the simulations. It was speculated that this may be because of the rough wall in the experiments. The roughness model in the solver may underestimate the effect of roughness on strongly accelerating flow such as present in the throat region. The relevance of including representative surface roughness in numerical predictions, either due to the experimental setup or turbine deterioration, was shown with a parameter study in which the local heat transfer coefficient was found to be up to 40 % increased locally compared to a smooth wall.

It was found that steady-state simulations greatly underpredicted the mixing of the cavity purge flow and main flow in the upper disk region, resulting in overpredictions of the endwall cooling effect by the purge flow. Great care must be taken when evaluating cooling effectiveness predictions of simulations that do not resolve the unsteady flow interactions in the cavity.

8.2.3. Heat Transfer on Cavity Extended Endwall Contouring with Purge Flow Injection

Experimental heat transfer measurements on a turbine rotor endwall with extended contouring into the disk cavity in a rotating axial turbine research facility were performed in combination with high-resolution aerodynamic probe measurements. The investigated endwall geometry resulted from a CFD-based optimisation cycle using only 1.5-stage aerodynamic efficiency as a target and limited design freedom for only one hill and trough. The non-axisymmetric contouring differs from conventional non-axisymmetric approaches based on the axial location of the hill and trough maximums upstream of the blade leading edge and the extended contouring into the cavity. This particular design, with the upstream endwall hill and the steep face into the cavity, was found to create a region of high heat transfer rate comparable to the horse-shoe vortex formation region. This phenomenon was found to be caused by the impingement of high-momentum main flow from the upstream stator. The impingement also caused a partial deflection of main flow into the upper cavity region, where a strong rim seal vortex structure was formed. This cavity vortex structure prevents the purge cooling flow from entraining the platform at this location and promoted the jet-like purge ejection into the main flow at a location upstream of the blade suction side. Due to this local purge flow entrainment, a significant cooling

effect of the purge flow on the endwall is only found locally at upstream portions of the platform.

Besides the nominal purge flow injection rate of 0.8 %, a high and low injection case with 1.2 % and 0.0 % injection were investigated to study the influence of purge flow variations on the heat transfer distribution. The laterally averaged differences were found to be within the measurement uncertainty. However, the lowest values in the front portion of the endwall up to 20 % axial chord were observed for the 0.8 % injection case. The axial extent of the influence of purge flow on the endwall was found to be limited by the pressure side horse-shoe vortex leg and its migration to the suction side. Local differences due to purge injection rate variations on the heat transfer coefficient greater than ±20 % were observed on the platform leading portion. The high-velocity flow around the blade leading edge suction side caused an increased heat transfer rate in the absence of purge air for 0.0 % injection. In the case of high purge flow injection (1.2 %), increased heat transfer on the suction side of the endwall hill was observed. This was attributed to the increased vorticity of the purge jet entraining the platform. The flow characteristics were not substantially changed, as seen by the similar observed cooling effectiveness pattern.

Additionally, the endwall heat transfer for a turbine off-design operation point with reduced mass flow (and thus negative flow incidence) was investigated. The qualitative distribution of the heat transfer coefficient was found to be similar between the two operating conditions. The characteristic region of increased heat transfer coefficient at the endwall hill upstream face was found for both operating points. The measured Stanton number ratio between the two cases was very close to the predicted ratio based on Reynolds' analogy using the rotor inlet Reynolds number. The prediction of this analogy did not hold in the throat region, where no distinct increase in Nusselt number was observed for the off-design pressure ratio case.

8.2.4. Heat Transfer of Different Rotor Blade Tip Geometries

Three different rotor blade tip geometries of a highly loaded turbine were investigated regarding their characteristic heat transfer coefficient distribution and sensitivity to the operating point and active tip coolant ejection. The geometries included three concepts developed for improved turbine aerodynamic efficiency compared to a baseline squealer tip. Additional aerodynamic probe measurements were performed using fast-response pres-

sure and temperature probes to characterise the rotor exit flow field and efficiency.

The integral 1- and 1.5-stage efficiency were increased over the baseline squealer for all investigated tip geometries. The largest increase of 0.22 p.p. and 0.30 p.p. was measured for the optimised squealer tip. Changes in the relative total pressure at the rotor exit were small—except for the notch tip geometry, where the tip leakage vortex pressure deficit increased while the pressure deficit from the passage and trailing edge shed vortex was reduced.

The peak heat transfer values measured on all geometries were found to be related to the local reattachment of the leakage flow in the squealer cavity or the blade tip. A direct comparison between the geometries was difficult due to their different local flow fields. In general, both squealer type blade tips showed lower peak Nusselt numbers compared to the trench and notch geometries. The average observed heat transfer coefficient was reduced by -12% (for the optimised squealer) and nearly -40% (for the notch tip) at the off-design turbine operating point. Despite this average reduction, local increases of up to 45% and 27% were measured for the optimised and baseline squealer tip, respectively.

The active tip coolant ejection created a blockage inside the squealer cavity and shifted the leakage flow attachment—and therefore the peak heat transfer region—towards the pressure side squealer rim. Particularly for the baseline squealer geometry, peak increases of up to 80% in heat transfer coefficient could be measured when compared to zero tip coolant. The sensitivity of the optimised squealer tip to coolant ejection was reduced. For both geometries, only a weak trace of enhanced cooling effectiveness downstream of the two dust holes could be measured. The general heat transfer pattern on the trench tip was not altered due to tip coolant ejection. In the flow reattachment zone from the trench, an increase in Nusselt number of up to 15% was observed. A more distinct trace of cooling from the dust hole could be measured for the trench tip, since the coolant is swept onto the suction side flat tip part of the tip with a lower clearance gap to the casing compared to the squealer cavity.

8.3. Suggestions for Future Work

The developed measurement setup and technique for custom made thin-film heating surfaces opens many possibilities for further heat transfer measure-

ments in rotating (and also stationary) research facilities, with potential applications reaching far beyond the field of turbomachinery. Using a chemical coating process, nearly all parts of a turbine rotor or stator row can be equipped with a surface heater. Moreover, the amount of individual inserts and non-uniformities in heat flux generation due to current concentrations at track turns can be reduced by using whole blade sections with endwall as inserts using a single heating surface. The optical accessability for cutting the heating tracks into the thin-film are the only limitation for this approach. Notably, detailed studies on heat release and a optimised track design reducing local overheating at track turns could significantly increase the effective measurement area, especially for geometries with cooling holes. Detailed investigations on the electrical characteristics of the chemical deposited nickel films could help to accurately predict heater resistance and thus heat flux generation in the design process. Future studies on the design of heating tracks to reduce overheating at turns could also include geometrical features such as blade fillets or even squealer fences to extend the effective measurement are.

Improvements to the non-uniformity calibration, more sophisticated experimental and numerical considerations and correction of transverse and lateral conduction would significantly improve measurement uncertainty. Furthermore, alternative high-emissivity coatings with lower thermal response times may also facilitate the measurement of transient heat transfer when used in a similar setup.

An alternative measurement procedure to the steady-state heating steps using transient cool-down measurements could also investigated to improve this technique. Potential benefits would include significantly reduced measurement time (since only one heating step must be reached with thermal equilibrium between the insert and environment) and reduced lateral conduction.

Finally, more detailed and systematic investigations on cavity extended endwall contouring and advanced tip geometries should be performed to exploit the potential of this alteration of geometries. The obtained experimental data in this work can serve as a starting point and validation for a purely numerical investigation.

Bibliography

[1] YI Abdel-Aziz and HM Karara. Direct linear transformation into object space coordinates in close-range photogrammetry. In *Proc. Symp. Close-Range Photogrammetry*, pages 1–18, 1971.

[2] R. S. Abhari and A. H. Epstein. An experimental study of film cooling in a rotating transonic turbine. *Journal of Turbomachinery*, 116(1):63–70, 1994. ISSN 0889-504X. doi: 10.1115/1.2928279.

[3] Thomas Adams, Christopher Grant, and Heather Watson. A simple algorithm to relate measured surface roughness to equivalent sand-grain roughness. *International Journal of Mechanical Engineering and Mechatronics*, 2012. ISSN 19292724. doi: 10.11159/ijmem.2012.008.

[4] A. Adibekyan, E. Kononogova, C. Monte, and J. Hollandt. High-accuracy emissivity data on the coatings nextel 811-21, herberts 1534, aeroglaze z306 and acktar fractal black. *International Journal of Thermophysics*, 38(6):89, 2017. ISSN 1572-9567. doi: 10.1007/s10765-017-2212-z.

[5] U.S. Energy Information Administration. *International Energy Outlook 2019*. U.S. Energy Information Administration, 2019. URL https://www.eia.gov/outlooks/ieo/pdf/ieo2019.pdf.

[6] International Energy Agency. *World Energy Outlook 2019*. International Energy Agency, 2019. doi: doi:https://doi.org/10.1787/caf32f3b-en. URL https://www.oecd-ilibrary.org/content/publication/caf32f3b-en.

[7] Jaeyong Ahn, M. T. Schobeiri, Je-Chin Han, and Hee-Koo Moon. Film cooling effectiveness on the leading edge of a rotating turbine blade. In *ASME 2004 International Mechanical Engineering Congress and Exposition*, volume Heat Transfer, Volume 1, pages 565–574, 2004. doi: 10.1115/imece2004-59852.

[8] Jaeyong Ahn, M. T. Schobeiri, Je-Chin Han, and Hee-Koo Moon. Film cooling effectiveness on the leading edge of a rotating film-cooled blade using pressure sensitive paint. In *ASME Turbo Expo 2005: Power for Land, Sea, and Air*, volume Volume 3: Turbo Expo 2005, Parts A and B, pages 375–384, 2005. doi: 10.1115/gt2005-68344.

[9] Jaeyong Ahn, M. T. Schobeiri, Je-Chin Han, and Hee-Koo Moon. Film cooling effectiveness on the leading edge region of a rotating turbine blade with two rows of film cooling holes using pressure sensitive paint. *Journal of Heat Transfer*, 128(9): 879–888, 2006. ISSN 0022-1481. doi: 10.1115/1.2241945.

[10] Jaeyong Ahn, M. T. Schobeiri, Je-Chin Han, and Hee-Koo Moon. Effect of rotation on leading edge region film cooling of a gas turbine blade with three rows of film cooling holes. *International Journal of Heat and Mass Transfer*, 50(1):15–25, 2007. ISSN 0017-9310. doi: 10.1016/j.ijheatmasstransfer.2006.06.028.

[11] A. A. Ameri, E. Steinthorsson, and D. L. Rigby. Effect of squealer tip on rotor heat

transfer and efficiency. *Journal of Turbomachinery*, 120(4):753–759, 1998. ISSN 0889-504X. doi: 10.1115/1.2841786.

[12] T. Astarita, G. Cardone, and G. M. Carlomagno. Infrared thermography: An optical method in heat transfer and fluid flow visualisation. *Optics and Lasers in Engineering*, 44(3-4):261–281, 2006. ISSN 01438166. doi: 10.1016/j.optlaseng.2005.04.006.

[13] Tommaso Astarita and Giovanni Maria Carlomagno. *Infrared thermography for thermo-fluid-dynamics*. Experimental fluid mechanics. Heidelberg : Springer, 2013. ISBN 978-3-642-29507-2. doi: 10.1007/978-3-642-29508-9.

[14] ASTM International. Standard test methods for rating adhesion by tape test, 2017.

[15] Marcel Aulich and Ulrich Siller. High-dimensional constrained multiobjective optimization of a fan stage. In *ASME 2011 Turbo Expo: Turbine Technical Conference and Exposition*, pages 1185–1196, Volume 7: Turbomachinery, Parts A, B, and C, 2011. doi: 10.1115/GT2011-45618.

[16] Gm Salam Azad, Je-Chin Han, Ronald S. Bunker, and C. Pang Lee. Effect of squealer geometry arrangement on a gas turbine blade tip heat transfer. *Journal of Heat Transfer*, 124(3):452–459, 2002. ISSN 0022-1481. doi: 10.1115/1.1471523.

[17] T. Behr, A. I. Kalfas, and R. S. Abhari. Unsteady flow physics and performance of a one-and-1/2-stage unshrouded high work turbine. *Journal of Turbomachinery*, 129 (2):348–359, 2006. ISSN 0889-504X. doi: 10.1115/1.2447707.

[18] T. Behr, A. I. Kalfas, and R. S. Abhari. Control of rotor tip leakage through cooling injection from the casing in a high-work turbine. *Journal of Turbomachinery*, 130(3): 031014–031014–12, 2008. ISSN 0889-504X. doi: 10.1115/1.2777185.

[19] Thomas Behr. *Control of rotor tip leakage and secondary flow by casing air injection in unshrouded axial turbines*. Thesis, Zürich, ETH, 2007.

[20] Jonathan Bergh, Glen C. Snedden, and Dwain I. Dunn. Optimization of non-axisymmetric endwall contours for the rotor of a low speed, 1 1/2 stage research turbine with unshrouded blades - optimization and experimental validation. *Journal of Turbomachinery*, pages 1–15, 2020. ISSN 0889-504X. doi: 10.1115/1.4045988.

[21] M. F. Blair. An experimental study of heat transfer and film cooling on large-scale turbine endwalls. *Journal of Heat Transfer*, 96(4):524–529, 1974. ISSN 0022-1481. doi: 10.1115/1.3450239.

[22] M. F. Blair. An experimental study of heat transfer in a large-scale turbine rotor passage. In *Turbo Expo: Power for Land, Sea, and Air*, volume Volume 4: Heat Transfer; Electric Power; Industrial and Cogeneration, page V004T09A012, Volume 4: Heat Transfer; Electric Power; Industrial and Cogeneration, 1992. doi: 10.1115/ 92-GT-195.

[23] M. F. Blair. An experimental study heat transfer in a large-scale turbine rotor passage. *Journal of Turbomachinery*, 116(1):1–13, 1994. ISSN 0889-504X. doi: 10.1115/1.2928273.

[24] M. F. Blair and R. D. Lander. New techniques for measuring film cooling effectiveness. *Journal of Heat Transfer*, 97(4):539–543, 1975. ISSN 0022-1481. doi: 10.1115/1. 3450425.

[25] M. F. Blair, R. P. Dring, and H. D. Joslyn. The effects of turbulence and stator/rotor interactions on turbine heat transfer: Part i—design operating conditions. *Journal of Turbomachinery*, 111(1):87–96, 1989. ISSN 0889-504X. doi: 10.1115/1.3262241.

[26] M. F. Blair, R. P. Dring, and H. D. Joslyn. The effects of turbulence and stator/rotor interactions on turbine heat transfer: Part ii—effects of reynolds number and incidence. *Journal of Turbomachinery*, 111(1):97–103, 1989. ISSN 0889-504X. doi: 10.1115/1.3262243.

[27] M. F. Blair, J. H. Wagner, and G. D. Steuber. New applications of liquid-crystal thermography in rotating turbomachinery heat transfer research, June 3 -6 1991.

[28] R. J. Boyle, C. M. Spuckler, B. L. Lucci, and W. P. Camperchioli. Infrared low-temperature turbine vane rough surface heat transfer measurements. *Journal of Turbomachinery*, 123(1):168–177, 2000. ISSN 0889-504X. doi: 10.1115/1.1333693.

[29] Stefan Brack, Rico Poser, and Jens von Wolfersdorf. A comparison between transient heat transfer measurements using tlc and ir thermography. In *XXII Biennial Symposium on Measuring Technique in Turbomachinery*, 2016. doi: 10.18419/opus-9702.

[30] Peter Bradshaw. Turbulence modeling with application to turbomachinery. *Progress in Aerospace Sciences*, 32(6):575–624, 1996. ISSN 0376-0421. doi: 10.1016/S0376-0421(96)00003-6.

[31] Steven W. Burd, Cynthia J. Satterness, and Terrence W. Simon. Effects of slot bleed injection over a contoured end wall on nozzle guide vane cooling performance: Part ii - thermal measurements. In *ASME Turbo Expo 2000: Power for Land, Sea, and Air*, volume Volume 3: Heat Transfer; Electric Power; Industrial and Cogeneration, V003T01A008, 2000. doi: 10.1115/2000-gt-0200.

[32] Mesures Bureau International des Poids et. *Guide to expression of uncertainty in measurement*. Genève : ISO, International Organization for Standardization [etc.], 1993. ISBN 92-67-10188-9.

[33] G. M. Carlomagno and G. Cardone. Infrared thermography for convective heat transfer measurements. *Experiments in Fluids*, 49(6):1187–1218, 2010. ISSN 0723-4864 1432-1114. doi: 10.1007/s00348-010-0912-2.

[34] Bogdan C. Cernat, Marek Pátý, Cis De Maesschalck, and Sergio Lavagnoli. Experimental and numerical investigation of optimized blade tip shapes—part i: Turbine rainbow rotor testing and numerical methods. *Journal of Turbomachinery*, 141(1): 011006–011006–13, 2018. ISSN 0889-504X. doi: 10.1115/1.4041465.

[35] Kam S. Chana and Terry V. Jones. An investigation on turbine tip and shroud heat transfer. *Journal of Turbomachinery*, 125(3):513–520, 2003. ISSN 0889-504X. doi: 10.1115/1.1575253.

[36] J. P. Clark and E. A. Grover. Assessing convergence in predictions of periodic-unsteady flowfields. In *ASME Turbo Expo 2006: Power for Land, Sea, and Air*, volume Volume 6: Turbomachinery, Parts A and B, pages 1831–1841, 2006. doi: 10.1115/gt2006-90735.

[37] C. De Maesschalck, S. Lavagnoli, G. Paniagua, T. Verstraete, R. Olive, and P. Picot. Heterogeneous optimization strategies for carved and squealer-like turbine blade tips. *Journal of Turbomachinery*, 138(12):121011–121011–12, 2016. ISSN 0889-504X. doi: 10.1115/1.4033975.

[38] Carsten Degendorfer, Reza S. Abhari, Klemens Vogel, and René Hunziker. Experimental and numerical investigation of blade resonance in a centrifugal compressor for varying gas properties. *Journal of the Global Power and Propulsion Society*, 2: 415–428, 2018. doi: 10.22261/jgpps.Q15crp.

[39] J. D. Denton. The 1993 igti scholar lecture: Loss mechanisms in turbomachines. *Journal of Turbomachinery*, 115(4):621–656, 1993. ISSN 0889-504X. doi: 10.1115/1. 2929299.

[40] Debashis Dey. *Aerodynamic Tip Desensitization in Axial Flow Turbines*. Thesis, Pennsylvania State University, 2001. URL https://etda.libraries.psu.edu/catalog/5894.

[41] Debashis Dey and Cengiz Camci. Aerodynamic tip desensitization of an axial turbine rotor using tip platform extensions. In *ASME Turbo Expo 2001: Power for Land, Sea, and Air*, volume Volume 1: Aircraft Engine; Marine; Turbomachinery; Microturbines and Small Turbomachinery, V001T03A069, 2001. doi: 10.1115/2001-gt-0484.

[42] Debashis Dey, Levent Kavurmacioğlu, and Cengiz Camci. Tip desensitization of an axial turbine rotor using partial squealer rims, 2008.

[43] F. Didier, R. Dénos, and T. Arts. Unsteady rotor heat transfer in a transonic turbine stage. *Journal of Turbomachinery*, 124(4):614–622, 2002. ISSN 0889-504X. doi: 10.1115/1.1505850.

[44] R. Dénos and G. Paniagua. Influence of the hub endwall cavity flow on the time-averaged and time-resolved aero-thermodynamics of an axial hp turbine stage. In *ASME Turbo Expo 2002: Power for Land, Sea, and Air*, volume Volume 3: Turbo Expo 2002, Parts A and B, pages 207–217, 2002. doi: 10.1115/gt2002-30185.

[45] R. P. Dring, M. F. Blair, and H. D. Joslyn. An experimental investigation of film cooling on a turbine rotor blade. *Journal of Engineering for Power*, 102(1):81–87, 1980. ISSN 0022-0825. doi: 10.1115/1.3230238.

[46] M. G. Dunn. Heat-flux measurements for the rotor of a full-stage turbine: Part i—time-averaged results. *Journal of Turbomachinery*, 108(1):90–97, 1986. ISSN 0889-504X. doi: 10.1115/1.3262029.

[47] M. G. Dunn and A. Hause. Measurement of heat flux and pressure in a turbine stage. *Journal of Engineering for Gas Turbines and Power*, 104(1):215–223, 1982. ISSN 0742-4795. doi: 10.1115/1.3227253.

[48] M. G. Dunn, P. J. Seymour, S. H. Woodward, W. K. George, and R. E. Chupp. Phase-resolved heat-flux measurements on the blade of a full-scale rotating turbine. *Journal of Turbomachinery*, 111(1):8–19, 1989. ISSN 0889-504X. doi: 10.1115/1.3262242.

[49] Srinath V. Ekkad, Shichuan Ou, and Richard B. Rivir. A transient infrared thermography method for simultaneous film cooling effectiveness and heat transfer coefficient measurements from a single test. *Journal of Turbomachinery*, 126(4):597–603, 2004. ISSN 0889-504X. doi: 10.1115/1.1791283.

[50] Alan H. Epstein. Aeropropulsion for commercial aviation in the twenty-first century and research directions needed. *AIAA Journal*, 52(5):901–911, 2014. doi: 10.2514/1. J052713.

[51] CAPA Center for Aviation. Global airline financial outlook, 2016. URL https://centreforaviation.com/analysis/airline-leader/global-airline-financial-outlook-282280.

[52] Samuel M. Futral and Donald E. Holeski. *Experimental Performance of a 5-Inch (13-cm) Axial-Flow Turbine Over a Range of Reynolds Number*. NASA Technical Memorandum. NASA, 1968.

[53] Jie Gao, Qun Zheng, and Guoqiang Yue. Reduction of tip clearance losses in an unshrouded turbine by rotor casing contouring. *Journal of Propulsion and Power*, 28(5):936–945, 2012. doi: 10.2514/1.B34565.

[54] S. Girgis, E. Vlasic, J.-P. Lavoie, and S. H. Moustapha. The effect of secondary air injection on the performance of a transonic turbine stage. In *ASME Turbo Expo 2002: Power for Land, Sea, and Air*, volume Volume 5: Turbo Expo 2002, Parts A and B, pages 147–158, 2002. doi: 10.1115/gt2002-30340.

[55] R. J. Goldstein and R. A. Spores. Turbulent transport on the endwall in the region between adjacent turbine blades. *Journal of Heat Transfer*, 110(4a):862–869, 1988. ISSN 0022-1481. doi: 10.1115/1.3250586.

[56] C. R. Gossweiler, P. Kupferschmied, and G. Gyarmathy. On fast-response probes: Part 1—technology, calibration, and application to turbomachinery. *Journal of Turbomachinery*, 117(4):611–617, 1995. ISSN 0889-504X. doi: 10.1115/1.2836579.

[57] Christoph R. Gossweiler. *Sonden und Messsystem für schnelle aerodynamische Strömungsmessung mit piezoresistiven Druckgebern*. Thesis, Zürich, ETH Zürich, 1993.

[58] Fabian Gottschlich. *FEM Simulation of Blade Tip Heat Load for Heater Design Optimization*. Masters thesis, ETH Zurich, 2016.

[59] D. Granser and T. Schulenberg. Prediction and measurement of film cooling effectiveness for a first-stage turbine vane shroud. In *ASME 1990 International Gas Turbine and Aeroengine Congress and Exposition*, volume Volume 4: Heat Transfer; Electric Power; Industrial and Cogeneration, V004T09A020, 1990. doi: 10.1115/90-gt-095.

[60] ATAG Air Transport Action Group. Facts & figures, 2020. URL https://www.atag.org/facts-figures.html.

[61] G. R. Guenette, A. H. Epstein, M. B. Giles, R. Haimes, and R. J. G. Norton. Fully scaled transonic turbine rotor heat transfer measurements. *Journal of Turbomachinery*, 111(1):1–7, 1989. ISSN 0889-504X. doi: 10.1115/1.3262231.

[62] J. E. Haas and M. G. Kofskey. Effect of rotor tip clearance and configuration on overall performance of a 12.77-centimeter tip diameter axial-flow turbine. In *ASME 1979 International Gas Turbine Conference and Exhibit and Solar Energy Conference*, volume Volume 1A: Gas Turbines, V01AT01A042, 1979. doi: 10.1115/79-gt-42.

[63] Jeffrey E. Haas and Milton G. Kofskey. *Cold-Air Performance of a 12.766-Centimeter-Tip-Diameter Axial-Flow Cooled Turbine*, volume III - Effect of Rotor Tip Clearance on Overall Performance of a Solid Blade Configuration. NASA, 1977.

[64] J. C. Hartland, D. G. Gregory-Smith, N. W. Harvey, and M. G. Rose. Non-axisymmetric turbine end wall design: Part ii — experimental validation. *Journal of Turbomachinery*, 122(2):286–293, 1999. doi: 10.1115/1.555446.

[65] N. W. Harvey, G. Brennan, D. A. Newman, and M. G. Rose. Improving turbine efficiency using non-axisymmetric end walls: Validation in the multi-row environment and with low aspect ratio blading. In *ASME Turbo Expo 2002: Power for Land, Sea, and Air*, volume Volume 5: Turbo Expo 2002, Parts A and B, pages 119–126, 2002. doi: 10.1115/gt2002-30337.

[66] Neil W. Harvey and Ken Ramsden. A computational study of a novel turbine rotor partial shroud. *Journal of Turbomachinery*, 123(3):534–543, 2000. ISSN 0889-504X. doi: 10.1115/1.1370166.

[67] Neil W. Harvey, Martin G. Rose, Mark D. Taylor, Shahrokh Shahpar, Jonathan Hartland, and David G. Gregory-Smith. Non-axisymmetric turbine end wall design: Part i — three-dimensional linear design system. In *ASME 1999 International Gas Turbine and Aeroengine Congress and Exhibition*, page V001T03A049, Volume 1: Aircraft Engine; Marine; Turbomachinery; Microturbines and Small Turbomachinery, 1999. doi: 10.1115/99-GT-337.

[68] William R. Hawthorne. Rotational flow through cascades part i: The components of vorticity. *The Quarterly Journal of Mechanics and Applied Mathematics*, 8(3): 266–279, 1955. ISSN 0033-5614. doi: 10.1093/qjmam/8.3.266.

[69] William Rede Hawthorne and Theodore von Karman. Secondary circulation in fluid flow. *Proceedings of the Royal Society of London. Series A. Mathematical and Physical Sciences*, 206(1086):374–387, 1951. doi: 10.1098/rspa.1951.0076.

[70] Shane Haydt and Stephen Lynch. Cooling effectiveness for a shaped film cooling hole at a range of compound angles. In *ASME Turbo Expo 2018: Turbomachinery Technical Conference and Exposition*, volume Volume 5C: Heat Transfer, V05CT19A011, 2018. doi: 10.1115/gt2018-75726.

[71] Howard Z Herzig, Arthur G Hansen, and George R. Costello. A visualization study of secondary flows in cascades. Report, Lewis Flight Propulsion Laboratory, Cleveland, Ohio, 1954.

[72] Donald E. Holeski and Samuel M. Futral. *Effect of Rotor Tip Clearance on the Performance of a 5-inch Single-Stage Axial-Flow Turbine*. NASA Technical Memorandum. NASA, 1969.

[73] Nicholas E. Holgate, Peter T. Ireland, and Eduardo Romero. An experimental-numerical method for transient infrared measurement of film cooling effectiveness and heat transfer coefficient in a single test. *The Aeronautical Journal*, 123(1270): 1982–1998, 2019. ISSN 0001-9240. doi: 10.1017/aer.2019.26.

[74] J. P. Holman. *Heat transfer*. McGraw-Hill series in mechanical engineering. Boston : McGraw Hill Higher Education, 10th ed. edition, 2010. ISBN 978-0-07-352936-3.

[75] H. J. Humm, C. R. Gossweiler, and G. Gyarmathy. On fast-response probes: Part 2—aerodynamic probe design studies. *Journal of Turbomachinery*, 117(4):618–624, 1995. ISSN 0889-504X. doi: 10.1115/1.2836580.

[76] Scott D. Hunter and Steven R. Manwaring. Endwall cavity flow effects on gaspath aerodynamics in an axial flow turbine: Part i — experimental and numerical investigation. In *ASME Turbo Expo 2000: Power for Land, Sea, and Air*, volume Volume 1: Aircraft Engine; Marine; Turbomachinery; Microturbines and Small Turbomachinery, V001T03A111, 2000. doi: 10.1115/2000-gt-0651.

[77] International Air Transport Association (IATA). Iata forecast predicts 8.2 billion air travelers in 2037, 24.10.2018 2018. URL `https://www.iata.org/en/pressroom/pr/2018-10-24-02/`.

[78] International Civil Aviation Organization (ICAO). Icao annual report 2018. Report, International Civil Aviation Organization (ICAO), 2018. URL `https://www.icao.int/annual-report-2018/Pages/default.aspx`.

[79] IPCC. Climate change 2014 synthesis report. contribution of working groups i, ii and iii to the fifth assessment report of the intergovernmental panel on climate change. Report, IPCC, Geneva, Switzerland, 2014.

[80] Ralf Jakoby, Thomas Zierer, Klas Lindblad, Jonas Larsson, Laurent deVito, Dieter E. Bohn, Joachim Funcke, and Achim Decker. Numerical simulation of the unsteady flow field in an axial gas turbine rim seal configuration. In *ASME Turbo Expo 2004: Power for Land, Sea, and Air*, volume Volume 4: Turbo Expo 2004, pages 431–440, 2004. doi: 10.1115/gt2004-53829.

[81] Philipp Jenny. *Interaction mechanisms between rim seal purge flow and profiled end walls in a low-pressure turbine*. Thesis, Zürich, ETH, 2012.

[82] Jin Young Jeong, Woobin Kim, Jae Su Kwak, and Jung Shin Park. Heat transfer coefficient and film cooling effectiveness on the partial cavity tip of a gas turbine blade. *Journal of Turbomachinery*, 141(7):071007–071007–9, 2019. ISSN 0889-504X. doi: 10.1115/1.4042647.

[83] I. Kaiser and J. P. Bindon. The effect of tip clearance on the development of loss behind a rotor and a subsequent nozzle. In *ASME 1997 International Gas Turbine and Aeroengine Congress and Exhibition*, volume Volume 1: Aircraft Engine; Marine; Turbomachinery; Microturbines and Small Turbomachinery, V001T03A011, 1997. doi: 10.1115/97-gt-053.

[84] Martin Kegalj, Gregor Schmid, Fabian Wartzek, Heinz-Peter Schiffer, and Lars Willer. Experimental and numerical investigation of tip leakage flow in a 1 1/2 stage turbine rig comparing flat and cavity-squealer tip geometries. In *ASME Turbo Expo 2012: Turbine Technical Conference and Exposition*, volume Volume 8: Turbomachinery, Parts A, B, and C, pages 1543–1557, 2012. doi: 10.1115/gt2012-69568.

[85] Anastasia Kharina and Daniel Rutherford. *Fuel Efficiency Trends for new Commercial Jet Aircraft: 1960 to 2014 (white paper)*. The International Council on Clean Transportation (icct), 2015. URL https://theicct.org/sites/default/files/publications/ICCT_Aircraft-FE-Trends_20150902.pdf.

[86] M.G. Kofskey. *Experimental Investigation of Three Tip-clearance Configurations Over a Range of Tip Clearance Using a Single-stage Turbine of High Hub to Tip Radius Ratio*. NASA, 1961. URL https://books.google.ch/books?id=ozokAQAAIAAJ.

[87] Milton G. Kofskey and William J. Nusbaum. *Performance Evaluation of a Two-Stage Axial-Flow Turbine for two Values of Tip Clearance*. NASA Technical Note. NASA, 1968.

[88] Peter Kupferschmied. *Zur Methodik zeitaufgelöster Messungen mit Strömungssonden in Verdichtern und Turbinen*. Thesis, Zürich, ETH Zürich, 1998.

[89] E. T. Kwor and S. Matteï. Emissivity measurements for nextel velvet coating 811-21 between -36 degrees c and 82 degrees c, 2001.

[90] Konstantinos G. Kyprianidis. *Tuture Aero Engine Designs: An Evolving Vision*, book section 1. IntechOpen, 2011. doi: 10.5772/19689.

[91] Ronald S. LaFleur, Timothy S. Whitten, and Juan A. Araujo. Second vane endwall heat transfer reduction by iceform contouring. In *ASME 1999 International Gas Turbine and Aeroengine Congress and Exhibition*, volume Volume 3: Heat Transfer; Electric Power; Industrial and Cogeneration, V003T01A094, 1999. doi: 10.1115/99-gt-422.

[92] L. S. Langston. Crossflows in a turbine cascade passage. *Journal of Engineering for Power*, 102(4):866–874, 1980. ISSN 0022-0825. doi: 10.1115/1.3230352.

[93] Lee S. Langston. Secondary flows in axial turbines—a review. *Annals of the New York Academy of Sciences*, 934(1):11–26, 2001. doi: 10.1111/j.1749-6632. 2001.tb05839.x. URL `https://nyaspubs.onlinelibrary.wiley.com/doi/abs/10. 1111/j.1749-6632.2001.tb05839.x`.

[94] S. Lavagnoli, C. De Maesschalck, and V. Andreoli. Design considerations for tip clearance control and measurement on a turbine rainbow rotor with multiple blade tip geometries, 2016.

[95] Benoit Laveau. *Investigation of the Heat Transfer Patterns on the Vane Endwall of an Axial Turbine*. Thesis, Zurich, ETH Zurich, 2014.

[96] Benoit Laveau, Reza S. Abhari, Michael E. Crawford, and Ewald Lutum. High resolution heat transfer measurement on flat and contoured endwalls in a linear cascade. *Journal of Turbomachinery*, 135(4):041020–041020–9, 2013. ISSN 0889-504X. doi: 10.1115/1.4007725.

[97] Benoit Laveau, Reza S. Abhari, Michael E. Crawford, and Ewald Lutum. High resolution heat transfer measurements on the stator endwall of an axial turbine. *Journal of Turbomachinery*, 137(4):041005–041005–10, 2014. ISSN 0889-504X. doi: 10.1115/1.4028431.

[98] S. Lazzi Gazzini, R. Schädler, A. I. Kalfas, and R. S. Abhari. Infrared thermography with non-uniform heat flux boundary conditions on the rotor endwall of an axial turbine. *Measurement Science and Technology*, 28(2):025901–025901–15, 2017. ISSN 0957-0233 1361-6501. doi: 10.1088/1361-6501/aa5174.

[99] S. Lazzi Gazzini, R. Schädler, A. I. Kalfas, R. S. Abhari, S. Hohenstein, G. Schmid, and E. Lutum. Effect of purge air on rotor endwall heat transfer of an axial turbine. *Journal of the Global Power and Propulsion Society*, 1:211–223, 2017. ISSN 2515-3080. doi: 10.22261/F29ZWY. URL `https://journal.gpps.global/a/F29ZWY/`.

[100] Sebastiano Lazzi Gazzini. *Infrared Thermography for Endwall Heat Transfer Measurements*. Thesis, Zurich, ETH Zurich, 2017.

[101] Nicolas Lecoq. Thermal investigation of turbine main flow and cavity flow. MTU Aero Engines AG, 2018.

[102] Christian Lenherr. *High Temperature Fast Response Aerodynamic Probe*. Thesis, Zürich, ETH, 2011.

[103] Joachim Lohrengel and Reinhard Todtenhaupt. Wärmeleitfähigkeit, gesamtemissionsgrade und spektrale emissionsgrade der beschichtung nextel-velvet-coating 811-21 (ral 900 15 tiefschwarz matt). *PTB-Mitteilungen 106*, 4/96:259–265, 1996.

[104] Ewald Lutum, Francois Cottier, Michael E Crawford, Benoit Laveau, and Reza S Abhari. A computational investigation of the effect of surface roughness on heat transfer on the stator endwall of an axial turbine. *Proceedings of the Institution of Mechanical Engineers, Part A: Journal of Power and Energy*, 229(5):454–464, 2015. doi: 10.1177/0957650915594705. URL `http://journals.sagepub.com/doi/abs/10.1177/0957650915594705`.

[105] Stephen P. Lynch, Narayan Sundaram, Karen A. Thole, Atul Kohli, and Christopher Lehane. Heat transfer for a turbine blade with nonaxisymmetric endwall contouring. *Journal of Turbomachinery*, 133(1):011019–011019–9, 2010. ISSN 0889-504X. doi: 10.1115/1.4000542.

[106] Gazi I. Mahmood and Sumanta Acharya. Measured endwall flow and passage heat transfer in a linear blade passage with endwall and leading edge modifications. In *ASME Turbo Expo 2007: Power for Land, Sea, and Air*, volume Volume 6: Turbo Expo 2007, Parts A and B, pages 917–930, 2007. doi: 10.1115/gt2007-28179.

[107] Michel Mansour, Ndaona Chokani, Anestis I. Kalfas, and Reza S. Abhari. Time-resolved entropy measurements using a fast response entropy probe. *Measurement Science and Technology*, 19(11):115401, 2008. ISSN 0957-0233 1361-6501. doi: 10.1088/0957-0233/19/11/115401.

[108] Michel Mansour, Patrick S. Rebholz, Anestis I. Kalfas, and Reza S. Abhari. An on-board wireless multi-sensor measurement system for rotating turbomachinery application. In *Proceedings of International Gas Turbine Congress 2015 Tokyo November 15-20, 2015, Tokyo, Japan*, 2015. ISBN 978-4-89111-008-6.

[109] R. M. Mathison, C. W. Haldeman, and M. G. Dunn. Heat transfer for the blade of a cooled stage and one-half high-pressure turbine—part i: Influence of cooling variation. *Journal of Turbomachinery*, 134(3), 2011. ISSN 0889-504X. doi: 10.1115/1.4003173.

[110] R. M. Mathison, C. W. Haldeman, and M. G. Dunn. Aerodynamics and heat transfer for a cooled one and one-half stage high-pressure turbine—part iii: Impact of hot-streak characteristics on blade row heat flux. *Journal of Turbomachinery*, 134 (1), 2011. ISSN 0889-504X. doi: 10.1115/1.4002996.

[111] Randall M. Mathison and Michael G. Dunn. A new rotating facility for investigating cooling passage internal heat transfer. In *Global Power and Propulsion Forum 2017*, volume Proceedings of the 1st Global Power and Propulsion Forum, 2017.

[112] Christopher McLean, Cengiz Camci, and Boris Glezer. Mainstream aerodynamic effects due to wheelspace coolant injection in a high-pressure turbine stage: Part i—aerodynamic measurements in the stationary frame. *Journal of Turbomachinery*, 123(4):687–696, 2001. ISSN 0889-504X. doi: 10.1115/1.1401026.

[113] Carosena Meola and Giovanni M. Carlomagno. Recent advances in the use of infrared thermography. *Measurement Science and Technology*, 15(9):R27–R58, 2004. ISSN 0957-0233 1361-6501. doi: 10.1088/0957-0233/15/9/r01.

[114] D. E. Metzger, R. S. Bunker, and M. K. Chyu. Cavity heat transfer on a transverse grooved wall in a narrow flow channel. *Journal of Heat Transfer*, 111(1):73–79, 1989. ISSN 0022-1481. doi: 10.1115/1.3250661.

[115] D. E. Metzger, R. S. Bunker, and G. Bosch. Transient liquid crystal measurement of local heat transfer on a rotating disk with jet impingement. *Journal of Turbomachinery*, 113(1):52–59, 1991. ISSN 0889-504X. doi: 10.1115/1.2927737.

[116] Bob Mischo, Thomas Behr, and Reza S. Abhari. Flow physics and profiling of recessed blade tips: Impact on performance and heat load. *Journal of Turbomachinery*, 130 (2):021008–021008–8, 2008. ISSN 0889-504X. doi: 10.1115/1.2775485.

[117] Robert J. Moffat. Describing the uncertainties in experimental results. *Experimental Thermal and Fluid Science*, 1(1):3–17, 1988. ISSN 0894-1777. doi: 10.1016/0894-1777(88)90043-X.

[118] Robert J. Moffat. What's new in convective heat transfer? *International Journal of Heat and Fluid Flow*, 19(2):90–101, 1998. ISSN 0142-727X. doi: 10.1016/S0142-727X(97)10014-5.

[119] Tiago Augusto Moreira, Alex Roger Almeida Colmanetti, and Cristiano Bigonha Tibiriçá. Heat transfer coefficient: a review of measurement techniques. *Journal of the Brazilian Society of Mechanical Sciences and Engineering*, 41(6):264, 2019. ISSN 1806-3691. doi: 10.1007/s40430-019-1763-2.

[120] Hasan Nasir, Srinath V. Ekkad, David M. Kontrovitz, Ronald S. Bunker, and Chander Prakash. Effect of tip gap and squealer geometry on detailed heat transfer measurements over a high pressure turbine rotor blade tip. *Journal of Turbomachinery*, 126(2):221–228, 2004. ISSN 0889-504X. doi: 10.1115/1.1731416.

[121] Hasan Nasir, Srinath V. Ekkad, and Ronald S. Bunker. Effect of tip and pressure side coolant injection on heat transfer distributions for a plane and recessed tip. *Journal of Turbomachinery*, 129(1):151–163, 2005. ISSN 0889-504X. doi: 10.1115/1.2366540.

[122] United Nations. Paris agreement, 2015. URL https://unfccc.int/process-and-meetings/the-paris-agreement/the-paris-agreement.

[123] United Nations. World population prospects 2019. Report, United Nations, 2019 2019.

[124] Jeremy B. Nickol, Randall M. Mathison, Michael G. Dunn, Jong S. Liu, and Malak F. Malak. Unsteady heat transfer and pressure measurements on the airfoils of a rotating transonic turbine with multiple cooling configurations. *Journal of Engineering for Gas Turbines and Power*, 139(9), 2017. ISSN 0742-4795. doi: 10.1115/1.4036059.

[125] M. Ochs, T. Horbach, A. Schulz, R. Koch, and H. J. Bauer. A novel calibration method for an infrared thermography system applied to heat transfer experiments. *Measurement Science and Technology*, 20(7):075103, 2009. ISSN 0957-0233. doi: 10.1088/0957-0233/20/7/075103.

[126] Rohit Oke, Terry Simon, Tom Shih, Bin Zhu, Yu Liang Lin, and Minking Chyu. Measurements over a film-cooled, contoured endwall with various coolant injection rates. In *ASME Turbo Expo 2001: Power for Land, Sea, and Air*, volume Volume 3: Heat Transfer; Electric Power; Industrial and Cogeneration, V003T01A025, 2001. doi: 10.1115/2001-gt-0140.

[127] Rohit A. Oke and Terrence W. Simon. Film cooling experiments with flow introduced upstream of a first stage nozzle guide vane through slots of various geometries. In *ASME Turbo Expo 2002: Power for Land, Sea, and Air*, volume Volume 3: Turbo Expo 2002, Parts A and B, pages 33–40, 2002. doi: 10.1115/gt2002-30169.

[128] Fabio Pagnacco, Luca Furlani, Alessandro Armellini, Luca Casarsa, and Anthony Davis. Rotating heat transfer measurements on a multi-pass internal cooling channel: I - rig development. In *ASME Turbo Expo 2016: Turbomachinery Technical Conference and Exposition*, volume Volume 5B: Heat Transfer, V05BT16A005, 2016. doi: 10.1115/gt2016-56308.

[129] Kapil V. Panchal, Santosh Abraham, Arnab Roy, Srinath V. Ekkad, Wing Ng, Andrew S. Lohaus, and Michael E. Crawford. Effect of endwall contouring on a transonic turbine blade passage: Heat transfer performance. *Journal of Turbomachinery*, 139 (1), 2016. ISSN 0889-504X. doi: 10.1115/1.4034411.

[130] G. Paniagua, R. Dénos, and S. Almeida. Effect of the hub endwall cavity flow on the flow-field of a transonic high-pressure turbine. *Journal of Turbomachinery*, 126 (4):578–586, 2004. ISSN 0889-504X. doi: 10.1115/1.1791644.

[131] M. Papa, V. Srinivasan, and R. J. Goldstein. Film cooling effect of rotor-stator

purge flow on endwall heat/mass transfer. *Journal of Turbomachinery*, 134(4): 041014–041014–8, 2011. ISSN 0889-504X. doi: 10.1115/1.4003725.

[132] Ilias Papagiannis. *Unsteady Steam Turbine Optimization using High Fidelity CFD*. Thesis, Zurich, ETH Zurich, 2019.

[133] Ron Parkinson. Properties and applications of electroless nickel deposits. *Technical Series No. 10081*, 1997.

[134] A. Pfau, J. Schlienger, A. I. Kalfas, and R. S. Abhari. Virtual four sensor fast response aerodynamic probe (frap®), 2002.

[135] A. Pfau, J. Schlienger, A. I. Kalfas, and R. S. Abhari. Unsteady, 3-dimensional flow measurement using a miniature virtual 4 sensor fast response aerodynamic probe (frap). In *ASME Turbo Expo 2003, collocated with the 2003 International Joint Power Generation Conference*, volume 1, pages 307–315, Volume 1: Turbo Expo 2003, 2003. doi: 10.1115/GT2003-38128.

[136] Luca Porreca, Marc Hollenstein, Anestis I. Kalfas, and Reza S. Abhari. Turbulence measurements and analysis in a multistage axial turbine. *Journal of Propulsion and Power*, 23(1):227–234, 2007. doi: 10.2514/1.20022.

[137] O. Raghu and J. Philip. Thermal properties of paint coatings on different backings using a scanning photo acoustic technique. *Measurement Science and Technology*, 17 (11):2945–2949, 2006. ISSN 0957-0233 1361-6501. doi: 10.1088/0957-0233/17/11/012.

[138] Clemens Rakenius, Heinz-Peter Schiffer, and Gregor Schmid. The unsteady effect of contoured endwalls on purge flow and secondary flow system in an axial turbine, 2013. URL http://tubiblio.ulb.tu-darmstadt.de/96366/.

[139] Nikhil M. Rao and Cengiz Camci. Axial turbine tip desensitization by injection from a tip trench: Part 1 — effect of injection mass flow rate. In *ASME Turbo Expo 2004: Power for Land, Sea, and Air*, volume Volume 5: Turbo Expo 2004, Parts A and B, pages 1075–1088, 2004. doi: 10.1115/gt2004-53256.

[140] Nikhil M. Rao and Cengiz Camci. Axial turbine tip desensitization by injection from a tip trench: Part 2 — leakage flow sensitivity to injection location. In *ASME Turbo Expo 2004: Power for Land, Sea, and Air*, volume Volume 5: Turbo Expo 2004, Parts A and B, pages 1089–1098, 2004. doi: 10.1115/gt2004-53258.

[141] Patrick S. Rebholz. *Aeromechanical Challenges of Shrouded Low Pressure Turbines for Geared Turbofan Engines*. Thesis, Zurich, ETH Zurich, 2017.

[142] K. Regina, A. I. Kalfas, and R. S. Abhari. Experimental investigation of purge flow effects on a high pressure turbine stage. *Journal of Turbomachinery*, 137(4): 041006–041006–8, 2014. ISSN 0889-504X. doi: 10.1115/1.4028432.

[143] Kai Regina. *High-Pressure Turbines with Novel Airfoils and End Walls Operating under Engine Representative Aero-Thermodynamic Effects*. Thesis, Zürich, ETH-Zürich, 2015.

[144] Abdul Rehman and Bo Liu. Numerical investigation and non-axisymmetric endwall profiling of a turbine stage. *Journal of Thermal Science*, 28(4):811–825, 2019. ISSN 1993-033X. doi: 10.1007/s11630-019-1154-0.

[145] Abdul Rehman, Bo Liu, and Muhammad Afzaal Asghar. Secondary flow and endwall optimization of a transonic turbine. *Energies*, 12(21):4103, 2019. ISSN 1996-1073. URL https://www.mdpi.com/1996-1073/12/21/4103.

[146] Kevin Reid, John Denton, Graham Pullan, Eric Curtis, and John Longley. The effect of stator-rotor hub sealing flow on the mainstream aerodynamics of a turbine. In *ASME Turbo Expo 2006: Power for Land, Sea, and Air*, volume Volume 6: Turbomachinery, Parts A and B, pages 789–798, 2006. doi: 10.1115/gt2006-90838.

[147] M. Rezasoltani, M. T. Schobeiri, and J. C. Han. Experimental investigation of the effect of purge flow on film cooling effectiveness on a rotating turbine with nonaxisymmetric end wall contouring. *Journal of Turbomachinery*, 136(9):091009–091009–10, 2014. ISSN 0889-504X. doi: 10.1115/1.4027196.

[148] Mohsen Rezasoltani, Kun Lu, Meinhard T. Schobeiri, and Je-Chin Han. A combined experimental and numerical study of the turbine blade tip film cooling effectiveness under rotation condition. *Journal of Turbomachinery*, 137(5):051009–051009–12, 2015. ISSN 0889-504X. doi: 10.1115/1.4028745.

[149] M. G. Rose, N. W. Harvey, P. Seaman, D. A. Newman, and D. McManus. Improving the efficiency of the trent 500 hp turbine using non-axisymmetric end walls: Part ii - experimental validation. In *ASME Turbo Expo 2001: Power for Land, Sea, and Air*, volume Volume 1: Aircraft Engine; Marine; Turbomachinery; Microturbines and Small Turbomachinery, V001T03A081, 2001. doi: 10.1115/2001-gt-0505.

[150] A. Roy, S. Jain, S. V. Ekkad, W. Ng, A. S. Lohaus, M. E. Crawford, and S. Abraham. Heat transfer performance of a transonic turbine blade passage in the presence of leakage flow through upstream slot and mateface gap with endwall contouring. *Journal of Turbomachinery*, 139(12):121006–121006–11, 2017. ISSN 0889-504X. doi: 10.1115/1.4037909.

[151] Arnab Roy, Dorian Blot, Srinath Ekkad, WingFai Ng, Andrew Lohaus, and Michael Crawford. Effect of endwall contouring in presence of upstream leakage flow in a transonic turbine blade passage: Heat transfer measurements. In *49th AIAA/ASME/SAE/ASEE Joint Propulsion Conference*, 2013. doi: 10.2514/6.2013-3744. URL https://arc.aiaa.org/doi/abs/10.2514/6.2013-3744.

[152] R. P. Roy, K. D. Squires, M. Gerendas, S. Song, W. J. Howe, and A. Ansari. Flow and heat transfer at the hub endwall of inlet vane passages — experiments and simulations. In *ASME Turbo Expo 2000: Power for Land, Sea, and Air*, volume Volume 3: Heat Transfer; Electric Power; Industrial and Cogeneration, V003T01A006, 2000. doi: 10.1115/2000-gt-0198.

[153] Rolls Royce. *The Jet Engine*. John Wiley & Sons, 5th edition, 2015. ISBN 978-1-119-06599-9. URL https://books.google.ch/books?id=kFEIogEACAAJ.

[154] Arun K. Saha and Sumanta Acharya. Computations of turbulent flow and heat transfer through a three-dimensional nonaxisymmetric blade passage. *Journal of Turbomachinery*, 130(3), 2008. ISSN 0889-504X. doi: 10.1115/1.2776952.

[155] Andrew J. Saul, Peter T. Ireland, John D. Coull, Tsun Holt Wong, Haidong Li, and Eduardo Romero. An experimental investigation of adiabatic film cooling effectiveness and heat transfer coefficient on a transonic squealer tip. *Journal of Turbomachinery*, 141(9), 2019. ISSN 0889-504X. doi: 10.1115/1.4043263.

[156] R. Schädler, A. I. Kalfas, R. S. Abhari, G. Schmid, and S. Voelker. Modulation and radial migration of turbine hub cavity modes by the rim seal purge flow. *Journal of Turbomachinery*, 139(1):011011–011011–10, 2016. ISSN 0889-504X. doi: 10.1115/1.4034416.

[157] Rainer Schädler. *Aerothermal Effects of High-Pressure Turbine Rim Seals and Blade Tip Geometries in the Presence of Cooling Flows.* Thesis, Zurich, ETH Zurich, 2019.

[158] Rainer Schädler, Dominic D. Hänni, Anestis I. Kalfas, Reza S. Abhari, Gregor Schmid, Ewald Lutum, and Carsten Schneider. Noise characteristics of a reduced blade count rotor with improved stage efficiency. *Journal of the Global Power and Propulsion Society*, 3:653–667, 2019. doi: 10.33737/jgpps/112303.

[159] Joël Pierre Schlienger. *Evolution of unsteady secondary flows in a multistage shrouded axial turbine.* Thesis, Zurich, ETH Zurich, 2003.

[160] Robert P. Schroeder and Karen A. Thole. Adiabatic effectiveness measurements for a baseline shaped film cooling hole. In *ASME Turbo Expo 2014: Turbine Technical Conference and Exposition*, volume Volume 5B: Heat Transfer, V05BT13A036, 2014. doi: 10.1115/gt2014-25992.

[161] P. Schuepbach, R. S. Abhari, M. G. Rose, T. Germain, I. Raab, and J. Gier. Improving efficiency of a high work turbine using non-axisymmetric endwalls: Part ii—time-resolved flow physics. In *ASME Turbo Expo 2008: Power for Land, Sea, and Air*, pages 1121–1133, Volume 6: Turbomachinery, Parts A, B, and C, 2008. doi: 10.1115/GT2008-50470.

[162] P. Schuepbach, R. S. Abhari, M. G. Rose, T. Germain, I. Raab, and J. Gier. Effects of suction and injection purge-flow on the secondary flow structures of a high-work turbine. *Journal of Turbomachinery*, 132(2):021021–021021–8, 2010. ISSN 0889-504X. doi: 10.1115/1.4000485.

[163] P. Schuepbach, R. S. Abhari, M. G. Rose, and J. Gier. Influence of rim seal purge flow on the performance of an endwall-profiled axial turbine. *Journal of Turbomachinery*, 133(2):021011–021011–10, 2010. ISSN 0889-504X. doi: 10.1115/1.4000578.

[164] M. Sell, J. Schlienger, A. Pfau, M. Treiber, and R. S. Abhari. The 2-stage axial turbine test facility "lisa". In *Turbo Expo: Power for Land, Sea, and Air*, volume Volume 1, page V001T03A076, Volume 1: Aircraft Engine; Marine; Turbomachinery; Microturbines and Small Turbomachinery, 2001. ISBN 978-0-7918-7850-7. doi: 10.1115/2001-GT-0492.

[165] O. P. Sharma and T. L. Butler. Predictions of endwall losses and secondary flows in axial flow turbine cascades. *Journal of Turbomachinery*, 109(2):229–236, 1987. ISSN 0889-504X. doi: 10.1115/1.3262089.

[166] C. H. Sieverding. Recent progress in the understanding of basic aspects of secondary flows in turbine blade passages. *Journal of Engineering for Gas Turbines and Power*, 107(2):248–257, 1985. ISSN 0742-4795. doi: 10.1115/1.3239704.

[167] Glen Snedden, Dwain Dunn, Grant Ingram, and David Gregory-Smith. The application of non-axisymmetric endwall contouring in a single stage, rotating turbine. In *ASME Turbo Expo 2009: Power for Land, Sea, and Air*, pages 831–840, Volume 7: Turbomachinery, Parts A and B, 2009. doi: 10.1115/GT2009-59169.

[168] H. B. Squire and K. G. Winter. The secondary flow in a cascade of airfoils in a nonuniform stream. *Journal of the Aeronautical Sciences*, 18(4):271–277, 1951. doi: 10.2514/8.1925.

[169] Henry Harrison Suplee. *The Gas Turbine: Progress in the Design and Construction of Turbines Operated by Gases of Combustion.* J.B. Lippincott Company, 1910. ISBN 9780342392667.

[170] A. Suryanarayanan, S. P. Mhetras, M. T. Schobeiri, and J. C. Han. Film-cooling effectiveness on a rotating blade platform. *Journal of Turbomachinery*, 131(1), 2008. ISSN 0889-504X. doi: 10.1115/1.2752184.

[171] A. Suryanarayanan, B. Ozturk, M. T. Schobeiri, and J. C. Han. Film-cooling effectiveness on a rotating turbine platform using pressure sensitive paint technique. *Journal of Turbomachinery*, 132(4), 2010. ISSN 0889-504X. doi: 10.1115/1.3142860.

[172] Phillip Swann, Ingo Jahn, and Hugh Russel. Tayler-couette-poiseuille flow heat transfer in a high taylor number test rig. In *GPPS Beijing 2019*. Global Power and Propulsion Society, 2019. doi: 10.33737/gpps19-bj-149.

[173] James A. Tallman, Charles W. Haldeman, Michael G. Dunn, Anil K. Tolpadi, and Robert F. Bergholz. Heat transfer measurements and predictions for a modern, high-pressure, transonic turbine, including endwalls. *Journal of Turbomachinery*, 131 (2):021001–021001–14, 2009. ISSN 0889-504X. doi: 10.1115/1.2985072.

[174] A. A. Thrift, K. A. Thole, and S. Hada. Effects of orientation and position of the combustor-turbine interface on the cooling of a vane endwall. *Journal of Turbomachinery*, 134(6):061019–061019–10, 2012. ISSN 0889-504X. doi: 10.1115/1.4004817.

[175] Fujuan Tong, Wenxuan Gou, Lei Li, Qingchang Liu, Zhufeng Yue, and Gongnan Xie. Investigation on heat transfer of a rotor blade tip with various film cooling holes arrangements and groove depths. *Advances in Mechanical Engineering*, 7(2): 1687814014568499, 2015. doi: 10.1177/1687814014568499.

[176] C. Waidmann, R. Poser, M. Göhring, and Jens Von Wolfersdorf. First operation of a rotating test rig for transient thermochromic liquid crystal heat transfer experiments. In *XXIV Biennial Sympositum on Measuring Techniques in Turbomachinery*, 2018. URL https://www.meastechturbo.com/paper-archives/2418-prague-2018.

[177] Zuojun Wei, Weiyang Qiao, Peijie Shi, Pingping Chen, and Lei Zhao. Tip-leakage flow loss reduction in a two-stage turbine using axisymmetric-casing contouring. *Chinese Journal of Aeronautics*, 27(5):1111–1121, 2014. ISSN 1000-9361. doi: https://doi.org/10.1016/j.cja.2014.08.009.

[178] Manuel Wilhelm and Heinz-Peter Schiffer. Experimental investigation of rotor tip film cooling at an axial turbine with swirling inflow using pressure sensitive paint. *International Journal of Turbomachinery, Propulsion and Power*, 4(3):23, 2019. ISSN 2504-186X. URL https://www.mdpi.com/2504-186X/4/3/23.

[179] Reinhard Willinger and Hermann Haselbacher. On the modeling of tip leakage flow in axial turbine blade rows. In *ASME Turbo Expo 2000: Power for Land, Sea, and Air*, volume Volume 1: Aircraft Engine; Marine; Turbomachinery; Microturbines and Small Turbomachinery, V001T03A106, 2000. doi: 10.1115/2000-gt-0633.

[180] Tomasz S. Wiśniewski. *Transient Heat Conduction in Semi-infinite Solid with Specified Surface Heat Flux*, pages 6164–6171. Springer Netherlands, Dordrecht, 2014. ISBN 978-94-007-2739-7. doi: 10.1007/978-94-007-2739-7_413.

[181] Lesley M. Wright, Sarah A. Blake, and Je-Chin Han. Film cooling effectiveness distributions on a turbine blade cascade platform with stator-rotor purge and discrete film hole flows. *Journal of Turbomachinery*, 130(3):031015–031015–10, 2008. ISSN 0889-504X. doi: 10.1115/1.2777186.

[182] Luzeng J. Zhang and Ruchira Sharma Jaiswal. Turbine nozzle endwall film cooling study using pressure-sensitive paint. *Journal of Turbomachinery*, 123(4):730–738, 2001. ISSN 0889-504X. doi: 10.1115/1.1400113.

[183] Fangpan Zhong, Chao Zhou, H. Ma, and Q. Zhang. Heat transfer of winglet tips in a transonic turbine cascade. *Journal of Engineering for Gas Turbines and Power*, 139(1), 2016. ISSN 0742-4795. doi: 10.1115/1.4034208.

[184] Diwei Zhu, Qiang Zhang, Shaopeng Lu, and Jinfang Teng. Relative casing motion effect on squealer tip cooling performance at tight tip clearance. *Journal of Thermal Science and Engineering Applications*, pages 1–18, 2020. ISSN 1948-5085. doi: 10.1115/1.4046518.

A. Nomenclature

Symbols

A	Surface area	$[\text{m}^2]$
b	Wien's displacement constant	$[\text{m K}]$
BR	Blowing ratio	$[\text{-}]$
c	Blade chord length	$[\%]$
CC	Correlation coefficient	$[\text{-}]$
c_p	Specific heat capacity	$[\text{J kg}^{-1}\,\text{K}^{-1}]$
C_{pt}	Normalized total pressure	$[\text{-}]$
d	Thickness	$[\text{m}]$
e	Thermal effusivity	$[\text{J K s}^{0.5}\,\text{m}^{-2}]$
E	Total energy radiated per unit surface area per time	$[\text{J s}^{-1}\,\text{m}^{-2}]$
h	Convective heat transfer coefficient	$[\text{W m}^{-2}\,\text{K}^{-1}]$
i	Incidence angle	$[°]$
I	Electrical current	$[\text{A}]$
IR	Purge flow injection ratio	$[\%]$
k	Thermal conductivity	$[\text{W m}^{-1}\,\text{K}^{-1}]$
k	Uncertainty coverage factor	$[\text{-}]$
k_s	Equivalent sand grain roughness parameter	$[\text{µm}]$
l	length	$[\text{m}]$
Nu	Nusselt number	$[\text{-}]$
p	Pressure	$[\text{Pa}]$
P	Electrical power	$[\text{W}]$
$\overline{p}$	time-averaged pressure part	$[\text{Pa}]$

$\tilde{p}$	Periodic pressure part	[Pa]
p'	Random pressure part	[Pa]
PR	Pressure ratio	[-]
$\dot{q}''$	Heat flux	[W m^{-2}]
r	radius	[m]
R	Electrical resistance	[Ω]
Ra	Surface roughness arithmetical mean deviation	[µm]
Rq	Surface roughness root mean squared	[µm]
Rz	Surface roughness maximum height of profile	[µm]
S_q	Local heat flux scaling factor	[-]
St	Stanton number	[-]
t	Layer thickness	[m]
t	Time	[s]
T	Temperature	[K]
TR	Tip coolant ejection ratio	[%]
U	Voltage	[V]
w	width	[m]
y^+	Non-dimensional wall distance	[-]

Greek

α	Thermal diffusivity	[mm^2 s^{-1}]
β	Diameter ratio	[-]
β	Relative flow angle	[°]
δ	Uncertainty in quantity	
Δ	Change in quantity	
ε	Surface emissivity	[-]
η	Efficiency	[-]
η	Cooling effectiveness	[-]
λ	Wavelength	[m]
Π	Turbine pressure ratio	[-]

ρ	Electrical resistivity	$[\Omega\,\text{m}]$
ρ	Density	$[\text{kg}\,\text{m}^{-3}]$
σ	Stefan-Bolzmann constant	$[\text{W}\,\text{m}^{-1}\,\text{K}^{-4}]$
τ	Thermal diffusivity time constant	$[\text{s}]$
ϕ	Flow coefficient	$[\text{-}]$
ψ	Stage loading	$[\text{-}]$

Subscripts

∞	Bulk fluid / main flow
0	Total or stagnation quantity
0	Zero tip coolant ejection rate
2	Design tip coolant ejection rate
ad	adiabatic
aw	adiabatic wall
ax	axial
bypass	Bypass air
c	compressor
c	coolant
cond	conduction
conv	convective
cross	cross-sectional
el	electric
in	Turbine inlet
leakage	Leakage flow
main	Main Flow
purge	Purge flow
rad	radiative
ref	reference quantity
rel	relative frame

s	solid body
span	blade span
sub	substrate
surf	surface
w	wall
x	Axial coordinate

Abbreviations

5HP	Five hole probe
blisk	Bladed rotor disk
CAD	Computer-aided design
CFD	computational fluid dynamics
CFX	Computation fluid dynamics software by Ansys
DAQ	Data acquisition
DLR	Deutsches Zentrum für Luft- und Raumfahrt / German Aerospace Center
DLT	Direct linear transformation
ETH	Swiss Federal Institute of Technology Zurich / Eidgenössische Technische Hochschule Zürich
EULER	High performance computer cluster at ETH Zurich
EWC	Endwall contouring
FEM	Finite element method
FENT	Fast response entropy probe
FRAP	Fast response aerodynamic probe
G-code	Computer numerical control programming language
GUM	Guide to the Expression of Uncertainty in Measurements
HTC	Heat transfer coefficient
ICAO	International Civil Aviation Organization
IR	Infrared

LEC	Laboratory for Energy Conversion
LISA	Axial research turbine at ETH Zurich
LWIR	Long-wavelength infrared band
MCT	Mercury cadmium telluride
Nd:YAG	Neodymium-doped yttrium aluminium garnet
OD	Off-design operating point
OECD	Organisation for Economic Co-operation and Development
PEEK	Polyether ether ketone (material)
p.p.	Percentage points
PVD	Physical vapor deposition
R	Rotor
RANS	Reynolds Averaged Navier-Stokes equation
RMS	Root mean square
RS	Rotor-Stator
S1	First stator
S2	Second stator
SST	Shear stress transport model
TLC	Thermochromic Liquid Crystals
ZnSe	Zinc selenide

B. List of Publications

Journal Publications

Hänni, D. D., Schädler, R., Abhari, R. S., Kalfas, A. I., Schmid, G., Lutum, E., & Lecoq, N. (2019). "Purge flow effects on rotor hub endwall heat transfer with extended endwall contouring into the disk cavity". Journal of the Global Power and Propulsion Society, 3, 555-568. doi:10.22261/jgpps.Kbbd71

Schädler, R., Hänni, D. D., Kalfas, A. I., Abhari, R. S., Schmid, G., Lutum, E., & Schneider, C. (2019). "Noise characteristics of a reduced blade count rotor with improved stage efficiency". Journal of the Global Power and Propulsion Society, 3, 653-667. doi:10.33737/jgpps/112303

Conference Contributions

Hänni, D. D., Schädler, R., Abhari, R. S., & Kalfas, A. I. (2019). "Variable Blade Tip Geometry Inserts for Combined Aerothermal Measurements for Bladed Disk Rotors". Paper presented at the GPPS Beijing Conference 2019, Beijing, China.

Hänni, D. D., Schädler, R., Abhari, R. S., Kalfas, A. I., Schmid, G., Lutum, E., & Lecoq, N. (2019, 15th-16th January). "Purge Flow Effects on Rotor Hub Endwall Heat Transfer with Extended Endwall Contouring into the Disk Cavity". Paper presented at the Global Power and Propulsion Technical Conference 2019, Zurich, Switzerland.

Schädler, R., Hänni, D. D., Kalfas, A. I., Abhari, R. S., Schmid, G., Lutum, E., & Schneider, C. (2019, 15th-16th January). "Noise Characteristics of a Reduced Blade Count Rotor with Improved Stage Efficiency". Paper presented at the Global Power and Propulsion Technical Conference 2019, Zurich, Switzerland.